Distribution Agreement

Signature:

Robert Lemasters	Date

Hot-Carrier Induced Nonlinear Optics in Plasmonic and Nanophotonic Systems

By
Robert Lemasters
Doctor of Philosophy
Physics

Hayk Harutyunyan, Ph.D
Advisor

Sidong Lei, Ph.D
Committee Member

Connie Roth, Ph.D
Committee Member

Ajit Srivastava, Ph.D
Committee Member

Sergei Urazhdin, Ph.D
Committee Member

Accepted:

Lisa A. Tedesco, Ph.D.
Dean of the James T. Laney School of Graduate Studies

Date

Hot-Carrier Induced Nonlinear Optics in Plasmonic and Nanophotonic Systems

By

Robert Lemasters
B.S. *cum laude*, College of Charleston, 2015

Advisor: Hayk Harutyunyan, Ph.D.

An abstract of
A dissertation submitted to the Faculty of the
James T. Laney School of Graduate Studies of Emory University
in partial fulfillment of the requirements for the degree of
Doctor of Philosophy
in Physics
2021

Abstract

Nonlinear optics describes a wealth of exciting phenomena. This includes ultrafast optical responses, frequency conversion, multiphoton processes, and enhancement of “forbidden” light-matter interactions. Some of the most novel of these effects are attributed to out-of-equilibrium or “hot” carrier dynamics. The scope of this dissertation is to discuss hot-carrier roles in plasmonic and nanophotonic systems composed of metallic and semiconducting materials.

Chapter 1 presents an outline of the relevant physics for reference of the reader for later chapters.

Chapter 2 contains a study of nonlinear light emission from spatially confined plasmonic nanostructures. A geometry of Au nanowires separated from Au films by nanometric SiO_2 layers controls the degree of spatial confinement of the resonant gap-mode plasmons, and thus probes the degree of momentum breakdown and its effect on photoluminescence (PL). Our results indicate that the PL signal from this nanoscale system has a nonlinear power law exhibiting two distinct linear regimes, differing from that of rough films, indicating that the physical mechanism of the nonlinear PL signal involving hot-carriers needs to be revisited.

Chapter 3 introduces a method for sputtering record-thin fully percolated Au films on an oxide substrate. We demonstrate wetting layer-free plasmonic gold films with thicknesses down to 3 nm obtained by deposition on substrates cooled to cryogenic temperatures. We systematically study the effect of substrate temperature on the properties of the deposited Au films, and show that substrate cooling suppresses the Vomer-Webber growth mode of Au, promoting early-stage formation of continuous Au films with improved surface morphology and enhanced optoelectronic properties.

Chapter 4 concludes with observations of negative extinction and sub-picosecond injected hot-carrier dynamics in an active amorphous Ge metasurface. We report pump–probe measurements performed on amorphous-Ge-based micro-resonator metasurfaces that exhibit strong resonant modes in the mid-infrared. We observe relative change in transmittance of $\Delta T/T \approx 1$ with subpicosecond ($\tau \sim 0.5$ ps) modulation speed, obtained with very low pump fluences of 50 μJ/cm^2. We attribute these observations to efficient free carrier promotion affecting light transmittance via high quality-factor optical resonances, followed by an increased electron-phonon scattering of free carriers due to the amorphous crystal structure of Ge.

Hot-Carrier Induced Nonlinear Optics in Plasmonic and Nanophotonic Systems

By

Robert Lemasters

B.S. *cum laude*, College of Charleston, 2015

Advisor: Hayk Harutyunyan, Ph.D.

A dissertation submitted to the Faculty of the

James T. Laney School of Graduate Studies of Emory University

in partial fulfillment of the requirements for the degree of

Doctor of Philosophy

in Physics
2021

Acknowledgments

There are so many people to thank for helping me get to this point. None of it is possible without you.

I want to thank everyone on my committee Ajit, Connie, Sergei and Sidong, for all the time and guidance they have given me. I want to thank Hayk for taking me into his lab and giving me a shot. I have learned so much from my time here and I feel that we got a lot accomplished together. Now I feel confident that I've acquired the tools I need to be successful in the future. To the staff here in the department, Barbara, Susan, J-Boss, Tom, Jose, Lowell, Horace, none of this work (or anyone else's in the department) is possible without your behind the scenes support. You all don't get nearly enough credit for the support you provide, and I want to thank you for it. I am grateful to all the professors here and the relationships I've built here. I want thank all the friends I've made here. You know who you are. This PhD process has been maybe the hardest thing I've ever seen through in my life, but you made it bearable.

I want to thank all my teachers at CofC, especially DW, Dr. Penny, Dr. Marshall, Dr. Preyer, Kat, and NK. You gave me a world-class education and a completely unfair advantage because of it. To Dr. Larsen, you are the best teacher I've ever had. Hands down. The standards you have always set for us and yourself have molded me into the person and scientist I am today. You always challenged me and I'm better for it. Please don't ever think that the efforts you make aren't important. Because for me, they were essential. To J, our conversations have always kept me going. There have been times where I have felt burnt out with research, but our talks have always only served to rekindle those good feelings about physics again. To all my friends at CofC, especially lil' Josh and Derek, you guys are great and I miss you.

Finally, I want to thank my family. My Mom, who has always been a rock in my life. She has been so supportive during both the good and bad times. Every interest I've ever had in my life was followed by you doing everything you could do to provide support for them. Whether it was physics, music, sports, or whatever, you never hesitated to bend over backwards if you thought it would help me in any way. I wouldn't be anywhere in life without the nurturing I got from you. My Dad, who always makes a point to get everyone together in the evening to see the sun go down, watch the colors change, and wait for the stars and planets to come out. And to this day continues to harangue me with his crazy dark matter theories (for some reason, gin and tonics seem to exacerbate this...). You helped me to see nature through a scientific perspective. And you put me through my education and left nothing wanting in that area. My sister Kim, who let me stay in her house when I was getting into school and even introduced me to DW from the physics department at CofC to which I eventually attended to start my career. Those were strange times in my life, and you helped me through it. But then again, you've always had my back and been an ally. Any bully of mine had better beware of you. My brother James, who helped spark my interest in physics by always challenging me with strange ideas to think about when we were growing up. Like why things fall back down when you toss them up. I remember we were at a bookshop and there was an astronomy book on display. You immediately knew what I was thinking, and so you told me that I was able to learn it if I really wanted to. That thought would have never occurred to me. To my aunts Debbie, Jeanne and Sue. Debbie and Sue, having your care packages and being able to have family support here in Atlanta was crucial. I don't think I would have made it through all this without having our visits to count on. I don't know how much longer I'll be here, but when I do leave, I am going to miss them dearly, but I'll remember them with great affection. Jeanne, I keep all the letters you sent to me over the years. I know I can always count on them and they brighten my day. I am always reminded that there is someone out there thinking of me. Also, I don't think anyone was more excited than you were when I got Scully. And I'm so glad we got to share that. To Anna-Liisa, you helped me get established down in Charleston and to take care of me as I did. As crazy as we all can get when we get together, you have always been around to play conciliator. All of our family relationships have improved since you came along. To Irma, the Moore's, and the Minter's, I love you all and I miss you. To my lifelong friends Erik, Nick, Drew, and Whit. You guys are the best. I'm so grateful for your friendship, but I consider you family. Whit, having you around in Atlanta made a huge difference for me. Us getting together and playing music together is something I could always count on and look forward to. Lastly, (and unironically) I want to acknowledge my cat, Scully. You got me through some dark times. And I love you.

I've had a hundred 2nd chances in my life. I know you're lucky to have even one person in your life who is always in your corner. But it seems like everywhere I look in my life, I see someone just like that.

Contents

List of Figures

List of Tables

Chapter 1

Introduction

1.1 Chapter Overview

Nanophotonics and plasmonics are an integral component to emerging fields in modern optics. Additionally, many applications in biological sensing, photocatalyst, and optical characterization techniques such as surface enhanced Raman scattering (SERS) are fundamentally possible through an established understanding of plasmonics. One of the most fascinating aspects of these subjects from a physics point of view is that these fields border on the classical and quantum regimes of electromagnetism, optics and material physics. The field of nano-optics is fundamentally based around nanoscale modes of optical fields. That is, classical solutions to Maxwell's equations solved for matter with geometries on the nanometer or micrometer scale. Excitations of these modes can be purely electromagnetic, known as "photonic" modes, or as as charge density oscillations, known as "plasmons." Manipulation and applications of these modes constitutes the field of photonics and plasmonics, respectively.

Photonic modes typical exist on either dielectric or semiconducting microresonators which are well described by classical Mie theory, but can also be propagating such as with fiber optic cables. Modes of these type have been seen to have incredibly long lifetimes. This allows a method of essentially "trapping" electromagnetic energy in the volume of these microresonators. This is attractive for light-matter interaction applications as enhancement can be achieved simply by the shear length of time that the mode energy is stored in one location. Another consequence of these long lifetimes are that these modes are sensitive to induced damping as their bandwidths are typically very narrow. This has applications in ultrafast signal modulation, a subject which will be the main focus of chapter 4.

Plasmon modes can propagate along interfaces of metals and dielectrics (surface plasmons) or be localized to resonate as classical Mie modes on metal nanoparticles, sometimes referred to as localized surface plasmon resonances (LSPRs). Plasmonic fields typically decay over very small distances, on the order of nanometers. When free-space light is made to couple with these plasmon modes, the result is a substantial spatial concentration of the electric field over very small regions.

Strong electric fields are always exciting from a physicist's point of view. Interesting things tend to happen when they are present. Classical electromagnetic phenomena such as frequency conversion in nonlinear optics and measurable Raman scattering are only possible in the presence of intense fields. In the Quantum regime, some of the most fascinating light-matter interactions are facilitated via their presence. Higher order "forbidden" electronic transitions such as electric quadrupole and momentum-assisted transitions as well as multi-photon absorption may be made made possible or significantly enhanced through the presence of strongly localized electric fields mediating the process.

Such enhancement of light-matter interactions can also lead to efficient promotion of highly energetic excited, or "hot" carriers from photo-excitation. The overall promotion, distributions and specific relaxation dynamics of hot carriers themselves can give rise to new physical processes. Additionally, advances in nano-fabrication allow engineering of metasurfaces to facilitate hot-carrier promotion, which can realize these novel physical phenomena experimentally. Several examples of this are highlighted in this thesis.

Preliminaries of the necessary fundamental physics in this thesis are given in this chapter. Many of the derivations and examples are given from books which are considered the primary resources ("Bibles") of their respective field. These sources include but are not limited to "Principles of Nano-Optics" by Lukas Novotny and Bert Hecht [1], "Electrodynamics of Continuous Media" by Lev Landau and Evgeny Lifshitz [2], "Nonlinear Optics" by Robert Boyd [3], "Fundamentals of Photonics" by Bahaa E. A. Saleh and Malvin C. Teich [4], "Optical Properties of Metal Clusters" by Uwe Kreibig and Michael Vollmer [5] and "Absorption and scattering of light by small particles" by Craig F. Bohren and Donald R. Huffman [6]. Another great resource referenced here are the online open-source lectures made available by Rick Trebino [7]. These lectures cover everything from basic optics, nonlinear and ultrafast optics, and principles of lasing, to ultrashort pulse creation and the technological fundamentals of the instrumentation used to realize these effects in modern research. I would advice the reader to seek out these sources if they are interested on the subjects presented in this thesis.

The following sections in this chapter are given to act as references and supplemental information for the physics used in sequential chapters of this dissertation. It is outlined in a way to hopefully give the reader a guideline and better outlook of the main substance of the thesis without being too detailed. Some sections are written with more brevity than others as necessary. Sections of more esoteric subjects are given in greater detail and with more references within.

1.2 Electromagnetism Review

1.2.1 Maxwell's Equations in Continuous Media

Maxwell's equations in a general form are given as

$$\vec{\nabla} \times \vec{E}(\vec{r},t) = -\frac{\partial \vec{B}(\vec{r},t)}{\partial t} \tag{1.1}$$

$$\vec{\nabla} \times \vec{H}(\vec{r},t) = -\frac{\partial \vec{D}(\vec{r},t)}{\partial t} + \vec{j}(\vec{r},t) \tag{1.2}$$

$$\vec{\nabla} \cdot \vec{D}(\vec{r},t) = \rho(\vec{r},t) \tag{1.3}$$

$$\vec{\nabla} \cdot \vec{B}(\vec{r},t) = 0, \tag{1.4}$$

where $\vec{E}$ is the electric field, $\vec{B}$ is the magnetic field, $\vec{H}$ is the auxilary magnetic field, $\vec{D}$ is the electric displacement field, $\vec{j}$ is the current density, and ρ is the charge density. The constituent fields, $\vec{D}$ & $\vec{H}$ are given as

$$\vec{D}(\vec{r},t) = \epsilon_0 \vec{E}(\vec{r},t) + \vec{P}(\vec{r},t) \tag{1.5}$$

$$\vec{H}(\vec{r},t) = \frac{1}{\mu_0}\vec{B}(\vec{r},t) - \vec{M}(\vec{r},t), \tag{1.6}$$

where $\epsilon_0 = 8.854\ 10^{-12}\ \mathrm{C \cdot V^{-1} m^{-1}}$ is the vacuum permittivity and $\mu_0 = 1.257\ 10^{-6}\ \mathrm{V \cdot s \cdot A^{-1} m^{-1}}$ is the vacuum permeability. In a medium, these constituent equations take the form

$$\vec{D}(\vec{r},t) = \epsilon_0 \epsilon \vec{E}(\vec{r},t), \qquad \vec{P}(\vec{r},t) = \epsilon_0 \chi_e \vec{E}(\vec{r},t) \tag{1.7}$$

$$\vec{B}(\vec{r},t) = \mu_0 \mu \vec{H}(\vec{r},t), \qquad \vec{M}(\vec{r},t) = \mu_0 \chi_m \vec{H}(\vec{r},t), \tag{1.8}$$

where ϵ & μ are the relative permittivity and permeability, and χ_e & χ_m are the electric and magnetic susceptibility. For linear isotropic media, these are constants, but in general they take a tensor form.

1.2.2 Free Electron Model and the Plasma Frequency

One of the defining features of metals are the presence of free electrons. Most of the characteristics of a metal such as it's optical and electronic responses can be understood by analyzing the free electron response. It is common practice to assume a "free" electron model in which the electrons are free to move unbounded to the positively charged lattice structure. With this point of view a metal may be considered similar to a plasma. By considering the response of electrons to an external field we may use this fact to determine a metals properties.

Consider charge-neutral metal sheet with a rigid ionic lattice and a free electron gas. Suppose a surface charge of $\pm\sigma = en\Delta z$ has built up on either side where e is the elementary charge, n is the charge carrier density and Δz is the displacement of the surface charge from equilibrium. This is illustrated in Fig. 1.1. This distribution will create a uniform homogeneous electric field between the two sides. This will result in a restoring force that acts on the electrons with an equation of motion of

$$m\frac{\mathrm{d}^2}{\mathrm{d}t^2}(\Delta z) = -eE = -\frac{ne^2}{\epsilon_0}\Delta z, \tag{1.9}$$

where m is the electron mass. This is the equation for a harmonic oscillator with frequency,

$$\omega_p = \sqrt{\frac{ne^2}{m\epsilon_0}}. \tag{1.10}$$

This quantity, ω_p, is called the Plasma Frequency. Materials have a characteristic ω_p which depends on the electron density of the material which can range from 2 to 20 eV.

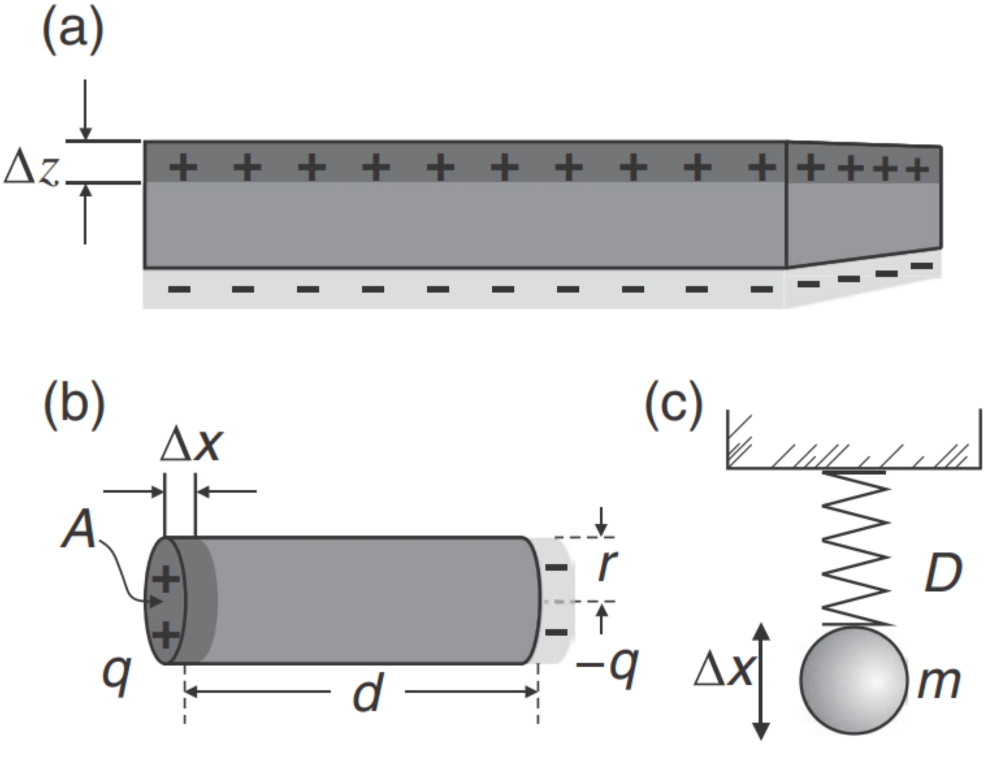

Figure 1.1: Simplified model for oscillating electronic response adapted from [1]. (a) Bulk response of an electron gas experiencing a displacement. (b) Particle plasmon resonance modeled as a capacitive displacement of charge dependent on the specific geometry. (c) Simple harmonic spring to model plasmonic response.

1.2.3 Permittivity (Drude and Interband Model)

The permittivity, ϵ, can be thought of as a measure of a materials response to an externally applied electric field. It is in general complex valued in the form

$$\epsilon = \epsilon' + i\epsilon'', \tag{1.11}$$

where ϵ' the real component and ϵ'' is the imaginary one. Both of the complex components have simple physical interpretations. These are visualized in Fig. 1.2. The real component corresponds to the strength and direction of the materials polarization response to an applied external field, the sign of which ($\pm$) corresponds to an aligned or anti-aligned response (a metal will try to cancel out and neutralize the external field in general, i.e. $\epsilon' < 0$), respectively. This sign flips and crosses $\epsilon' = 0$ at the plasma frequency for the Drude model and an internal resonance in the interband model described next. This corresponds to the electronic response be able to "catch up" to external field frequency given how they are collectively allowed to oscillate at the resonant conditions of the material. When the material aligns with the field, the response can be thought of as a "dielectric response" analogous to the field inside a capacitor. The imaginary component represents the phase of the polarization to the external field. The phase relation of these quantities determines the attenuation of the field into the medium, and so can be interpreted as the energy loss/gains of the material. This is made clearer below when we describe the optical material response in terms of damped driven oscillators where imaginary components naturally represent gains and losses. By a sign convention, positive imaginary components correspond to out-of-phase response and represent losses/damping. Negative imaginary components represent in-phase responses which implies gain. This is found in for example the gain media with population inversion used in lasing systems. These interpretations are especially important to keep in mind for section 3 where the improved plasmonic performance of thin Au films is quantified by ϵ' and ϵ'' values.

For metals, the optical response can be broken into two regimes: one for the conduction electrons, and the other for bound electrons. The physical reason for this distinction is due to the presence of an atomic like resonance in the otherwise homogeneous interactions in the medium which must be accounted for when finding the total resonance. In general then [8], the overall response that determines the optical properties of noble metals such as gold, $\epsilon(\omega)$, is given by

$$\epsilon(\omega) = \epsilon_D(\omega) + \epsilon_I(\omega), \tag{1.12}$$

where ϵ_D is the permittivity for the conduction electrons given by the so-called Drude model and ϵ_I is the permittivity due to the presence of an interband resonance which accounts for the valence, or bound, electrons.

From the constituent relations for Maxwell's equations in matter in section 1.2.1 we have

$$\vec{P} = \epsilon_0 \chi_e(\omega) \vec{E} \tag{1.13}$$

$$\vec{D} = \epsilon_0 \epsilon(\omega) \vec{E} = \epsilon_0 \vec{E} + \vec{P}, \tag{1.14}$$

where χ_e is the electric susceptibility, $\vec{P}$ is the macroscopic polarization, $\vec{D}$ is the induced electric displacement, and $\vec{E}$ is the electric field. From these two relations we get

$$\epsilon(\omega) = 1 + \chi_e(\omega). \tag{1.15}$$

We start first with the Drude term. To calculate $\vec{P}$ and χ_e we must calculate the electronic displacement, $\vec{r}$. An electron in an applied electric field will experience a displacement, $\vec{r}$, which will induce a dipole moment of $\vec{p} = e\vec{r}$. For a material with a concentration, n, of these dipoles, we get a polarization of

$$\vec{P}(\vec{r}) = n\vec{p} = ne\vec{r}. \tag{1.16}$$

Next, we solve for the equation of motion of the conduction electrons to get $\vec{r}$. The equation of motion is

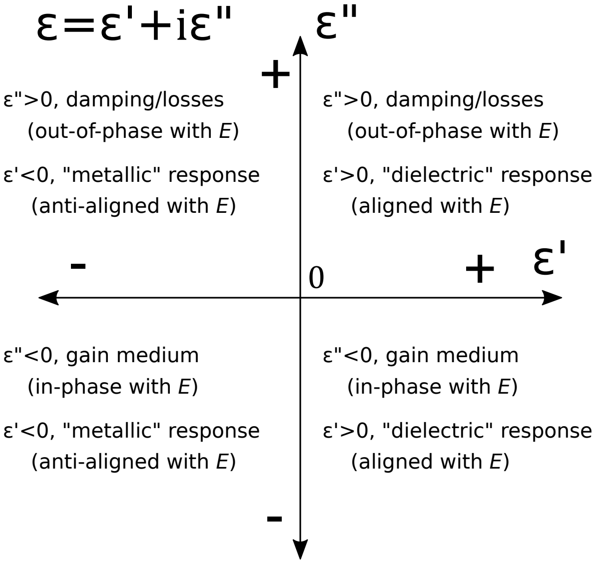

Figure 1.2: Physical interpretations of the real and imaginary components of the permittity, ϵ.

given as

$$m_e \frac{\partial^2 \vec{r}}{\partial t^2} + m_e \Gamma \frac{\partial \vec{r}}{\partial t} = e\vec{E}_0 \mathrm{e}^{-i\omega t} \tag{1.17}$$

where e & m_e are the electron charge and mass, and $\vec{E}_0$ & ω are the amplitude and frequency of the applied electric field. The second term acts as a damping term, and Γ captures the various scattering that the electron will experience. The finer details of Γ is discussed in section 1.4.2. This is the equation for a damped driven oscillator, so we assume a solution of $\vec{r}(t) = \vec{r}_0 \mathrm{e}^{-\omega t}$. From this, we can plug into the equations of motion in Eq. 1.17 to get

$$\epsilon_D = 1 - \frac{\omega_p^2}{\omega^2 + i\Gamma\omega} \tag{1.18}$$

These equations of motion can be the same as for the example given in section 1.2.2 except with the addition of a damping term. It should be no surprise that ω_p shows up again, and indeed it does. We see the importance of the free electron plasma model in describing metals. The real and imaginary components, ϵ'_D & ϵ''_D, can be separated to give

$$\epsilon'_D = 1 - \frac{\omega_p^2}{\omega^2 + \Gamma^2} \tag{1.19}$$

$$\epsilon''_D = \frac{\Gamma\omega_p^2}{\omega(\omega^2 + \Gamma^2)}. \tag{1.20}$$

The real and imaginary components of ϵ_D can be seen in Fig 1.3 (a). The Drude model, however, does not account for interband transitions that may occur in metals. This model is only strictly valid for the infrared region as interband transitions typically occur in the visible to ultraviolet. The electrons involved in these interband transitions will be the bound electrons in the inner valence shells rather than free conduction electrons. These carriers may be excited to the conduction band given incident radiation with energy of that of the band gap.

Now we address the response of bound electrons in a metal. The equation of motion will be

$$m \frac{\partial^2 \vec{r}}{\partial t^2} + m\gamma \frac{\partial \vec{r}}{\partial t} + \alpha \vec{r} = e\vec{E}_0 \mathrm{e}^{-i\omega t} \tag{1.21}$$

where m is the effective mass of the bound electrons which in general will be different from that of a free electron, γ represents the radiative damping, and α is the restoring spring constant off the bound electrons. The same harmonic oscillator may be assumed which yields

$$\epsilon_I = 1 + \frac{\tilde{\omega}_p^2}{(\omega_0^2 - \omega^2) - i\gamma\omega}, \tag{1.22}$$

where $\tilde{\omega}_p = \sqrt{\tilde{n}e^2/m\epsilon_0}$ and $\tilde{n}$ is the bound electron density. The real and imaginary components, ϵ_I' & ϵ_I'', can be separated to give

$$\epsilon_I' = 1 + \frac{\tilde{\omega}_p^2(\omega_0^2 - \omega^2)}{(\omega_0^2 - \omega^2)^2 + \gamma^2\omega^2} \tag{1.23}$$

$$\epsilon_I'' = \frac{\gamma\tilde{\omega}_p^2\omega}{(\omega_0^2 - \omega^2)^2 + \gamma^2\omega^2}. \tag{1.24}$$

With both ϵ_D & ϵ_I solved for the total permmitivity may be given by the sum of the two. However, depending on the relevant spectral range you are interested in, simplifications can be made. Typically, the Drude model is valid only for frequencies far from any interband resonance while the interband model is valid for frequencies near them. For gold, this cutoff happens for wavelengths shorter than around 600 nm when bound electrons begin to have a significant influence. As interband resonances will keep appearing at shorter wavelengths and will appear to "pile up" in the short wavelength as more spectral resolution would

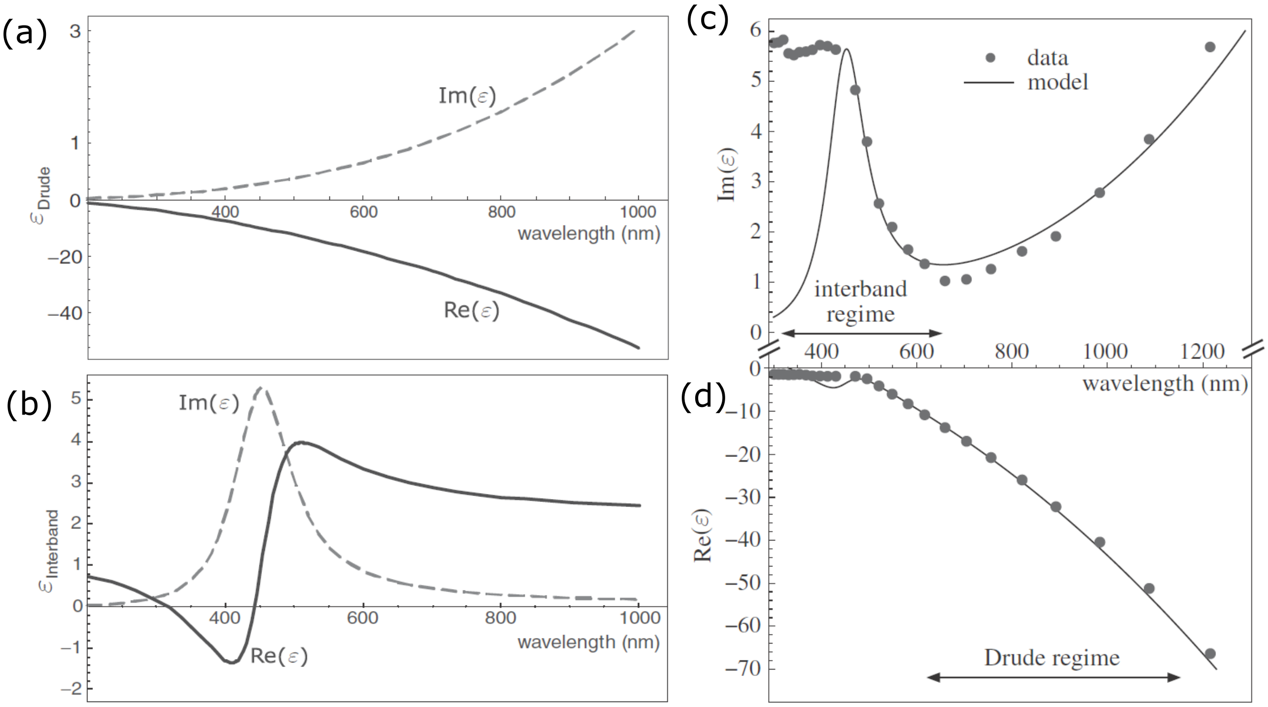

Figure 1.3: (a) Drude, (b) interband, and the (c) imaginary and (d) real components of the Drude + interband permittivies [1].

be needed to distinguish them. For this reason an offset usually referred to as ϵ_∞ is used to approximate in the so-called interband region. Such is the case in Fig. 1.3 c where a value of $\epsilon_\infty \approx 5.6$ is used as an offset to capture this region.

1.2.4 Kramers - Kronig Relations (ϵ' & ϵ'' Correspondence)

In general the electromagnetic response of a medium to stimuli can be represented by it's permittivity, $\epsilon(\omega)$, as

$$\vec{D}(t) = \vec{E}(t) + \int_0^\infty f(\tau)\vec{E}(t-\tau)\ \mathrm{d}\tau, \tag{1.25}$$

where $f(\tau)$ is the response of the system at some previous time, τ. ϵ is in general a complex variable as previously discussed. This formulation essentially ensures causality in the response of the system: The present response of the system can only be a function of it's previous history (τ is integrated from $-\infty$ to $t = 0$). The imposed causality restrictions captured in eq. 1.25 has important consequences for the relationship between the real and imaginary components of the permittivity. By Fourier transforming the electric field in the relationship of eq. 1.25, the permittivity may be written as

$$\epsilon(\omega) = 1 + \int_0^\infty f(\tau)e^{-i\omega t}\ \mathrm{d}\tau. \tag{1.26}$$

As ϵ is complex valued, eq. 1.26 must be integrated over the complex plane. As shown in [2], the appropriate contour integration of eq. 1.26 over the complex plane yields, after using Cauchy's residue theorem, a characteristic equation of

$$P\int_{-\infty}^{+\infty} \frac{\epsilon(\omega)-1}{\omega-\omega_0}\ \mathrm{d}\omega - i\pi\left[\epsilon(\omega_0)-1\right] = 0, \tag{1.27}$$

where P is principal value of the contour integration. Separating the real and imaginary components of ϵ then yields

$$\epsilon'(\omega) = 1 + \frac{1}{\pi}P\int_{-\infty}^{+\infty} \frac{\epsilon''(\Omega)}{\Omega-\omega}\ \mathrm{d}\Omega \tag{1.28}$$

$$\epsilon''(\omega) = -\frac{1}{\pi}P\int_{-\infty}^{+\infty} \frac{\epsilon'(\Omega)-1}{\Omega-\omega}\ \mathrm{d}\Omega. \tag{1.29}$$

Thus, we see that the real and imaginary components of the permittivity are coupled to one another. The interpretation of this is that a change in one component of the permittivity will necessarily change the other and vise versa. This effect is due simply to requiring causality to the material response, which is a strong statement. This is a powerful tool in photonics/plasmonics, especially when accounting for ultrafast changes to the electronic and optical properties of a system. A example of this will be given in Section 4.

1.2.5 Nonlinear Optics

Nonlinear optics describes electromagnetic interactions when dealing with very intense electric fields. In particular, when these intense optical fields push the electrons in some media so far out of equilibrium, the polarization must be described nonlinearly to correctly account for the resulting material response. Intense fields such as this are present in the near vicinity of plasmonic nanoparticles. As such, applications and platforms for the enhancement of nonlinear optical effects often employ plasmonic nanoparticles to mediate the process via field enhancement [9–11].

In optics, an electrons response to an external electric field is typically modeled as a harmonic oscillator as in a mass and spring model. However, there is nothing dictating that this must always be the case. In general an electrons motion can be quite complex depending on the nature of the restoring force potential with the lattice. This is expected to be the case especially when dealing with light fields of high intensity and the electrons experience a higher electric field amplitude. In general, the general response of the electrons may be written in terms of the polarizability, $\vec{P}(t)$, as

$$\vec{P}(t) = \epsilon_0 \left(\chi^{(1)} \vec{E}(t) + \chi^{(2)} \vec{E}^2(t) + \chi^{(3)} \vec{E}^3(t) + ... \right), \tag{1.30}$$

where $\chi^{(n)}$ is the nth order susceptibility tensor. At first glance, eq. 1.30 may appear as simply a Taylor type expansion series which is used for slightly more correct approximations by including more terms. However, each single term in this series actual contains a rich collection of physical phenomena, the more exotic of which are captured in the increasingly higher order terms.

This is better illustrated by examining the first few terms. First, we consider a time harmonic incident light field of, $E = E_0 \cos(\omega t)$. The first term in in eq. 1.30 is simply

$$\epsilon_0 \chi^{(1)} \vec{E}(t) = \epsilon_0 \chi^{(1)} E_0 \cos(\omega t). \tag{1.31}$$

This of course is just the familiar linear response of the polarization to an external applied field. A physical quantity determined from this first term is the index of refraction, n_0, of a material given by [12]

$$n_0^2 = \left(n_0' + i n_0''\right)^2 = 1 + \chi^{(1)}. \tag{1.32}$$

The 2nd term when expanded gives

$$\epsilon_0\chi^{(2)}\vec{E}^2(t) = \epsilon_0\chi^{(2)}\left[E_0\cos(\omega t)\right]^2 \simeq \underbrace{\frac{1}{2}\epsilon_0\chi^{(2)}E_0^2}_{\text{OR}} + \overbrace{\epsilon_0\chi^{(2)}E_0^2\cos(2\omega t)}^{\text{SHG}}, \tag{1.33}$$

where OR stands for optical rectification and SHG stands for second harmonic generation. The OR term represents physically a static uniform field in the nonlinear medium. The SHG term represents a new frequency component emerging in the nonlinear medium at twice the incident frequency.

Expanding the third term yields

$$\epsilon_0\chi^{(3)}\vec{E}^3(t) = \epsilon_0\chi^{(3)}\left[E_0\cos(\omega t)\right]^3 \simeq \underbrace{\frac{3}{4}\epsilon_0\chi^{(3)}E_0^3\cos(\omega t)}_{\sim\Delta\text{n}} + \overbrace{\frac{1}{4}\epsilon_0\chi^{(3)}E_0^3\cos(3\omega t)}^{\text{THG}}, \tag{1.34}$$

where THG stands for third harmonic generation which corresponds to new frequencies at triple the incident field. The 1st term is labeled as $\sim \Delta n$. In fact this term adds to the index of refraction as it is also proportional to the incident field at the same frequency as in eq. 1.31. This index of refraction for this nonlinear term, n_2, is given as [3]

$$n_2 = \frac{3}{4n_0^2\epsilon_0 c}\chi^{(3)} \tag{1.35}$$

This term is responsible for the nonlinear Kerr effect which is a nonlinear change in the index of refraction. Because of the extra factor of E_0^2, the contribution of n_2 scales nonlinearly with the incident field intensity to give the total index of refraction as

$$n_{\text{Kerr}} = n_0 + n_2 I, \tag{1.36}$$

where $I = \frac{1}{2}n_0\epsilon_0 c E_0^2$. This change in refractive index originates physically from the nonlinear promotion of electrons to higher states, effectively altering the electron density of the material. As evident by eqs. 1.10 & 1.18 the electron density plays a large role in determining the optical and electronic response. This effect is important to reference in chapter 4.

For an arbitrary optical emission signal, $\phi(\omega)$, which has an unknown nonlinear response corresponding to an excitation power of I can be expressed as

$$\phi(\omega) \propto I^{p(\omega)}, \tag{1.37}$$

where $p(\omega)$ is the power scaling exponent for a signal at frequency, ω. As discussed above, many nonlinear signals may be present and can overlap with one another, especially at increasingly higher excitation powers. For some analysis purposes it is useful to extract the effective scaling exponent for a particular frequency which represents an average of all the nonlinear contributions at that same frequency. For some reference value, ϕ_0, at a power, I_0, the power law corresponding to each frequency, ω can be extracted as

$$p(\omega) = \frac{\mathrm{d}}{\mathrm{d}\log\left(\frac{I}{I_0}\right)} \log \frac{\phi(\omega)}{\phi_0(\omega)}. \tag{1.38}$$

This analysis is directly applied in chapter 2.

1.3 Nanoparticle Optics

1.3.1 Particle Plasmon Resonance

The free-electron-plasma response in section 1.2.2 was limited to the bulk response in our simple geometry example. However, the geometry of a metal object can result in very different “plasmonic” responses as compared to the bulk and can lead to more sophisticated resonant behavior. Geometry plays a crucial role in determining the electromagnetic response of small metal particles. Next we will discuss a simple cylinder particle resonator example given by Novotny [8]. Consider a metallic cylinder with the same free-electron constituent properties as in the previous example. It has dimensions of a length, d, radius, r, and cross-sectional area, $A = \pi r^2$. Suppose there is charge displacement, Δx, at the ends as in Fig. 1.1. The magnitude of the charge bulidup will again be proportional to the electron density, n, but also now the cross-sectional area, i.e. $q = neA\Delta x$.The Couloumb potential energy between the two sides is then given as,

$$W(\Delta x) = \frac{1}{4\pi\epsilon_0}\frac{q^2}{d} = \frac{1}{4\pi\epsilon_0}\frac{(neA)^2}{d}\Delta x^2 \tag{1.39}$$

The restoring force, F, will then be

$$F(\Delta x) = -\frac{\partial W(\Delta x)}{\mathrm{d}x} = \frac{1}{4\pi\epsilon_0}\frac{q^2}{\ell} = \frac{1}{4\pi\epsilon_0}\frac{(neA)^2}{d}\Delta x = -D\Delta x \tag{1.40}$$

The particle resonance, ω_R, is found to be,

$$\omega_R = \sqrt{\frac{D}{m_{\text{tot}}}} = \frac{\omega_p}{2\sqrt{2}}\frac{1}{R} = \frac{\omega_p}{2\sqrt{2}}\frac{2r}{d}, \tag{1.41}$$

where, $R = d/2r$, is the aspect ratio of the cylinder. Clearly geometry played a crucial role in the optical response of small metal particles which deviate from that of the bulk response, ω_p. This has incredibly useful applications in optics and plasmonics as this allows a particles resonance be tuned to a specific frequency. However, geometry also plays a large role in the losses of an optical resoanator as well as field localization. There are also more complications which require corrections simply when dealing with particles which are comparable to the wavelength of light. These will be discussed in the next successive sections.

1.3.2 Mie Theory

The exact analytical expression for light scattering from a homogeneous sphere, σ_{sca}, and extinction, σ_{sca}, coefficients are given by Mie as,

$$\sigma_{\text{sca}} = \frac{2\pi}{|\vec{k}|^2} \sum_{L=0}^{\infty} (2L+1) \left[\left| t_L^E(m,X) \right|^2 + \left| t_L^M(m,X) \right|^2 \right] \tag{1.42}$$

$$\sigma_{\text{ext}} = \frac{2\pi}{|\vec{k}|^2} \sum_{L=0}^{\infty} (2L+1) \, \mathrm{Re} \left[t_L^E(m,X) + t_L^M(m,X) \right] \tag{1.43}$$

where, $\vec{k}$ is the wavevector of the light, L is the multipole index (i.e. dipole: L=1, quadrupole: L=2 ...), and, t_L^E & t_L^M, are the electric and magnetic scattering coefficients of the Lth multipole moment, respectively. These coefficients are complex valued and composed of a combination of spherical Bessel and Hankel functions and their first derivatives [5]. t_L^E & t_L^M are functions of $m = n_p/n_m$ where, n_p & n_m are the complex valued permittivity functions of the particle and surrounding material, respectively, and, X, is a size parameter which is defined as

$$X = |\vec{k}|R = 2\pi R/\lambda, \tag{1.44}$$

with R being the diameter of the sphere and, λ, the wavelength of light. The first (electric dipole) term dominates in situations where the sphere is much smaller than the wavelength of light, i.e. small particle limit or long-wavelength limit. The exact full electrodynamic calculation is obtained via including higher order modes to describe the changes of electric field inside the particle when the quasi-static approximation no longer holds.

For a homogeneous sphere in the quasi-static limit (i.e. $\vec{E}$ =const.) the polarizability, α, is given by the dipole term in eq. 1.42 as

$$\alpha(\omega) = 3V_{\text{sphere}}\epsilon_0 \frac{\epsilon(\omega) - \epsilon_m}{\epsilon(\omega) + 2\epsilon_m}, \tag{1.45}$$

where ϵ_m is the permittivity of the surrounding material which is usually taken to be a constant. The resonant frequencies of the nanoparticles can now be found with these expressions for the permittivity function. Resonance is found were there is the greatest response of the system according to eq. 1.45. This is found by setting the denominator of eq. 1.45 to zero where the polarizability will be at a maximum and solving for the associated frequency. For a Drude metal with small losses (i.e. $\Gamma \ll \omega_p$), the permittivity becomes $\epsilon(\omega) \to 1 - \omega_p^2/\omega^2$. Setting to zero and plugging this into the denominator gives

$$\left[1 - \frac{\omega_p^2}{\omega^2}\right] + 2\epsilon_m = 0 \Rightarrow \omega = \frac{\omega_p}{\sqrt{1 + 2\epsilon_m}}. \tag{1.46}$$

This clearly demonstrates an important quasi-static result which is the resonance is dependent on material properties and indepenent of overall size so long as the particle is small compared to the wavelength of light, i.e. $X \to 0$.

1.3.3 Gans Theory

Common nanoparticles used in hot-carrier catalaysis tend to be small spheres or rods. To estimate the LSPR frequency of the nanoparticles it is a good approximation to assume the shape to be that of a general oblate spheroid with principle axes of $a,\ b,\ \&\ c$, and volume equal to, $V = (4\pi/3)abc.$. This particular geometry has been solved in the electrostatic approximation using Gans theory [6]. For these types of particle geometries, the polarizability $\alpha_i(\omega)$ is given by

$$\alpha_i(\omega) = V\epsilon_0 \frac{\epsilon(\omega) - \epsilon_m}{L_i\epsilon(\omega) + (1 - L_i)\,\epsilon_m}, \tag{1.47}$$

where ϵ & ϵ_m are the permittivity functions of the nanoparticle and surrounding medium, respectively. L_i is a shape factor in the $i = x, y, z$ orientations that accounts for the eccentricities of the axes of the particle which varies from $L_x = L_y = L_z = 1/3$ for a sphere and tends towards 1 for a needle like shape while the equality $\sum_i L_i = 1$ holds for all shapes. The resonant frequency is found where the polarizability is a maximum, i.e. when the denominator is set to zero:

$$\epsilon = \epsilon' + i\epsilon'' \approx \epsilon_m \left(1 - \frac{1}{L}\right), \tag{1.48}$$

where the strict equality does not hold due to the imaginary component of ϵ. For dielectric media ϵ_m can be considered a constant, but for most noble metals $\epsilon' = 1 - \omega_p^2/\omega^2$ where ω_p is the material plasma frequency. Since ϵ gets progressively more negative for lower frequencies, it can be seen that the $1/L$ term must get larger meaning that $L \rightarrow 0$. This implies that the resonant frequency of a nanoparticle will decrease with increasing aspect ratio, i.e. a redshifting of its energy. This is an important and fairly universal feature of the electromagnetic resonances of nanostructures. It is important to keep this in mind when selecting a spectral range to be used depending on what particular application or experiment is being conducted. It is also important to note that the equations presented in this section are valid for nanostructures much smaller than the wavelength of light, the so-called “quasi-static” regime. This terminology comes from the fact that since the particle is smaller than the wavelength of light, the effective electric field it “sees” is constant throughout its volume. For increasingly larger sizes these equations will not be valid, and a full electrodynamic Mie theory calculation is necessary [5]. However, in this case too the plasmon resonance will still redshift, but not simply as a function of aspect ratio. This is because inhomogeneites in the induced electric field of the particle begin to appear due to retardation effects of the field. As the particle size increases, the distance that the collective electron “travel” also increases, resulting in a lowering of the frequency of oscillation, and hence a redshift.

1.3.4 Quasi-Static and Electrodynamic Regimes

The resonant particles frequencies depend greatly on the relative sizes of the particle to that of the wavelength of light. When the particle is much smaller than the wavelength of light the field that the particle ”sees” is a homogeneous uniform field throughout. Therefore the resonance only depends on it’s geometry and the material properties of the particle and it’s environment. When the particle is comparable to the wavelength of light, i.e. $2R \simeq \lambda$, it will begin to experiences the phases of the light passing through. This is illustrated

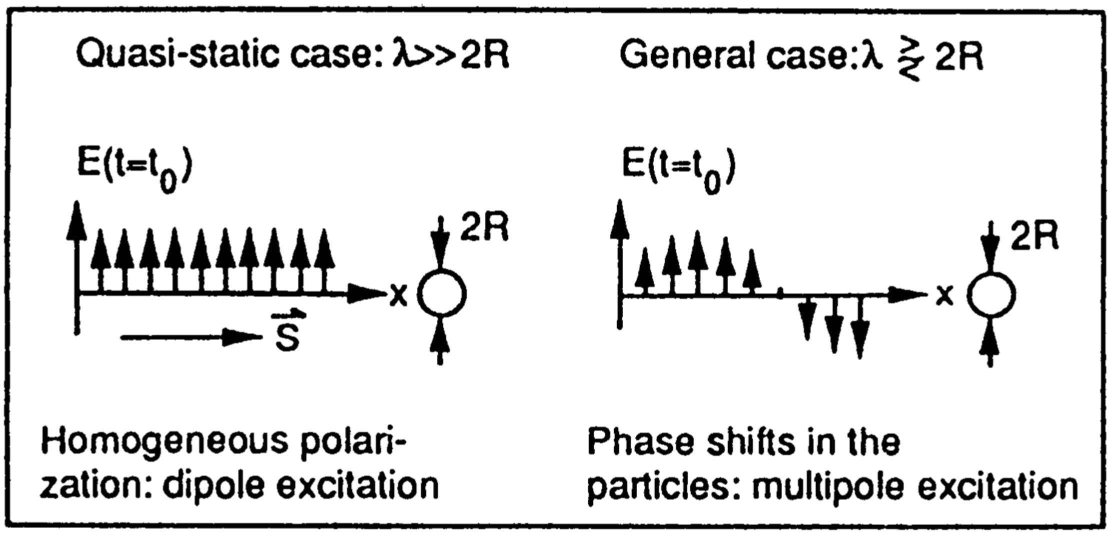

Figure 1.4: Quasi static (dipole approximation) and electrodynamic regimes for various size parameters [5].

in Fig 1.4.

Eventually the particles resonance will no longer be defined by only it's materials and aspect ratio as the size paramter, X, is increased. What will happen is a redshifting of the resonance due to the electrons in the plasmon mode having to "move farther" to keep in oscillatory phase with the incident light field. This can be seen analytically for that of a sphere by taking the next multipole term of the Mie scattering series to get a polarizability of the electrodynamic regime, α_{ED}, of

$$\alpha_{\mathrm{ED}} = 3V_{\mathrm{sphere}}\epsilon_0 \frac{1 - 0.1\left[\epsilon(\omega) - \epsilon_m\right]X^2/4 + O(X^4)}{\frac{\epsilon(\omega)+2\epsilon_m}{\epsilon(\omega)-\epsilon_m} - \left[0.1\epsilon(\omega) + \epsilon_m\right]X^2/4 - i(2/3)\epsilon_m^{3/2}X^3 + O(X^4)}, \tag{1.49}$$

where, O, represents the next order correction of the size parameter [13, 14]. Clearly when in the regime governed by eq. 1.49, numerical solutions for the optical response are necessary. It can be seen that in the quasi-static limit, i.e. $X \to 0$, this returns the polarization result for a small sphere.

1.3.5 Q-factor and Microresonators

Traditionally, the Q factor has been used to represent a measure of the losses of an oscillating circuit, e.g. the bandwidth of an LC circuit operating at microwave frequencies. It has been used as a measure of the "quality" or robustness of a resonance which experiences losses, hence the name. A high Q factor represent small to almost no loss, while a low Q factor represents substantial loss. In modern applications, the Q factor has shown to be a useful measure for systems such as optical antennas and ultrafast laser media. However, modern applications usually incorporate the energy stored in a resonator as well as the loss. This is typically given as some ratio between the two:

$$Q \sim \frac{\text{Energy Stored}}{\text{Energy Loss}}. \tag{1.50}$$

Q factor is generally defined as the ratio of the energy stored in an oscillator to it's losses per cycle. This has useful interpretations in Q-switched laser systems and RLC circuits for example. The Q-factor for an optical cavity is given by

$$Q = \left[\frac{\omega}{\Delta\omega}\right]_{\mathrm{R}} = \frac{\mathrm{Re}\left[\alpha(\omega)\right]}{2\left|\mathrm{Im}\left[\alpha(\omega)\right]\right|} = \frac{\omega_R}{2\Gamma}, \tag{1.51}$$

where $[\omega/\Delta\omega]_{\mathrm{R}}$ is the frequency and bandwidth evaluated at resonance, α is the polarizability, ω_R is the resonant frequency, and Γ is the damping term which is typically given by the FWHM. By this definition, one can get a good idea of the relative strengths of optical resonators even in different spectral regions. Γ is determined by the contributions of all damping via the Mathenius rule (eq. 1.72) mentioned later on along with more detail in section 1.4.2. In a similar way, the total Q-factor, Q_{total}, can be expressed as

$$\frac{1}{Q_{\text{total}}} = \frac{1}{Q_{\text{theory}}} + \frac{1}{Q_{\text{other}}}, \tag{1.52}$$

where Q_{theory} is the ideal theoretical maximum value for a given resonator and Q_{other} is the decay contributions from all other sources.

For a Mie resonator or microresoantor which supports a photonic resonance, the electric field in the cavity always satisfies the Helmholtz equation,

$$\left(\vec{\nabla}^2 - \frac{\epsilon_c}{c^2}\frac{\mathrm{d}^2}{\mathrm{d}t^2}\right)\vec{E}(\vec{r},t) = 0, \tag{1.53}$$

where ϵ_c is the permittivity of the cavity. Solutions for eq. 1.53 can be found by seeking solutions in the form

$$\vec{E}(\vec{r},t) = e^{-i\omega t}\sum_n E_n(t)\vec{u}_n(\vec{r}), \tag{1.54}$$

where $\vec{u}_n$ are the eigenmodes which characterize the resonator given the specific geometry. For Mie resonators, the electric field is simply found as

$$\vec{E}(t) = \vec{E}_0 \exp\left[\left(i\omega_R - \frac{\omega_R}{2Q_{\text{total}}}\right)t\right]. \tag{1.55}$$

Microresonator dynamics when perturbations are present are discussed in chapter 4.

1.3.6 Coupling to Nearby Nanostructures

The resonant energies may also be shifted through proximity to other nanostructures [15, 16]. Typically, a nanoparticle coupled to another structure will result in a redshift of its localized plasmon resonance due to an increased interaction energy with its image charge [17]. Particle-particle coupling has been seen to persist for separations up to 2.5-3 times the particle diameter [15]. In another study of the role of plasmonic coupling between nanodisks found that the resulting photoluminescence spectra shifted along with the plasmonic scattering resonance. Coupling effects were studied for nanodisk pairs of fixed diameter separated by distances ranging from 90-10 nm. The photoluminescent peaks were seen to shift along with the plasmon peak and also to have shown an incomplete depolarization of the photoluminescence from the coupled nanostructures. As photoluminescence from metal should not have any preferential polarization, the fact that the incomplete depolarization showed preference to the direction of the coupled plasmon mode was attributed to the non-uniform distribution of hot electrons in the metal particle [16].

Common metal-dielectric-metal (MDM) geometries may also be modeled in the so-called "generalized circuit model for coupled plasmonic systems." This model is not limited to only image charge type interactions but are also valid for dimer type plasmonic systems as well. For a gap size, g, and particle characteristic size, R, the capacitance of the image charge system is found to be [18]

$$C = 2\pi\epsilon_g^{1.14} \ln\left(1 + \frac{R}{2g}\Theta^2\right) \tag{1.56}$$

where ϵ_g is the permittivity of the gap layer and Θ is a geometric factor accounting for the lateral component of the gap-confined electric fields. This dependence results in a roughly $1/g$ dependence for the interaction energy between the mode and its image charge, analogous to what would be expected for the potential between two point charge distributions.

1.3.7 Multipole Expansion

In general, a electric potential may be expressed as a Taylor expansion. This method allows a means to describe potentials which can be in general quite complicated into manageable chunks by expressing them in terms of statistical moments which have convenient physical interpretations. This is given as

$$V(\vec{r}) \simeq V(\vec{r}_0) + \frac{1}{2!}\vec{r}\cdot\vec{\nabla}V(\vec{r}_0) + \frac{1}{3!}\vec{r}\vec{r} : \vec{\nabla}\vec{\nabla}V(\vec{r}_0) + ..., \tag{1.57}$$

where $\vec{r}_0$ is some reference position usually taking to be the origin ($\vec{r}_0 = 0$). Using the relationship of $\vec{E} = -\vec{\nabla}V - \partial\vec{A}/\partial t$, we have (in the Coloumb gauge, i.e. $\vec{\nabla}\cdot\vec{A} = 0$)

$$V(\vec{r},t) \simeq V(\vec{r}_0,t) - \frac{1}{2!}\vec{r}\cdot\vec{E}(\vec{r}_0,t) - \frac{1}{3!}\vec{r}\vec{r} : \vec{\nabla}\vec{E}(\vec{r}_0,t) + ... \tag{1.58}$$

$$= \overbrace{V(\vec{r}_0,t)}^{\text{monopole}} - \underbrace{d_i\cdot\vec{E}(\vec{r}_0,t)}_{\text{dipole}} - \overbrace{Q_{ij} : \vec{\nabla}\vec{E}(\vec{r}_0,t)}^{\text{quadrupole}} + ..., \tag{1.59}$$

where d_i and Q_{ij} are the electric dipole and quadrupole moments, respectively. Similarly for the relationship of $\vec{B} = \vec{\nabla}\times\vec{A}$ we have

$$\vec{A}(\vec{r},t) \simeq \frac{1}{2!}\vec{B}(\vec{r}_0)\times\vec{r} + \frac{1}{3!}\vec{r}\cdot\vec{\nabla}\vec{B}(\vec{r}_0)\times\vec{r} + ... \tag{1.60}$$

$$\tag{1.61}$$

which we can multiply by $-\frac{e}{m}\vec{p}\,\cdot$ to get the magnetic contribution to the potential of,

$$V(\vec{r},t) = -\frac{e}{m}\vec{p}\cdot\vec{A}(\vec{r},t) = -\underbrace{m_i\cdot\vec{B}(\vec{r}_0)}_{\text{dipole}} - \overbrace{M_{ij}:\vec{\nabla}\vec{B}(\vec{r}_0)\times\vec{r}}^{\text{quadrupole}} + ..., \tag{1.62}$$

where $e = 1.602\times10^{-19}$ C is the elementary charge, $m = 9.11\times10^{-31}$ kg, $\vec{p}$ is the momentum operator, and m_i & M_{ij} are the magnetic dipole and quadrupole moments, respectively. This gives a total potential of

$$V(\vec{r},t) \simeq \overbrace{V(\vec{r}_0,t)}^{\text{elec. monopole}} - \underbrace{d_i\cdot\vec{E}(\vec{r}_0,t)}_{\text{elec. dipole}} - \overbrace{Q_{ij}:\vec{\nabla}\vec{E}(\vec{r}_0,t)}^{\text{elec. quadrupole}} - \underbrace{m_i\cdot\vec{B}(\vec{r}_0)}_{\text{mag. dipole}} - \overbrace{M_{ij}:\vec{\nabla}\vec{B}(\vec{r}_0)\times\vec{r}}^{\text{mag. quadrupole}} + ... \tag{1.63}$$

It can be seen that higher order moments will depend correspondingly on higher order derivatives of the electric field. So the more complicated a given field distribution is, the more multipole moments are needed to describe it.

From this perspective, convenient simplifications may be made corresponding to the physical situation under investigation. For example, a small spherical particle interacting with a wavelength of light much larger than the particle can be assumed to follow the quasi-static field approximation as discussed earlier. This corresponds to the particle only "seeing" a uniform and homogeneous electric field, i.e. a field with no gradients. In this case, the only terms that are nonzero in Eq. 1.63 are the monopole and dipole terms, and all higher order terms (quadrupole and further) are identically zero. This is known as the "dipole approximation" assumption. In fact, it is only when an electric field is seen to change significantly over small distances and produce spatial gradients do higher order moments begin to contribute. These field spatial gradients also result in large associted wavevectors which provide the larger momentum associated with plasmonic resonances.

1.3.8 Reciprocity Principle, Far- and Near-Field Coupling

An important consequence of the multipole expansion of the electric potential is that of the reciprocity principle. Consider a current density $\vec{j}_1$ at $\vec{r}_1$ oscillating at frequency ω. This will produce electromagnetic wave fields with characterized by $e^{-i\left(\vec{k}\cdot\vec{r}-\omega t\right)}$, and will have from Maxwell's equations in matter

$$\vec{\nabla}\times\vec{E}_1 = \frac{i\omega}{c}\vec{B}_1 \tag{1.64}$$

$$\vec{\nabla}\times\vec{H}_1 = -\frac{i\omega}{c}\vec{D}_1 + \frac{4\pi}{c}\vec{j}_1. \tag{1.65}$$

Also suppose another current density $\vec{j}_2$ at $\vec{r}_2$ oscillating at the same frequency ω. This will produce analogous fields for $\vec{E}_2$ & $\vec{H}_2$. If the media are assumed to be linear and symmetric, then it can be shown [2] that

$$\vec{\nabla} \cdot \left[\vec{E}_1 \times \vec{H}_2 - \vec{E}_2 \times \vec{H}_1\right] = \frac{4\pi}{c} \left[\vec{j}_1 \cdot \vec{E}_2 - \vec{j}_2 \cdot \vec{E}_1\right]. \tag{1.66}$$

This can be rewritten via the divergence theorem to

$$\oint_S \left[\vec{E}_1 \times \vec{H}_2 - \vec{E}_2 \times \vec{H}_1\right] \cdot \mathrm{d}\vec{S} = \int_V \frac{4\pi}{c} \left[\vec{j}_1 \cdot \vec{E}_2 - \vec{j}_2 \cdot \vec{E}_1\right] \mathrm{d}V. \tag{1.67}$$

If we now integrate over all space, the LHS will be equal to zero. This will leave

$$\int_{V_1} \vec{E}_2(\vec{r}) \cdot \vec{j}_1 \, \mathrm{d}V_1 = \int_{V_2} \vec{E}_1(\vec{r}) \cdot \vec{j}_2 \, \mathrm{d}V_2. \tag{1.68}$$

The $\int \vec{j}\mathrm{d}V$ term is the time derivative of the total dipole moment, $\vec{p}$. Since the field is harmonic, $\mathrm{d}\vec{p}/\mathrm{d}t = i\omega\vec{p}$, and we have

$$\vec{E}_2(\vec{r}_1) \cdot \vec{p}_1 = \vec{E}_1(\vec{r}_2) \cdot \vec{p}_2. \tag{1.69}$$

This is the reciprocity theorem, and it states that two dipole sources and their associated fields can be completely interchanged without changing any physics. An identical expression for the magnetic dipole sources and the magnetic fields can also be derived. This dipole expression has assumed that the sources do not vary substantially over space. For this reason they can be considered to be in the quasi-static regime. As the sources begin to spatially vary non-negligibly, a similar result for quadrupolar distributions is found to be [2]

$$\left(\frac{\partial \vec{E}_{2i}(\vec{r}_1)}{\partial x_j} + \frac{\partial \vec{E}_{2j}(\vec{r}_1)}{\partial x_i}\right) Q_{1,ij} = \left(\frac{\partial \vec{E}_{1i}(\vec{r}_2)}{\partial x_j} + \frac{\partial \vec{E}_{1j}(\vec{r}_2)}{\partial x_i}\right) Q_{2,ij} \tag{1.70}$$

where $Q_{1,ij}$ & $Q_{2,ij}$ are the quadrupole moments of the sources at 1 & 2, respectively.

This theorem leads to an "apples to apples" symmetry relationship among source distributions, which may be composed of many multipole contributions, and their resulting fields experienced by another source. A dipole can only couple to another dipole type distribution, a quadrupole can only couple to another quadrupole type distribution, and so on. Essentially this states that a source of light emission and a detector can be completely interchanged without changing anything: an emitter can work as a receiver as well. This is all because of the symmetry of reciprocity of the fields and charge distributions. These symmetries dictate the standard spectroscopy selection rules encountered in optical spectroscopy [1].

At first glance, this seems as if free-space light (which is dipolar by nature) cannot couple to plasmon resonances which can be composed of higher order moments. One immediate consequence of this theorem is that quadrupole (and higher moment) distributions cannot be coupled to by far-field light excitation which are dipolar by nature. This leads to terms such as “bright” and “dark” resonant modes, meaning they are (bright) or are not (dark) able to couple to free-space light fields. There are however exceptions to the reciprocity relations when dealing with plasmonic fields of nanoparticles.

A succinct explanation for this is given by Novotny [1]: “The dipole interaction is determined by the electric field at the center of the charge distribution, whereas the quadrupole interaction is defined by the electric field gradient at the center. Thus, if the electric field is sufficiently homogeneous over the dimensions of the particle, the quadrupole interaction vanishes. This is why in small systems of charge, such as atoms and molecules, often only the dipole interaction is considered. This dipole approximation leads to the standard selection rules encountered in optical spectroscopy. However, the dipole approximation is not necessarily sufficient for nanoscale particles because of their larger size compared with that of an atom. Furthermore, if the particle interacts with an optical near-field it will experience strong field gradients. This increases the importance of the quadrupole interaction and modifies the standard selection rules. Thus, the strong field gradients encountered in near-field optics have the potential to excite usually forbidden transitions in larger quantum systems and thus extend the capabilities of optical spectroscopy.”

1.4 Plasmon Dynamics

1.4.1 Lorentzian Lineshape

A plasmonic resonance consists of electron reacting to an incoming light field causing them to accelerate. As they are displaced, they experience a restoring force causing them to oscillate as some function of the plasma frequency, ω_p. The mode also experience damping from various origins. So, a plasmon resonance can be modeled as a classical damped driven oscillator. The resonance will exponentially decay in the time domain. The functional form of a LSPR light scattering spectrum $\phi(\omega)$ is then given by a Fourier transform resulting in a Lorenzian function which is a solution to a classical damped driven oscillator. This lineshape is given by,

$$\phi(\omega) = \frac{1}{1 + \left(\frac{\omega - \omega_R}{\Gamma/2}\right)^2} \tag{1.71}$$

which is defined by two parameters, ω_R, the resonant frequency of the nanoparticle as calulated in the previous section, and, Γ, the full width at half maximum (FWHM.) The FWHM can be physically interpreted as the decay rate or inverse lifetime of the LSPR mode due to damping or scattering.

1.4.2 Damping Mechanisms

Nanoparticle geometry plays a very important role in both its spectral properties and also its damping properties. Damping and the associated loss and short lifetimes of plasmonic modes is a well-known obstacle in the field. However, these damping properties are what are mostly responsible for the promotion of hot-carriers in metal nanoparticles. Clearly identifying plasmon decay mechanisms is crucial to understanding hot-carrier excitation. Typically all of the scattering events which may take place and their associated damping times can be summed according to the so-called Mathenius Rule [5]:

$$\Gamma = \sum_i \tau_i^{-1}, \tag{1.72}$$

where τ_i is the ith characteristic scattering time associated with a particular scattering event. This includes but is not limited to surface scattering, defect scattering, radiation damping, doping, etc. Geometry and size of nanoparticles begin to play a very large role in the damping process of LSPR's. For example, the original damping coefficient in bulk material is

$$\Gamma = v_f/\ell \tag{1.73}$$

where v_f is the Fermi velocity and ℓ is the mean free path is just a characteristic time associated with the mean free time between collisions in the bulk. A large damping effect for very small particles is scattering at the surface of a nanoparticle. This can be accounted for by adding an extra term to the bulk scattering term, Γ, as

$$\Gamma = \frac{v_f}{\ell} + \frac{Av_f}{R}, \tag{1.74}$$

where R is some characteristic size of the particle and A is a surface scattering parameter which depends on the geometry. It can be seen then that this surface scattering term vanishes for increasingly larger particles as expected. For very small particles (<5 nm) the amount of radiative damping is negligible, as radiative damping is proportional to the volume of the particle. As size is increased, however, radiative damping can

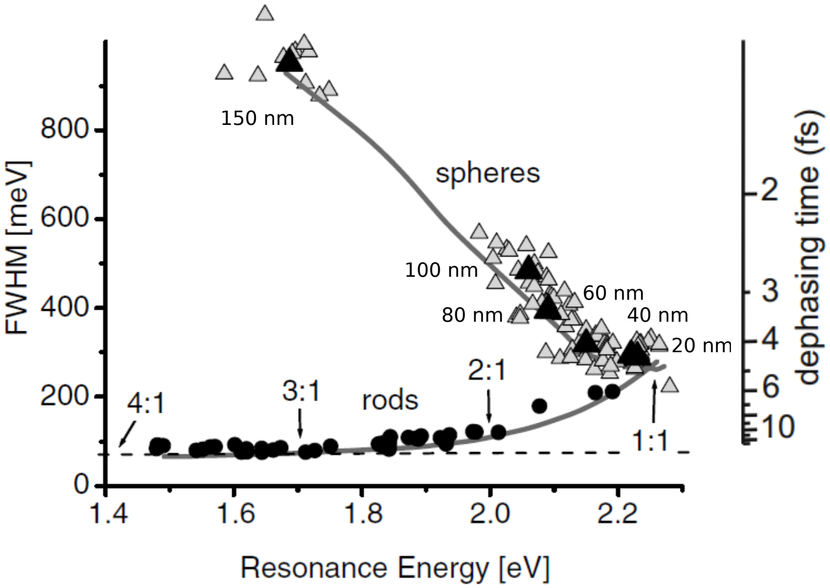

Figure 1.5: FWHM, lifetime and plasmonic resonance energy for various nanoparticle geometries given by [19]. Comparison of FWHM and resonant energy can be made via eqs. 1.75 and 1.48, respectively. Spheres start out in the quasistatic regime described by eq. 1.46 but shift substantially as they increase in size and approach the electrodynamic regime (eq. 1.49)

be accounted for by again adding an extra term to eq. 1.74 as

$$\Gamma = \frac{v_f}{\ell} + \frac{Av_f}{R} + 2\hbar\kappa V, \tag{1.75}$$

where V is the volume of the particle, $\hbar$ is the reduced Plancks constant, and κ is a constant which characterizes the radiative efficiency. This third term is related to the imaginary part of eq. 1.47, and so can also be a function of aspect ratio. It is noted that this term is only strictly valid in the quasi-static regime and Γ will not increase without bound in reality. A nice illustration of experimental observations of nanoparticle geometry role in FWHM, characterictic lifetimes, and resonant energy is given by [19] and shown in Fig. 1.5.

Eq. 1.75 describes a more or less general model of damping which is applicable to all particle plasmon modes experience just due to their geometries. Other damping mechanisms such as mode coupling and non-radiative decay channels are possible. This can vary case by case for the particular plasmonic system in question and its environment and their corresponding electronic and optical properties. A generic placeholder expression for Γ can be

$$\Gamma_{\text{total}} = \Gamma_{\text{intrinsic}} + \Gamma_{\text{geometry}} + \Gamma_{\text{other}}. \tag{1.76}$$

Increasing LSPR lifetimes is of interest for some applications, and for example, geometries such as gold nanorods have been seen to be able to control plasmon radiative decay mechanisms by fabricating rods with particle plasmon resonances below the Au interband transition energies, thus eliminating the ability for the plasmon to couple to that decay path [19, 20]. Additionally, the methods of analyzing plasmon resonance spectral widths to infer the suppression of plasmon decay mechanisms in those studies, may offer insight to hot-electron lifetimes, decay modes/transport, and dynamics [21].

1.4.3 Landau Damping

Following photoexcitation of a nanoparticle, the induced plasmons will oscillate coherently in phase. Shortly after, they will quickly dephase through various scattering events. However, not all of the damping experienced by the plasmon is due to the geometric scattering or radiative/non-radiative decay channels as described in the previous section. In fact, the plasmons will experience an inherent dephasing through a process known as Landau damping. This process is a general consequence for how a plasma will react to a perturbation. The inquiry is how an initial electronic plasma distribution, $f_0(\vec{v})$, will react to disturbances and how the carrier distributions will evolve because of this given the electronic field restoring forces. The altered electronic distribution, F, when out of it's equilibrium state by an amount, $f(\vec{v})$, can be represented by

$$F = f_0(\vec{v}) + f(\vec{v}, \vec{r}, t), \tag{1.77}$$

where f is small compared to f_0. The plasma will evolve via the Boltzmann transport kinetic equation of [22]

$$\frac{\partial f}{\partial t} + \vec{v} \cdot \vec{\nabla} f - \frac{e}{m} \vec{\nabla} \phi \cdot \frac{\partial f_0}{\partial \vec{v}} = 0, \tag{1.78}$$

where the first two terms represent the kinetic material derivative and the last term is the electric interaction with the electronic potential, ϕ, which obeys the Laplacian

$$\vec{\nabla}^2 \phi = -4\pi e \int f \mathrm{d}\tau, \quad \text{with } \mathrm{d}\tau = \mathrm{d}v_x \mathrm{d}v_y \mathrm{d}v_z. \tag{1.79}$$

Eq. 1.78 represents a coupled set of equations relating the carrier distribution, velocity distribution, and electric fields to one another. It is important to note that eq. 1.78 describes a collisionless plasma with the only interaction among the constituents being the electric fields. Vlasov initially solved eq. 1.78 by seeking solutions of the form $\exp\left[-i\left(\omega t - \vec{k}\cdot\vec{r}\right)\right]$ to yield a dispersion relation of [23]

$$1 + \frac{\omega_p^2}{k^2}\int \frac{\partial f_0/\partial \vec{v}}{(\omega/k - \vec{v})}\, \mathrm{d}\vec{v} = 0, \tag{1.80}$$

which is correct in the limit of $k \to 0$. Landau's key insight to this problem was to recognize that that solutions could obtained in the form of [22]

$$f_k(\vec{v}, t)e^{i\vec{k}\cdot\vec{r}}. \tag{1.81}$$

rather than the traditional term for an excitation, i.e. $\exp\left[-i\left(\omega t - \vec{k}\cdot\vec{r}\right)\right]$. That is, that there need not be a well defined dispersion relationship between ω and k. Also, by expanding the electric field response to include higher order moment corrections,

$$\omega \simeq \omega_p\left(1 + \frac{3}{2}a^2k^2\right), \tag{1.82}$$

where a is the electronic Debeye radius, Landau showed that by considering this (along with careful contour integration), the general result included a damping term in the dispersion in the form of

$$1 + \frac{\omega_p^2}{k^2}\left[\text{P.V.}\int \frac{\partial f_0/\partial \vec{v}}{(\omega/k - \vec{v})}\, \mathrm{d}\vec{v} - i\pi\left(\frac{\partial f_0}{\partial \vec{v}}\right)_{\vec{v}=\omega/k}\right] = 0, \tag{1.83}$$

where P.V. is the principal value (a constant of integration) and the new second term corresponds to damping given the complex factor of i. That is, depending on the sign of the last term there will be additional damping when considering 2nd order (wavevector) corrections to the plasma frequency. Landau showed that his damping should coefficient, $\gamma_L(k)$, should be

$$\gamma_L(k) = \omega_0\sqrt{\frac{\pi}{8}}\frac{1}{(ka)^3}e^{-\frac{1}{2(ka)^2}}. \tag{1.84}$$

It is seen from eq. 1.84 then that lower energy excitations are dampened exponentially less than higher energy excitations. However, this damping results not in energy loss, but a reorganization of the spatial and velocity distributions. So, it is a type of spatial dispersion.

Landau damping plays an essential role in the damping process of plasmons, especially at early stages. It also plays a large role in dissipating the plasmon energy and momentum to the electrons of the supporting material (section 1.6). For applications such as increased hot-carrier production, Landau damping can be desirable as it will help mediate this process. A study on enhancing Landau damping and the resulting hot-carrier distributions is presented in chapter 2.

1.4.4 Wave Uncertainty

Consider a small metal particle which supports strongly localized plasmonic hot spots. The electric field of the hot spot, $\vec{E}(\vec{r})$, is defined over some spatial extent, $\vec{r} = (x, y, z)$. The structure of the electric field can be equally well described by expressing it by what spatial frequencies, $\vec{\xi}$ (wavevectors, $\vec{k} = \frac{1}{2\pi}\vec{\xi}$) compose it. This is done via a Fourier transform defined as

$$\hat{\vec{E}}(\vec{\xi}) = \int_{-\infty}^{+\infty} \vec{E}(\vec{r}) e^{-i\vec{\xi}\cdot\vec{r}} \cdot \mathrm{d}\vec{r}, \tag{1.85}$$

and it's inverse

$$\vec{E}(\vec{r}) = \frac{1}{2\pi}\int_{-\infty}^{+\infty} \hat{\vec{E}}(\vec{\xi}) e^{i\vec{\xi}\cdot\vec{r}} \cdot \mathrm{d}\vec{\xi}. \tag{1.86}$$

For brevity we'll just limit to one dimension and drop the vector notation for now. To derive the uncertainty relationships we start with the effective spatial extent, δr, of the hot spots. We will also assume the field is centered at the origin ($r = 0$) where it is also at a maximum. Similar to that of the full-width at half-max (FWHM) in spectral signals, we can define [7]

$$\delta r \equiv \frac{1}{E(r=0)} \int_{-\infty}^{\infty} |E(r)| \ \mathrm{d}r. \tag{1.87}$$

Because the electric field in general will have both positive and negative value over a distribution, it is necessarily true that

$$\delta r \geq \frac{1}{E(\vec{r}=0)} \int_{-\infty}^{\infty} E(r) \ \mathrm{d}r. \tag{1.88}$$

Then by multiplying by a convenient factor of 1 we get

$$\frac{1}{E(r=0)} \int_{-\infty}^{\infty} E(r) \ \mathrm{d}r = \frac{1}{E(r=0)} \int_{-\infty}^{\infty} E(r) \overbrace{e^{(-i(\xi=0)\cdot r)}}^{=1} \ \mathrm{d}r = \frac{\hat{E}(\xi=0))}{E(r=0))}, \tag{1.89}$$

based on the definition of the Fourier transforms mentioned. Then doing the same method for $\hat{E}(\xi)$:

$$\delta\xi \geq \frac{1}{\hat{E}(\xi=0)} \int_{-\infty}^{\infty} \hat{E}(\xi) \ \mathrm{d}\xi = \frac{1}{\hat{E}(\xi=0)} \int_{-\infty}^{\infty} \hat{E}(\xi) \overbrace{e^{(-i(r=0)\cdot\xi)}}^{=1} \ \mathrm{d}\xi = \frac{2\pi E(r=0))}{\hat{E}(\xi=0))}. \tag{1.90}$$

Multiplying these two together yields

$$\delta r\ \delta \xi \geq 2\pi \frac{\cancel{E(r=0))}\ \cancel{\hat{E}(\xi=0))}}{\cancel{\hat{E}(\xi=0))}\ \cancel{E(r=0))}}. \tag{1.91}$$

Replacing the angular frequency component with the normal frequency component $\vec{\xi} = 2\pi\vec{k}$ gives

$$\delta r\ \delta k \geq 1, \tag{1.92}$$

which is the classical wave uncertainty relationship.

It is common to come across many different versions of the uncertainty principle in the Plasmonics/Photonics literature. This because the particular definition of your uncertainty can result in slightly different magnitudes of the uncertainty inequality. For example, using the root-mean-sqaure (RMS) uncertainty value results in $\delta r_{\mathrm{RMS}}\ \delta k_{\mathrm{RMS}} \geq \frac{1}{2}$ (a Gaussian distribution saturates this quantity, i.e. $\delta r_{\mathrm{Gauss}}\ \delta k_{\mathrm{Gauss}} = \frac{1}{2}$), and a periodic structure such as a grating yields, $\delta r\ \delta k \sim \pi$. Although the magitudes may differ with different definitions, all the uncertainty relations show that a localization in space results in delocalization in reciprical (wavevector) space, and vise versa. It is noted that these definitions and the definitions used in this dissertation are not from Heisenberg uncertainty. They are simply due to classical wave uncertainty. Heisenberg uncertainty refers to wave properties of matter, but with classical action (particle nature) of the order of Planck's constant, h, as a principal value [24].

This uncertainty relationship is key to the experimental ideas presented in chapter 2. By designing nanoscale spatial geometries, these large associated wavevectors may be responsible for increasing the Landau damping in plasmonic systems. As apparent by eq. 1.84, larger wavevectors are dampened faster. By imposing characteristic wavevectors, absorption into a material may be faster resulting in more efficient hot-carrier distributions (section 1.6). The electronic processes for this are described in section 1.5.

1.4.5 Angular Spectrum Representation

A convenient way to represent optical fields in homogeneous media is with the so-called angular spectrum representation. This representation allows a convenient way to describe a superposition plane waves and evanescent waves with variable amplitudes and propagation direction. Suppose that the electric field, $\vec{E}(\vec{r})$, is known everywhere in space, $\vec{r} = (x, y, z)$. The angular sprecturm method is done by first by defining a constant plane in the z axis. Then we define the 2-dimensional Fourier transform as

$$\hat{\vec{E}}(k_x, k_y; z) = \frac{1}{(2\pi)^2} \iint_{-\infty}^{+\infty} \vec{E}(x, y, z) e^{-i(k_x x + k_y y)}\ \mathrm{d}x\ \mathrm{d}y \tag{1.93}$$

and the inverse,

$$\vec{E}(x,y,z) = \iint_{-\infty}^{+\infty} \hat{\vec{E}}(k_x, k_y; z) e^{i(k_x x + k_y y)}\ \mathrm{d}k_x \mathrm{d}k_y. \tag{1.94}$$

In this case we assume that the medium is homogeneous, linear, and free of sources. We only assume the presence of some incident and scattered field, $\vec{E} = \vec{E}_{\mathrm{inc}} + \vec{E}_{\mathrm{scatt}}$ (Fig. 1.6). In this case, an optical field always satifies

$$\left(\vec{\nabla}^2 + k^2\right)\vec{E}(\vec{r}) = 0, \tag{1.95}$$

where $k = n\omega/c$ and $n = \sqrt{\epsilon\mu}$. The time dependence of the electric field is given as

$$\vec{E}(\vec{r},t) = \mathrm{Re}\left[\vec{E}(\vec{r})e^{-i\omega t}\right]. \tag{1.96}$$

In this way the z component of the wavevector is uniquely determined as

$$k_z = \begin{cases} \sqrt{k^2 - |k_x + k_y|^2}\ , & \text{for} \quad |k_x + k_y| \leq k, \quad \text{(plane waves)} \\ i\sqrt{|k_x + k_y|^2 - k^2}\ , & \text{for} \quad |k_x + k_y| > k. \quad \text{(evanescent waves)} \end{cases} \tag{1.97}$$

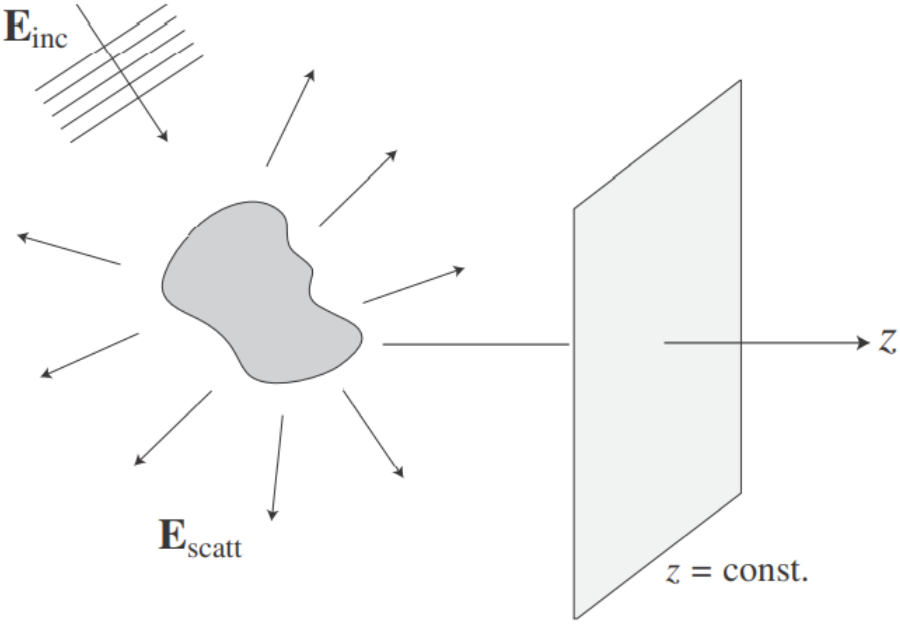

Figure 1.6: Angular spectrum scattered fields [1].

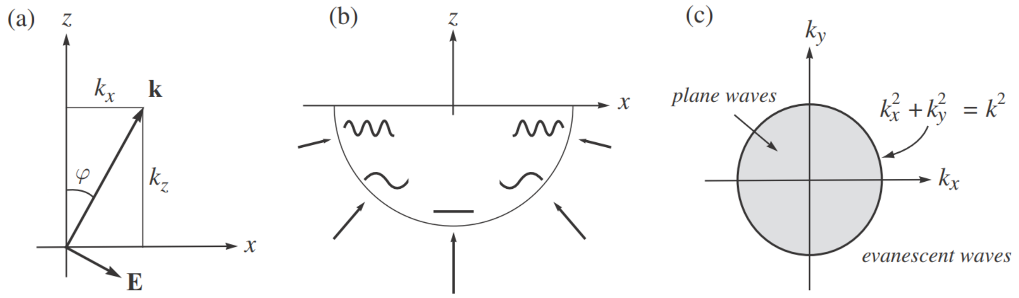

Figure 1.7: Angular spectrum showing plane and evanescent fields [1].

With this definition of the wavevector, the electric field can be fed into eq. 1.95 to get the z component as

$$\hat{\vec{E}}(k_x, k_y; z) = \hat{\vec{E}}(k_x, k_y; 0)e^{\pm i k_z z}. \tag{1.98}$$

Finally, we can define the total field as

$$\vec{E}(x, y, z) = \iint_{-\infty}^{+\infty} \hat{\vec{E}}(k_x, k_y; 0)e^{i(k_x x + k_y y \pm k_z z)} \, \mathrm{d}k_x \mathrm{d}k_y. \tag{1.99}$$

This analysis allows for incident angle dependence as well as evanescent components. These are illustrated in Fig. 1.7.

1.5 Optical and Electronic Transitions

1.5.1 Absorption/Emission Mechanisms (Fermi Golden Rule)

Fermi's golden rule estimates the transition rates of otherwise stationary states of a general perturbed system. This uses first-order perturbation theory to predict a transition from an energy eigenste of a system to that of a continuum. It is expressed as [25]

$$\Gamma_{i \to f} = \frac{2\pi}{\hbar^2} \sum_f \left| \langle f | \, \hat{H}_{\text{int}} \, | i \rangle \right|^2 \delta(\omega_i - \omega_f), \tag{1.100}$$

where $\Gamma_{i \to f}$ is the transition probability rate from the initial, $|i\rangle$, to final, $\langle f|$ states with frequencies, ω_i & ω_f, respectively, and $\hat{H}_{\text{int}}$ is the perturbative interaction Hamiltonian [25]. Typically $\hat{H}_{\text{int}}$ is taken to be simply the dipole operator, $\hat{d} \cdot \hat{E}$, such as for an <u>inter</u>band transition. <u>Intra</u>band transitions, on the other hand, require a quadrupole or higher order transition in order to break the symmetry of the initial and final states (dipole forbidden). Transitions of these sort also require momentum conservation as there is horizontal movement as seen on a band structure diagram. This momentum can be provided via quasiparticle excitations (plasmon, phonon, etc.) or by spatial discontinuities such as an interface.

1.5.2 Band Structure

The electronic and optical properties of a material are captured in its band structure [26]. This is a 4-dimensional dispersion relationship representation [1 energy (frequency), 3 momentum (wavevector)] which encompasses essentially all the electronic eigenstates and their occupation numbers. The electron occupation numbers generally represented by a density of states function along with a Fermi distribution are superimposed on top. Qualitative information such as whether a material is a conductor, semiconductor or insulator is quickly discerned from this. Determining what electronic transitions are allowed or forbidden by constraints such as energy and momentum conservation can also be easily made apparent.

Band structure can be interpreted as a direct consequence of Pauli's exclusion principle. If two identical particles become overlapped with one another there will be a discrete splitting of the atomic energy levels due to Pauli exclusion principle. In the limit of $N \to \infty$ identical particles overlapping on one another, continuous energy "bands" begin to form as the actual discreteness of the individual states becomes infinitesimal and essentially vanish altogether. Band structures of materials form are determined by both the overlap and resulting splitting of the atomic orbital energy levels as well as the crystal lattice symmetry and the resulting boundary conditions the electronic wavefunctions encounter because of this. These conditions are captured in Bloch's theorem which is essentially a statement on the fact that if an electron moves from one lattice point to an adjacent one in a crystal, it will "see" an identical structure as before because the lattice is unchanged, and there are modified boundary conditions which follow due to this. This theorem states that for electrons in a crystal there are basis electron wavefunctions, $\psi(\vec{r})$, which have certain properties: (1) $\psi(\vec{r})$ is the electron eigenstates of the system, (2) the states can be represented in the form

$$\psi(\vec{r}) = e^{i\vec{k}\cdot\vec{r}} u_k(\vec{r}), \tag{1.101}$$

and (3) the wavefunction has the same periodicity of the crystal lattice of

$$u_k(\vec{r}) = u_k(\vec{r} + \vec{R}), \tag{1.102}$$

where u_k is a periodic function known as Bloch waves which are characteristic to the crystal lattice structure with periodicity, $\vec{R}$. These Bloch waves serve as natural basis functions for representing the electronic wavefunctions for a given material and it's internal lattice symmetries. Numerical calculations of band structure require estimates of the periodic potential,

$$V(\vec{r}) = \sum_{\vec{k}} V_{\vec{k}} e^{i\vec{k}\cdot\vec{R}}, \tag{1.103}$$

which are determined given the particular details of the type of matter composing the lattice. Common approches to estime $V(\vec{r})$ include the Nearly Free Electron Model, Tight-Binding Model, and Kronig-Penney Model to name a few [2].

These allowed states will be filled according to their density of electronic states and to Fermi-Dirac statistics. This overlap of the Fermi energy and the conduction band is the reason gold is such a good conductor. The occupation statistics at a given temperature, T, and energy level, ϵ, for both Fermions and Bosons are given as

$$n_F(\epsilon, T) = \frac{1}{e^{(\epsilon-\epsilon_F)/kT}+1}, \quad \text{(Fermion Statistics)} \tag{1.104}$$

$$n_B(\epsilon, T) = \frac{1}{e^{(\epsilon-\epsilon_F)/kT}-1} \quad \text{(Boson Statistics)}, \tag{1.105}$$

where $k_B = 1.38 \times 10^{-23}\ \mathrm{J}\cdot\mathrm{K}^{-1}$ is Boltzmann's constant and ϵ_F is the Fermi energy which corresponds to the energy level state which has a 50-50 chance of being occupied/unoccupied. The vacancy states, i.e. lack of electrons, are termed "holes", and are simply related to the electron occupation as

$$p_F(\epsilon, T) = 1 - n_F(\epsilon, T), \tag{1.106}$$

where p_F is the Fermi occupation number for holes. Additionally, these holes can be thought of having opposite charge of electrons but not nessecarily the same mass. This will be discussed in section 1.5.4.

1.5.3 Optical Transitions in Metals

It is impossible to completely visualize the entire band structure of a material as it is 4-dimensional. A cut of a band structure along a high symmetry axis known as a band diagram shows the dispersion of momentum and energy along the axis. A simplified band diagram for Au is shown in Fig. 1.8 (a). The band diagram shows two bands, one corresponding to valence electrons (d bands) and the other corresponding to conduction electrons (sp band). Any allowed transition in a material must start and end on points along these lines in the band structure corresponding to allowed electron eigenstates. This corresponds to production of both an electron and hole pair. Any vertical or horizontal change in a transition corresponds to the addition or gain/loss of energy and momentum, respectively. A transition corresponding to the absorption of a photon which has energy, $\Delta E = \hbar\omega$, and momentum, $\Delta p = \hbar k \approx 0$, will result in a d band to sp band vertical transition called an interband transition. This transition is illustrated by the blue arrows in Fig. 1.8 (b). This type of vertical transition is due to the small photon momentum relative to the momenta of the electrons in the material, and hence no substantial horizontal change. If an incident photon has too little energy (red Fig. 1.8 (b)) than it will not be absorbed via the interband process.

A transition may have horizontal component corresponding to momentum exchange. This transition is illustrated by the red arrows in Fig. 1.8 (c). The momentum mismatch may be provided from spatial symmetry breaking such as surface roughness or finite particle size [27]. In this case a quasiparticle or collective oscillation such as a phonon or plasmon with inherently larger momentum compared to free-space light will mediate the transition. The characteristics of the plasmon's, and hence of the transition's, energy and momentum are determined by the geometry of the nanoparticle. This will result in a sp band to sp band diagonal transition called an intraband transition.

We also mention that intraband transitions are typically termed "forbidden" transitions as they do not couple to free-space light in a simple way. In addition to requiring a large momentum kick, they are also quantum mechanically forbidden as their initial and final states share the same symmetry (same band). However, because of the sharp electric field gradients of plasmons, this restriction is lifted as higher elecric field moments provide the symmetry breaking of the transition integral and yields non-zero values [1].

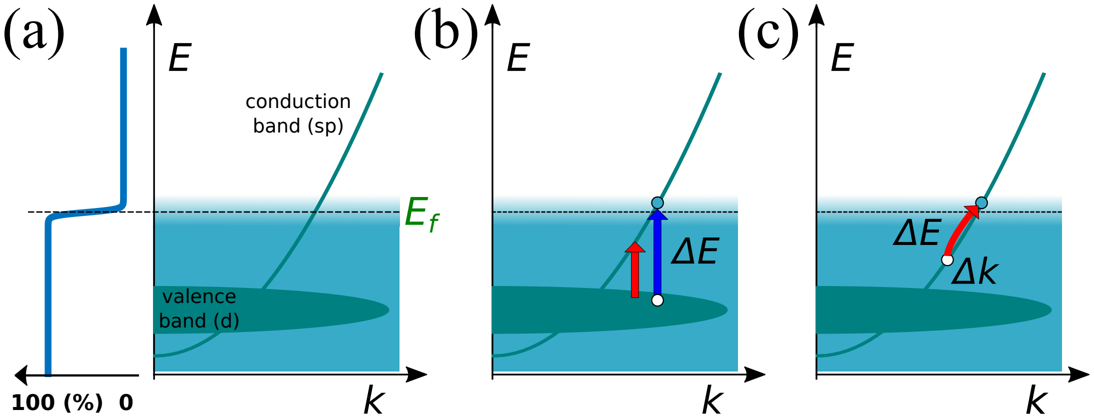

Figure 1.8: (a) Simplified band diagram showing dispersion between energy (frequency) and momentum (wavevector). Band structure consisting of a valence (d band) and conduction (sp band). (b) Energy threshold for absorbing a photon from one band to another (interband transition). (c) Energy and momentum threshold for absorbing a photon with a momentum scattering event such as a plasmon from within the conduction band (intraband transition).

1.5.4 Optical Transitions in Semiconductors

Band diagrams allow a way to quickly get an idea of the general characteristics of a material. For example, the location of the Fermi energy on a band diagram can quickly convey whether the material is a conducting, insulating or semi-conducting. For metals, the Fermi energy lies right in the middle of the conduction band as in Fig 1.8 (a). This means that the states just below and just above the Fermi energy lie within a continuous distribution of available states, and are easily thermally occupied. Hence, the free electron picture of a metal can be interpreted from this. Additionally, some metals have their conduction bands directly overlap with the valence bands, such is the case for gold.

For insulators and semi-conductors the Fermi level lies within in a band-gap. As mentioned earlier, band structure appears as a consequence of overlapping of atomic orbitals from $N \to \infty$ identical particles in a crystal lattice. This overlap can result in a band continuum of states, but also regions where there are no allowed states. This results in lapses of states, or gaps, between neighboring bands. The Fermi energy of insulators and semi-conductors happen to lie inside a band-gap. Therefore, to induce a transition in one of these materials, there is a band-gap energy, E_g, which acts as a threshold for promoting an electron to a higher state.

Insulators typically have a very large E_g meaning that these materials are opaque to visible light. Additionally, higher occupied states aren't easily occupied at high temperatures when the spread of the Fermi

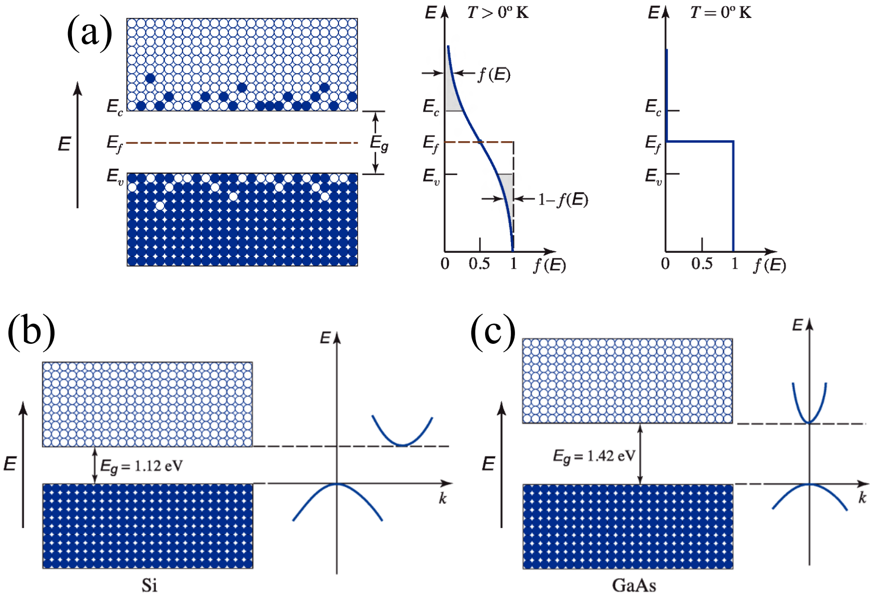

Figure 1.9: Semiconductor band diagram and occupation distribution given by Ref. [4]. (a) Carrier distribution and thermal occupation number for an intrinsic semi-conductor (b) Example of an indirect band gap material such as silicon. (c) Example of a direct band gap material such as gallium arsenide.

distributions are larger. On the other hand, the Fermi energy of semiconductors lie in the regions of a band-gap where they are just barely able to partially fill states in the conduction and valence bands (Fig. 1.9 (a)). Additionally, the bands gaps may be categorized as direct or indirect. These are defined by whether the states at the top of the lower band and the bottom of the upper band are separated by some wavevector mismatch (indirect) or not (direct). This is shown in Fig. 1.9 (b) & (c) for silicon and gallium arsenide which have indirect and direct band gaps, respectively. This has important consequences for optical transitions as now the momentum (wavevector) mismatch must be accounted for, analogous to the intraband transitions in metals like in Fig. 1.8 (c).

The dispersion relationship of the band is usually modeled as a free carrier resulting in a parabolic dispersion. However, depending on the details and symmetry of the lattice and the collective response of the material, the carriers may feel a slightly different inertial response. This is captured in the effective mass of the dispersion. That is, the dispersion takes the form

$$E(k) = E_c + \frac{\hbar^2 k^2}{2m_{\mathrm{eff,e}}}, \quad \text{Conduction Band} \tag{1.107}$$

$$E(k) = E_v - \frac{\hbar^2 k^2}{2m_{\mathrm{eff,p}}}, \quad \text{Valence Band,} \tag{1.108}$$

where E_c & E_v are the energy levels at the bottom of the conduction band and the top of the valence band, respectively, and $m_{\mathrm{eff,e}}$ & $m_{\mathrm{eff,h}}$ are the effective masses for the conduction electrons and valence holes, respectively. m_{eff} is related to the curvature of the band as

$$\frac{1}{m_{\mathrm{eff}}} = \frac{1}{\hbar^2}\frac{\partial^2 E(k)}{\partial k^2}. \tag{1.109}$$

The permittivity of a semiconductor is also dependent on proper accounting of both the electrons and holes. This is done typically by adding another term to the Drude model (eq. 1.18) which accounts for holes.

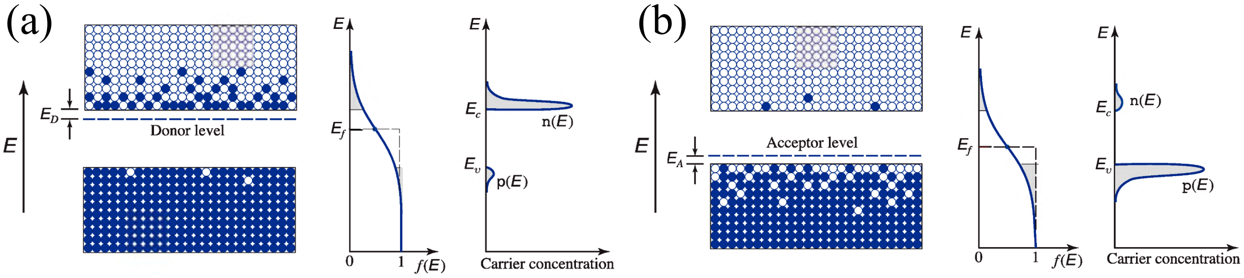

Figure 1.10: n (a) and p (b) type semiconductor band diagrams given by Ref. [4]. (a) n type has higher electron carrier occupation than holes. (b) p type has higher hole carrier occupation than electrons.

This is given as

$$\epsilon = 1 - \frac{\omega_{p,e}^2}{\omega^2 + i\Gamma_e\omega} - \frac{\omega_{p,h}^2}{\omega^2 + i\Gamma_h\omega}, \tag{1.110}$$

where Γ_e & Γ_h are the decay rates for electrons and holes, respectively, and

$$\omega_{p,e}^2 = \frac{N_e e^2}{m_{\mathrm{eff,e}}\epsilon_0} \tag{1.111}$$

$$\omega_{p,h}^2 = \frac{N_h e^2}{m_{\mathrm{eff,h}}\epsilon_0}, \tag{1.112}$$

where N_e & N_h are the carrier concentration for electrons and holes, respectively.

The carrier concentration is shown for an intrinsic semiconductor (one whose Fermi energy lies in the middle of a band gap) in Fig. 1.9 (a). However, some semiconductors lie closer to one side or the other, resulting in an asymmetric distribution of electrons and holes. These are termed n-type and p-type when the Fermi level is closer to the valence or conduction band, respectively. This is shown in Figs. 1.9 (a) & (b). This intrinsic carrier concentration is what largely determines a semiconductors optical and electronic responses. This is of special importance to chapter 4 where a study is presented in which hot-carriers are injected into semiconductor structures, altering the carrier concentrations, resulting in a novel optical response.

1.6 Hot-Carrier Dynamics

1.6.1 Hot-Carrier Production Timeline

The coherent plasmon modes eventual dephase through scattering event and Landau damping processes mentioned previously. Shortly thereafter, the energy of the plasmons are absorbed by the material. This is the process of promoting energetic carriers in plasmonic structures. The outline of the generation and life cycle of these carriers is outlined in Fig. 1.11 [28, 29].

1.6.2 Non-Fermi (Athermal) Electron Distribution

Shortly after plasmon dephasing the energy absorbed by electrons in the Au and promotes carriers to higher energies. This sudden absorption induces an energy distribution which is intermittently non-thermal. Non-thermal meaning the electron distribution at that moment cannot be described by a simple Fermi-Dirac distribution. This instantaneous change in electron energy distribution from Fermi-Dirac after absorption is

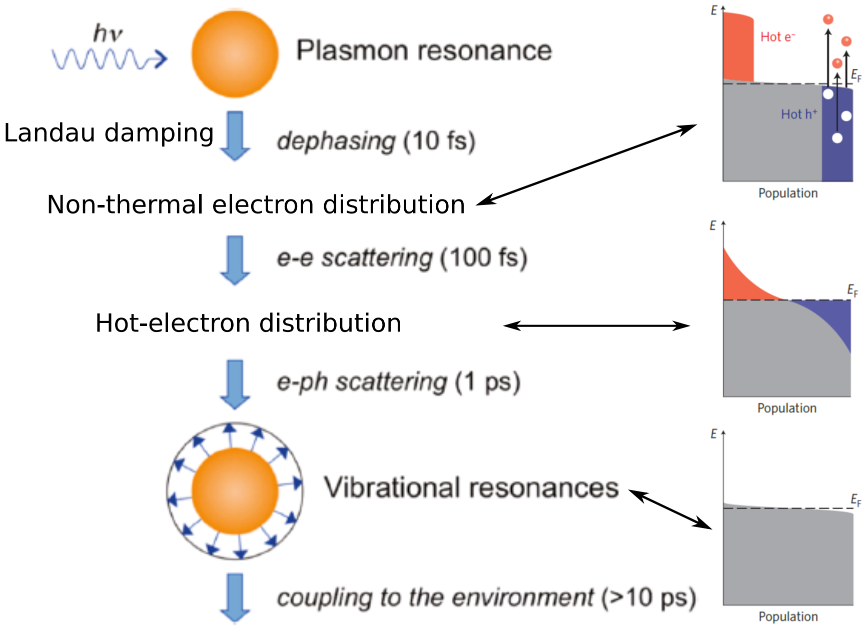

Figure 1.11: Outline of plasmon dynmics [28, 29].

given by [30] as

$$\Delta\rho_{\rm nf} = \Delta\rho^0_{\rm nf}\Big(f_0(\epsilon-\epsilon_p)\left[1-f_0(\epsilon)\right] - f_0(\epsilon)\left[1-f_0(\epsilon+\epsilon_p)\right]\Big), \tag{1.113}$$

$$f_{\rm nf}(\epsilon) = f_0(\epsilon) + \Delta\rho_{\rm nf}(\epsilon), \tag{1.114}$$

where $\Delta\rho^0_{\rm nf}$ is the population change amplitude which depends on the intensity of the light source, ϵ_p is the photon energy of the absorbed photon and f_0 is the distribution prior to any absorption. An example distribution of this type can be seen in Fig. 1.12. It is important to note that this distribution is only approximate for a real material, as eq. 1.113 is only a simple model which does not take into account the nature of the allowed transitions as determined by band structure.

The non-Fermi electron distributions are not thermodynamically stable, and quickly return to a Fermi distribution with a higher effective temperature. The energy rate and time associated with this electron-electron thermalizing is given by [31], as

$$\frac{\hbar}{\tau_{ee}(E)} \approx 2\frac{e^2}{2a_0}\frac{\pi^{1/2}}{32(\alpha r_s)^{3/2}}\left[\tan^{-1}\left(\frac{\pi}{\alpha r_s}\right)^{1/2} + \frac{(\alpha r_s/\pi)^{1/2}}{1+\alpha r_s/\pi}\right]\frac{(x^2-1)^2}{x}, \tag{1.115}$$

where $\alpha = \sqrt{4/9\pi}$, $x = \sqrt{E/E_f}$, and $r_s = (3/4\pi n)^{1/3}$. For Au, and an electron energy of $E = \epsilon_f + \hbar\omega_p$ with a plasmon wavelength of 1250 nm, [17] calculate this time to be approximately $\tau_{ee}(E_f + \hbar\omega_p) \approx 45$

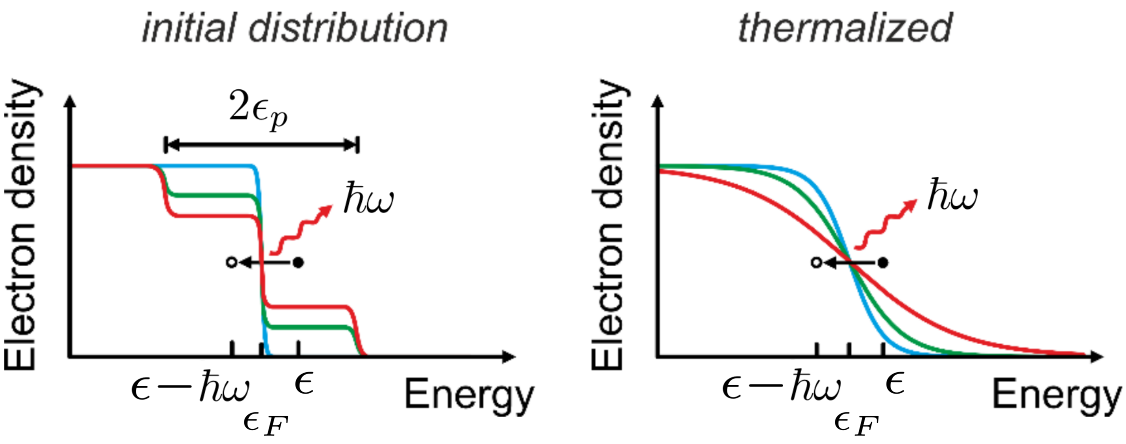

Figure 1.12: Initial athermal electron distribution and thermalized "hot" electron distributions [35].

femtoseconds. This value puts a upper limit on any spectral dynamics that may occur due to these athermal electrons. It is important to note the energy dependence of eq. 1.115. Higher energies are thermalized faster than lower energies analogous to Landau damping, although they are two separate mechanisms.

It should be noted however, that eq. 1.115 is still somewhat of an approximation. Non-thermal electron dynamics can be quite involved to completely describe. Theoretical models of non-thermal electron dynamics has been explored in several works [19–21, 27, 32–34]. A common theme in these works is the effect of particle size on the energy distribution of the induced hot-carriers. For particles of small enough sizes such as 10 nm nanocube, the plasmon resonance is scattered more readily thus broadening the energy range of the electrons in the metal.

1.6.3 Hot-Carrier (Thermal) Distributions

The non-thermal electron distribution will quickly thermalize into a Fermi-Dirac distribution via various electron-electron scattering events. Although no longer non-thermal, this distribution will still be out of equilibrium. That is, the distribution will have the form of Fermi-Dirac except it will be described by some elevated effective temperature, $T^* \gg T_0$, rather than its initial temperature, T_0, i.e. a "hot-electron" distribution (Fig. 1.12). Values for $T*$ have been estimated to exceed several thousand Kelvin in some case [36]. These elevated temperature distributions are crucial for understanding the origin of nonlinear light emission from rough metal films.

For very high temperatures, the Fermi distribution (and also the Bosonic distributions) approach that of a Boltzmann distribution

$$n_F(\epsilon, T^* \gg T) \to e^{-(\epsilon-\epsilon_F)/k_B T}. \tag{1.116}$$

This correspondence can be interpreted as the Fermi (and Bose) distributions losing their “quantum” behavior at high temperatures. In this regime they behave like a classical gas.

1.6.4 Thermalisation and Phonon Coupling

The final stages of electron thermalisation is usually described by energy dissipation through electron-phonon interactions, and then finally to the environment. The electron-phonon coupling is modeled by a two temperature coupled rate equations

$$C_e(T_e)\frac{\mathrm{d}T_e}{\mathrm{d}t} = -g(T_e - T_\ell) \tag{1.117}$$

$$C_\ell\frac{\mathrm{d}T_\ell}{\mathrm{d}t} = g(T_e - T_\ell), \tag{1.118}$$

where T_e & T_ℓ are the electronic and lattice (phonon) temperatures, C_ℓ is the lattice heat capacity, $C_e(T_e) = \Gamma T_e$ is the temperature dependent electronic heat capacity, and g is the electron-phonon coupling constant [29]. An estimate of the phonon relaxation time, τ_{ep}, can be given by [29]

$$\tau_{ep} \sim \frac{\gamma(T_0 + \Delta T)}{g}, \tag{1.119}$$

where T_0 is the ambient temperature and ΔT is the light induced temperature increase. For gold, experimental results show that $\tau_{ep} \approx 1-10$ picoseconds [29], although this may not be the case for other materials. This time is much longer than the characteristic timescales of plasmon dephasing and hot-electron generation. This section is given for the sake of completeness and for ruling out phonons as a significant damping factor for these dynamics.

Chapter 2

Hot-Electron Induced Nonlinear Light Emission

Contributors:

Manoj Manjare[†], Ryan Freeman[†], Feng Wang[†], Gordon Hua[†], Luka Pierce[†], Guoce Yang[†], Chentao Li[†], Sergei Urazhdin[†] and Hayk Harutyunyan[†].

[†]Department of Physics, Emory University.

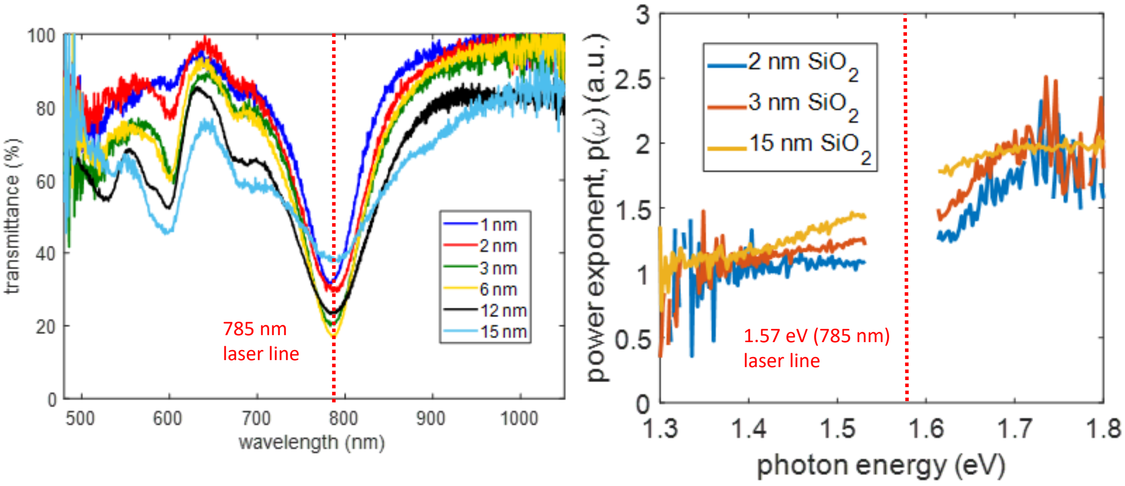

2.1 Chapter Overview

2.2 Introduction

Photoluminescence (PL) from plasmonic nanostructures with spatial inhomogeneities have been demonstrated to exhibit an interesting nonlinear character [8, 37–39]. Previous studies on rough metal films have shown the PL signal to have a wavelength dependent nonlinear scaling exponent which increases linearly with emitted photon energy [35, 36]. This result was attributed to recombination of nonequilibrium electrons within the conduction band mediated by the breakdown of momentum restrictions as a consequence of the spatial inhomogeneities of the surface.

However, the role of intraband transitions in PL from plasmonic materials is not fully understood. Photon-induced direct intraband transitions in materials are typically forbidden for two reasons: 1. the transition is dipole forbidden because the initial and final states share the same symmetry, and 2. there is momentum (or wavevector, k) mismatch between the initial and final states which cannot be provided by free-space photons. Previous works have shown that surface feature inhomogeneities can relax these restrictions by having high-gradient electric fields and supporting surface plasmons . The former lifts the dipole restriction and the latter is lifted due to the inherent momentum of plasmons. Further, it has been shown that gap-mode plasmons are very efficient at facilitating these transitions .

2.3 Plasmonic Metal PL Literature and Anomalies

A lot of effort has been made in order to better understand the general emission process from plasmonic metals. In spite of this, the exact mechanisms and origin of continuum generation has remained unclear or incomplete for nearly 20 years. The is no general consensus on the origin. A lot of the the work has shown that the specific details of each scenario may give varying results. A common thread among the extensive research is that of spatial structure and local wavevector uncertainty [8, 17, 35–37]. Whether it is from rough films, single particles, coupled particles, this property is key to understand the phenomena. One of the biggest controversies is that of whether the PL (specifically the upconverted portion of the spectrum) originates from intraband electron-hole recombination [8, 36], inelastic Raman scattering [35], or multiphoton processes [37, 38]. However, it is generally agreed on that hot-carriers are responsible and necessary for facilitating these mechanisms and are plasmon mediated. The history and science developed on PL from plasmonic metals is discussed next.

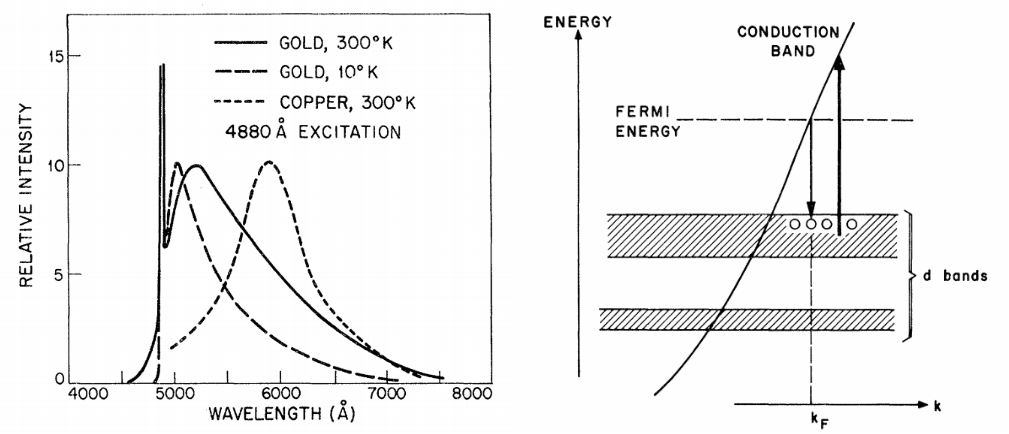

Figure 2.1: First report of photoluminescence from rough metal films from Mooridian 1968 [40]. (a) PL emission spectra with CW laser excitation wavelength of 488 nm. (b) Proposed mechanism of single photon absorption and electron-hole recombination emission via interband resonances.

2.3.1 Smooth vs. Rough Film PL

PL from metals was first observed by Mooradian [40]. In this study Au and Cu films were excited with various CW laser excitation (488, 512 nm Ar laser, 400-500 nm Hg vapor arc lamp) and the emission was recorded with the films at varying temperatures. The metals exhibited broad emission at lower wavelengths and was independent on excitation laser energy. The shape of the emission seemed to only depend on the temperature and/or the metal in question, and not on the intensity of of the laser excitation field. Because of this, the emission was assigned to radiative interband electron-hole recombination of sp conduction electrons and d

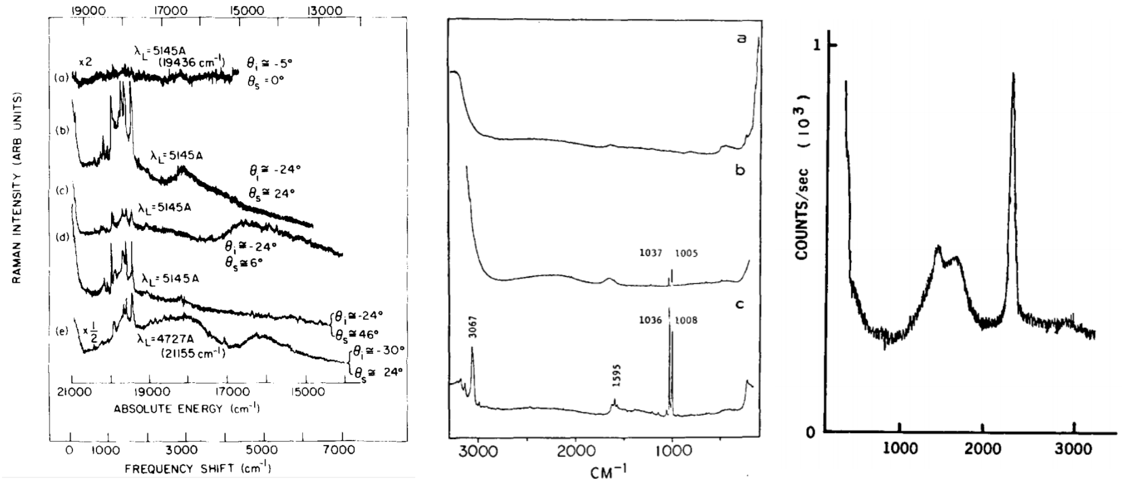

Figure 2.2: Examples of early reports of continuum generation in SERS experiements [41–43]. The sharp features of the signals correspond to the vibration modes of the molecules whose signal is amplified due to the strong and localized electric fields from sharp features of the metal films. A continuous background can be superimposed on top of the SERS signal. This continuum generation background does not have any defining features.

band vacancies (Fig. 2.1). Because the emission was independent of the laser wavelength, Raman scattering was ruled out as the mechanism because the Stokes emission should differ from the laser wavelength by a fixed amount.

Shortly after Mooradians observations, continuum generation was observed in the background of Surface Enhanced Raman Spectroscopy (SERS) spectra [41–43]. This observation suggested that Raman scattering plays a role in the emission process. Raman scattering is known scale linearly with excitation power, and this response is matched well by the observations of Mooradian. However, later studies via time-resolved measurements confirmed that the timescales of the emission observed by Mooradian were much longer than expected for inelastic light scattering such as Raman scattering [41]. This ultrafast response discrepancy is one of the many inconsistencies and complications that would follow with understanding this emission process.

Until this point nonlinear effects had been neglected as a source of the continuum generation. However, multiphoton absorption was also observed to produce continuum generation in rough and smooth plasmonic metal films. Specifically, two- and three-photon PL (2PPL, 3PPL) was observed by Boyd [37]. Additionally, the emission spectrum showed 2nd and 3rd harmonic generation superimposed on a continuum background. Interestingly, they also found that there was significant discrepancies between smooth and rough films and

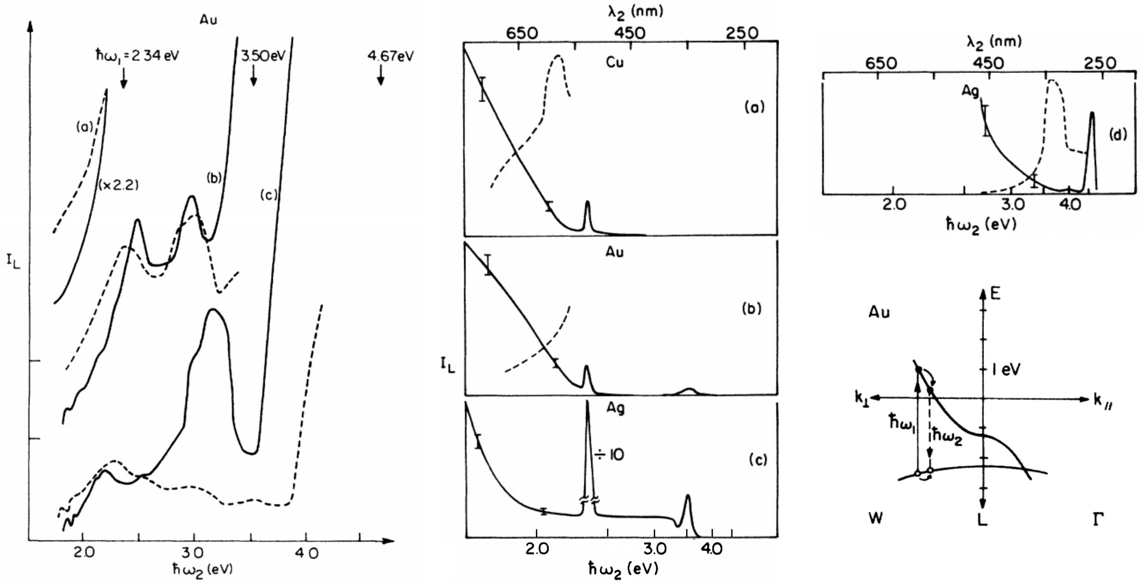

Figure 2.3: First reports of multiphoton absorption and PL in metal films given by Boyd 1986 [37]. (a) PL emission from rough (dashed) and smooth (solid) films for gold films after 2.34, 3.50, 4.67 eV CW laser excitation. (b) Multiphoton induced PL from rough (dashed) films of Cu, Au, and Ag from 1.7 eV CW laser excitation. One photon PL for reference (dashed). Peaks corresponding to 2nd and 3rd harmonic generation are clearly seen superimposed over a continuum background. (c) Multiphoton PL for Ag with 2.34 eV CW laser excitation. (d) Multiphoton absorption and emission process.

that their model was not abe to capture this.

Multiphoton PL seemed to be lessened by the presence of roughness while SERS PL is heightened by it. The latter is not surprising as the mechanism for SERS is fundamentally dependent on surface features. The source of nonlinear PL (NPL) from rough surfaces was still not fully understood. NPL from rough metal films was revisited by Novotny 2003 [8]. In this work they excited plasmonic hot spots with near-IR excitation. This choice of laser energy was chosen so as to limit the probing of the electronic resonances to just intraband, as the energy of 780 nm was below the interband threshold. Both CW and pulsed laser excitation was used and yielded different emission spectra. Specifically, CW excitation emissions consisted primarily of only down-converted light whereas pulsed excitation produced both up- and down- converted emission.

Power scaling analysis was performed on the emission spectra. The power dependence of the integrated up- and -down converted spectral regions exhibited different scaling. The up-converted emission demon-

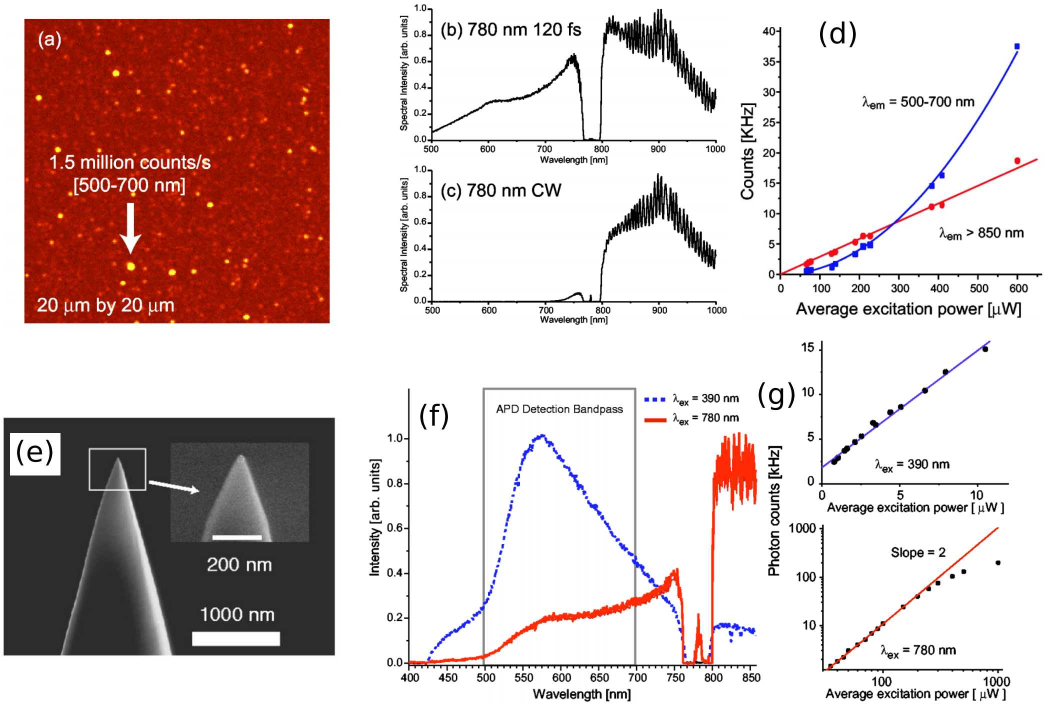

Figure 2.4: NPL studies on rough Au films and tips by Novotny 2003 [8]. (a) Near-IR irradiation of rough films emitting CG from localized plasmonic hot spots as shown in APD scanning maps. (b) Rough film emission from (c) pulsed and (d) CW laser excitation. Down-converted light shows same spectral shape independent of excitation while up-coverted emission is only present with the pulsed laser type. (d) Power dependent measurements of spectrally averaged rough film PL. Down-converted emission shows linear dependence while up-converted emission show quadratic dependence. (e) SEM image of sharp metal cantilever tip used for PL experiment. (f) Up-converted emission from sharp Au tips from both 390 and 780 nm excitation. (g) Power dependence of 390 and 780 nm excitations. 390 nm excitation shows linear dependence while 780 nm excitation shows quadratic dependence.

strated quadratic power dependence ($p = 2$) while the down-converted appeared to scale linearly ($p = 1$). Additionally, the emission from a metal cantilever tip was also taken in order to recreate a more localized plasmon resonance as compared to the rough film with random features. The power dependence of the integrated up-converted emission from both 390 nm (above interband threshold) and 780 nm (below interband threshold) was measured and 390 nm excitation yielded $p = 1$ similar to the results of Mooradian [40] while 780 nm excitation again yielded quadratic dependence.

This work provided power dependence measurements on plasmonic structures by restricting the allowed electronic transitions via the excitation energy. The conclusions drawn from these results implied that the down-converted emission could only be attributed to single-photon intraband PL. These observations were explained through the presence of strongly localized plasmon modes whose sharp electric field gradients providing the necessary momentum and symmetry-breaking to achieve intraband electronic transitions. Additionally, the exponent of $p = 1$ supported an intraband transition as single photon absorption at this excitation energy was not past the interband threshold needed to produce d-band hole. The up-converted region was attributed to two-photon absorption (TPA) given its quadratic dependence. However, an unexpected flaw in this study turned out to be the spectral averaging while performing power law analysis, i.e. integrating the entire up- and down- converted spectral regions, respectively. This was not an unreasonable assumption but it turns out to have important consequences.

Discrepancies were again found when NPL from rough Ag and Au films was revisited by Haug 2015 [36]. In this work they employed a more detailed power law analysis on the nonlinear light emission. Rather than summing the entire range of signal for both up and down converted light spectral regions before power law analysis, respectively, they instead extracted a power law for each respective emitted photon energy. When this analysis was performed noninteger power exponents were observed. That is, they found that the power exponent itself was a function of the emitted photon energy in the form

$$p(\hbar\omega) \propto \hbar\omega. \tag{2.1}$$

They were able to explain this behavior qualitatively by considering the effective temperature of the electron distribution opening up electron hole recombination. However, they found that this elevated temperature electron distribution recombination was responsible for both the up and down converted spectral regions. This is in contrast to [8] where the intraband luminescence was assigned to the down-converted light alone and the up converted light was suspected to be due to two-photon absorption coupling to the interband resonance. This was due to the spectrally integrated and averaged power law analysis which led to a value close to $p = 2$. This work showed that although the averaged spectral analysis still gives close $p = 2$,

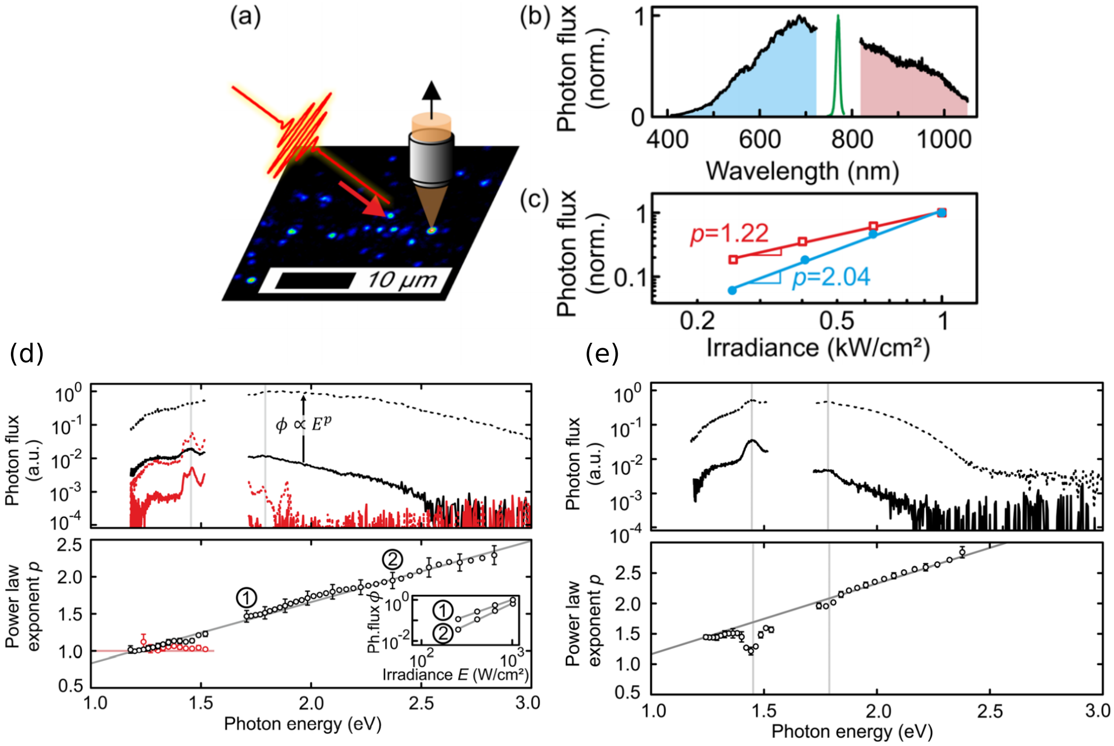

Figure 2.5: NPL studies on rough Au and Ag films by Haug 2015 [36]. (a) NIR pulsed excitation on rough metal films exhibiting strong emission from plasmonic "hot" spots as evident in an AFM emission mapping. (b) Broadband continuum generation spectrum from NIR excitation. (c) Spectrally averaged power law extracted for both up and down converted emission showing scaling of $p \approx 1$ and $p \approx 2$, respectively, consistent with the observations of Novotny et al. 2003 [8]. (d) Emission spectra for pulsed (black) and CW (red) excitation on Rough Ag films. Extracted power law without any spectral averaging. A clear linear lineshape is seen for pulsed excitation. (e) Emission spectra and extracted power law lineshpae for Au Au films.

finer resolved power analysis showed that there was indeed a characteristic lineshape function of the power exponent, i.e. $p(\omega)$.

More importantly, the technique of [36] allowed fitting the power law to a more physically meaningful and specific parameter, namely, the temperature. The power law lineshape was attributed to very efficient intraband transitions due to spatial inhomogeneities similar to [8] resulting in pronounced hot-carrier distributions. These hot-carriers were described by an effective temperature, T_{eff}. Additionally, momentum and quadrupole symmetry rules were determined to be completely lifted due to the random structuring of the surface, i.e. any wavevector needed to perform and intraband transition was provided via the range of surface feature sizes supporting the plasmon modes. With these assumptions, the electron-hole recombination and resulting photo-emission dictated by Fermi's golden rule in eq. 1.100 becomes a simple overlap integral. This is because the the initial and final states are not discrete but a continuum and there are no quantum mechanical restrictions to be considered in the interaction Hamiltonian. So the intraband initial and final states are more or less transitioning from one continuum to another once momentum mismatch can be neglected. An estimate of the resulting PL spectrum, $\phi(\omega)$, for intraband electron-hole recombination for randomly oriented plasmon hot spots in rough metal films is then given by [36] as

$$\phi(\omega) \propto \int_{-\infty}^{\infty} f_e(\epsilon, T_{\text{eff}})\rho(\omega) f_h(\epsilon - \hbar\omega, T_{\text{eff}})\mathrm{d}\epsilon, \tag{2.2}$$

where f_e is the electron distribution, $f_h = 1 - f_e$ is the hole distribution, and $\rho(\omega)$ is the local photonic mode density given by the plasmon scattering spectrum which plays the role of the antenna which facilitates the transition in this example. This essentially counts the recombination rate of electrons at energy, ϵ, with holes in a lower state corresponding with the emission of a photon of energy, $\hbar\omega$. At room temperature the overlap integral of eq. 2.2 is very small due to the narrow range of electron and hole occupancies. In fact it is only at high temperatures do the Fermi distributions begin to add up in a significant way. Increasing the irradiance, P, of the excitation will increase the internal temperature as

$$T_e = T_{e,0}\left(\frac{P}{P_0}\right)^{1/a}, \tag{2.3}$$

where $T_{e,0}$ is the ambient electronic temperature, a is the effective thermal power coefficient (which is $a = 2$ for a metal) and P_0 is some reference irradiance corresponding to a spectrum of $\phi_0(\omega)$. where a is a thermal coefficient of the material, k_B is Boltzmann's constant, and T_e is the effective temperature of the system. This power dependence is then captured in the scaling exponent, $p(\omega)$, for the spectrum in eq. 2.2 which is calculated via eq. 1.38 to get

$$p(\omega) = \frac{\hbar\omega}{ak_B T_{\text{eff}}}, \tag{2.4}$$

thus predicting the observed linear lineshape of $p(\omega)$, the slope of which depends on the effective electron temperature.

2.3.2 Ultrafast Hot-Carriers

Hot-carrier distributions have been observed experimentally via a inverted pump-probe reflectivity experiments on Au films [44]. In this study, 30 nm Au films were pumped in the NIR to induce intraband transitions of conduction electrons, and then the corresponding optical response of the interband resonance was monitored via a visible probe. As more hot-carriers are promoted, there are less vacancies available for interband transitions into the conduction band, as it is more populated due to intraband transitions, and so

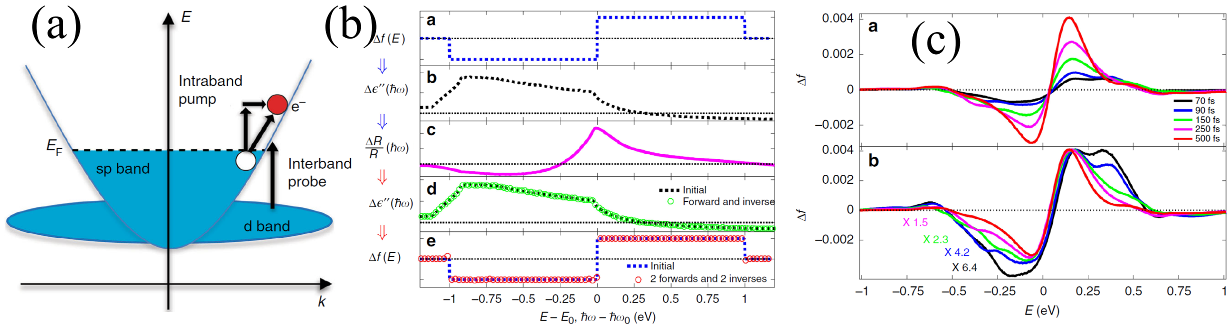

Figure 2.6: Hot-carrier distribution study by [44]. (a) Experimental concept. Hot-carriers are excited via near-IR Pump excitation to induce intraband transitions. The carrier distribution is monitored via an interband probe. (b) Process for inferring hot-carrier distributions via inversion methods. (c) Inferred hot-carrier distributions at various delay times.

more final states are occupied (Fig 2.6 (a)).

An inversion method of the transient ultrafast spectra was employed to infer hot-carrier distributions. This process is highlighted in Fig. 2.6 (b).The experimentally obtained differential reflectivity, $\Delta R/R\ (\hbar\omega)$, was used to infer the change to the complex component of the permitivity, $\epsilon''(\hbar\omega)$, which was then used to infer change in occupation number, $\Delta f(E)$, i.e.,

$$\frac{\Delta R}{R}(\hbar\omega) \Rightarrow \epsilon''(\hbar\omega) \Rightarrow \Delta f(E). \tag{2.5}$$

The inferred change in carrier distribution showed a temporal evolution of the carrier distribution (Fig 2.6 (c)). At early times, a distribution reminiscent of a non-Fermi one as outlined in section 1.6.2 was observed. As time progressed, this non-Fermi distribution was seen to thermalize into a hot-electron one as in Fig. 1.12. Additionally, these experiments were performed in a geometry which facilitated surface plasmons, and so the observed effects were attributed to enhanced Landau damping.

The role of hot-carriers is key to understanding NPL from plasmonic nanostructures. A key study to understanding this is first identifying ways to promote them more efficiently. Such a study was performed in Ref. [17] where ultra-fast optical measurements on confined plasmonic hot spots were reported. It was found that gap confined plasmonic modes showed anomalously strong hot-carrier generation at “hot-spot’ locations in the geometry (Fig. 2.7). The estimated carrier promotion, δn, was given as

$$\delta n \sim \frac{|E_{\text{gap}}|^2}{\omega^4}. \tag{2.6}$$

where, E_{gap}, the enhanced fields of the MDM structures for a given laser excitation of energy $\hbar\omega$. It was shown in Ref. [17] that the enhanced fields of the thinnest MDM gap modes were on the order of, $E_{\text{gap}} \sim 200E_0$,

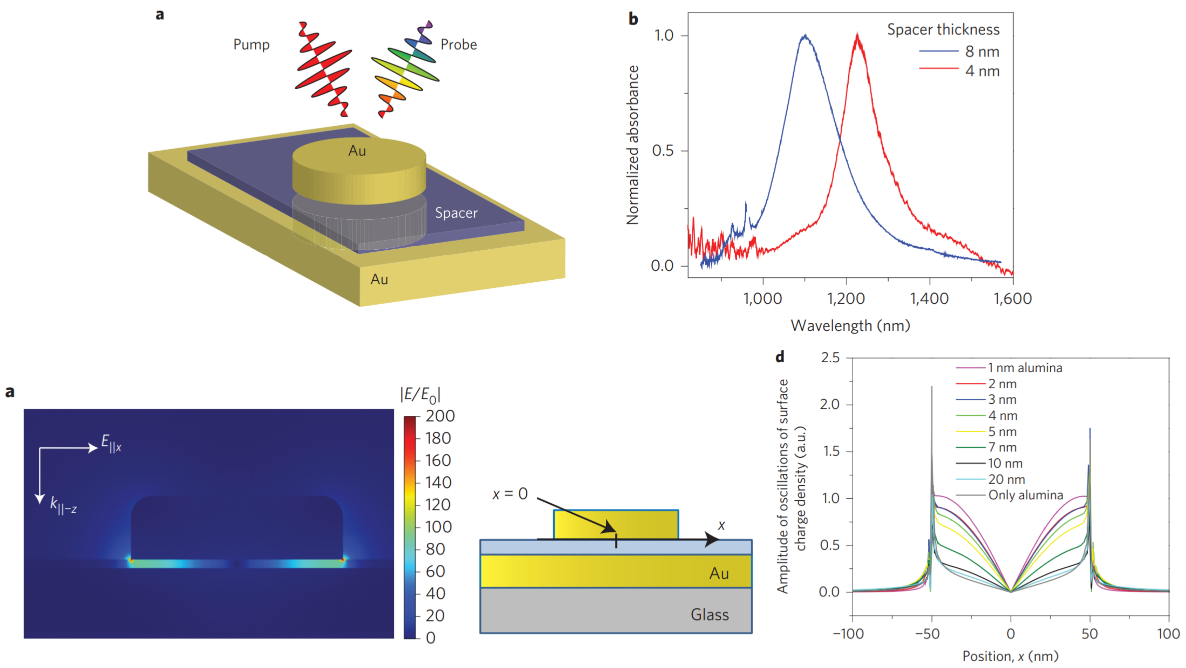

Figure 2.7: Geometries and experimental schematic for [17]. Gap confined plasmonic modes showed anomalously strong hot-carrier generation at "hot-spot' locations in the geometry.

where E_0 is the free space electric field prior to confinement. This dramatically increases the energetic carrier distribution number, and thus this geometry may offer a promising platform for studying NPL.

2.4 Experiment

We have discussed the various processes which ultimately lead up to hot-electron generation. It has been seen that confined metal nanoparticles display a broadened range of carrier energies due to the resulting opening up of k-space. The observations of [17] in this same geometry suggest very efficient production of hot electrons on ultrafast timescales. However, the pump-probe measurements which were done were limited by pulsewidth of the laser which was 130 fs. Photoluminescence measurements on this geometry may give insight to the the dynamics going on at this ultrafast timescale. If it is indeed gap-plasmon confinement which is leading to efficient hot electron generation, then the excitation with a monochromatic light source should result in a broader emission energies, as more "diagonal" transitions would be allowed. Reducing the dimensions would offer a way of tuning this broadening further, and would give insight to the full dynamics of the allowed transitions involved in this process, and would suggest a way for exciting hot electrons directly rather than as an inefficient by product of thermalizing scattering events.

2.4.1 Proposed Experiment

One property that is lacking in investigation is the role the degree of spatial confinement has on PL signals. As discussed earlier, the degree of spatial confinement is typically probed via binary experimental methods. Methods such as comparing smooth versus rough surfaces, or single nanoparticle versus single nanoparticle aggregates. When studying the PL properties of strongly localized plasmon modes, the breakdown of translational symmetry has often been simply assumed to be due to randomly sized surface features from film roughness. Thus, the degree of momentum breakdown and its effect on PL are not obvious from these results. Importantly, these experimental findings show differing optical responses and PL spectra. This shows that the degree of confinement plays a crucial role in these different cases. A systematic study which controls the breakdown and onset of translational symmetry has not been done and is necessary.

A convenient and experimentally realizable geometry to study spatial confinement is a film coupled antenna array, or a metal-dielectric-metal (MDM) geometry. In [17], such a systematic study of spatial dependence was performed to offer insight of the ultrafast optical and electronic responses from the con-

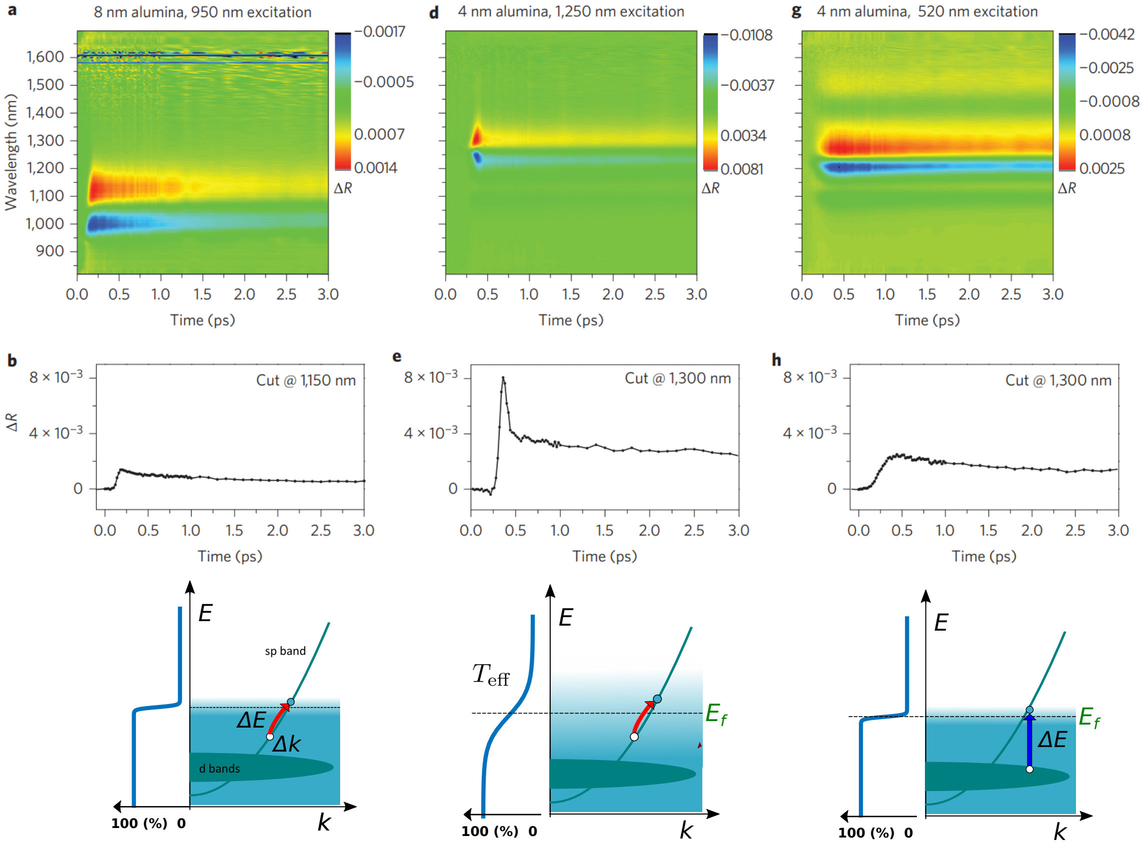

Figure 2.8: Ultrafast electronic responses for gap mode resonators probing the various allowed transitions in Au [17].

finement of plasmon modes. In this work nanodisks of fixed diameters were used among varying spacer thicknesses and their ultrafast optical responses were monitored via pump-probe measurements (Fig. 2.8). The MDM structure used in this work offers an attractive and controllable way to investigate the effects of spatial confinement on NPL. However, one potential issue when using analogous structures to investigate NPL signals is the laser excitation energy. In [17] the nanodisk resonance energies varied as the spacer thickness changed and not due to their characteristic particle sizes which was fixed. Although the plasmon modes were still able to be pumped near or at their resonant energies, this could be problematic for NPL experiments. For intraband transitions in the sp conduction band, the dispersion relationship is roughly parabolic. For a given laser energy and plasmonic wavevector, there is a unique diagonal transition which can occur at each point on the conduction band (Fig. 2.9 (a) & (b)). This is in contrast to interband

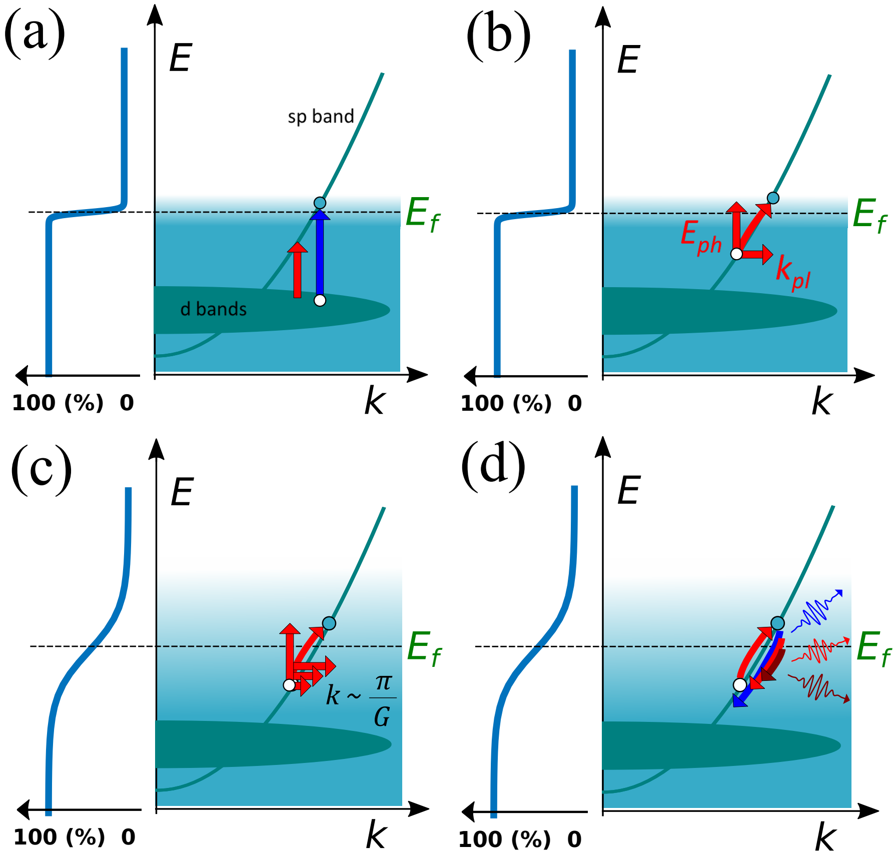

Figure 2.9: Various electronic transitions occurring in Au and the corresponding Fermi-Dirac distributions. (a) Availability of electronic transitions to couple with free-space photons. Blue vertical arrow represents the interband transition in gold of 2.38 eV (520 nm), and the red vertical arrow represents the laser energy used in these experiments of 1.58 eV (785 nm), which cannot couple directly to free-space photons. (b) Plasmon-mediated intraband transition results in “diagonal” intraband transition. (c) Plasmon-mediated intraband transition with varying wavevector for a given spatial confinement of a gap-plasmon mode. (d) Continuum generation from intraband PL, including both up and down-converted photons, from elevated electron temperature population.

transitions as there are many initial and final electron and vacancy states available. This is due to the “sea” of initial d band electronic states and the efficiency of promotion to the conduction band only depends on the Fermi distribution number. A large role in determining what absorption or scattering processes can be involved in the absorption and emission of light. Depending on the laser energy used for excitation, whether it be UV to near-IR will determine whether interband, intraband, multiphoton, etc., transitions may occur.

The geometry of the proposed experiment of the system is an Au layer-spacer patch antenna nanowire array similar to what was done in [17]. In this case the spacer thicknesses will be varied as well as varied wire widths. By controlling the wire widths and the gap thickness, the particle plasmons may be tuned to a particular resonance in the MDM geometry. In particular, a blueshift will occur for decreasing nanowire width, and a redshift with decreasing gap thickness. This is experimentally shown in Fig. 2.10. In this geometry, we then can say that the particle plasmon resonance, ω_{pp} is a function of both the wire width, W, and gap height, G, i.e.

$$\omega_{pp} \to \omega_{pp}(W, G). \tag{2.7}$$

First, we consider two isolated Au nanowires of fixed thickness, but varied widths, ℓ, and, L, with $L > \ell$. The particle plasmon resonances given the difference in aspect ratio of the two via Gans theory (eq. 1.48) is

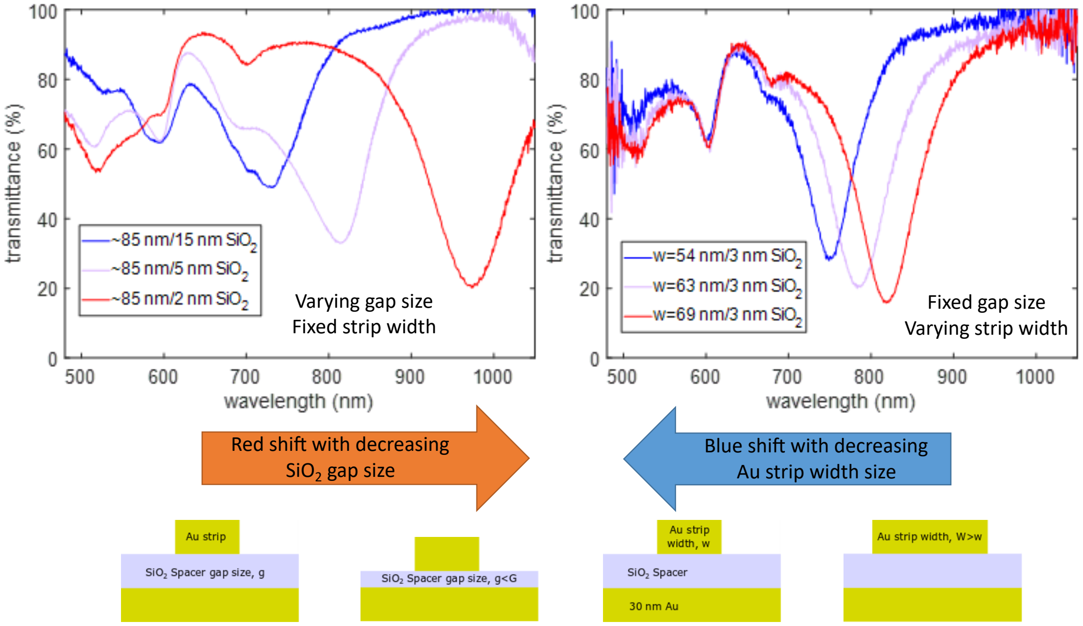

Figure 2.10: Redshifting due to fixed fixed strip width and decreasing gap size. Blueshifting due to decreasing nanowire strip width on fixed gap size.

in general

$$\omega_{pp}(L) < \omega_{pp}(\ell). \tag{2.8}$$

This is illustrated in Fig. 2.11. Now suppose the wire is placed near a film separated by a gap thickness, $G = H$. If H is fairly large, we may assume weak redshifting and

$$\omega_{pp}(L) \approx \omega_{pp}(L, G). \tag{2.9}$$

Now, given the two degrees of freedom there is in which to tune this resonance, there may exist for the other particle of size, $W = \ell$, as before, but with a gap thickness, $G = h < H$, such that

$$\omega_{pp}(\ell, g) < \omega_{pp}(\ell). \tag{2.10}$$

By tuning h appropriately, we may match the resonances:

$$\omega_{pp}(L, H) = \omega_{pp}(\ell, h). \tag{2.11}$$

This method allows us to match the resonant plasmon energies and at the same time probe the spatial confinement, and hence wavevector. Following [1], and referencing section 1.4.4, this wavevector is approximated

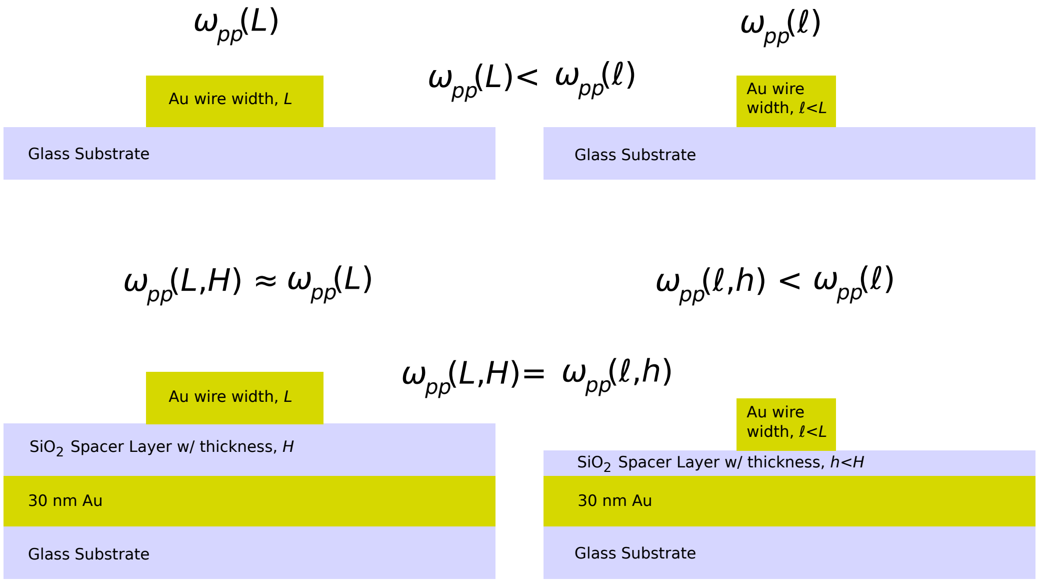

Figure 2.11: Setup of proposed experiment. Detailed description is given in the text.

as

$$k \sim \frac{\pi}{G}. \tag{2.12}$$

By varying the spacer thickness and shifting the aspect ratios to match the resonance, this approach offers a way to probe the opening up of allowed momentum state transitions for a fixed plasmon energy (Fig. 2.9 (c)). Differences in the PL emission spectra between the two setups may offer insights to identify the effects of spatial confinement on induced hot-electron distributions (Fig. 2.9 (d)).

2.4.2 Nanowire Array Design (Gradient Gratings)

It is well-known that the PL from plasmonic structure tends to follow the plasmonic scattering spectrum [16]. This is not not surprising as it fairly agreed upon that the strong plasmon fields are responsible for mediating the various internal processes from the various proposed mechanisms for NPL. When the excitation energy and plasmon peak do not overlap the overall PL yield is supressed. It is therefore crucial to design plasmonic particle resonators having as close overlap as possible with the excitation laser to maximize emission. This is easily achievable for single particle PL experiments which involve spin coating of nanoparticles on to a substrate [8, 35, 39], as nanoparticles with free-space resonances tailored to match common commercial laser excitation energies are readily available [45]. For MDM geometries this is not suitable solution. This is because of the induced redshifting of the particle resonances when in the close proximity to metal films due to image charge interactions. This necessitates nanofabrication of particles which are tailored in size to achieve the desired resonance given the anticipated proximity to the metal under film separated by the nanometric dielectric spacer gap.

In principle it would be possible to numerically estimate the particle resonance given it's size and proximity to the under film given the gap size. Then careful nanofabrication procedures would result in a more or less homogeneous array of resonators which have the desired peak resonance. However, this is easier said than done. Full electrodynamic simulations for each gap thickness would be required to predict the resonance for each gap thickness. Additionally, uncertainties in nanofabrication can result in discrepancies as the resonances are very sensitive small changes in their environment. Besides this, another problem then is the lack of tunablity of the resonance post-fabrication which are "burnt-in". If a resonator array is matched to a particular laser energy, then another array would be required to match a different laser energy. This is undesirable as it has been shown that laser excitation energies alone can determine the various electronic dynamics and tunability of the plasmon mode would be ideal.

To achieve this tunablility of the plasmon resonances in the MDM geometry we employ a "gradient-

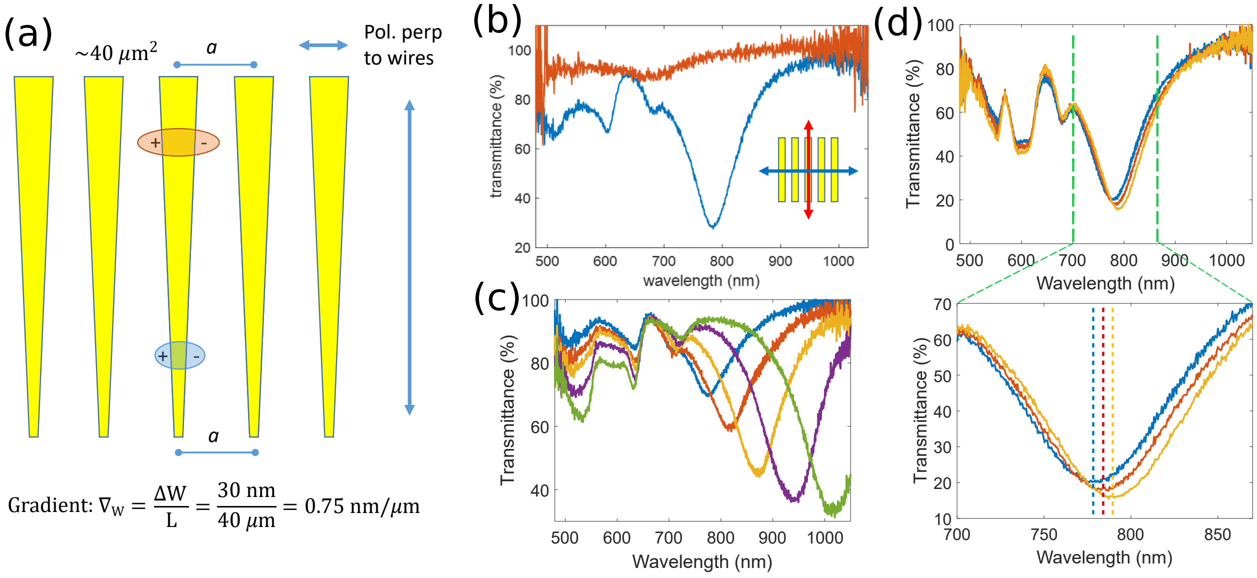

Figure 2.12: (a) Schematic of gradient nanowire strip array design. (b) Polarization dependence of wire resonance. (c) Broad tunability range of the fundamental mode in one array of fixed gap size. (d) Highly accurate (< 5 nm) fine tuning of plasmon mode peak resonance. Precision of this peak resonance is limited only by the bandwidth of the mode.

width" nanowire strip array. This design schematic can be seen in Fig. 2.12 (a). The nanowires are in a 40 μm by 40 μm array with periodicity of $a = 350$ nm. These nanowires have their widths tapered from one end of the array to the other by about $\Delta W = 30$ nm. This tapering of the width causes a shift in plasmon resonance due to the change in aspect ratio (eq. 1.48). Additionally, the widths are a tapered with a very small gradient, ∇_W, over the length of the array, $L = 40$ μm. The gradient is estimated to be $\nabla_W \approx \Delta W/L = 30$ nm/40 μm $= 0.75$ nm/μm. This small gradient allows for fine tuning the plasmon resonances over a broad range of detectable wavelengths of ~ 300 nm from 750 - 1050 nm ($\Delta(\hbar\omega_{pp})$ =0.53 eV) (Fig. 2.12 (c)). We note that these resonances tend to further shift into the NIR which then must be detected with different detectors. This design also convienently allows correlation of the PL signal with polarization angle as only incident light polarized perpendicular to the nanowire strip will excite the plasmon mode (Fig. 2.12 (b)). We also note that the grating mode, i.e. the photonic mode associated with the periodicity of the structure, will share the same polarization dependence. However, the periodicity, a, can be chosen such that this mode is blueshifted out of the PL spectral region of interest. Finally, these modes offer a way to finely tune the resonance peaks with a precision of < 5 nm which offers a way for optimizing overlap with the laser energy (Fig. 2.12 (d)). This overcomes inhomogenous resonance distributions commonly encountered with commercially obtained nanoparticles which are typically grown via wet chemistry methods.

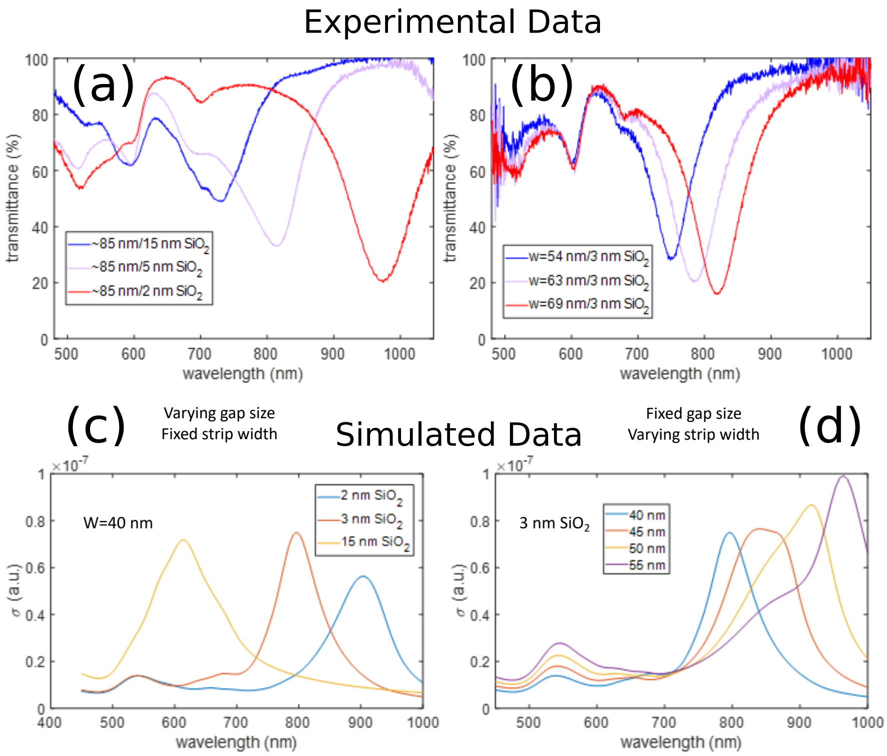

Figure 2.13: FDTD simlated gap plasmons scattering cross secions, σ (bottom), compared to experimental transmittance data (top).

2.4.3 Experimental Setup

The experimental setup is shown in Fig. 2.14. For transmittance measurements, white light was provided by a halogen lamp. An iris is placed just after the lamp to limit the anglular distribution of light rays incident

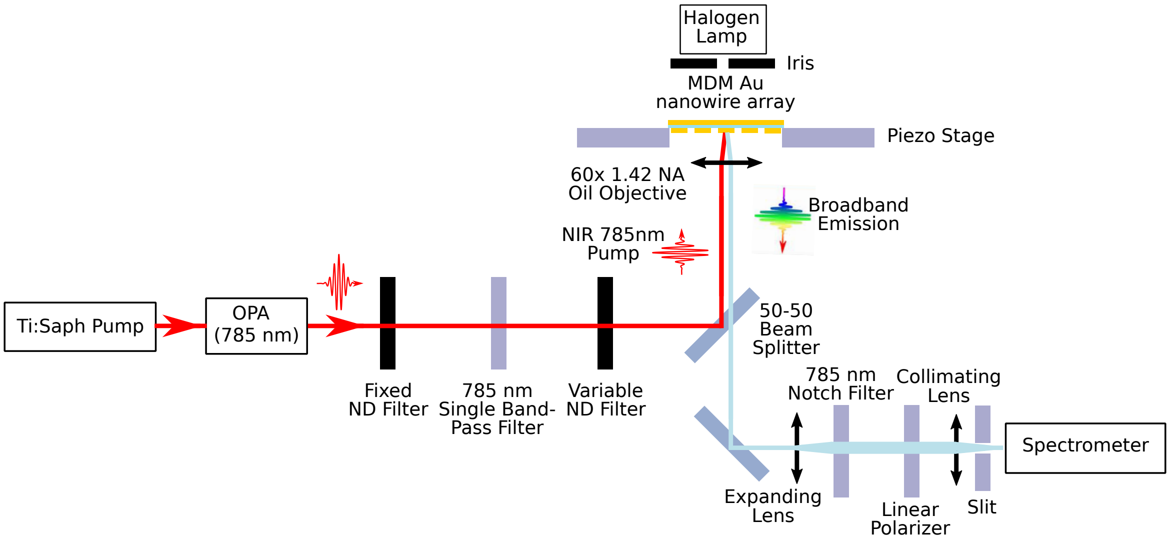

Figure 2.14: NPL and optical transmittance experimental setup. Detail is given in the main text.

on the sample. This was done so as not to excite any higher order grating modes which could potentially overlap with the fundamental gap mode spectral region. The MDM nanowire array is placed on a piezo stage, as fine tuning of the position along the gradient gratings is crutial for selection of the gap mode center resonance. The scattered light is collected by a 60x NA = 1.42 oil objective for maximal light collection. The MDM structure is intentionally immersed in the oil of the objective which is a bit non-traditional. This was done for three main reasons: 1. The index matching and larger scattered wavevector resolution eliminates the undesirable Fano lineshape which is produced from interference between the scattered and incident light fields due to an induced phase mismatch upon passing through the surface [46], 2. the oil significantly reduces long term oxidation effects on the dielectric spacer layer which can result in unwanted surface roughness, and 3. for PL measurements the Au under layer acts as a mirror for the light emission and so enhances the signal yield. The scattered light is then passed through an expanding lense before passing through a polarizer which is aligned to the polarization dependent resonance of the nanowire array. Finally the light is sent through a collimating lens before it is passed through two perpendicular 150 μm slits (one of which is internal to the spectrometer and adjustable) which act as a pinhole to confocally isolate the collected signal from the MDM structure ensuring the signal is just from the spatially and spectrally tuned nanowires. The spectrometer is a CCD Silicon chip 1024 by 128 pixel array cooled to -70 °C.

For NPL measurements, a Ti:Saph pump provides a 785 nm wavelength, 150 fs pulsed laser output at an 80 MHz repetition rate. The pulse is passed through an optical parametric amplifier (OPA) system where it is simply passed through and unaltered spectrally, but is reduced to 20% of it's initial intensity with an output from the laser window of ≈ 20 mW. The output intensity is again lowered by a fixed neutral density (ND) filter by 2 orders of magnitude before being passed through a 785 ± 15 nm single-band pass filter to eliminate any sidebands of the laser pulse as well as any residual luminescence from the Ti:Saph laser. The pulse is then passed through a variable ND filter for fine tuning of the power intensity for performing power dependent emission measurements. The power fluences used for NPL experiments on gap modes were over a range of $\approx 2 - 16$ μW. Given the pulse length, repetition rate and spot size, this corresponds to peak powers of $\approx 0.01 - 0.05$ $\mathrm{GW \cdot cm^{-2}}$ at the excitation spot. A 50-50 beam splitter sends the pulse to the the objective where it is focused on the MDM structure where it has been previously positioned such that the plasmonic resonance is at the desired value at the laser spot location. The laser pulse is horizontally polarized and the polarization dependent MDM structures are aligned accordingly. The transmittance of the plasmon resonance is taken both before and after pulsed laser excitation to ensure no spectral shifting due to melting/reshaping of the nanowires occured, as the field enhancement in the gap is large and the combined peak power of the laser can indeed cause this. The continuum PL emission is collected through the same objective where it is then passed through the 50-50 beam splitter and sent to the emission filters.

The emission is sent through a 785 nm notch filter which rejects wavelengths of 785 ± 15 nm to remove any residual laser pulse from blinding the spectrometer. The emission is passed through a polarizer which is aligned to the polarization dependent resonance of the nanowire array. Finally the emission passed through a collimating lense and before entering the spectrometer, the external slit is removed and the spectrometer slit is set to 200 μm to increase signal count while still maintaining decent spectral resolution.

2.5 Fabrication Procedures

2.5.1 Gradient Nanowire Arrays

Glass substrates were sonicated in a solution of deionized water and detergent for 20 minutes at 50° C followed by an 20 minute acid wash using a 3:1 piranha acid solution of H_2SO_4 and H_2O_2 before being stored under isopropyl alcohol. The Au-spacer sample was fabricated by first thermally evaporating 30 nm of Au onto a glass substrate under vacuum at a rate of 20 Å/s. This was followed by sequential monolayer deposition by plasma Atomic Layer Deposition (ALD) to produce the SiO_2 dielectric spacer layer of varying thickness. The nanowire arrays were fabricated by using standard positive resist electron-beam lithography using spin-coated MMA and PMMA-950 for the bottom and top resist layers respectively. A modified dose procedure was employed to produce smaller features as well as the gradient width. Much smaller area doses of an elongated trapezoidal shape defined by a slowly tapered width starting at 15 nm and steadily decreasing to 12 nm over the 40 μm length of the wire in the CAD design file. This is intentionally done as film development via this method depends more on utilizing the secondary electron scattering rather than the primary dose as is traditional ebl methods. The period of the wire spacing in the grating array was set to be 350 nm. In addition to the small initial dose, significant secondary electron scattering provides an additional "double" dosing to the pattern because of the close proximity to adjacent wires. This results in nanowires with widths ranging from >100 nm down to $\sim$ 30 nm, much larger than the CAD software design of $\sim$ 12 - 15 nm. This provides the controlled tunability of the plasmon resonance with a monotonically changing single-directional width gradient as described in the previous section. This smaller grating periodicity also has the benefit of blueshifting the grating mode resonance to around 550 nm, out of the spectral window of the emission spectra. Following pattern etching, the sample is development in a 1:1 solution of MIBK:IPA for 15 seconds at 0° C. Differential contrast microscopy is used to monitor and confirm the development of the polymer film via color contrast, as occasional inhomogeneities of the PMMA/MMA thickness necessitate further development in MIBK:IPA. Once pattern development is confirmed, another 30 nm layer of Au is deposited by thermal evaporation, then the sample is put under acetone to remove any excess polymer. The excess metal film is washed off and the finished sample is transferred to isopropyl alcohol and then blown dry with N_2 gas. The micro-arrays are then examined using a Zeiss scanning electron microscope to ensure the quality of the nanostructures.

2.5.2 ALD

Atomic Layer Deposition (ALD) was performed with a Cambridge FIJI Plasma ALD system to produce the nanometric dielectric spacer layers. Fabrication of these layers were performed in a class 100 cleanroom to prevent contamination during the process. A succinct explanation of ALD is given by Ref. [47]. ALD deposition is a process by which a film is grown on a substrate by exposing its surface sequentially to alternate gaseous species referred to as precursors. The precursors are never present simultaneously in the reactor, but they are inserted as a series of sequential, non-overlapping pulses. In each of these pulses the precursor molecules react with the surface in a self-limiting way, so that the reaction terminates once all the reactive sites on the surface are consumed. Consequently, the maximum amount of material deposited on the surface after a single exposure to all of the precursors (a so-called ALD cycle) is determined by the nature of the precursor-surface interaction. By varying the number of cycles it is possible to grow materials uniformly and with high precision on arbitrarily complex and large substrates [47].

Two types of dielectric spacers were used, SiO_2 and Al_2O_3. Both processes were plasma assisted and deposited at 150° C. The deposition rates of SiO_2 and Al_2O_3 were 0.6 Å/cycle and 1.04 Å/cycle, respectively. These thicknesses were confirmed by both ellipsometry measurements and an AFM "scratch" test. ALD is more favorable than other deposition techniques such as thermal evaporation and sputtering as it produces pinhole free films with ultra-high aspect ratio features. This is due to ALD being a self-limiting process. SiO_2 ALD is done using tris(dimethylamino)silane and O_2 precursors while Al_2O_3 requires a trimethylaluminum and H_2O precursor. One important parameter we wished to explore was that of field enhancement of the plasmon mode. One simple way to alter this is by changing material in the dielectric spacer layer. However, any substrate which is oxidized easily, such as Ag and Al, cannot be done with O_2 precursors. This limits the types of spacer layers that may be deposited onto these substrates without the need of wetting layers which add undesirable optical effects. For this reason the only plasmonic metals used in this study was Au which is more chemically inert and therefore can have several types of ALD layers deposited without contaminating the film.

One complication with the ALD method is with very thick films. Adhesion between Au and SiO_2 is inherently poor and typically film quality suffers when they share an interface. Thermal methods such as evaporation or sputtering worsen this effect as liquid-like clustering dominates early growth resulting in rougher films (as discussed in more detail in Chapter 3). ALD deposition can get around this as it is a an inherently self-limiting process and is not thermal and therefore more controllable. However, this method has its limitations, particularly for thick films. This is due to inherent stress which builds up in the film which scales with thickness. A telltale consequence is the appearance of protrusions or “bubbles” appearing on the surface as shown in Fig. 2.15. These bubbles are thermodynamically favorable as the surface free energy of the interface is reduced as they form because they effectively lower the surface area of the film and thus lowering the surface free energy associated with the interface (dicussed further in section 3.2.1). As seen in the AFM images in Fig. 2.15 an initial film of 15 nm of SiO_2 after time will form these bubble clusters of heights up to nearly double the initial film thickness. The diameter of these bubbles are $\approx 1\mu$m with a distribution of $\approx$ 10 bubbles/10 μm^2 and are detrimental when doing roughness dependent NPL measurements. It was empirically found that this effect was general unavoidable for films $\gtrsim$ 15 nm, and these thickness were avoided. However, the wavevectors associated with 12 nm SiO_2 ($k \sim \pi/12$nm) are still small enough compared to the mean wavevector mismatch in the Au intraband transition mismatch of ($\Delta k \sim \pi/(<5$nm) [8] to be considered a limiting case for the level of spatial confinement of the gap mode. That is, 12 nm would represent no gap confinement, and 2 nm would represent significant gap confinement.

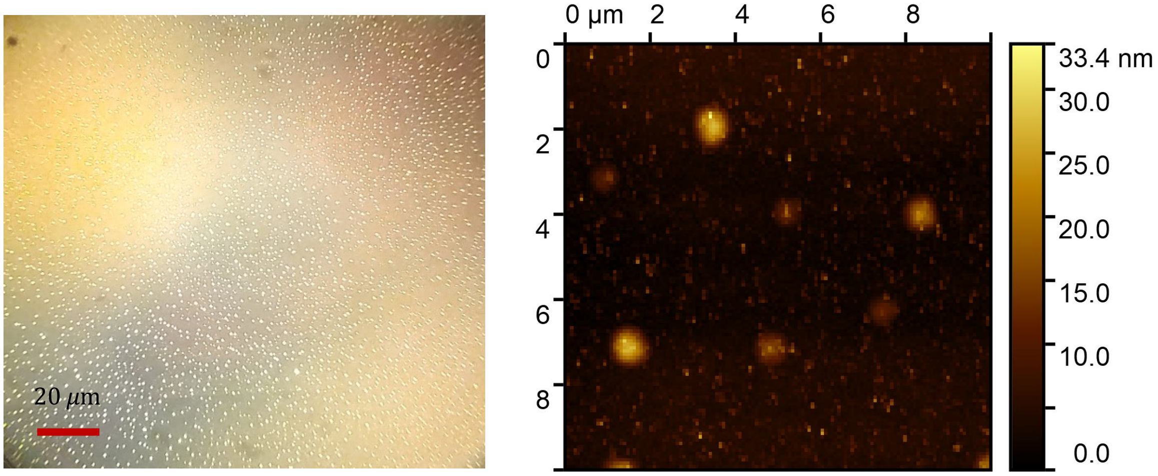

‘bubbles’ on 15 nm SiO2

10 x 10 μm²

Figure 2.15: “Bubbles” on thick SiO_2. Opctical microscope image (left) and AFM image (right).

2.5.3 Cryogenic Sputtering

Substrate roughness can be conceived as adding additional PL signal from the nanostructures. Smooth versus rough gap modes and the effects of imposed wavevectors on PL were investigated as well. To explore the effects of substrate roughness on PL, it is then necessary to produce separate samples made with substrates which are smooth as possible. For this a cryogenic sputtering technique was developed to produce ultra-smooth Au underlayers. Additionally, we find that this technique allows for the production of record thin ultra-smooth Au films. This technique is discussed in detail in Chapter 3. An example of the significance of using this method can be seen in AFM images of cyrogenic sputtering versus thermal evaporating methods in Fig. 2.20.

2.6 Results

2.6.1 Gap Size Dependent NPL

Plasmon resonance matching for dielectric gap spacer thicknesses ranging from 1 to 15 nm of SiO_2 can be seen in Fig. 2.16. Additionally, finite difference time domain simulations of the electric field in this different

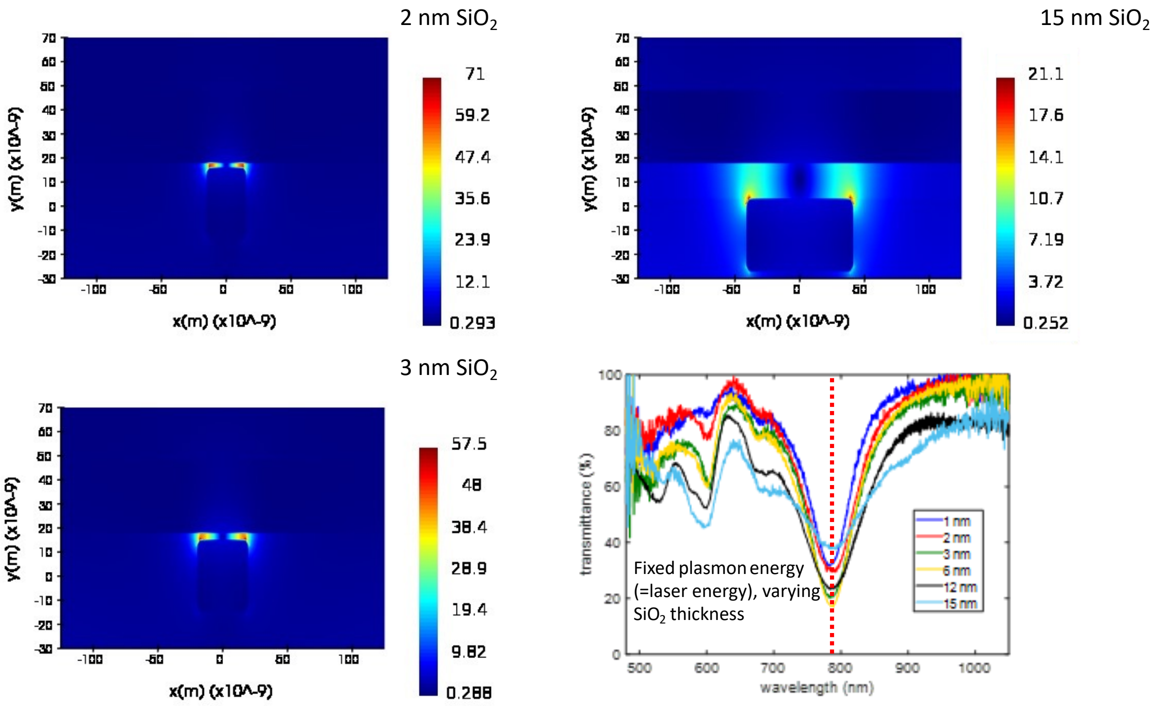

Figure 2.16: Fixed gap FDTD field enhancements and experimental transmittance of matched plasmon resonances.

spacer thicknesses are calculated for 2, 3 and 12 nm gap sizes at their 785 nm resonance. The confinement of the electric field is clearly seen to increase with decreasing gap thickness and the relative field enhancement compared to the free space light reaches up to ~ 70.

The MDM nanostructures are excited on resonance with a 785 nm Ti:Saph pulsed laser. The resonances are tailored to be 785 nm so as to get a large as possible PL signal. The laser has a 150 fs pulse length and 80 MHz repetition rate, giving a maximum peak power of ~ 0.1 GW/cm^2 used in these experiments. The spectra for a particular spacer thickness are taken with several different laser powers. The power exponent, $p(\omega)$, is then calculated by fitting the spectral signals, $\phi(\omega)$, to the corresponding laser powers, P, via eq. 1.38. An ansatz for this experiment is that increasing characteristic wavevectors (decreasing SiO_2 thickness) would put electrons in the metal further from equilibrium resulting in a "hotter" electron distribution, and a relatively larger T_e^* in [36]. This would result in a "flatter" scaling exponent slope that would tend to zero, i.e. $p(\omega) \to 1$. This can be interpreted as the signal of a photon energy becoming more "efficient", as less power is needed to increase the signal when the power exponent is smaller. This is indeed what is observed; as the spacer thickness is decreased the values for $p(\omega)$ are reduced.

However, we also observe the appearance of two distinct linear regimes in the scaling exponent slope occurring with decreasing spacer size shown in Fig. 2.17. These two distinct slopes occur on either side of the plasmon/laser energy. For increasing spacer thicknesses we observe a trend towards a more-or-less linear slope as observed on Au films with a tapering out around $p = 2$. These results are surprising, and proposed theories in previous works do not fully capture the observed effects. This indicates that the physical mechanism of the nonlinear PL signal originating from thermalized hot electron relaxation needs to be revisited in these structures.

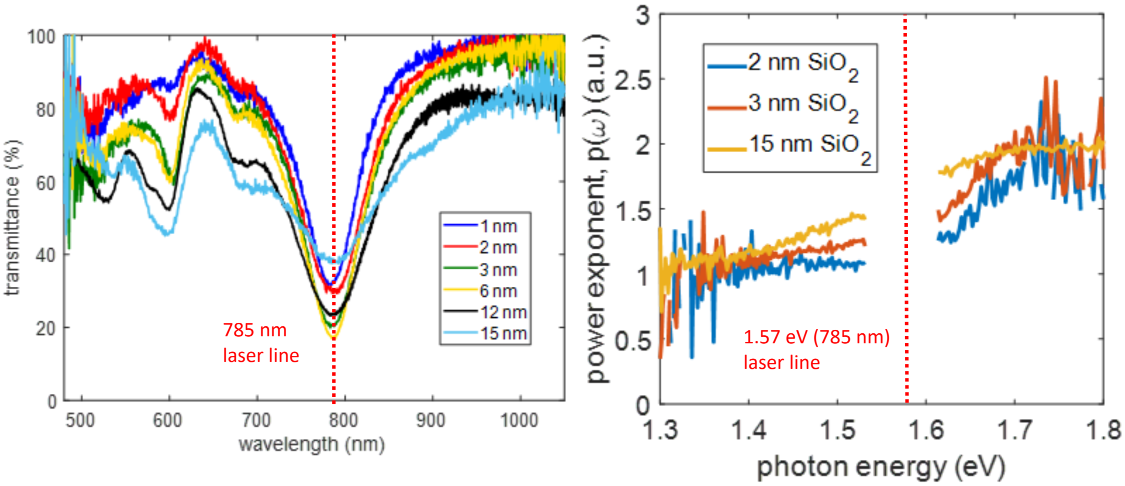

Figure 2.17: Fixed gap resonant matched (left) and extracted PL power law (right).

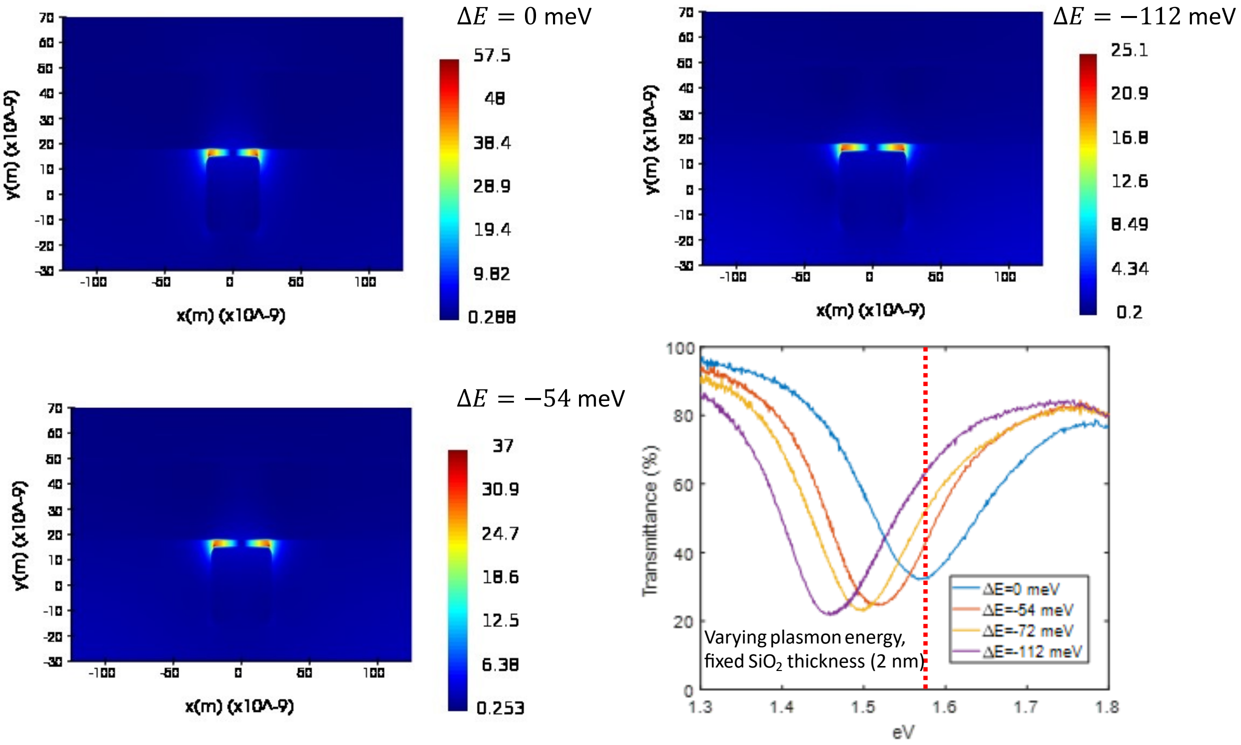

Figure 2.18: Fixed gap FDTD field enhancements and experimental transmittance of detuned plasmon resonances.

2.6.2 Plasmon Detuning NPL

It is crucial to determine whether this effect is due to the imposed characteristic wavevector or simply an enhancement effect due to the strongly enhanced electric fields. As noted in Fig 2.16, the electric field dramatically increases in the gap mode for small thicknesses. To investigate this, we simply detune the plasmon mode from the laser energy to make it slightly off-resonance. By doing this, there will still be spectral overlap between the plasmon mode and the laser, but the overall field enhancement will be lowered. Spectra of the detuned mode along with the FDTD simulations of the electric field at 785 nm is shown in Fig. 2.18. The field enhancement drops accordingly for increasing detuning. PL power analysis on these detuned modes for 2 nm SiO2 gaps are shown in Fig. 2.19. Interestingly, the two linear regime lineshape is maintained for the detuned resonances. However, a clear increase of the overall value of $p(\omega)$ with increased detuning is observed. This may indicate that the overall efficiency (lowered p) is field enhanced, while the overall lineshape, $p(\omega)$, is indeed due to spatial confinement and resulting large wavevectors.

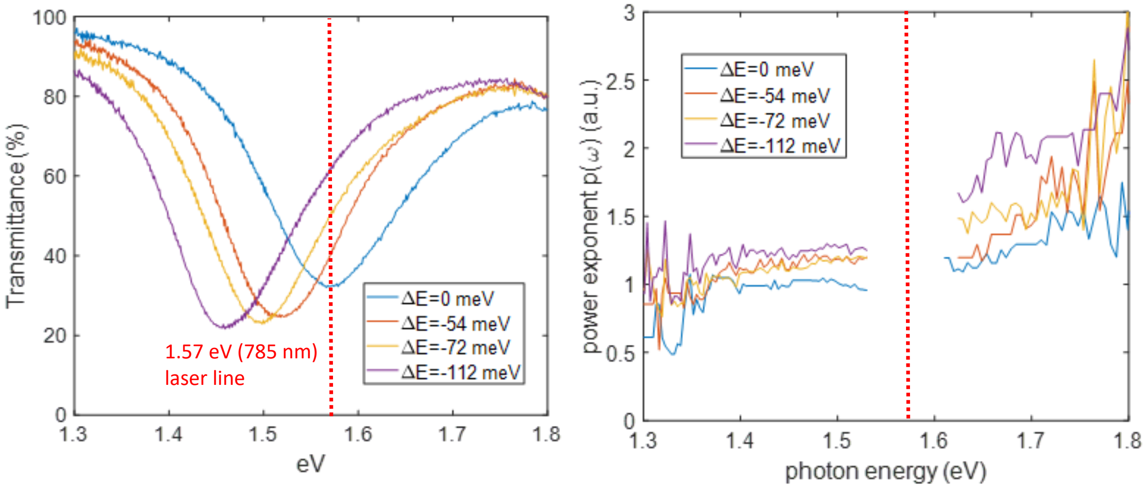

Figure 2.19: Detuned plasmon mode (left) and extracted PL power law (right).

2.6.3 Effects of Surface Roughness

An important factor to consider is the film quality of the interface of the MDM structure. As mentioned extensively, surface roughness is known to mediate several emission processes. For this reason, separate samples with Au underlayers made via cryogenic sputtering methods to produce ultrasmooth films were utilized to ensure that the observed signal is not due to roughness at the interface. For each thickness we have two spectra to consider: $\phi_R^G(\omega)$ & $\phi_S^G(\omega)$ which are the emission spectra corresponding to same

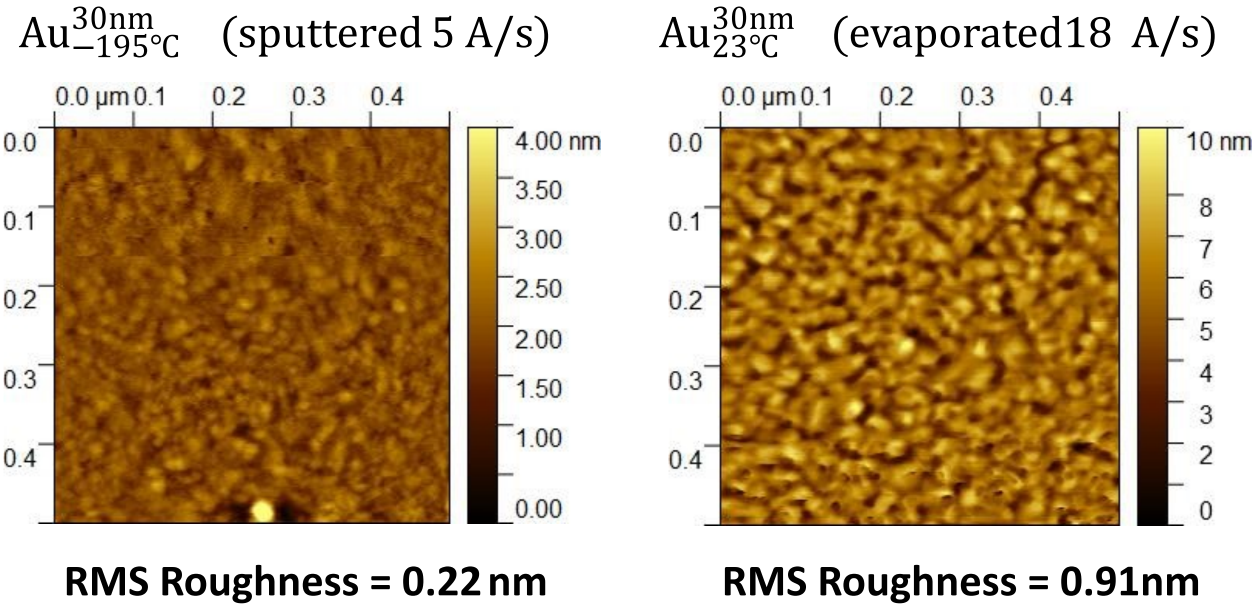

Figure 2.20: AFM images of underlayer Au films produced via cyrogenic sputtering (left) and thermal evaporation (right).

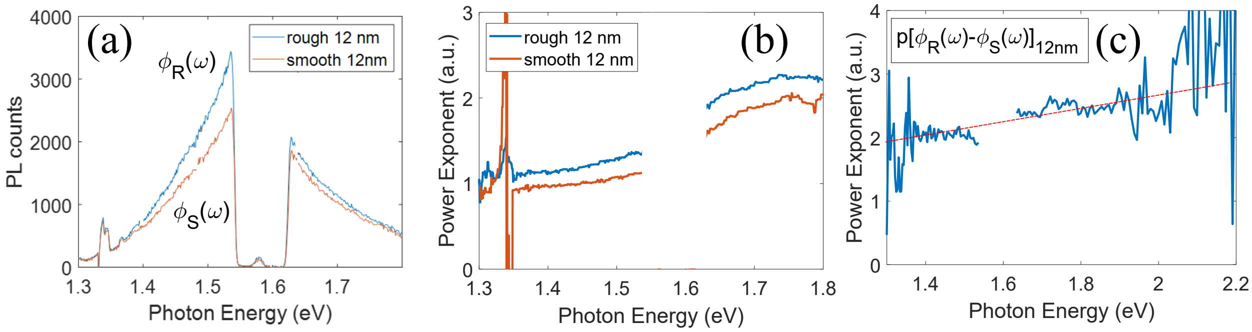

Figure 2.21: (a) $\phi_R(\omega)$ and $\phi_S(\omega)$ at equally high fluence for 12 nm SiO2 with rough and smooth underlayers, respectively. Clearly the rough sample is more emissive (b) Extracted power law line shape for the set of $\phi_R(\omega)$ and $\phi_S(\omega)$ at varying powers. (c) Power law extracted from the difference of $\phi_R(\omega) - \phi_S(\omega)$. A clear linear slope is observed indicating the greater emission from the rough film is due to roughness.

excitation power from a rough and smooth film, respectively, with gap size, G. The raw PL spectra at a fluence of $\sim 16\ \mu\text{W/cm}^2$ for the two cases is shown in Fig. 2.21 (a). Clearly the rough film is more emissive than the smooth film indicating the extra roughness may be contributing. In addition, the smooth film power law more closely resembles that of the thinner gaps which exhibit the two distinct linear regimes. The calculated $p(\omega)$ lineshapes for the two cases is shown in Fig. 2.21 (b). Again, a difference between the two is evident. To potentially disern the origin of the differences in emission bewtween the two, we take the difference between the two, $\phi_R^{12\text{nm}}(\omega) - \phi_S^{12\text{nm}}(\omega)$, and calculate the corresponding power law. This is shown in Fig 2.21 (c) A clear linear slope is observed, indicative of the thermal emission contribution expected from rough surfaces predicted by [36] given by eq. 2.4.

Ultrasmooth underlayer films for 2 nm were also fabricated. The difference in raw spectra at $\sim 12\ \mu\text{W/cm}^2$

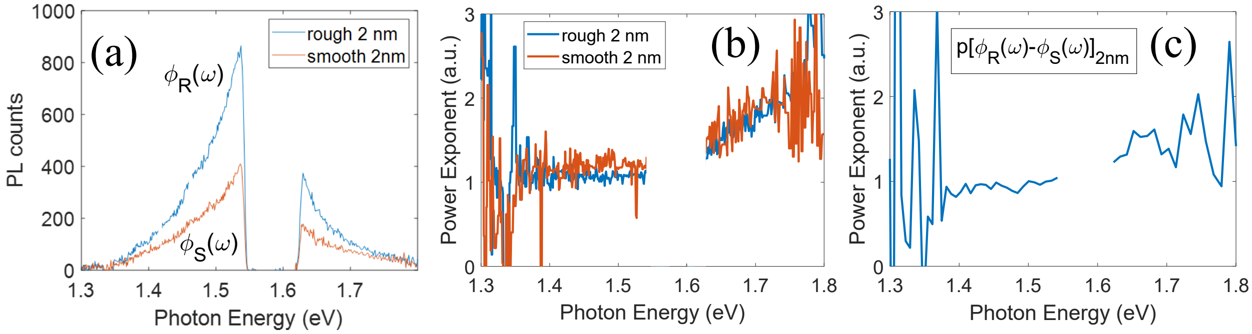

Figure 2.22: (a) $\phi_R(\omega)$ and $\phi_S(\omega)$ at equally high fluence for 2 nm SiO$_2$ with rough and smooth underlayers, respectively. Clearly the rough sample is more emissive (b) Extracted power law line shape for the set of $\phi_R(\omega)$ and $\phi_S(\omega)$ at varying powers. (c) Power law extracted from the difference of $\phi_R(\omega) - \phi_S(\omega)$. A clear resemblance to the individual power law extracted lineshapes is observed indicating the the effect of gap confinement at this thickness more or less dominates the observed signal. Surface roughness seems to increase the yield of this effect.

of the two are shown in Fig. 2.22 (a). Again, the rough films are seen to be more emissive similar to the 12 nm films, but additionally differ by roughly a power ~ 2. The power laws for each respective film are shown in Fig. 2.21 (b). Interestingly, the lineshapes for the two remain very similar to one another and retain the two distinct linearly sloped regimes. The power law extracted from the difference of $\phi_R^{2\text{nm}}(\omega) - \phi_S^{2\text{nm}}(\omega)$ is given in Fig. 2.22. A clear resemblance to the individual power law extracted lineshapes is observed indicating the the effect of gap confinement at this thickness more or less dominates the observed signal. Surface roughness seems to increase the yield of this effect.

2.6.4 Low Fluence Emission

One issue with the MDM structures used in this study are their sensitivity to peak powers and sensitivity to melting as mentioned in section 2.4.3. The initial ansantz of this experiment was a raising of the effective temperature, T_{eff}, of the electron distribution for decreasing gap thickness due to the resulting enhanced intraband momentum scattering into the conduction band. It is observed that there is an overall lowering of $p(\omega)$ and this picture is somewhat accurate. However, this ansantz should hold equally well by simply changing the excitation fluence to a different range as implied by eq. 2.3. However, these structure are

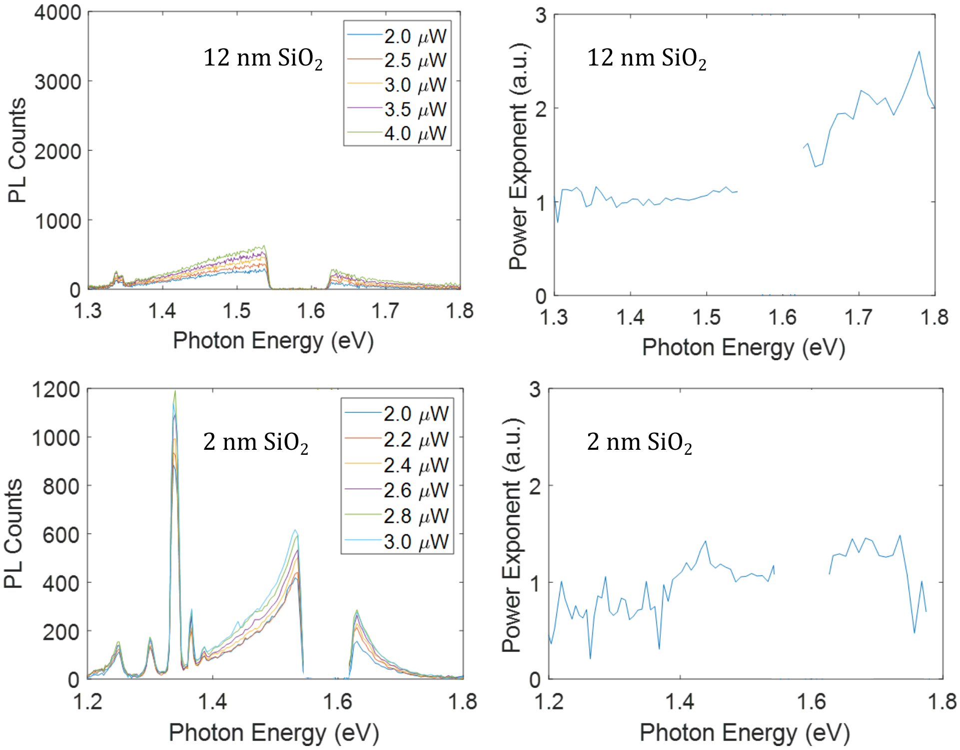

Figure 2.23: Low fluence power analysis on 2 and 12 nm SiO$_2$ for fluences of $2-3$ μWcm^{-2} and $2-4$ μWcm^{-2}, respectively. 2 nm signal was integrated for 1 hour. 12 nm signal was integrated for 2 minutes.

prone to melting at very low fluences and this limits the excitation power ranges which can be used. High excitation power will result in melting and spectral shifting of the plasmon mode, and too low of power will result in poor signal-to-noise, particularly for 2 nm SiO2 with ultrasmooth underlayer films, which are not very emissive (Fig. 2.22 (a)). The data shown thus far corresponds to fluence regions that border on, but do pass the empirically found fluence cutoff in which spectral reshaping occurs. For this reason, the only fluence range which can be explored is at lower fluences.

The emission spectra for 12 and 2 nm gaps for fluences of $\sim 2 - 4\ \mu\text{Wcm}^{-2}$ are shown in Fig. 2.23. It is noted that significantly longer exposure times were necessary to obtain this data, as the emissivity of the smooth film are already small even for high fluences. For 12 nm gaps the PL emission looks very similar to the lineshapes for 2 nm gap sizes shown in Fig. 2.22. So, the overall offset decreases with lowering of fluence power, contrary to our original ansantz. The same trend is observed for 2 nm gap where a nearly flat lineshape is observed for all emission energies, again contrary to our original ansantz.

2.7 Modeling

A summary of all the main processes which lead to nonlinear light emission and the respective predictions for the power law lineshape are given in figure Fig. 2.24. Given even all of these mechanisms, none seem to quite capture the essence of our observations. Even using combinations of these models do not adequately reproduce the data. This may imply that the assumptions and ansantz's that come along with these models may need to be revisted as well.

A recent study on single particle light emission from CW excitation [39] showed remarkably similar lineshapes to what is presented here. A summary of this study is shown in Fig. 2.25. In this work sets of single Au nanorods were excited near their fundamental modes with CW excitation wavelengths of 633 and 785 nm. These wavelengths were chosen so as to probe the intraband transition. Incident CW power fluences of $\sim 0.01 - 1\ \text{MWcm}^{-2}$) were used and PL was recorded and power analysis was performed shown in Fig. 2.25 (c). As can be seen, two distinct linear regimes are observed for the power law obtained from light emission, and these power laws only depend on the excitation energy. They qualitatively explain the observed power law lineshapes by making a claim regarding the characteristic times between excitation and themalization processes. In this case, CW laser excitation rate of carriers ($\sim$ 3.6 ps) was on par with the electron-phonon thermalization rate. This long photon absorption spacing because of this low power CW excitation ensures that a distinction between a nonequilibrium electronic and equilibrated lattice temperature is no longer possible [39] in contrast to the two-temperature model decribed in section 1.6.4. This effectively limits the number of photons which may be involved with electron-hole recombination resulting light emission. For example, a two-photon process is impossible in this picture because the characteristic excitation time needed to have both an initial photon absorbed followed by another at a later time is much longer than the time it takes for the initial excitation to damped from the system. So although there still is a weak thermal redistribution of energy via some intraband transition processes, a value of $p < 2$ is always maintained.

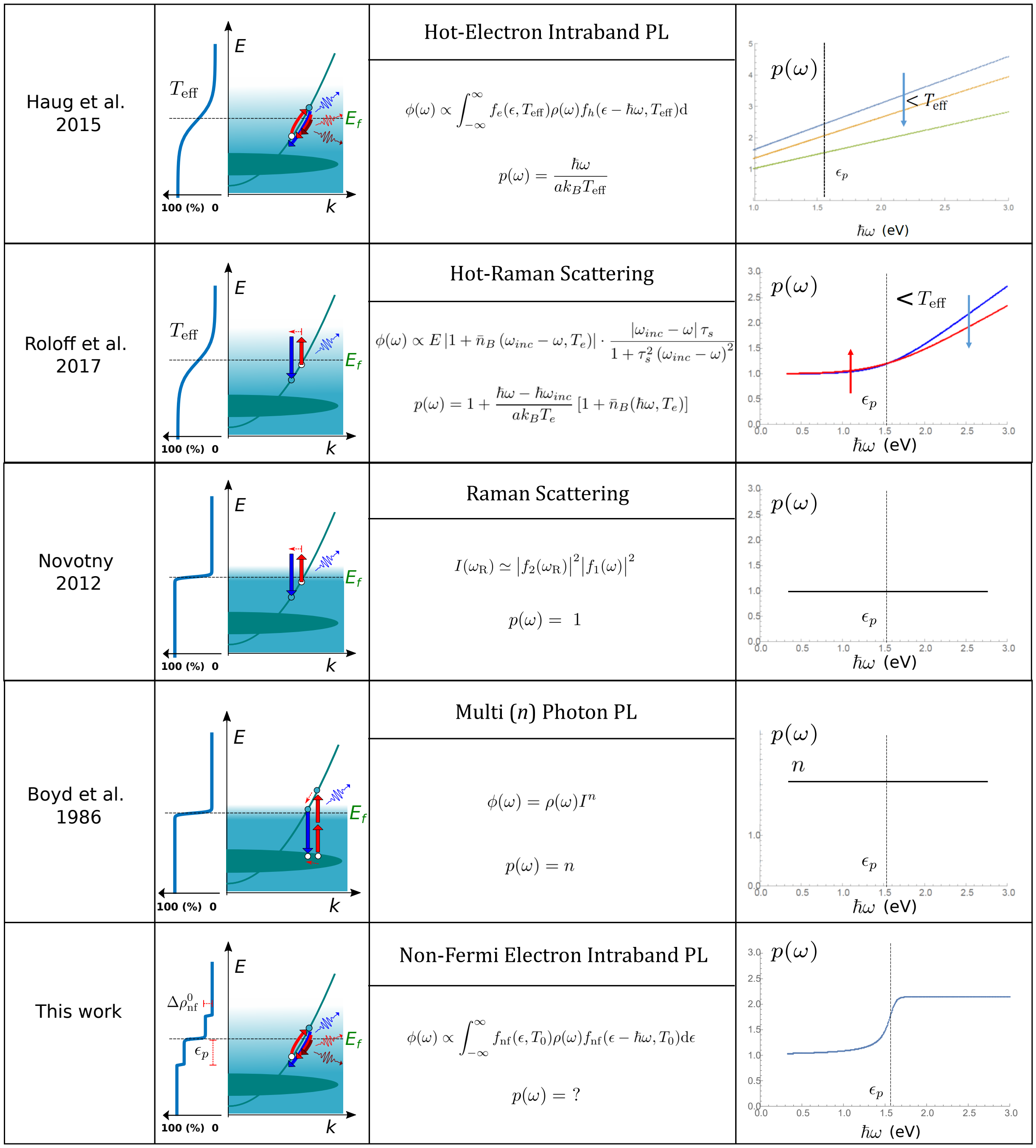

Figure 2.24: Various nonlinear light emission mechanisms from different works, the expected spectra, $\phi(\omega)$ and their expected power law lineshape, $p(\omega)$. The referenced works from top to bottom are: [36], [35], [1], [37] and this presented work.

This similarity with [39] is quite surprising as pulsed and CW laser regimes are thought to produce entirely different effects. Comparison to our low fluence smooth film data is shown in Fig. 2.26. As seen in [17], the MDM structures used in this presented study are known to produce energetic carriers with significantly improved efficiency and is thought to originate from enhanced Landau damping in the system. A claim similar to [39] could be made by instead suggesting that this could be a similar effect involving the relative lifetimes of carriers and thermalization, just shifted: the excitation rate via the pulsed laser is on par with the enhanced Landau damping and resulting extended lifetime of thermalized hot-carriers of the confined systems. So again, $p > 2$ is going to be suppressed as the pulse width of the laser is on par with the hot-electron lifetime of several hundred fs when the characteristic wave vector is increased when going from 12 nm to 2 nm spacer layers. Additionally, the detuning of the plasmon modes from the laser line on the 2 nm shows the general lineshape staying the same, but with an overall increase of the power law as the overall efficiency dimishes with electric field reduction This may imply the hot-carrier distribution lifetime diminishes with it, resulting in more photons being allowed to be involved with the process.

One regime of the excited carrier lifetime which is commonly over looked is that of the athermal, or non-Fermi distribution. It is commonly assumed that the non-Fermi distributions will not have any meaningful

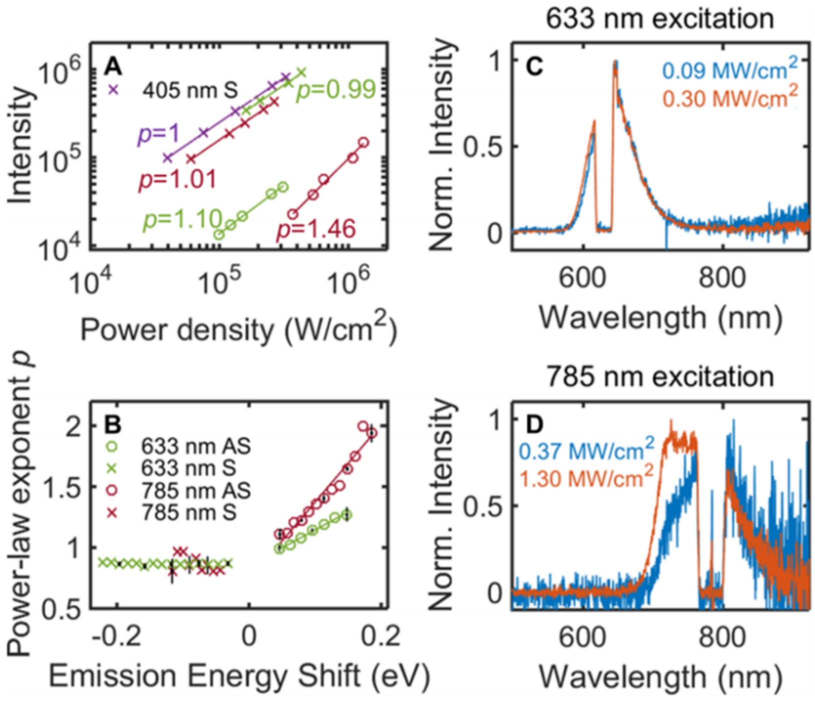

Figure 2.25: Single particle light emission from CW excitation [39]. (a) Emission intensity as a function of excitation power for different laser energies. (b) Raw emission spectra for 633 nm excitation. (c) Calculated power law lineshapes for excitation wavelengths of 633 and 785 nm. (d) Raw emission spectra for 785 nm excitation.

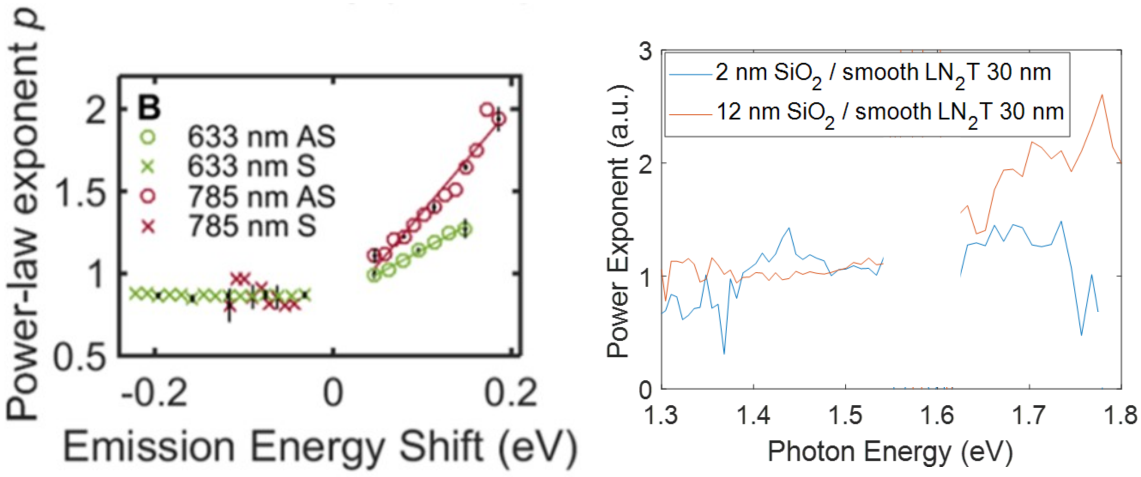

Figure 2.26: Comparison of low fluence power analysis on 2 and 12 nm SiO_2 to CW measurements by [39]

PL yield or a characteristic power law lineshape, and and-waving arguments are usually given. Two main reasons which are given for this are 1) the short lifetime of the distribution compared to the pulsewidth of the laser and therefore thermal relaxation will dominate the signal [36], and 2) because of the flat shape of the transient distribution, there ought not be any power dependent spectral features [35]. The short lifetime argument may have merit, but the 2nd point may be an overestimation. In fact, closer inspection of the non-Fermi distributions do show spectral signs, particularly at the ends of the laser induced $2\epsilon_p$ distribution range (Fig. 1.12). Since this is the range in which higher energy emission would correspond to, it wouldn't be surprising if the up-converted NPL region reflected this spectrally as well as in its power law lineshape. Additionally, much more careful treatment of non-Fermi distributions that give quantum treatment of the excitation process given the bandstructure and dimensions of the system predict far more complicated athermal carrier distributions then step-like distribution increase outlined in Section 1.6.2. To the best of our knowledge no numerical calculation of the power law lineshape for non-Fermi distributions has been made.

It was shown by [17] that the enhanced fields of the MDM structures, E_{gap}, dramatically increases the energetic carrier distribution number, δn. This field enhancement relation combined with the enhanced landau damping associated with the confined gap modes, a significant non-Fermi distribution could be expected to be established. Additionally, [17] estimated the relaxation time of these non-Fermi electrons via eq. 1.115 to be $\sim$ 45 fs. Although this is less than the pulsewidth of the excitation laser used in this study, it is still well within an order of magnitude, and perhaps some signature of these non-Fermi distributions may still be observed.

To estimate the the non-Fermi PL we use the same assumption of of lifting wavevector restrictions used by [36] like in eq. 2.2. Next, we simply input a non-Fermi distribution, f_{nf}, from eq. 1.114 in place of the hot-electron one. This gives

$$\phi(\omega) \propto \int_{-\infty}^{\infty} f_{\mathrm{nf},e}(\epsilon, T_0)\rho(\omega) f_{\mathrm{nf},h}(\epsilon - \hbar\omega, T_0) \mathrm{d}\epsilon, \tag{2.13}$$

where T_0 is chosen as the temperature because thermalization to a hot-electron distribution is assumed to not have occurred yet. By inspection, eq. 2.13 is difficult to analytically solve due to the complicated form of the athermal population change, $\Delta\rho_{\mathrm{nf}}(\omega)$ given by eq. 1.113. Eq. 2.13 is instead solved numerically,and the results can be seen in Fig. 2.24. It not only does it capture the curvature and distinct regions on either side of the laser line, but it also asymptotically approaches $p \approx 2$ for larger energies and $p \approx 1$ for smaller energies. This lineshape is in surprisingly good agreement with the observed power laws. More so for the thicker gap spacer samples, although thinner sizes may also be represented by this lineshape with better fitting parameters. The difficulty in fitting to experimentally obtained lineshapes is due to the lack of an analytically known solution to the integral of the anticipated spectrum given by eq. 2.13. Further theoretical and computational work are needed to address this.

2.8 Conclusions

In conclusion, power dependent NPL measurements from spatially confined MDM gap modes of different degrees were performed. Power law analysis was performed to yield characteristic lineshapes for the respective geometries. Additionally, comparison between smooth and rough underlayer films was conducted to ensure the integrity of the gap geometry and isolate any spectral differences. Indeed, the extra roughness is seen to introduce thermal emission from these structures. It is found that increased spatial confinement results in an overall decrease of the scaling lineshape. This is accompanied by the observation of two distinct linearly sloped regimes on either side of the laser line. Additionally, ultra smooth 2 nm gap modes excited with low fluences showed roughly linear emission efficiency consistent with our original ansantz. It is found that the best agreement of the observed data correspond to two possible mechanisms: non-Fermi intraband NPL and suppression of photon participation number due to enhanced Landau damping and shorter hot-carrier lifetimes. This is supported by the good agreement to the observed lineshapes and comparison the observations of previous work.

Chapter 3

Ultrathin Wetting Layer-Free Plasmonic Gold Films

Contributors:

Cheng Zhang[*,+], Manoj Manjare[†], Wenqi Zhu[*,+], Junyeob Song[*,‡], Sergei Urazhdin[†], Henri J. Lezec[*], Amit Agrawal[*,+] and Hayk Harutyunyan[†].

[†]Department of Physics, Emory University.

[*]Physical Measurement Laboratory, National Institute of Standards and Technology.

[+]Maryland Nanocenter, University of Maryland.

[‡]Department of Electrical and Computer Engineering, Virginia Tech.

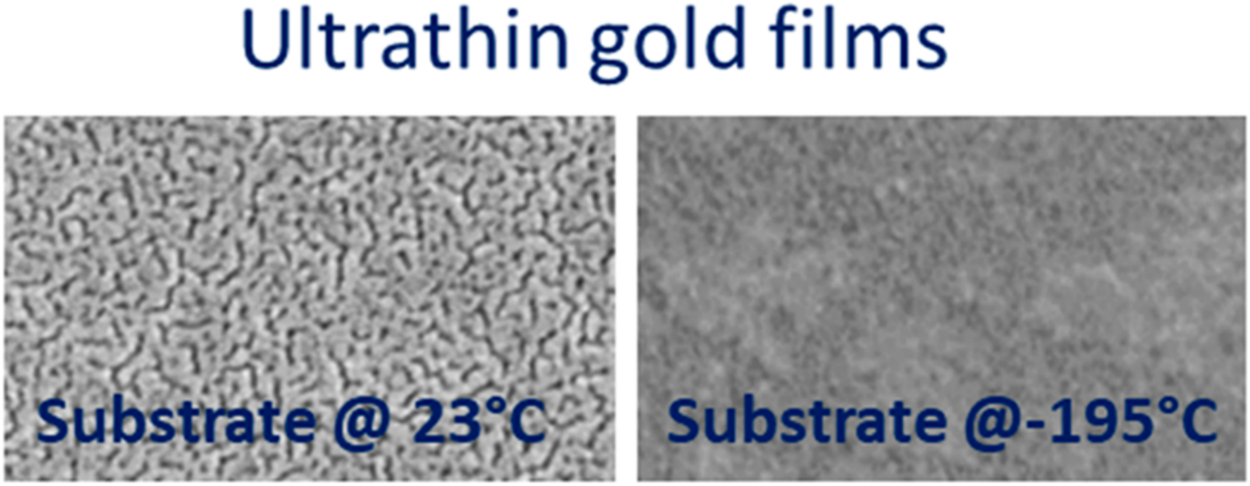

3.1 Chapter Overview

This chapter is based on results from the following publiciation [48]:

R. Lemasters, C. Zhang, M. Manjare, W. Zhu, J. Song, S. Urazhdin, H. Lezec, A. Agrawal and H. Harutyunyan, “Ultrathin Wetting Layer-Free Plasmonic Gold Films.” *ACS Photonics* **6**(11), 2600-2606, (2019).

Ultrathin and ultrasmooth gold films are attractive for plasmonic and metamaterial devices, thanks to their useful optical and optoelectronic properties. A direct application showing the merit of obtaining smooth films is demonstrated in chapter 2 where ultrasmooth films were necessary to eliminate light emission originating surface roughness. However, deposition of ultrathin continuous Au films of few nanometer thickness is challenging and generally requires wetting layers, resulting in increased optical losses and incompatibility with optoelectronic device requirements. It is demonstrated that wetting layer-free plasmonic gold films with thicknesses down to 3 nm are obtained by deposition on substrates cooled to cryogenic temperatures. The effect of substrate temperature on the properties of the deposited Au films is systematically studied, and it is shown that substrate cooling suppresses the Vomer-Webber growth mode of Au, promoting early-stage formation of continuous Au films with improved surface morphology and enhanced optoelectronic properties. These results pave the way for straightforward implementation of ultrathin Au-based optoelectronic and plasmonic devices, as well as metamaterials and metasurfaces.

3.2 Introduction

Nanoscale thin metal films are essential for the implementation of many nanophotonic and plasmonic devices [49–54]. The most common metals employed for applications in the visible and near-infrared optical range are silver (Ag) and gold (Au), due to their low optical loss. These metals also feature a large negative part of the permittivity in this frequency range, enabling the occurrence of surface plasmon polaritons (SPPs) at their interfaces [55]. Au is significantly more chemically stable than Ag, making it the material of choice for a variety of applications including plasmonic interconnects [56], modulators [57], resonators [58], sensors [59, 60], and metamaterials [61, 62].

In applications utilizing SPPs, optical loss is approximately inversely proportional to the thickness of the metallic layer, because of the scaling of the fraction of the total modal energy localized in the thin metal film. While performance improvement at small film thicknesses comes at a cost of reduced field confinement, the latter is not essential for many applications. For instance, the loss in a long-range SPP waveguide, embedded in free space, is reduced by a factor of 20 when the metal thickness is reduced from 50 nm to 5 nm, even though the field spillover into free space increases from 300 nm to 1.5 μm for the long-range antisymmetric mode with the free-space wavelength of 780 nm [56] (see Simulations in section 3.4, and Fig. 3.15). The reduction in loss with thinner metal films is true if only the ohmic losses in an ideal metal slab are considered. In practice, scattering from impurities, defects, or surface roughness become the dominant damping channel in the ultrathin metal film regime [63].

Thin metallic films are also advantageous for their use as transparent and flexible electrodes in optoelectronic devices such as photovoltaics, diodes and photodetectors [64–68]. Furthermore, they find applications in metal-dielectric heterostructures with hyperbolic or negative index response [69]. In such systems, optical loss diminishes with decreasing thickness of interstitial metal layers. Moreover, using the effective medium approximation is more valid for thin films as they better mimic a homogenous medium [70]. Finally, as the thickness of the metal layer reaches few monolayers, the resulting strong confinement can lead to the emergence of quantum effects, facilitating fundamentally different plasmonic device functionalities [71, 72].

Fabrication of continuous ultrathin (< 10 nm) Au films is challenging, because Au grows in the Vomer-Webber (three-dimensional) mode on common substrates such as fused-silica or silicon [73]. In the initial stage of film growth, the deposited Au atoms cluster together and form isolated islands. As the deposition continues, these isolated islands increase in size, and eventually merge to form a percolated conductive thin Au film. Such a three-dimensional (3D) growth mode leads to a minimum thickness value, commonly referred as the “percolation threshold”, below which the deposited Au layer is discontinuous and exhibits a rough surface morphology. The tendency of Au to form clusters has been utilized for the fabrication of low-cost and large-scale plasmonic structures [74, 75].

To reduce the percolation threshold of thin Au films and improve their surface morphology, a thin wetting layer of a different material is generally utilized before Au deposition. Among the common wetting layers are metals such as Ti and Cr [76], metal oxides such as copper oxide and Al-doped ZnO [63, 77], organic molecules such as mercapto-silane [78], transition metal dichalcogenides [79], and polymers [80]. While the wetting layers are effective in reducing the percolation threshold and improving the surface morphology of thin Au films, some wetting materials such as Cr and Ti also introduce additional optical losses and potentially make them incompatible with the devices’ functional requirements. To demonstrate this we have fabricated a 5 nm Au sample with a 1 nm Cr wetting layer and have compared the its permittivity with that of a 5 nm Au sample without one. As it can be seen from Fig. 3.1, the real part of the permittivity becomes less negative whereas the imaginary part increases indicating a decreased plasmonic response and increased loss, respectively.

Furthermore, a recent study shows that an ultrathin Au film with a mass-equivalent thickness as small

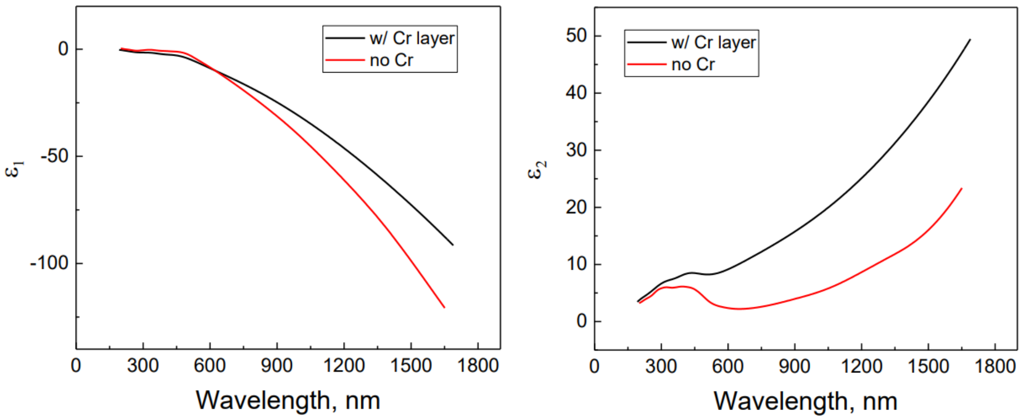

Figure 3.1: The real (left panel) and imaginary (right panel) parts of the permittivity for two samples: 5nm Au deposited at -195°C (red line) and 1nm Cr / 5nm Au deposited at -195°C (black line). Cr layer introduces additional loss as evident by the larger imaginary part of the permittivity. Data obtained at Physical Measurement Laboratory, National Institute of Standards and Technology.

as 5.4 nm can be prepared using a mercapto-silane wetting layer on fused silica substrate, but due to the interference from this layer, the film's optical transmittance is significantly lower than expected for an ideal Au film of the same mass-equivalent thickness [78]. Finally, wetting layer-free epitaxial growth of crystalline Ag layers has been recently demonstrated on Si substrates with remarkably small thickness and sheet resistivity [81]. However, the need for non-transparent crystalline substrate and complex fabrication method can limit the applications of this method.

The influence of the substrate temperature on the growth of thin metal films is well known [65, 82–85]. Numerous studies have been dedicated to uncover the mechanisms of temperature-dependent growth mechanisms and to find optimal conditions for material deposition. However, most of these studies either have used wetting layers or have metal films deposited on non-transparent substrates such as metals [86–90]. To the best of all the author's knowledge, ultrathin ($\leq$ 5nm) wetting layer-free plasmonic metals on optically transparent substrates, such as fused-silica, have not been reported prior to this work.

3.2.1 Thin Film Growth

The growth of metals on oxides fairly well understood and follows well-established multistep processes. A great introduction of this growth process is given by [65] and we follow that here, verbatim at points. The processes involved with metal-oxide film growth is shown in Fig. 3.2. The process is as follows: the nucleation and evolution of discrete nanoscopic clusters (I,II); complete coalescence between relatively small and regular clusters (III), followed by incomplete coalescence between large and irregular clusters (IV); the formation of a nanotrough network at the percolation threshold (V); and the transition from a nanotrough

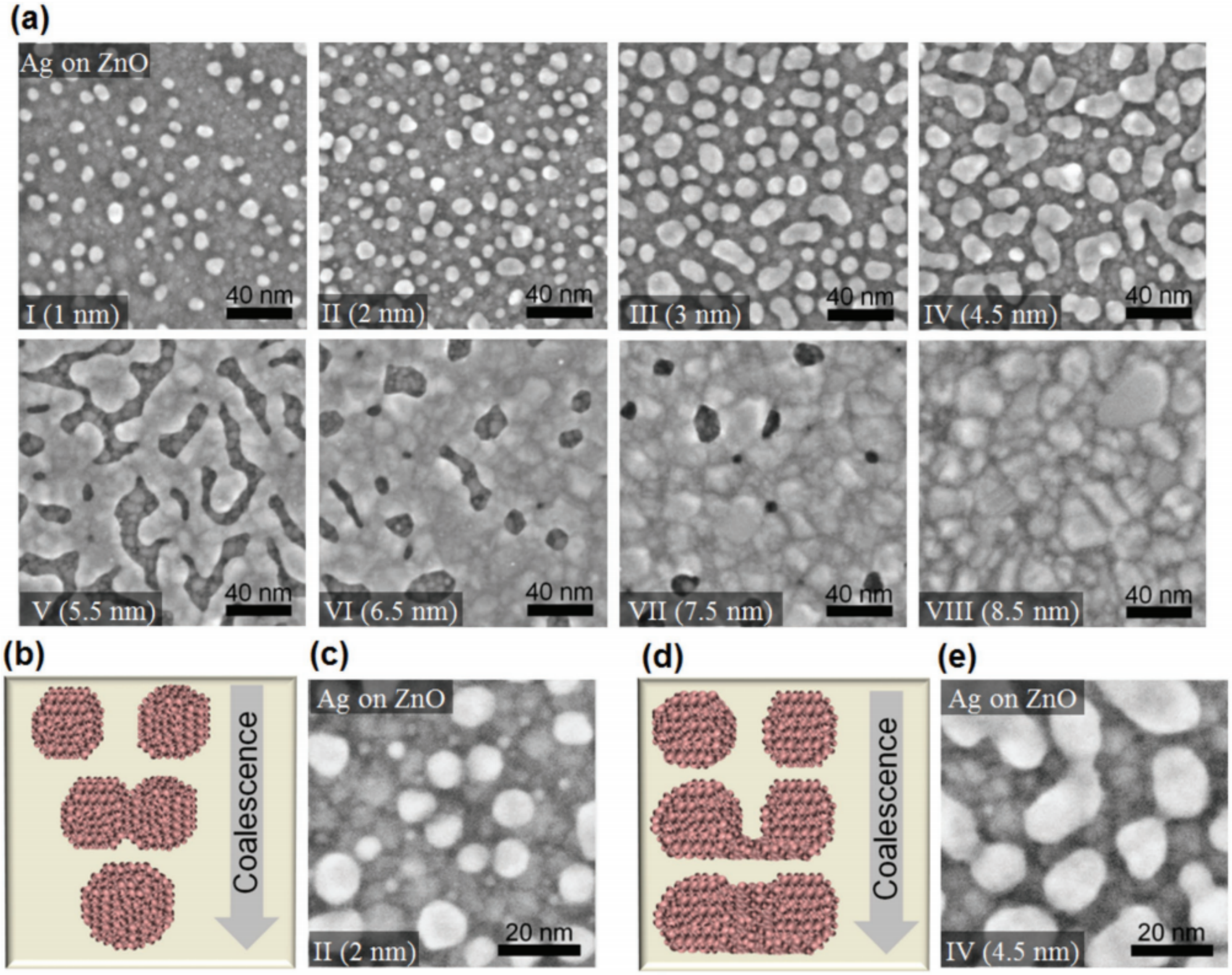

Figure 3.2: Cluster growth and coalescence process given by [65]: Typical early growth stages of coinage metals on an oxide. a) Highly magnified field emission scanning electron microscopy images highlighting the very early growth stages of Ag on ZnO films as a function of the metal thickness. b) Schematic and c) microscopy image of the incomplete coalescence mode driven by liquid-like clustering, and d) schematic and e) microscopy image of the complete coalescence mode driven by solid-like clustering

network to a continuous film (VI–VIII) with increasing metal thickness. Because the nuclei and cluster density seem to continuously decrease with metal growth, their coalescence should be a primary concern for controlling the morphological evolution of metal films, instead of their initial density and distribution. Cluster coalescence resulting from active atomic and cluster migration is readily expected for coinage metals on oxides, considering the weak character of metal–oxide adhesion, in contrast to the strong character of metal–metal cohesion [65].

The thermodynamic condition which determines the type of film growth in the early stages before percolation can be determined by minimizing the free energy of the system. Coalescence is driven by lowering the surface free energy of clusters by decreasing the total surface area of the metal clusters. The interfacial

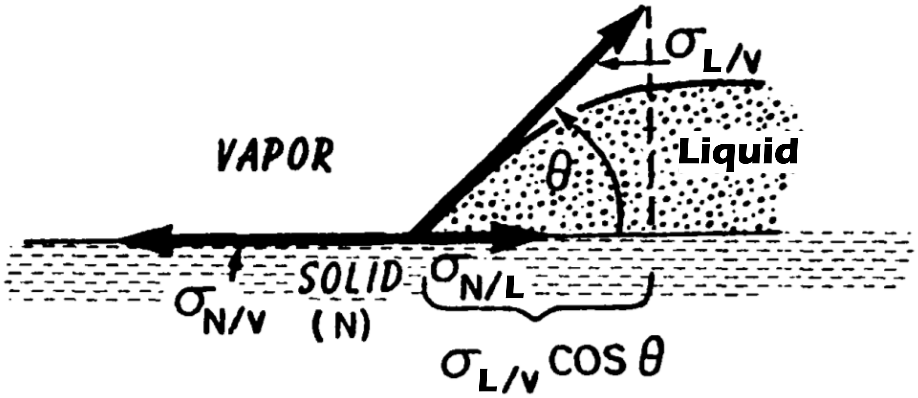

Figure 3.3: Diagram of Young's equation at the interface of a solid, liquid and vapor from [91]. The surface tension and energies associated with drop formation determine the wetting of the drop and the contact angle to the wetted surface.

configuration of this is seen in Fig. 3.3 in a diagram from [91]. At this interface between the metal and oxide, the surface tensions defining the drop is

$$\sigma_{\mathrm{N/L}} + \sigma_{\mathrm{L/V}} \cos\theta = \sigma_{\mathrm{N/V}}, \tag{3.1}$$

where θ is the contact angle, $\sigma_{\mathrm{L/V}}$ is the surface tension between the liquid and vapor and $\sigma_{\mathrm{N/L}}$ & $\sigma_{\mathrm{N/V}}$ are the surface tensions between the liquid & vapor to the normal component of the surface, respectively. The free energy argument for this system follows from this and is given as

$$\gamma_m + \gamma_i \cos\theta < \gamma_s, \tag{3.2}$$

where γ_m is the surface free energy of the metal, γ_i is the interfacial free energy of the metal-substrate, and γ_s is the surface free energy of the substrate [65]. Wetting of the liquid on the surface only occurs when this inequality is met. Further, the surface free energy is always reduced with cluster coalescence. This is because a large cluster, formed as a result of the coalescence between two smaller neighboring clusters, has a smaller surface area compared with the total surface area of the two original clusters. This lowers the free energy of the system and therefore is thermodynamically favorable [65].

The early stages of cluster growth are dominated by liquid-like clustering that exhibits the complete coalescence of two discrete clusters into a new cluster via cluster migration and reconstruction (Fig. 3.2b). The initial and resulting clusters both exhibit a polygonal, truncated octahedron shape (Fig. 3.2c). Such coalescence behavior hinders improvement in the wetting of metals on oxides because the coalescence mode causes a significant delay in filling the gaps between clusters. As coalescence progresses, the driving force for cluster coalescence is weakened by the increase in the cluster size [65].

The later growth stages of clusters with larger sizes are dominated by solid-like clustering that exhibits incomplete cluster coalescence via the formation of bridges connecting irregularly shaped clusters (Fig. 3.2d). In these stages, clusters are dimensionally too large and energetically too stable to migrate freely on oxide surfaces and fuse completely into a monolithic unit. Instead, coalescence proceeds with widening and thickening of the bridges (Fig. 3.2e). Bridge-induced cluster coalescence leads to a continuous increase in the coverage of metals on oxides, with gradual filling of the gaps between clusters. The fast development of a completely continuous film is a result of this type of coalescence. Therefore, the fabrication of metal films with a superior morphology on oxides requires an early transition from the liquid-like complete-coalescence mode to the solid-like incomplete-coalescence mode, which can lead to a reduction in the metal thickness for the percolation threshold and continuous film [65].

This liquid-like coalescence is determined by the ability of the metal clusters to diffuse on the oxide substrate. This diffusion coefficient, D, for a particle with radius, R, is dependent on temperature as [92]

$$D(R) \propto \frac{1}{R^4} \exp\left[\frac{\mu(R) - \mu(\infty)}{k_B T}\right], \tag{3.3}$$

where μ is the chemical potential which is a function of the particle radius. It can be seen clearly that the temperature of the metal clusters has significant weight on the magnitude of the diffusion constant. Here, we demonstrate that wetting layer-free, ultrathin and plasmonic Au films can be fabricated by deposition directly on fused-silica substrates cooled to cryogenic temperatures. We analyze the effect of substrate temperature on the properties of the deposited ultrathin Au films and find that substrate cooling helps to reduce the mobility of Au atoms on the substrate and thus promotes the formation of ultrathin Au films with improved surface morphology and enhanced optoelectronic characteristics, including lower optical loss and sheet resistance, and higher optical transmittance. We utilize the demonstrated substrate cooling approach to fabricate record-thin, 3 nm thick Au films with good plasmonic properties, i.e., large negative real part and small imaginary part of the permittivity. The ultrathin thickness is further verified by the parameter uniqueness test using spectroscopic ellipsometry. Our work establishes a new practical approach for the fabrication of high-quality wetting layer-free ultrathin Au films, paving the way for their applications in optoelectronic and plasmonic devices, as well as metamaterials and metasurfaces.

3.3 Results and Discussion

3.3.1 Deposition of Ultrathin Au Films at Different Temperatures

Ultrathin Au films are deposited on 500 μm thick fused-silica substrates, with substrate temperatures ranging from room temperature (23 °C) down to liquid nitrogen (LN) temperature (-195 °C), using magnetron sputtering in high-vacuum chamber with a base pressure of less than 2.7×10^{-5} Pa. Fused-silica substrates were cleaned by sonication in deionized water and detergent, acetone, and isopropyl alcohol sequentially for 20 minutes at room temperature. The substrates were then dried with nitrogen and then transferred into the sputtering chamber. The temperature of the substrate are controlled by attaching the sample holder to a cold finger (Fig. 3.4). To facilitate a good thermal contact between the substrate and cold finger, a 1-mm-thick indium layer is inserted between the sample holder and the edge areas of the substrate. This ensures that no indium residue is left on the central part of the substrate, which would have compromised the subsequent optical characterization of the film. To cool the substrate, LN is siphoned into the cold finger reservoir at a rate of $\approx$ 400 standard cubic centimeters per minute (sccm). For the lowest temperature used in these experiments, the flow is turned off once the minimum temperature of -195 °C is achieved (as monitored by a thermocouple gauge attached to the sample holder). To consistently achieve intermediate temperatures during deposition, a more involved method was developed. As the LN flow begins to flow and the temperature begins to drop, the LN flow is turned off well before the target temperature is reached. The substrate temperature continued to drop due to the residual LN in the reservoir. Once the temperature stabilizes, this process is repeated with smaller spurts of LN that are allowed to evaporate until the substrate temperature is stabilized just below the target temperature. The natural warming at the calibrated rate of $\approx$ 1 °C/min then results in the increase of the substrate temperature towards the desired value. This process of lowering the temperature just below the target value and allowing it to warm back up to this value is repeated several times to ensure equilibrium between the cold finger and the substrate at the target temperature value.

After the substrate reaches the target temperature, the Au deposition is performed in 0.4 Pa of ultrapure Argon (Ar), at a rate of 0.5 nm/s determined by a calibrated quartz crystal monitor. The deposited thickness is controlled by the opening time of the mechanical shutter. After the deposition, the sample is kept inside the chamber at the base pressure, until it warmed up to room temperature, to avoid any water vapor condensation or ice crystal formation on the deposited film when exposed to atmosphere. Due to the relatively small difference in the coefficient of thermal expansion of Au and silica substrate and their weak dependence on temperature we do not expect large compressive strain in our samples. Such strain would lead to the “warping” of the film over microscopic regions, which have not been observed even in the samples fabricated at the lowest temperature of -195 °C.

3.3.2 Optoelectronic Characteristics and Surface Morphologies of 5 nm Thick Au

The effect of substrate cooling on the optoelectronic properties and surface morphology of the Au films was studied for 5 nm thick films, deposited on fused-silica substrates at temperatures ranging from the room temperature (23 °C) down to the liquid nitrogen temperature (-195 °C). Seven different temperature values are chosen: 23 °C, 0 °C, -30 °C, -50 °C, -80 °C, -120 °C, and -195 °C. The corresponding Au films are denoted as $\mathrm{Au}^{5\mathrm{nm}}_{23°\mathrm{C}}$, $\mathrm{Au}^{5\mathrm{nm}}_{0°\mathrm{C}}$, $\mathrm{Au}^{5\mathrm{nm}}_{-30°\mathrm{C}}$, $\mathrm{Au}^{5\mathrm{nm}}_{-50°\mathrm{C}}$, $\mathrm{Au}^{5\mathrm{nm}}_{-80°\mathrm{C}}$, $\mathrm{Au}^{5\mathrm{nm}}_{-120°\mathrm{C}}$ and $\mathrm{Au}^{5\mathrm{nm}}_{-195°\mathrm{C}}$, respectively.

Spectroscopic ellipsometry is utilized to determine the relative electric permittivity of ultrathin Au samples as a function of free-space wavelength, $\epsilon_r(\lambda_0) = \epsilon_1(\lambda_0) + i\epsilon_2(\lambda_0)$, over the wavelength range from 200 nm to 1650 nm. The ellipsometry characterization of deposited Au films is performed using M-2000 ellipsometer (J. A. Woollam Co. Inc.), and data analysis is performed using the CompleteEASE software (J. A. Woollam Co. Inc.). The frequency-dependent permittivity value of each sample is modeled by a combination of Gaussian, Tauc-Lorentz and Drude oscillators. To precisely characterize the thin semi-transparent

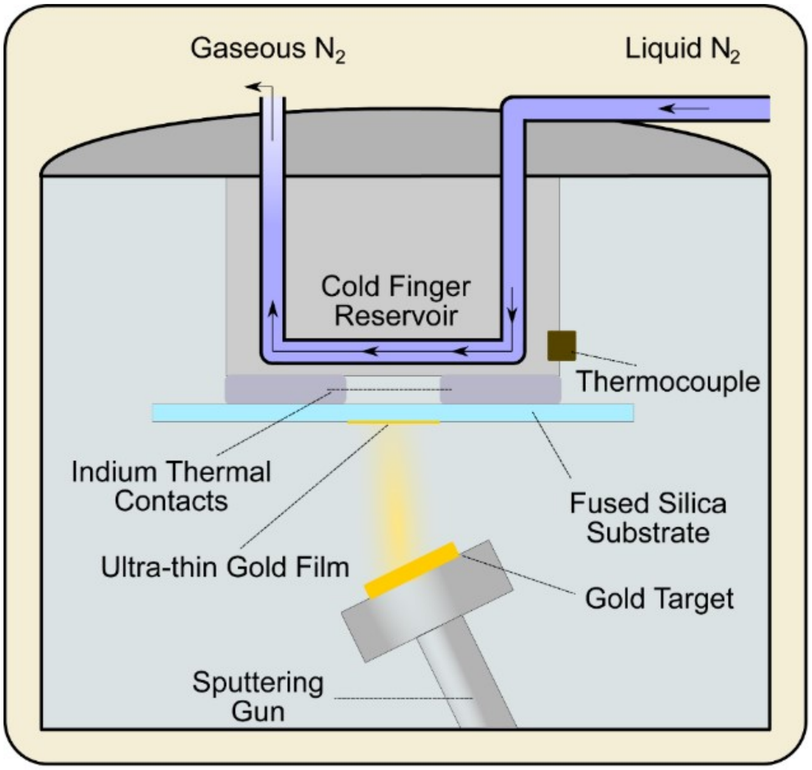

Figure 3.4: Schematic representation of the deposition chamber and the process for the fabrication of ultra-thin Au films.

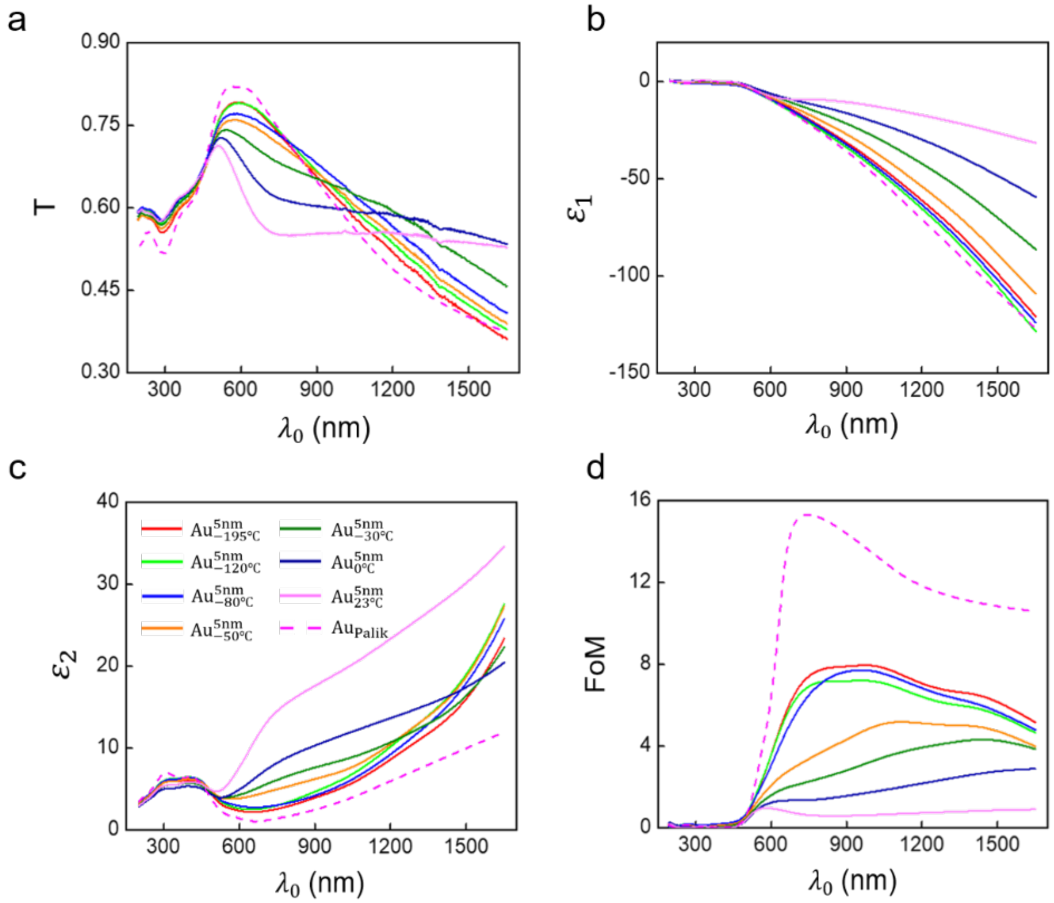

Figure 3.5: (a) Measured transmittance, T, versus free-space wavelength λ_0 for samples $\mathrm{Au}^{5\mathrm{nm}}_{-195°\mathrm{C}}$, $\mathrm{Au}^{5\mathrm{nm}}_{-120°\mathrm{C}}$, $\mathrm{Au}^{5\mathrm{nm}}_{-80°\mathrm{C}}$, $\mathrm{Au}^{5\mathrm{nm}}_{-50°\mathrm{C}}$, $\mathrm{Au}^{5\mathrm{nm}}_{-30°\mathrm{C}}$, $\mathrm{Au}^{5\mathrm{nm}}_{0°\mathrm{C}}$, and $\mathrm{Au}^{5\mathrm{nm}}_{23°\mathrm{C}}$. The reference ($T = 1$) for all measurements is transmittance through air. The calculated transmittance $\mathrm{T}(\lambda_0)$ obtained by transfer matrix method for a 5.66 nm thick Au film on a 500 μm thick fused silica substrate is plotted as well (dashed line). The chosen thickness of 5.66 nm is the same as the measured thickness of sample $\mathrm{Au}^{5\mathrm{nm}}_{-195°\mathrm{C}}$ using spectroscopic ellipsometry. The index of Au employed in the calculation is based on Ref. [93]. (b-c) Measured real (b) and imaginary (c) parts of the relative electric permittivity, ϵ_1 and ϵ_2, of samples deposited at -195°C to 23°C. The permittivity of Au film from [93] is plotted for reference (dashed line). (d) FoM$= |\epsilon_1(\lambda_0)|/(\epsilon_2(\lambda_0))$ for samples deposited at -195°C to 23°C. The FoM calculated based on the permittivity of Au from [93] is plotted for reference (dashed line). Legend of Fig. 3.5c also applies to Figs. 3.5a, 3.5b and 3.5d. Data obtained at Physical Measurement Laboratory, National Institute of Standards and Technology.

absorbing films, the "spectroscopic ellipsometry + transmission (SE + T)" scheme was employed [94, 95], where (i) the complex electric field reflection coefficients for s and p polarizations at three different angles of incidence (55°, 65°, and 75°), and (ii) optical transmittance at normal incidence, are utilized to extract the complex permittivity and the thickness of the Au layer. In addition, surface morphology of the Au samples was characterized by scanning electron microscopy, and the sheet resistance, R_s, was measured by the four-point probe method. The SEM characterization tool used in this study was JEOL 7800F Field Emission Scanning Electron Microscope. The 4-point resistance measurements were done on Four Dimensions 280DI sheet resistance mapping system.

The best-fit thickness values along with mean-squared-error (MSE) for different samples determined by spectroscopic ellipsometry are given in Table 3.1. These values closely match the targeted deposition thickness of 5 nm. The small deviations from this value are likely caused by the fluctuations of the sputtering rate during the deposition of the samples. Similar thickness values are obtained using AFM measurements as shown in Fig. 3.6. The AFM imaging was performed on Bruker Dimension FastScan Atomic Force Microscope.

The measured transmittance spectra (Fig. 3.5a) for the two highest temperature samples $\mathrm{Au}^{5\mathrm{nm}}_{0^\circ\mathrm{C}}$ and $\mathrm{Au}^{5\mathrm{nm}}_{23^\circ\mathrm{C}}$ exhibit a broad dip in the wavelength range of $\approx$ 600 nm to $\approx$ 1000 nm. This resonant dip can be attributed to the localized surface plasmon absorption of the Au island-like grains in non-percolated films (Figs. 3.7a and 3.7b). The detrimental effect of such grains on the film's optical properties is also evidenced in the measured permittivity curves of the two films, shown in Figs. 3.5b and 3.5c. Here, the real part of the permittivity exhibits less negative values compared to the films deposited at lower temperatures, indicating a degraded metallic property. Similarly, the imaginary part shows the highest values among all the samples over the large portion of the studied spectral range, suggesting an increased optical absorption.

For the samples deposited at the reduced substrate temperature, the absorption dip corresponding to the localized surface plasmon resonance gradually diminishes, and transmittance of the film improves, in particular for the wavelength range from 500 nm to 800 nm (Fig. 3.5a). It is worth noting that in these samples, the relatively lower transmittance at longer wavelengths is not due to the increased optical absorption of the film, but rather due to the increased reflection, hinting at improved metallic property of the deposited Au film. Monitoring the surface morphology using SEM imaging also further confirms this

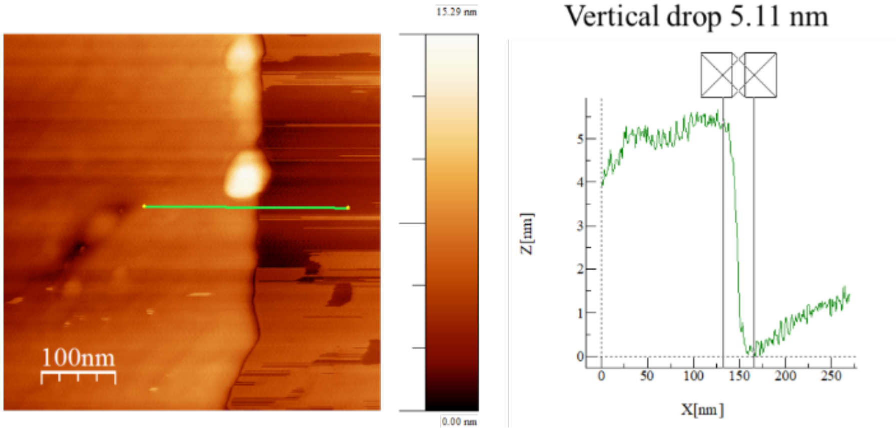

Figure 3.6: Film thickness determined by AFM measurements. AFM scan (left panel) and cross section (right panel). The thickness value of 5.11 nm agrees well with the ellipsometry measurements. Data obtained at Maryland Nanocenter, University of Maryland.

Table 3.1: Film thicknesses determined by ellipsometry and sheet resistance of the samples. Data obtained at Physical Measurement Laboratory, National Institute of Standards and Technology.

	$\mathrm{Au}^{5\mathrm{nm}}_{23°\mathrm{C}}$	$\mathrm{Au}^{5\mathrm{nm}}_{0°\mathrm{C}}$	$\mathrm{Au}^{5\mathrm{nm}}_{-30°\mathrm{C}}$	$\mathrm{Au}^{5\mathrm{nm}}_{-50°\mathrm{C}}$	$\mathrm{Au}^{5\mathrm{nm}}_{-80°\mathrm{C}}$	$\mathrm{Au}^{5\mathrm{nm}}_{-120°\mathrm{C}}$	$\mathrm{Au}^{5\mathrm{nm}}_{-195°\mathrm{C}}$
best-fit thickness, nm	≈ 5.66	≈ 5.06	≈ 5.09	≈ 5.47	≈ 5.85	≈ 6.32	≈ 5.64
regression-analysis-fitting MSE	2.742	2.789	5.698	4.706	3.653	6.866	2.765
averaged sheet resistance, $\Omega/\square$	15.76	19.77	22.80	23.77	31.37	42.33	70.37

picture. Reducing the substrate temperature from $\mathrm{Au}^{5\mathrm{nm}}_{-30°\mathrm{C}}$ to $\mathrm{Au}^{5\mathrm{nm}}_{-120°\mathrm{C}}$, results in gradually reduced void spots on the film, finally leading to a void-free film for $\mathrm{Au}^{5\mathrm{nm}}_{-195°\mathrm{C}}$ sample (Figs. 3.7c to 3.7g). In contrast to the high substrate temperature samples, the measured transmittance curve for $\mathrm{Au}^{5\mathrm{nm}}_{-195°\mathrm{C}}$ does not exhibit localized surface plasmon resonance. Its peak amplitude and spectral shape are in a good agreement with the theoretical transmittance spectrum of a continuous, 5.66 nm thick Au film on fused-silica substrate, calculated using transfer matrix method (Fig. 3.5a). The thickness of 5.66 nm used in the theoretical transmittance calculations matches the thickness of sample $\mathrm{Au}^{5\mathrm{nm}}_{-195°\mathrm{C}}$ experimentally determined from the spectroscopic ellipsometry. Here, the complex permittivity values for Au used in the calculations (plotted as dashed lines in Figs. 3.5b and 3.5c), were taken from a common reference for the permittivity of the bulk Au material [93]. Gradually decreasing the substrate temperature leads to a more negative real part of the permittivity ϵ_1 (improved metallic properties of the film) and a gradual decrease of the imaginary part ϵ_2, i.e. reduced losses. The figure of merit

$$\mathrm{FoM} = |\epsilon_1(\lambda_0)|/(\epsilon_2(\lambda_0)), \tag{3.4}$$

which characterizes the quality of the plasmonic film [96], increases with decreasing deposition temperature over the same wavelength range (Fig. 3.5d). It is useful to notice the resemblence of the FoM to the Q-factor (eq. 1.51) and the analogous use of comparing response strength and loss as mentioned above. Finally, the improved optoelectronic properties of ultrathin Au films are further evidenced by the measured sheet resistance of the film (Fig. 3.7h), which monotonically decreases as the deposition temperature decreases. The averaged sheet resistance values of the samples are given in Table 3.1. Aging of the samples are observed over 6 months period where the sheet resistance deteriorates by ~30% for samples kept in a nitrogen-purged sample box. The annealing at 120°C and 150°C temperatures does not have any significant effects on the sheet resistance of the samples. This is shown in Fig. 3.8.

Interestingly, the absence of wetting layer in these samples does not significantly affect their adhesion to the substrate. To test the adhesion of the Au films, Kapton tape is applied to each sample, pressed to have a good contact between the tape and the Au film, and then peeled off the tape. The results of these simple assessments after 3 peeling attempts are shown in the photographs shown in Fig. 3.9. No noticeable changes are visible on the films that are fabricated with and without 1 nm Cr adhesion layer. The

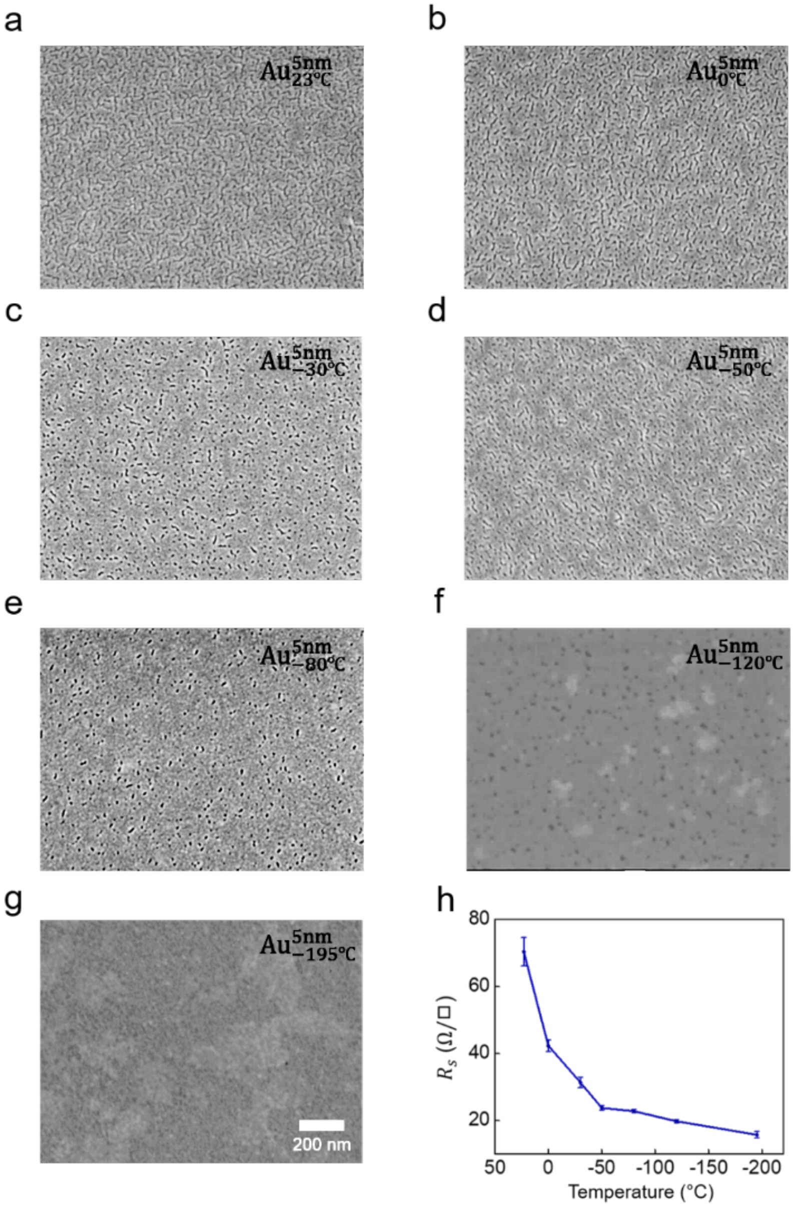

Figure 3.7: (a-g) Scanning electron micrographs (SEMs) of details of sample $\mathrm{Au}^{5\mathrm{nm}}_{23^\circ\mathrm{C}}$ (a), $\mathrm{Au}^{5\mathrm{nm}}_{0^\circ\mathrm{C}}$ (b), $\mathrm{Au}^{5\mathrm{nm}}_{-30^\circ\mathrm{C}}$ (c), $\mathrm{Au}^{5\mathrm{nm}}_{-50^\circ\mathrm{C}}$ (d), $\mathrm{Au}^{5\mathrm{nm}}_{-80^\circ\mathrm{C}}$ (e), $\mathrm{Au}^{5\mathrm{nm}}_{-120^\circ\mathrm{C}}$ (f), and $\mathrm{Au}^{5\mathrm{nm}}_{-195^\circ\mathrm{C}}$ (g). Scale bar of Fig. 3.7g applies to Figs. 3.7a to 3.7f. (h) Measured sheet resistance of the ultrathin Au film as a function of deposition temperature. Error bars show one standard deviation of the measured data obtained from several consecutive measurements. Data obtained at Physical Measurement Laboratory, National Institute of Standards and Technology.

optical (permittivity) and electrical (sheet resistance) methods are chosen to characterize the samples since these measurements provide the most technologically relevant information about the averaged optoelectronic properties of our samples. However, to quantitatively study the morphology of the samples atomic force microscopy (AFM) imaging are performed. The roughness analysis and topographic patterns provided by these measurements are in a good agreement with other characterization methods used in this study. These measurements are shown in Fig. 3.10. Namely, root mean square (RMS) roughness of the films monotonically increases with the deposition temperature, with $\mathrm{Au}^{5\mathrm{nm}}_{-195^\circ\mathrm{C}}$ exhibiting the smoothest surface.

Based on the results presented above, it can be concluded that at the early stages of metal deposition, isolated nanoscopic metal clusters begin to nucleate and eventually begin to coalesce and increase in size [65]. This is followed by the percolation, and eventually the formation of a continuous film. The coalescence process of the initial clusters is driven by the minimization of the surface free energy of the system [92]. In this process, smaller clusters with larger relative surface areas diffuse on the surface, and coalesce in a “liquid-like” manner into bigger clusters with smaller relative surface areas, lowering the total surface free energy [97]. This makes three-dimensional metal growth thermodynamically more likely than two-dimensional surface growth on the metal-oxide interface given that the metal-metal cohesion is much stronger than metal-oxide adhesion. Surface quality features are therefore determined by how large the coalescing clusters can get before wetting the surface at the percolation threshold followed by continuous film formation [82]. If the percolation threshold can be reached sooner, then smaller film features should follow. Cooling down the substrate decreases the diffusion rate of the metal atoms, thus, enabling the formation of stable metal nanoclusters of smaller sizes. This suppresses the 3D clustering and favors the formation of percolated

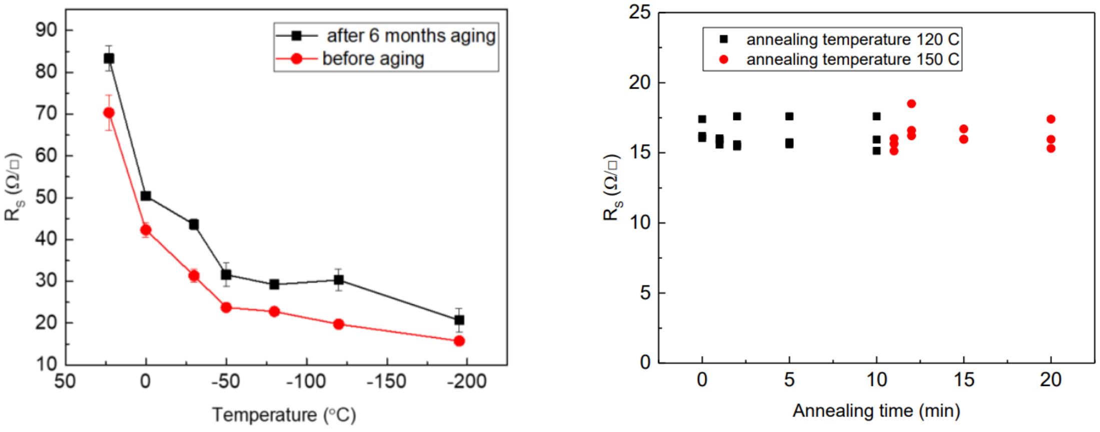

Figure 3.8: The effects of aging (left panel) and annealing (right panel) of the samples. The sheet resistance deteriorates by ∼ 30% over 6 months storage in a nitrogen-purged sample box. The annealing at 120°C and 150°C temperatures does not have any significant effects on the sheet resistance of the samples. Data obtained at Physical Measurement Laboratory, National Institute of Standards and Technology.

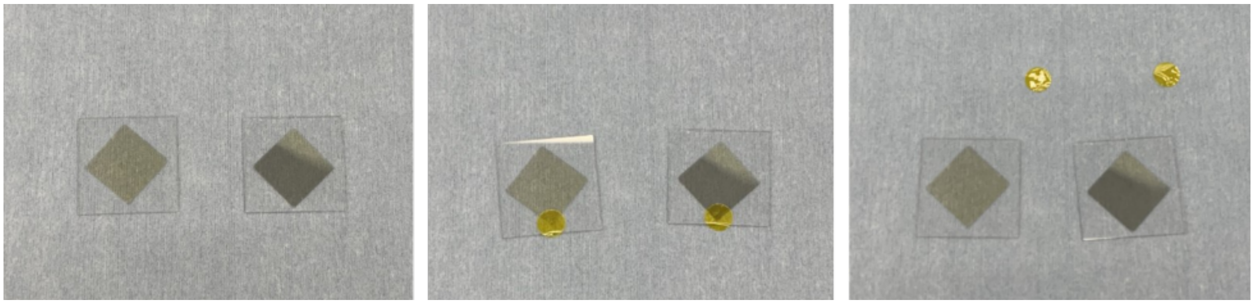

Figure 3.9: Photographs of two 5 nm Au samples with and without 1nm Cr adhesion layer. The left panel shows the films before the application of the adhesive tape, the middle panel shows the application of the tape, and the right panel shows the films after the adhesive tape have been peeled off. The procedure has been applied 3 times. Data obtained at Physical Measurement Laboratory, National Institute of Standards and Technology.

ultrathin metal films. Similarly, faster deposition rates facilitate the formation of continuous films which is evidenced by slight improvement of the optical losses as shown in Fig. 3.11.

To determine the crystalline sizes in the ultrathin films X-ray diffraction (XRD) measurements are also performed. Grazing incidence XRD measurement were performed on Rigaku SmartLab X-ray diffraction system (Copper K-α line at 1.5406 Å). The angle of incidence was 0.7° scan speed was set as 1°/min, and the scan step was 0.05°. The crystalline sizes are estimated from the widths of the X-ray peaks using Scherrer equation. Fig. 3.12 shows the results of our XRD measurements on three 5nm samples fabricated at -195°C, -50°C and 23°C. Given the ultrathin nature of the films the spectra have considerable background. However several peaks corresponding to various crystalline directions are visible. The position of the peaks perfectly correspond to gold diffraction peaks (such as (111), (200), (220) and so on). Based on the width of these 2θ

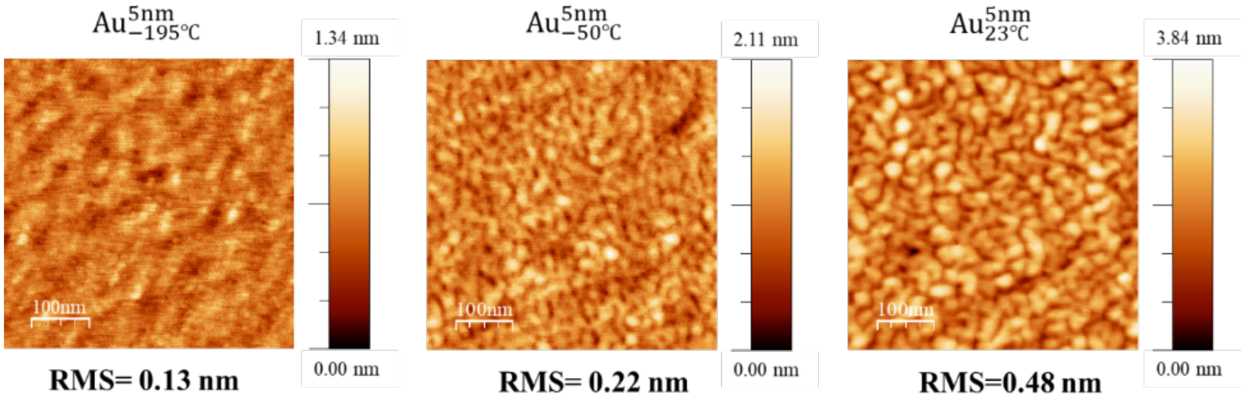

Figure 3.10: AFM images of three 5 nm samples deposited at different temperatures of -195° C -50° C, 23° C. The RMS roughness of the topography monotonically increases with the deposition temperature confirming that the cryogenic deposition of the 5 nm Au yields continuous films. Data obtained at Maryland Nanocenter, University of Maryland.

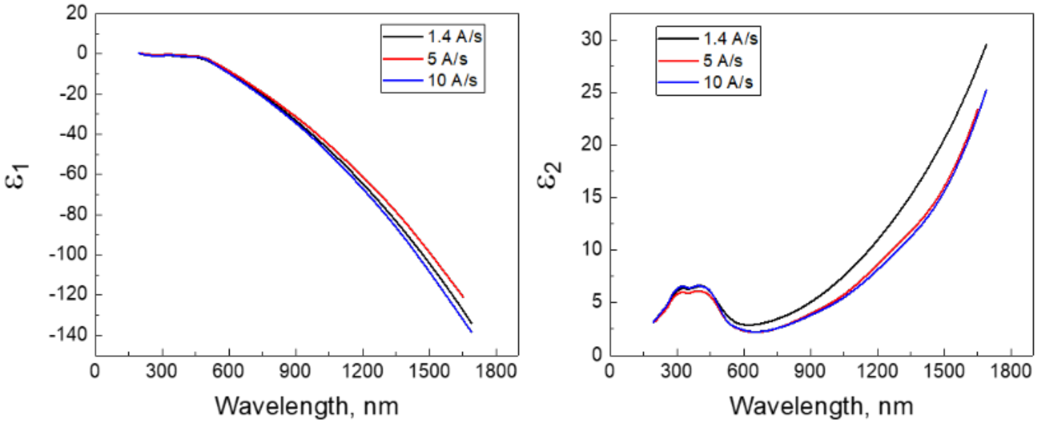

Figure 3.11: The optical properties of $\mathrm{Au}^{5\mathrm{nm}}_{-195^\circ\mathrm{C}}$ samples deposited at three different rates: 1.4 Å/s (black line), 5 Å/s (red line), 10 Å/s (blue line). Lower rates of 1.4 Å/s result in slightly larger optical loss. Data obtained at Physical Measurement Laboratory, National Institute of Standards and Technology.

resonances, one can estimate the crystallite size in the films using Scherrer equation,

$$L = \frac{k\lambda}{B(2\theta)\cos\theta}, \tag{3.5}$$

where L is the crystallite size, $k = 0.89$ is a constant, $\lambda = 1.54$ Å is the wavelength of the X-rays, B is the width of the peak, and θ is the incidence angle. Using the widths of (111) and (220) peaks we have estimated the crystalline size L for all three samples. The results of are shown in Table 3.3.2. Based on this analysis, it appears that lower temperature of the substrate results in smaller crystallites, in consistence with the diffusion suppression growth picture. However, it is noted that the crystalline sizes determined by this method are very close to the 5 nm thickness of the film. Thus, it is plausible that the widths of the

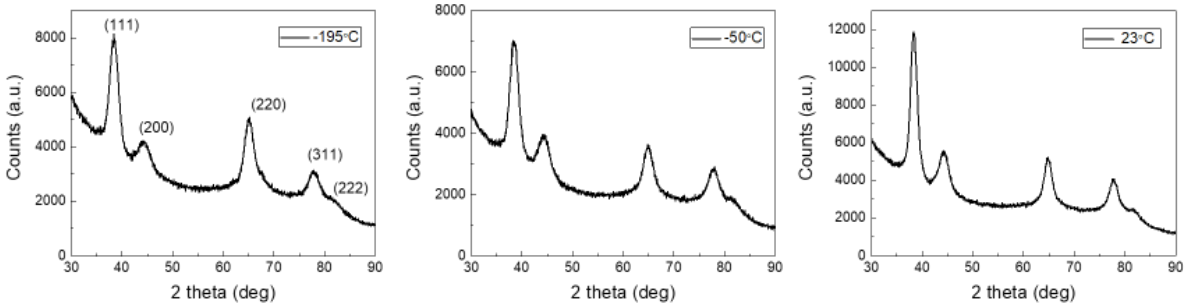

Figure 3.12: XRD measurements on $\mathrm{Au}^{5\mathrm{nm}}_{-195^\circ\mathrm{C}}$ (left panel), $\mathrm{Au}^{5\mathrm{nm}}_{-50^\circ\mathrm{C}}$ (middle panel) and $\mathrm{Au}^{5\mathrm{nm}}_{23^\circ\mathrm{C}}$ (right panel) samples. Data obtained at Physical Measurement Laboratory, National Institute of Standards and Technology.

Table 3.2: Estimated the crystalline size L for $\mathrm{Au}^{5\mathrm{nm}}_{23^\circ\mathrm{C}}$, $\mathrm{Au}^{5\mathrm{nm}}_{-50^\circ\mathrm{C}}$, and $\mathrm{Au}^{5\mathrm{nm}}_{-195^\circ\mathrm{C}}$ using the (111) and (220) XRD peaks. Data obtained at Physical Measurement Laboratory, National Institute of Standards and Technology.

	θ (deg)	$B(2\theta)$ (deg)	L (nm)
$\mathrm{Au}^{5\mathrm{nm}}_{23^\circ\mathrm{C}}$ (111)	38.28	1.59	5.25
$\mathrm{Au}^{5\mathrm{nm}}_{23^\circ\mathrm{C}}$ (220)	64.73	1.89	4.92
$\mathrm{Au}^{5\mathrm{nm}}_{-50^\circ\mathrm{C}}$ (111)	38.35	2.1	3.96
$\mathrm{Au}^{5\mathrm{nm}}_{-50^\circ\mathrm{C}}$ (220)	64.79	2.39	3.96
$\mathrm{Au}^{5\mathrm{nm}}_{-195^\circ\mathrm{C}}$ (111)	38.34	2.18	3.82
$\mathrm{Au}^{5\mathrm{nm}}_{-195^\circ\mathrm{C}}$ (220)	65.14	2.49	3.74

peaks are mainly determined by the film thickness.

3.3.3 Plasmonic 3-nm-thick Au Films

Leveraging the beneficial effect of substrate cooling on the formation of ultrathin Au films, as revealed by the study described above, we further explore the possibility of realizing even thinner plasmonic Au films. A nominally 3 nm thick film, $\mathrm{Au}^{3\mathrm{nm}}_{-195^\circ\mathrm{C}}$, is deposited on fused silica substrate at the liquid nitrogen temperature (deposition rate: 0.5 nm/s), and characterized by spectroscopic ellipsometry, scanning electron microscopy and four-point probe method.

Compared to the nominally 5 nm thick Au film prepared at the same temperature ($\mathrm{Au}^{5\mathrm{nm}}_{-195^\circ\mathrm{C}}$), sample $\mathrm{Au}^{3\mathrm{nm}}_{-195^\circ\mathrm{C}}$ exhibits a higher transmittance over the spectral range of the measurement (200 nm to 1650 nm), thanks to its reduced film thickness (Fig. 3.13a). Meanwhile, it also exhibits degraded relative electric permittivity compared to $\mathrm{Au}^{5\mathrm{nm}}_{-195^\circ\mathrm{C}}$. This is manifested by a smaller negative real part of measured permittivity, ϵ_1, and a larger positive imaginary part of measured permittivity, ϵ_2 (Fig. 3.13b). Nevertheless, the measured ϵ_1 still monotonically decreases beyond 450 nm, confirming the plasmonic behavior of the film. The degraded optical properties could be attributed to the defects remaining from the early stage of the continuous film formation, as evidenced by the void spots in the SEM images (Fig. 3.13c). The averaged sheet resistance is 124.42 $\Omega/\square$. The best-fit thickness value determined from spectroscopic ellipsometry is $\approx$ 2.95 nm, closely matching the targeted thickness value of 3 nm. The measurements done on samples with 4 nm thickness show that gradual deterioration of the film properties is observed at 3-5 nm thickness range as shown in Fig. 3.14. The sheet resistivity is 49 $\Omega/\square$, which is in-between the values observed for $\mathrm{Au}^{5\mathrm{nm}}_{-195^\circ\mathrm{C}}$ 5nm (15.76 $\Omega/\square$) and $\mathrm{Au}^{3\mathrm{nm}}_{-195^\circ\mathrm{C}}$ 3nm (124.42 $\Omega/\square$).

Finally, a parameter uniqueness test is performed to further verify the achieved record-small thickness of

2.95 nm for a wetting layer-free gold film. This test is done by first choosing the thickness of the Au film (t_{Au}) as a test parameter, then define a set of 100 test values (evenly spaced between 0.5 nm and 6.5 nm) around its best-fit value ($t_{\mathrm{Au}} = 2.95$ nm), and then compute the corresponding regression-analysis-fitting MSE in ellipsometry. In the computation, t_{Au} is fixed at each test value, whereas all the other model parameters are allowed to vary, and the resulting MSE(t_{Au}) is recorded. Such a uniqueness test generates a plot of the MSE versus the pre-defined test parameter values of t_{Au}. As shown in Fig. 3.13d, the curve of MSE(t_{Au}) displays a well-defined minimum around the best-fit value of 2.95 nm. This suggests that the measured film thickness is reliable and uniquely defined, since no other combination of the remaining fit parameters is able to produce a similar MSE for the ellipsometry characterization.

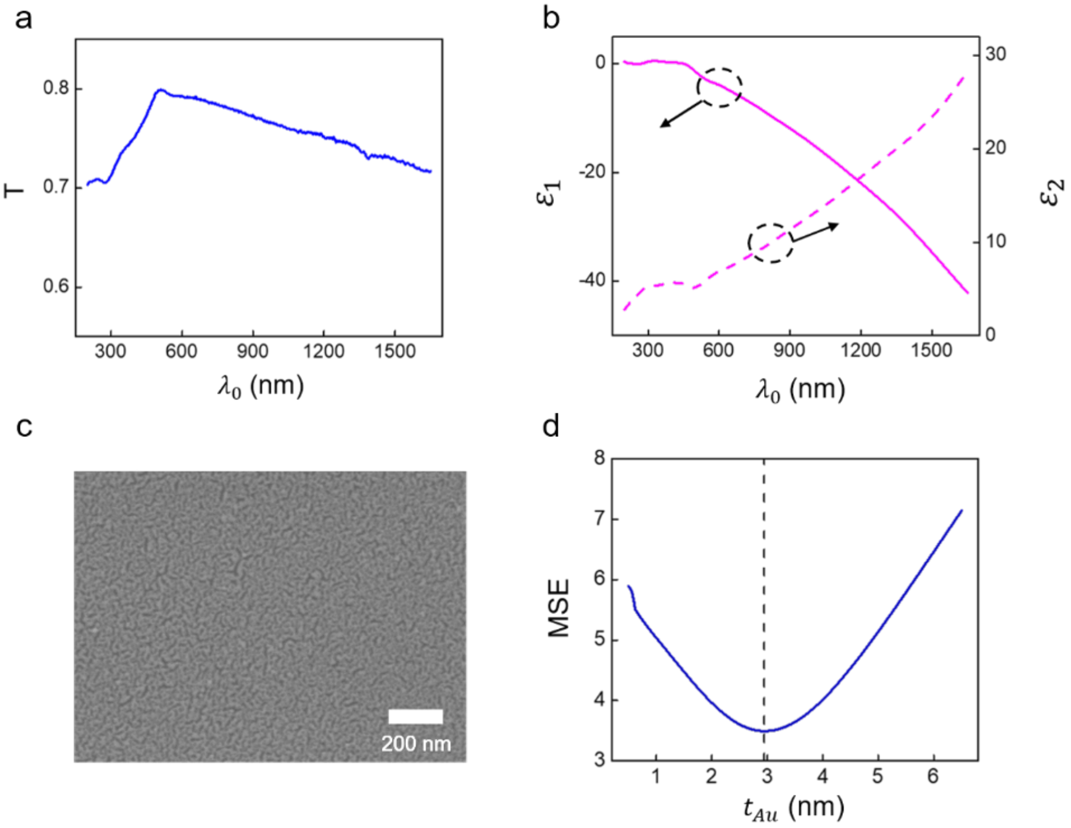

Figure 3.13: (a) Measured transmittance T versus free-space wavelength λ_0 for sample $\mathrm{Au}^{5\mathrm{nm}}_{-195^\circ\mathrm{C}}$ deposited on a 500 μm thick fused silica substrate. The reference (T = 1) for this measurements is transmittance through air. (b) Measured real (solid line) and imaginary (dashed line) parts of the relative electric permittivity, ϵ_1 and ϵ_2, of samples $\mathrm{Au}^{3\mathrm{nm}}_{-195^\circ\mathrm{C}}$. (c) SEM of details of sample $\mathrm{Au}^{3\mathrm{nm}}_{-195^\circ\mathrm{C}}$. (d) Parameter uniqueness test of the thickness of the Au film of sample $\mathrm{Au}^{3\mathrm{nm}}_{-195^\circ\mathrm{C}}$. The dashed line denotes the best-fit thickness value $t_{\mathrm{Au}} = 2.95$ nm. Data obtained at Physical Measurement Laboratory, National Institute of Standards and Technology.

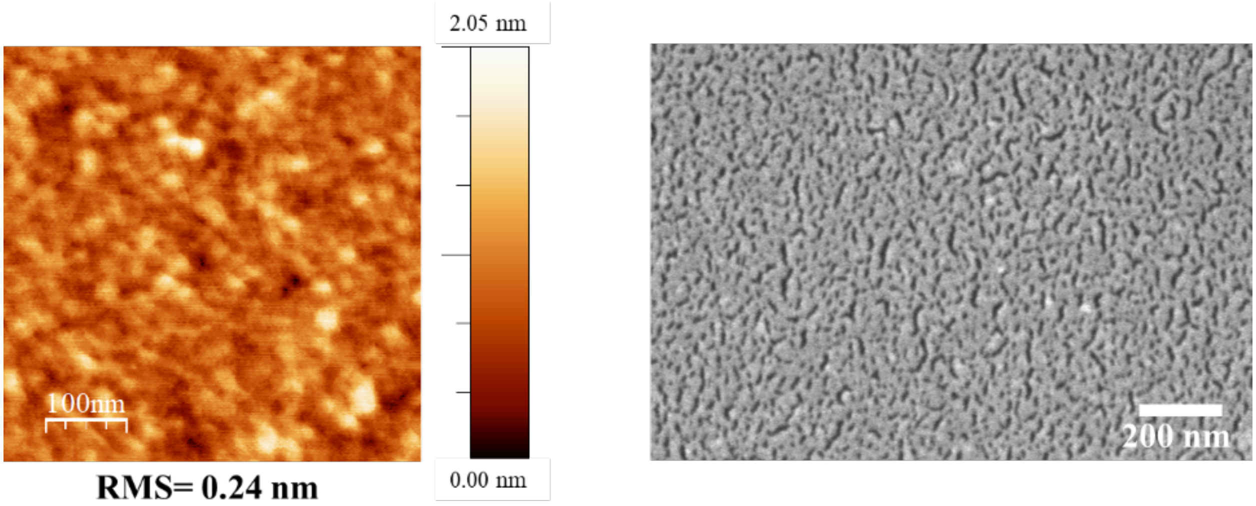

Figure 3.14: AFM (left panel) and SEM images of 4 nm Au film $\left(\mathrm{Au}^{4\mathrm{nm}}_{-195^\circ\mathrm{C}}\right)$. The topography shows deteriorated RMS roughness compared to the 5 nm films. The sheet resistance of this sample is $49\ \Omega/\square$. SEM data obtained at Physical Measurement Laboratory, National Institute of Standards and Technology and AFM data at Maryland Nanocenter, University of Maryland.

3.4 Simulations

Mode analysis of long-range surface plasmon polaritons (LRSPPs) on 5-nm-thick and 50-nm-thick Au films are performed at the wavelength of 780 nm using Lumerical finite-difference time-domain simulation package. The lowest-order LRSPP mode on a 50-nm-thick, 10-μm-wide Au stripe embedded in glass (assuming refractive index of 1.45) shows an effective refractive of 1.451, a propagation loss of $\approx$ 63 dB/cm, and a 1/e out-of-plane decay length of $\approx$ 500 μm. The lowest-order LRSPP mode on a 5-nm-thick, 10-μm-wide Au

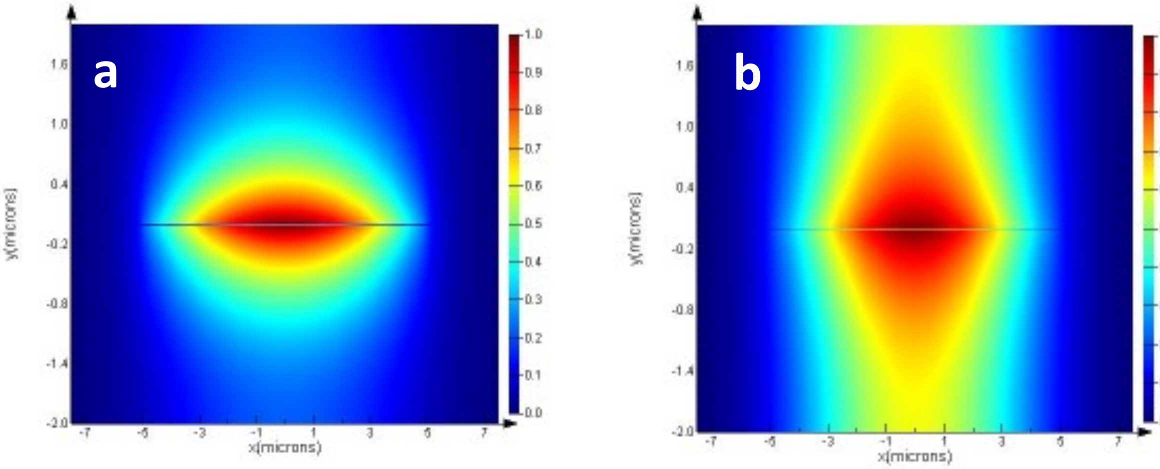

Figure 3.15: Simulated mode intensity profiles of LRSPPs on (a) 50-nm-thick and (b) 5-nm-thick, 10-μm-wide Au stripes at the wavelength of 780 nm.

stripe embedded in glass shows an effective refractive of 1.450, a propagation loss of $\approx$ 3.4 dB/cm, and a 1/e out-of-plane decay length of $\approx$ 2.7 μm. The LRSPPs mode intensity profiles in both cases are shown in Fig. 3.15.

3.5 Conclusion and Discussion

The effect of substrate temperature on the optoelectronic properties and surface morphology of thin Au films deposited on fused silica is systematically studied. It is observed that cooling down the substrate suppresses the Vomer-Webber growth mode of Au, enabling the formation of ultrathin continuous Au films with enhanced optoelectronic properties and improved surface morphologies. Wetting layer-free, plasmonic Au films down to the measured layer thickness of 2.95 nm were achieved by depositing the films on a substrate at the liquid nitrogen temperature. This work suggests a new approach to the fabrication of wetting layer-free and high-quality ultrathin Au films, which could benefit various Au-based optoelectronic and plasmonic devices, as well as metamaterials and metasurfaces.

A direct application of the 5 nm samples fabricated using in this method is with enhanced NPL from these films. It has been recently observed that nonclassical corrections to the Au bandstructure due to decreasing film thicknesses can result in increased PL yield [98]. In fact the prediction was that the PL yield should dramatically increase with decreasing film thickness so long as the films were very smooth. However, this study was limited experimentally as thin films below 12 nm were not able to be fabricated via their wet chemistry methods. Additionally, the thinnest films fabricated had surface roughness of $\sim$ 0.7 nm RMS. As discussed in Section 2 roughness on metal films can dramatically effect the emssion processes as well as the yield. The methods provided in this section allows a way to push this theory to it's limits. Our preliminary results of PL yields from 12 and 5 nm thin Au films made with the cryogenic sputtering method is shown in Fig. 3.16. We find substantial increase of PL yield among the two (Fig. 3.16 (a) (a)) as well as a $\sim$ 500 times increase in the up-converted PL in the 5 nm film as compared to the 12 nm (Fig. 3.16 (b)).

Additionally, this PL exhibits unexpected nonlinear character. It was shown by Ref. [98] that the origin of the PL enhancement was due to increased two-photon photoluminescence (2PPL) resulting from band structure modification due to electronic wavevector (in this case, Heisenberg) uncertainty relaxing the momentum mismatch restraints as described in section 1.5. They observed the up-converted PL region yield to increase dramatically as thickness was reduced and calculated a power law of $\approx$ 2 seeming to support their hypothesis. They were only able to fabricate films down to 12 nm before surface roughness became substantial.

However, we find that films down to 5 nm deviate from the expected value of $p = 2$ and exhibits an

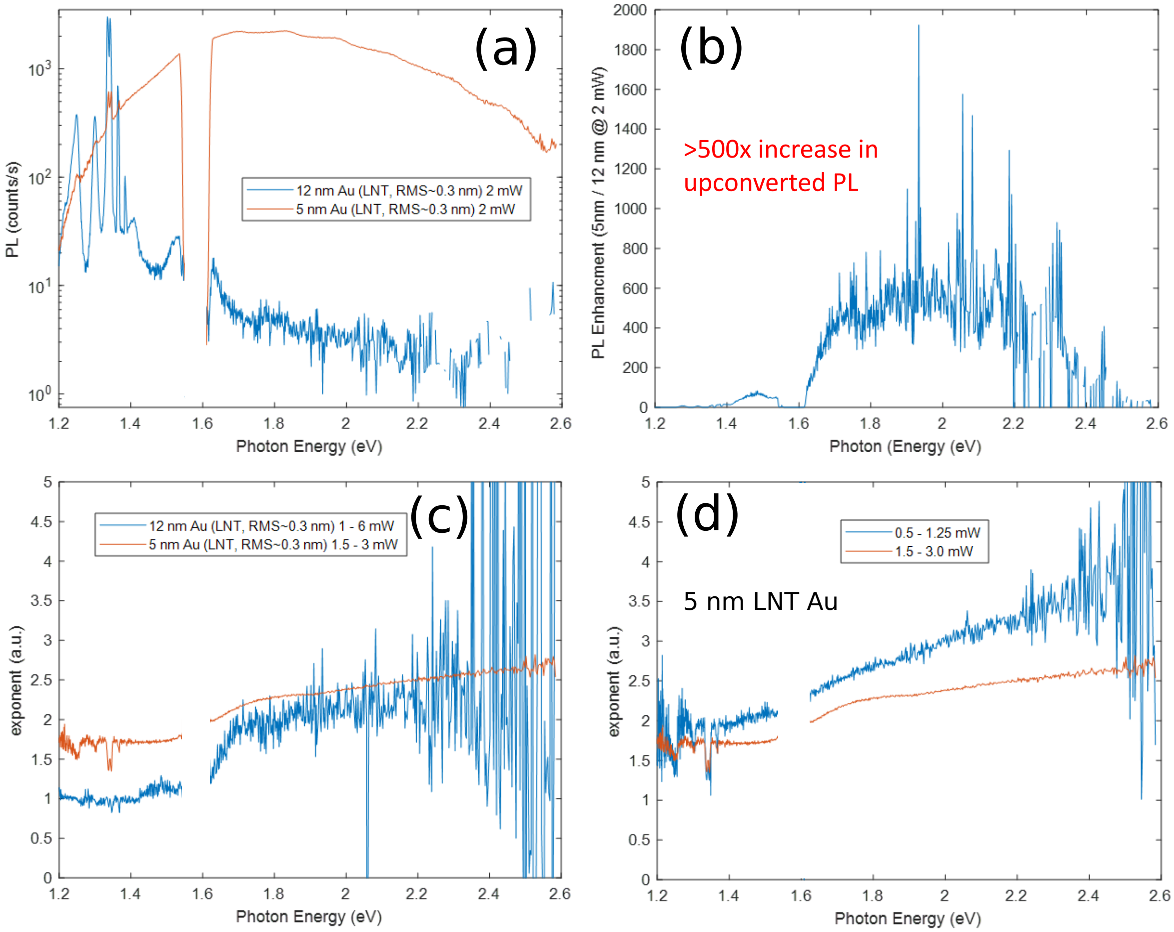

Figure 3.16: Preliminary PL data from 12 and 5 nm films atop glass substrates via cryogenic sputtering [unpublished]. (a) The PL signal is dramatically enhanced as the thickness is lowered. (b) Ratio of PL yield per wavelength of the 5 nm film to the 12 nm. An increase of ~ 500 is found for up-converted emission. (c) Extracted power exponent lineshape for 12 and 5 nm films. (d) Extracted power exponent lineshape for 5 nm films over two non-overlapping power ranges.

unexpected nonlinear character. We calculate $p(\omega)$ as described in chapter 2 for 12 and 5 nm films which are shown in Fig. 3.16 (c). We find that the up-converted spectral region for the 12 nm film is close to $p = 2$ while the 5 nm film deviates from it. Additionally, our films even at 5 nm were smoother than the thickest films presented in their study. Therefore, thermal emission from rough surfaces cannot be a hand-waved explanation for these observed deviations. We also probe the 5 nm film PL at various fluences and again observe unexpected trend. For low fluences, the PL exhibits a linear slope similar to eq. 2.4 as predicted for hot-carrier electron-hole recombination. However, as power is increased, $p(\omega)$ begins to appear suspiciously similar for that expected from non-Fermi electron-hole recombination PL, the power law of which is shown in Fig. 2.24. These preliminary findings clearly demonstrates that the origin for NPL of gold films predicted by [98] needs to be revisited.

Chapter 4

Deep Optical Switching on Subpicosecond Timescales in an Amorphous Ge Metasurface

Contributors:

Maxim R. Shcherbakov[*], Guoce Yang[†], Jia Song[+], Tianquan Lian[+], Hayk Harutyunyan[†] and Gennady Shvets[*].

[†] Department of Physics, Emory University.

[*] School of Applied and Engineering Physics, Cornell University.

[+] Department of Chemistry, Emory University.

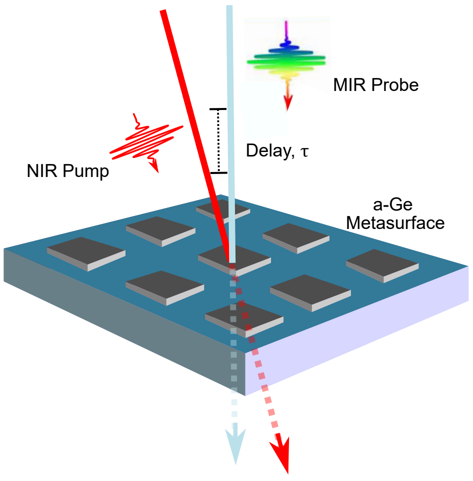

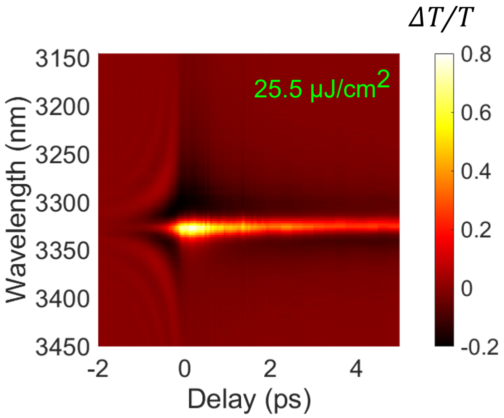

4.1 Chapter Overview

This chapter is based on results from the following publiciations [99, 100]:

R. Lemasters, M. R. Shcherbakov, G. Yang, Z. Fan, J. Song, T. Lian, H. Harutyunyan and G. Shvets, "Deep Optical Switching on Subpicosecond Timescales in an Amorphous Ge Metasurface." *Advanced Optical Materials* **9**(10), 2100240, (2021).

M. R. Shcherbakov, R. Lemasters, Z. Fan, J. Song, T. Lian, H. Harutyunyan and G. Shvets, "Femtosecond Frequency Conversion by Dynamic Losses in a Time-Variant Metasurface." *Optica* **6**(11), 1441-1442, (2019).

Active nanostructured optical components show promise as potential building blocks for novel light-based computing and data processing architectures. However, nanoscale all-optical switches that have low activation powers and high-contrast ultrafast switching have been elusive so far. In this study, pump–probe measurements are performed on amorphous-Ge-based micro-resonator metasurfaces that exhibit strong resonant modes in the mid-infrared. Relative change in transmittance of $\Delta T/T \approx 1$ with picosecond ($\tau \sim 0.5$ ps) modulation speed, obtained with very low pump fluences of 50 μJ/cm^2 are observed. These observations are attributed to efficient free carrier promotion, affecting light transmittance via high quality-factor optical resonances, followed by an increased electron-phonon scattering of free carriers due to the amorphous crystal structure of Ge. Full-wave simulations based on a permittivity model that describes free-carrier damping through crystal structure disorder finds excellent agreement with the experimental data. These findings offer an efficient and robust platform for all-optical switching at the nanoscale.

4.2 Introduction

4.2.1 Active Metamaterials

Properties such as permittivity are usually assumed to be determined by bulk material parameters which can be limiting. A goal in current research is focused on manipulating the properties of materials to produce new overall effects. Nanofabrication of metasurfaces has become ubiquitous to this end. Although material properties can be manipulated by various methods, these changes are "burnt in", or they do not change as a function of time and cannot be further tuned post fabrication. "Active" metasurfaces on the other hand, have their electromagnetic properties explicitly vary as a function of time. There are several platforms which can achieve this using various modulation schemes. Several examples of these include optical, thermal, electronic,

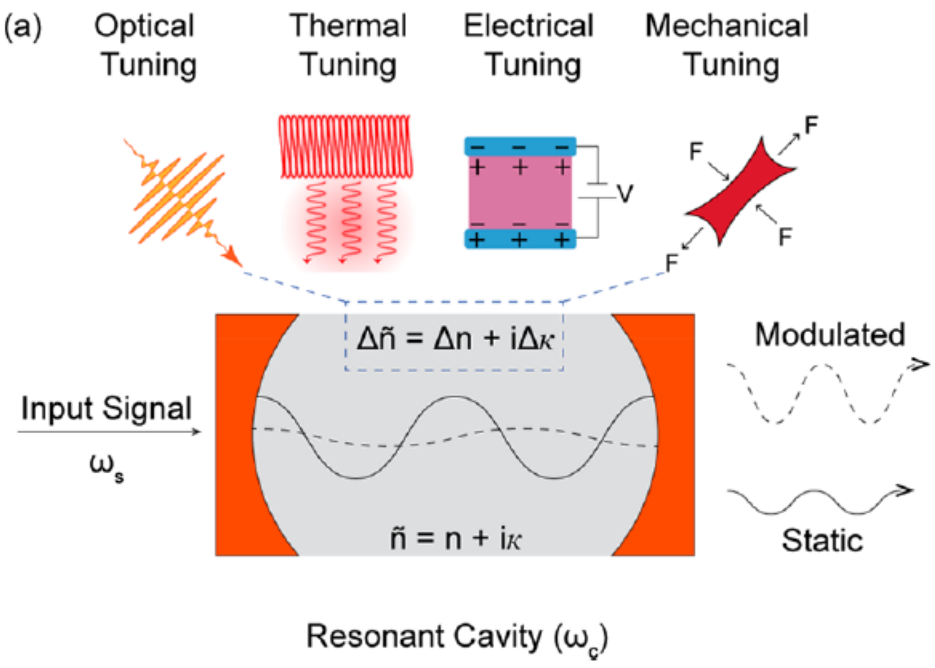

Figure 4.1: Optical, thermal, electronic, and mechanical modulation scheme examples. Refractive index tuning resulting in modulated output signals [12].

and mechanical, methods which are highlighted in Fig. 4.1. A main focus area of research is modification of the index of refraction/permittivities at the interface of a metasurface via these methods [12]. This includes the 3rd order nonlinear effects described in section 1.2.5 which describe an intensity dependent index of refraction.

In general, optical systems may couple with external driving forces which can alter their spectrum. Here we follow an example given by Ref. [1]. A schematic of this simple example is given in Fig. 4.2 (a) where a mirror is attached to a harmonic spring oscillator with natural frequency $\Omega_0 = \sqrt{K_0/m}$. For light incident on the mirror with energy (frequency), $E_{\mathrm{in}} = \hbar\omega$, the mechanical motion of the mirror will introduce a doppler-like shift on the reflected light as

$$E_{\mathrm{R}} = \hbar\left(\omega \pm \Omega_0\right). \tag{4.1}$$

This spectral altering can be seen in Fig. 4.2 (b).

Next, we reexamine the example of the microresonator from section 1.3.5 and look at the effects of a perturbation and resulting dynamics on the resonator. Given the eqs. 1.53 and 1.54 governing the resonant

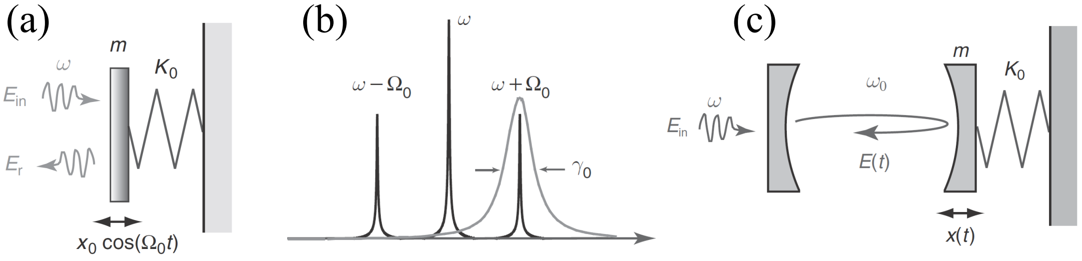

Figure 4.2: Modulated microresonator cavity dynamics [1]. (a) A mirror which oscillates at a frequency, Ω_0, couples to the light and (b) results in shifting of the spectrum of the incident light. (c) An optical cavity can be modulated and the Q-factor may be shifted accordingly.

mode, we get a characteristic eigenvalue equation of

$$\left(\vec{\nabla}^2 + \frac{\omega_n^2}{c^2}\right)\vec{u}_n = 0, \tag{4.2}$$

where ω_n is the eigenfrequency of the mode given its geometry and material composition. Next suppose that this microresonator has one of its ends be the oscillating mirror as described above. If the bandwidth of the resonator, γ_0, has spectral overlap with the oscillation induced spectral sidebands (Fig. 4.2 (b)), then there will be coupling of the microresonator mode and the mechanical mode. First, by solving for the fundamental mode ($n = 0$) of eq. 4.2, we can get the relation for the incoming light and the microresonator after some algebra to be,

$$\frac{\mathrm{d}}{\mathrm{d}t}\vec{E}_0(t) = \left[i\left(\omega - \omega_0\right) - \gamma_0\right]\vec{E}_0(t) + \kappa\vec{E}_{\mathrm{in}}(t), \tag{4.3}$$

where ω_0 is the fundamental frequency of the resonator and κ is the coupling strength of the incoming light. That is, γ_0 corresponds to losses (out-coupling) in the mode and κ corresponds to gains (in-coupling) from the incident light.

The effects of the oscillating mirror is accounted for by noticing that it is effectively changing the width of the resonator as shown in Fig. 4.2 (c). This affects the spectral behavior of the resonator as resonator frequencies are largely dependent on their geometry, i.e. boundary conditions. For a small change, Δx, of the cavity, this will introduce a shift of the resonance by

$$\Delta\omega_0 = -\omega_0\frac{\Delta x}{L}, \tag{4.4}$$

where L is the length of the cavity. This is accounted for in the differential equation of the coupled mode in eq. 4.3 as

$$\frac{\mathrm{d}}{\mathrm{d}t}\vec{E}_0(t) = \left[i\left(\omega - \omega_0\left[1 - \frac{x(t)}{L}\right]\right) - \gamma_0\right]\vec{E}_0(t) + \kappa\vec{E}_{\text{in}}(t). \tag{4.5}$$

It is important to note that the varying length of the cavity in eq. 4.5 is not the only perturbation which can alter the resonator. Any thing which alters the cavity resonance, such as index of refraction/permittivity variation, will have an analogous effect. In this chapter we discuss a method of doing just that via injection of hot-carriers. Additionally, the damping terms in eq. 4.5 can be made to be dynamic due to the injection of hot-carriers, and also from increased dynamic scattering. Such scattering is present in amorphous materials and is discussed in section 4.5.

4.2.2 Q-Switching

This results of the previous section highlights the importance of the Q-factor as discussed in section 1.3.5. If slightly more complicated temporal perturbations are applied, this will result in a both a shift in the resonant energy, $\omega \to \omega + \Delta\omega$, but also the bandwidth, $\gamma \to \gamma + \Delta\gamma$, in general. For example, if the applied perturbation such as the oscillating mirror is itself periodically applied, then this will result in a shifting of the frequency back and forth from $\omega \leftrightarrow \omega + \Delta\omega$, which will naturally broaden the averaged spectral bandwidth shape. However, the general nature of the perturbation is more complicated than the simple example of constant modulation over period, $T = 2\pi/\Omega_0$ as in eq. 4.5. For example the optical injection of hot-carriers induces an ultrafast and typically nonlinear change in the material permittivity, resulting in complicated time dependence of the temporal gradient resulting in metasurface resonance shifts. When both ω_0 and γ_0 are changing, the Q-factor can help to track the overall dynamics in these more complicated cases.

In some applications it is desirable to tune the Q factor of the resonant system to different values, a technique known as Q-switching. For example, Q-switching is a well known technique used in pulsed laser

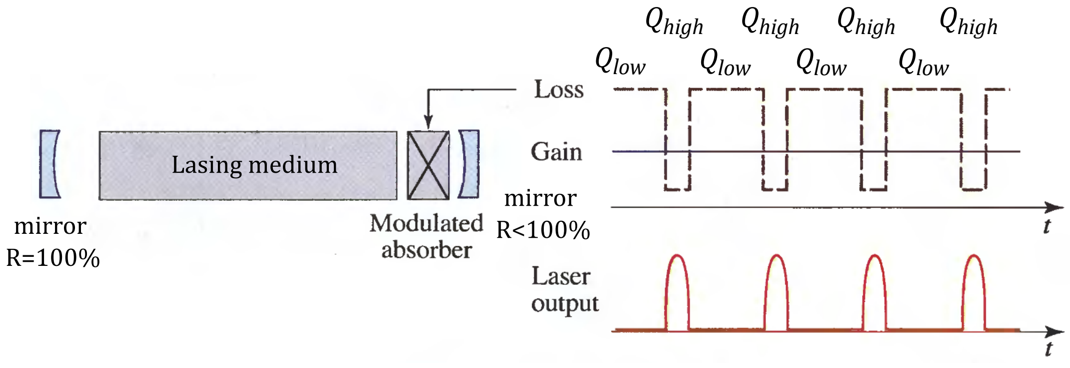

Figure 4.3: Q-switched pulsed laser system schematic [4].

systems. A laser consists of gain medium placed in a resonant cavity with two mirrors on each side, one of which is partially transmitting as seen in Fig. 4.3. A Q-switched lasing system produces pulsed laser signals by controlling the lasing process via a modulated absorber placed in the cavity. Strong absorption corresponds to low Q, and no lasing as losses are high and amplification is not possible. When the absorber is switched off (Q-switched), the resonant cavity is now at high Q, and amplification and lasing can begin. This way short laser pulses are emitted in a train of impulses in a controlled way rather than a continuous wave.

4.2.3 All-Optical Switching

A limiting factor of the Q-switching laser system described above is that the laser pulse duration and repetition rate are limited by the speed of the modulator in the lasing cavity. An example of this modulator can be a simple fan chopper (mechanical modulation) or a liquid crystal in a nematic phase (electrical modulator) as we refer back to Fig. 4.1. These types modulators are typically not the fastest option and can be undesirable for this reason. This is the appeal of all-optical switching which uses light to induce modulations and therefore operates at faster frequencies and speed than other methods. The fastest candidate includes utilization and manipulation of the nonlinear Kerr effect which is discussed in detail in section 1.2.5. The relative speeds and also power consumption to perform a Q-switch is shown in Fig. 4.4. Platforms for all-optical performance a highly desirable.

One last feature of importance which the Q factor does not capture is that of the overall modulation strength of the oscillator. It says nothing about the amplitude of the signal, but just the quality of the

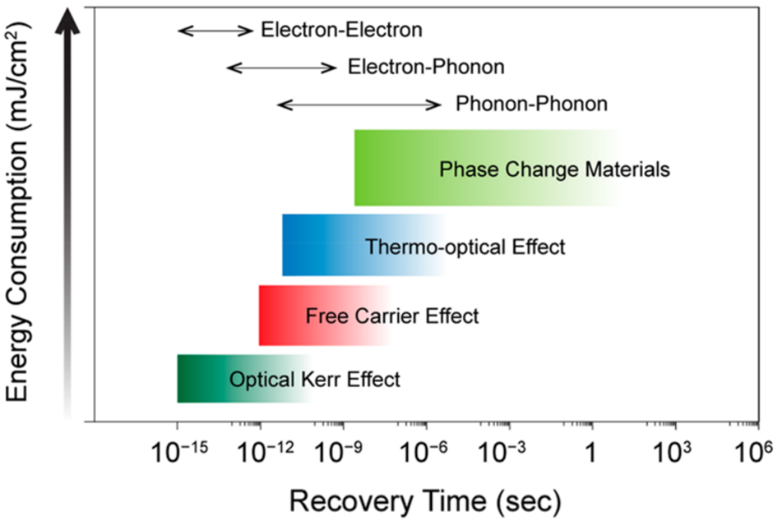

Figure 4.4: Modulator Speed and power consumption for various switching platforms [12].

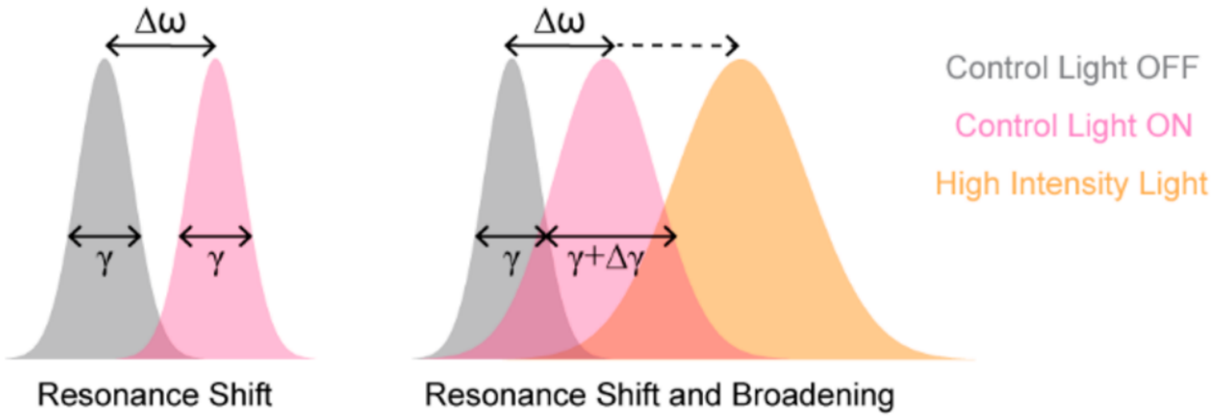

Figure 4.5: Resonance shifting via active metasurfaces [12].

resonator as a whole. Although high Q factor resonators still do not capture this quantity, they do offer more distinguishability of a modulation of that same resonance. A resonance with large bandwidth (low Q) experiences a shift in frequency which is small compared to the bandwidth, this difference will be hard to identify in practical measurements. If however the bandwidth is quite narrow (high Q) then a small shift in frequency may be more apparent and distinguishable. This is roughly illustrated in Fig. 4.5. This is highly desirable in the application of optical switching. An optical switch is a (usually high Q) resonance which is capable of producing a binary "on" and "off" state. This ability is a necessary trait for any sort of communication device. In the case of an all-optical switch this can be done by modulating the resonance from a ground state (off) to a frequency shifted final state (on). This is demonstrated in Fig. 4.5, where a frequency shift on a narrow bandwidth resonance shows less overlap of the "on" and "off" states, whereas a shift that also includes a broad bandwidth of either the ground or excited states has greater spectral overlap and so are less distinguishable in general. This last consideration can be captured in the raw change of signal power of an optical measurement such as transmittance or differential transmittance. This will be discussed in the following sections.

4.3 Semiconductor Active Metasurfaces

Optical metasurfaces [12, 101] have the ability to enhance light-matter interaction through highly localized electromagnetic modes [102–105]. This includes tailoring of the spatial distribution of the electromagnetic fields to create flat optics elements [106, 107], as well as polarization devices [108] and spectral properties. Furthermore, metasurfaces enable unprecedented control over the nonlinear optical phenomena [10, 109–112]. Despite the myriad of new possibilities offered by the metasurfaces, the scope of their applications typically suffers from a major disadvantage in the lack of tunability. In other words, the properties of metasurfaces are determined by their geometric parameters and material composition and typically cannot be tuned after the fabrication process has been completed. Semiconductor-based active metasurfaces (SAMs), on the other hand, offer a tunable electromagnetic response as their optical properties are an explicit function of time [100, 113–115]. The tunability of SAMs can pave the way for various applications based on active control in photonic devices [12].

One exciting application of SAMs in the field of photonics is all-optical switching and ultrafast signal processing. Typically, the merit of these processes is determined by considering three main factors: (*i*) the modulation depth, i.e. on-off switching ratio which determines the strength and distinguishability of the signal; (*ii*) the modulation speed; and (*iii*) the power consumption needed to complete an operation. Different techniques and approaches have been employed to optimize many of these factors. All-optical switching has been investigated extensively in dielectric, metallic and semiconductor nanostructures. Silicon-based nanostructures [113, 116, 117] show deep switching but exhibit slow temporal dynamics and require high excitation powers due to heating effects and dependencies on nonlinear processes such as two–photon absorption (TPA) [12] and the nonlinear Kerr effect (section 1.2.5). Plasmonic nanoparticles [110, 118, 119] show a femtosecond-scale ultrafast response (as discussed in sections 1.4.2 & 1.4.3) and require low power excitation, but have poor modulation depth due to very high initial free carrier (FC) density. Direct band gap semiconductors have shown to require low excitation power, deliver good switching depth and exhibit ultrafast modulation speed [114, 120, 121]. The latter is enabled by the presence of a direct electronic gap, which facilitates ultrafast relaxation of FCs and showing recombination times as short as several picoseconds. Although typically, indirect band gap materials do not employ efficient FC relaxation pathways to reduce the relaxation time to the sub-picosecond time scale [12, 26, 116, 117, 122–126], amorphous materials [125, 127] have shown promise for nanophotonic devices and ultrafast FC relaxation. The lack of long-range order in amorphous materials leads to disappearance of extended states (e.g. Bloch states for electrons) resulting in localized states which leads to a stronger electron-phonon coupling and faster free carrier relaxation. Additionally, these materials are usually easy to fabricate, affordable and CMOS-compatible, which makes it amenable for various on-chip applications. Efficient germanium-based ultrafast all-optical switches will assist the progress of mid-infrared photonics [128], where in recent years, many devices have been conceived, such as integrated laser sources [129], low-loss waveguides [130] and sensors [131].

In this study, amorphous Ge (a-Ge) is employed to design and fabricate a SAM that enables picosecond all-optical switching in the mid-infrared, where the ultrafast optical response of a-Ge has not been extensively investigated. The frequent electron scattering events alleviate the momentum restriction imposed by the indirect band gap found in crystalline Ge. The ultrafast temporal dynamics and switching response in these structures is investigated using ultrafast pump–probe experiments. The findings demonstrate strong FC injection with estimated densities of up to $2.1 \cdot 10^{19}$ cm^{-3}, leading to relative transmittance of $\Delta T/T \approx 1$ at fluences as low as 50 μJ/cm^2 and relaxation times of down to $\tau = 0.47$ ps, faster than what has been demonstrated in other nanostructured all-optical switches [114, 115, 120, 132]. a-Ge metasurfaces represent a novel class of semiconductor nanostrucutres that can find applications in active spatiotemporal beam control schemes and ultrafast all-optical data processing.

4.4 Experimental

4.4.1 Overview and Sample Specifications

Pump–probe measurements are performed on high Q factor a-Ge microstructure arrays which exhibit resonances in the mid-infrared (MIR) spectral range. For metasurface fabrication, two layers of PMMA (100 nm of 950K over 600 nm of 495M) were spun on a crystalline CaF$_2$ substrate, baked at 170°C for 15 min each, covered by a layer of Espacer 300Z spun at 6000 rpm, e-beam exposed at 1000 μC/cm^2 (JEOL 9500FS), and

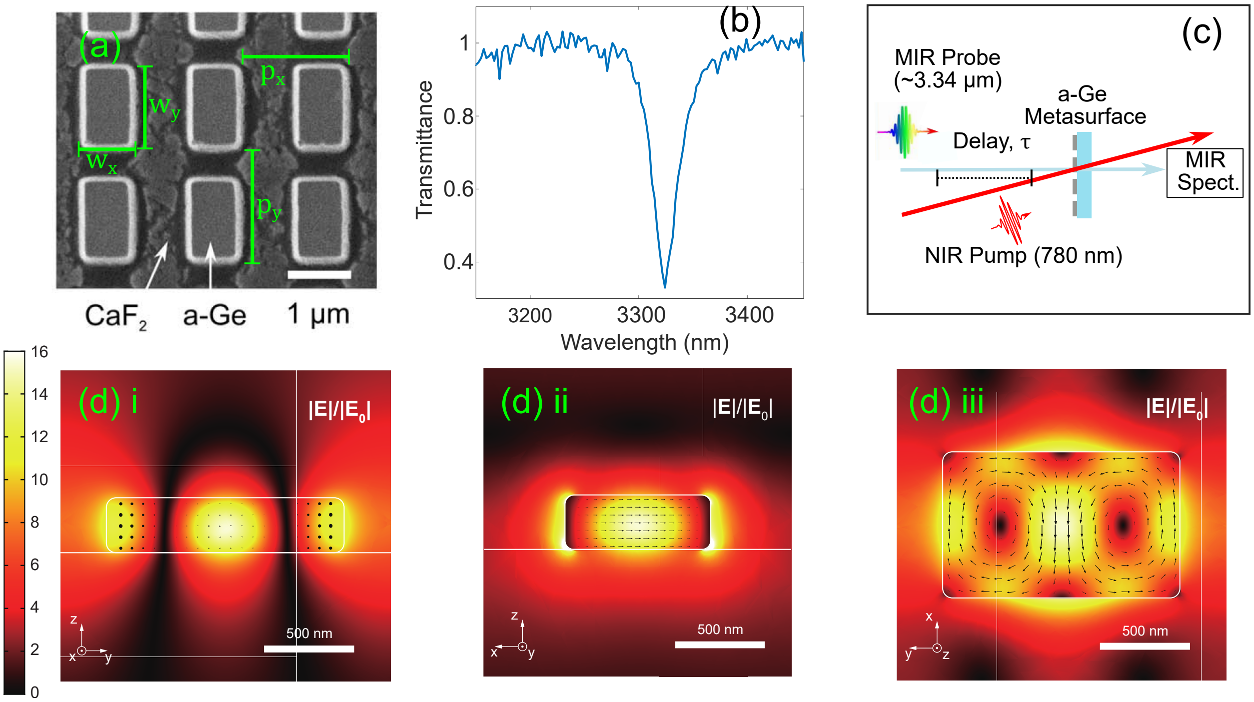

Figure 4.6: (a) SEM image of the a-Ge metasurface. The dimensions of the rectangle are $w_x = 0.8$ μm by $w_y = 1.3$ μm with an array periodicity of $p_x = 1.7$ μm and $p_y = 1.8$ μm. The thickness of the a-Ge layer is $h = 300$ nm. (b) Transmittance spectra of the MIR photonic mode at equilibrium shows a resonance around $\lambda_{\text{res}} = 3.32$ μm. (c) Experimental pump–probe setup and apparatus. A NIR pump ($\lambda_{\text{pump}} = 780$ nm) is followed (preceded) by a broadband probe pulse centered at $\lambda_{\text{probe}} = 3.34$ μm for positive (negative) delay times. (d) Simulations of the electric field distribution over the resonator at the resonant wavelength along the x (i), y (ii) and z (iii) axes.

developed in MIBK:IPA 1:3 for 90 s. A 5 s mild descum oxygen-plasma etch (Oxford Plasmalab 80) was performed to remove 10–20 nm of undeveloped resist to ensure good adhesion of Ge to the substrate. By electron-beam evaporation, 300 nm of Ge was deposited through the mask, which was then subject to lift-off in the sonicated acetone for 60 s at room temperature. The resulting samples, after being coated by Espacer 300Z, were characterized with a scanning electron microscope (Zeiss Ultra). Before the measurements, the Espacer layer was removed in DI water. Samples were fabricated using standard e-beam lithography methods.

Scanning electron microscopy images of the a-Ge based SAM are shown in Fig. 4.6a. The a-Ge layer thickness is $h = 300$ nm and the lengths of the rectangular microstructures were $w_x = 0.8$ μm by $w_y = 1.3$ μm in the x and y directions with an array periodicity of $p_x = 1.7$ μm and $p_y = 1.8$ μm in the x and y directions, respectively. These structures were designed to have a MIR resonance around $\lambda_{\text{res}} = 3.32$ μm which can be seen as a dip in the transmittance spectra shown in Fig. 4.6b and in the simulated electric field distribution in Fig. 4.6d. The low absorbance of a-Ge in this range and the low radiative loss in the quadrupole mode enables a high Q-factor resonance of $Q \approx 100$, which facilitates efficient FC-induced all-optical switching. This value differs from the theoretical value of $Q \approx 150$ as seen in the calculated band structure.

Amorphous materials do not have a well-defined k vector and band structure due to the disorder. The absorption transitions would be allowed between any valence and conduction band pairs without restriction of momentum conservation (phonon absorption and emission) but still with the conservation of energy. Hence, it is reasonable to assume the absorbed energy of each photon will just lead to an electron transition from valence band to conduction band, just like direct band-gap absorption transition. However, with the increase of pump fluence the electrons tend to be depleted, so the free carrier concentration would be overestimated. It could also be seen that the resonance of simulated transmittance spectra is bluer than the measured.

The microstructures in this work are not pumped at the fundamental resonance. The simulated cross-

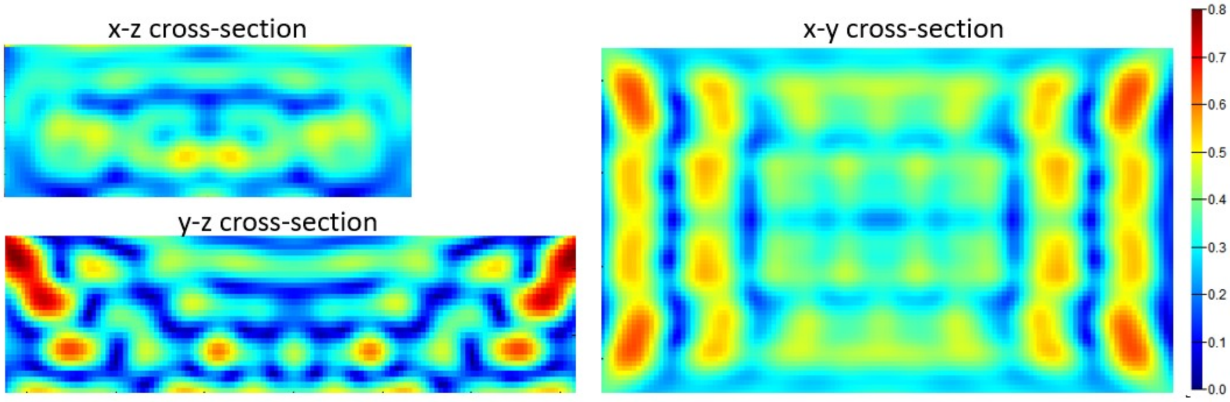

Figure 4.7: Electric field distribution calculated at the pump energy.

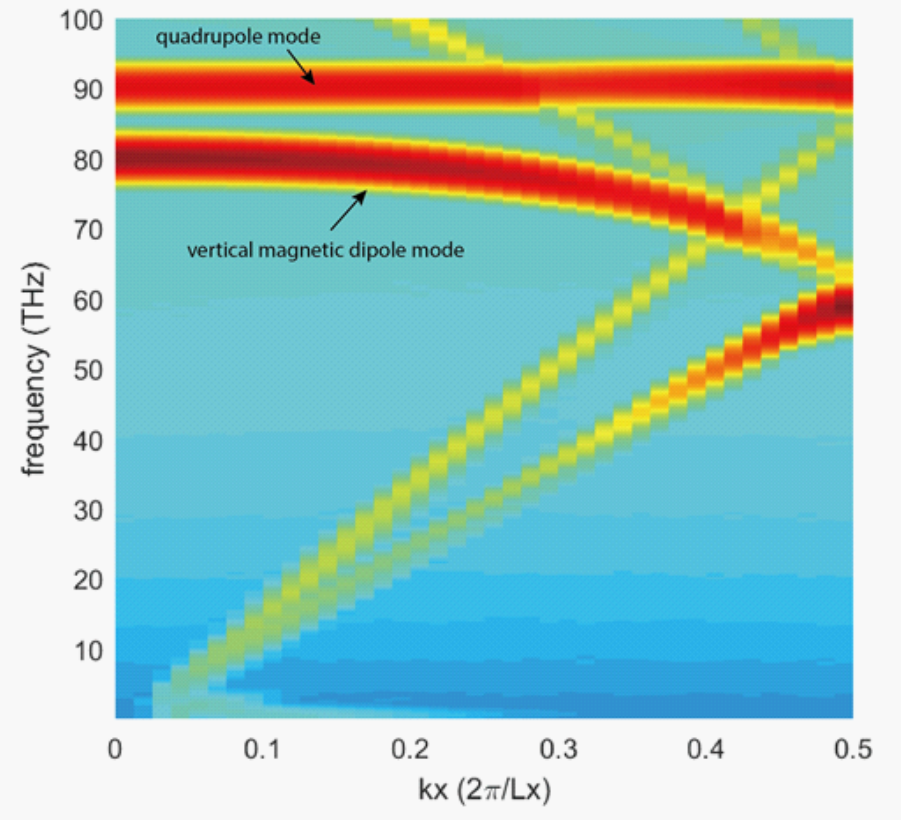

Figure 4.8: Photonic band structure the Ge metasurface from Γ point to X point.

sectional electric field distributions in the Ge structure at the pump wavelength of 780 nm are shown in Fig 4.7. Although there are still some fluctuations and hot spots of field, the overall distribution of them can be approximately regarded as uniformly distributed. However, if a nanoresonator was pumped at the fundamental frequency, the electric field distribution would be significantly non-uniform, such as a magnetic dipole mode in silicon sphere and thus the resulted inhomogeneous carrier distribution should be taken into account.

The photonic band structure of the Ge metasurface from Γ point to the X point is show in Fig. 4.8. At the frequency of interested, there are two main high Q modes: the quadrupole mode that is used in this study and a vertical magnetic dipole mode which is a dark mode that is protected by the symmetry of the structure and cannot be coupled to the far-field excitation. The quadrupole mode (whose Eigen-frequency is calculated as $90 + 0.3i$ THz) here still has a small radiative rate so a plane wave can excite it to get a high Q resonance in the far field spectrum. Here, the band structure was calculated by Lumerical FDTD but the Q-factor would be underestimated due to the limited simulation time and Gaussian apodization. The accurate Eigen-frequency was calculated by COMSOL Multiphysics. The mismatch between the observed and predicted Q-factors of the resonance used to show the deep ultrafast all-optical switching is caused by

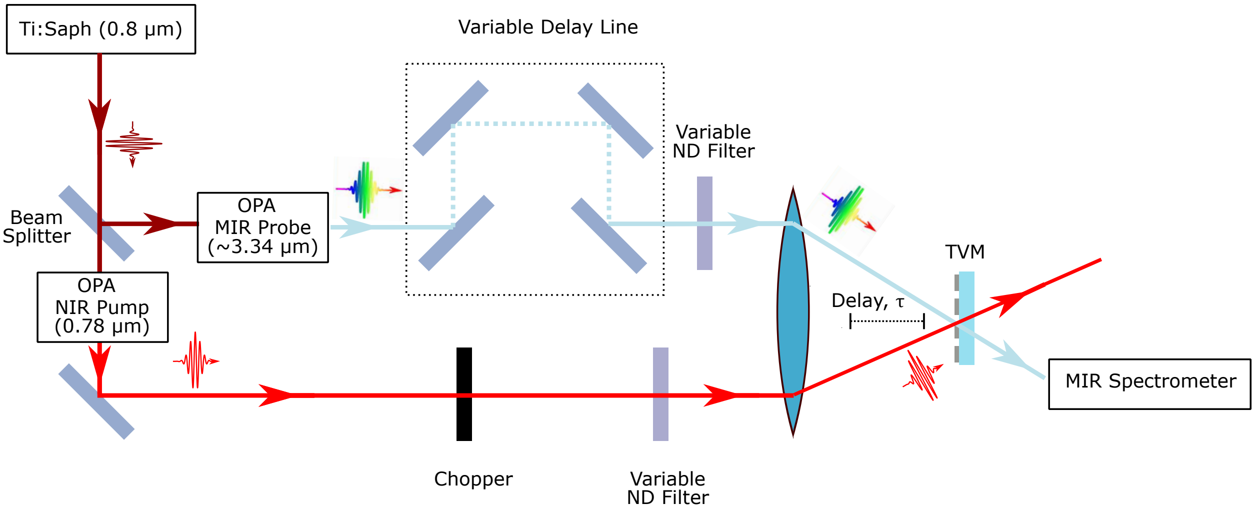

Figure 4.9: Experimental pump-probe setup. Description given in main text.

fabrication imperfections, as shown in previous work [133].

4.4.2 Pump-Probe Spectroscopy

The experimental pump–probe configuration is illustrated in Fig. 4.6c and in greater detail including the entire optical path in Fig. 4.9. The SAM is pumped with a near infrared (NIR) pulse at $\lambda_{\text{pump}} = 780$ nm beam produced by a 35 fs 1 kHz amplified Ti:Sapphire system. After excitation by a pump pulse, the system's dynamic state is monitored by measuring the transmittance of a time-delayed broadband mid-infrared (MIR) probe centered at $\lambda_{\text{probe}} = 3.34$ μm which is polarized along the orientation of the photonic mode. By varying the delay between the NIR and MIR, the spectral and temporal dynamics of the SAM can be observed. The pump has a photon energy much higher than the energy of the resonant photonic mode of the SAM and the band gap of Ge, leading to photoinjected FCs. This change in carrier concentration effectively changes the refractive index of the material and therefore, results in a shift and broadening of SAM's resonance [12]. The changes in the spectral response of the microstructures can be seen in the MIR probe transmittance spectra, manifesting in pronounced all-optical switching profiles.

The mid-IR transient spectrometer is based on a Ti:Sapphire amplifier laser system (Coherent Astrella, 1 kHz repetition rate at 800 nm, 35 fs, 5 mJ/pulse). The 800 nm fundamental output of the amplifier is split into two beams to pump two fully integrated, computer-controlled femtosecond optical parametric amplifiers (OPA) to generate the tunable pulse for the pump (UV to near-IR) and probe (near to mid-IR) beams, respectively. The pump and probe beams are overlapped on the sample, after which the probe beam is redirected into the mid-IR femtosecond transient absorption spectrometer configured with a multi-pixel array detector (HELIOS IR, Ultrafast Systems LLC). The typical instrument response time of the mid-IR transient absorption measurement was determined to be ∼ 170 fs using a Si substrate with 700 nm pump and 3.34 μm probe.

The measured differential transmission is given by

$$dT(\lambda,\tau) = \frac{\Delta T(\lambda,\tau)}{T(\lambda)}, \tag{4.6}$$

$$\Delta T(\lambda,\tau) \equiv T(\lambda,\tau) - T(\lambda,\infty), \tag{4.7}$$

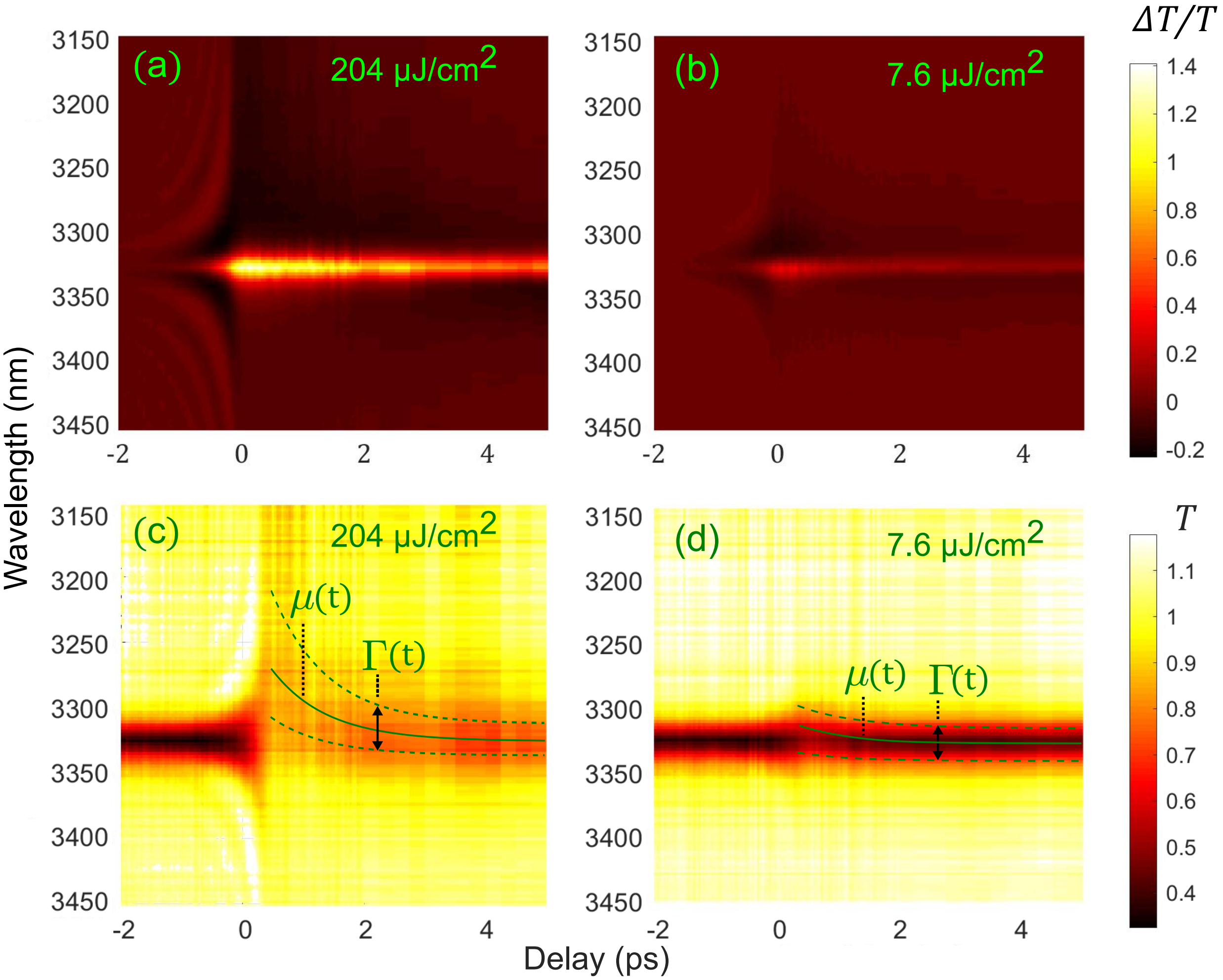

Figure 4.10: (a), (b) Differential transmittance, $\Delta T/T$, for pump fluences of 204 μJ/cm^2 and 7.6 μJ/cm^2, respectively. A clear undulating dynamic spectral shape can be seen for negative probe delay times, while a slowly decaying signal may be seen for positive times. (c), (d) Absolute transmittance, T, for pump fluences of 204 μJ/cm^2 and 7.6 μJ/cm^2, respectively. The same characteristic dynamic spectral lineshapes can be seen for negative and positive delay times as for the $\Delta T/T$. A decaying exponential is used as an envelope function to fit the dynamic spectral shape to the Gaussian lineshape starting at $t = 0$ ps. This lineshape is defined by the mean energy, $\mu(t)$, and FWHM, $\Gamma(t)$, which can be seen schematically overlaid on the plots.

where $T(\lambda, \infty)$ is the steady-state transmission coefficient. Fig. 4.10a shows the differential transmittance, $\Delta T/T$, of the metasurfaces as a function of probe delay time for excitation fluence $P_{\text{pump}} = 204\ \mu\text{J/cm}^2$. It can be seen that $\Delta T/T$ shows a very strong spectral response in both positive and negative probe delay times. The dynamics can be seen to be drastically different for positive and negative delays and is more pronounced at higher pump power as evident from the comparison with a lower fluence ($P = 7.6\ \mu\text{J/cm}^2$) transient transmittance data shown in Fig. 4.10b. These two regimes correspond to the pump pulse preceding the probe pulse (positive delay time) and the probe pulse preceding the pump pulse (positive delay time). The two pulses overlap at $t = \tau$. This is illustrated in Fig 4.11.

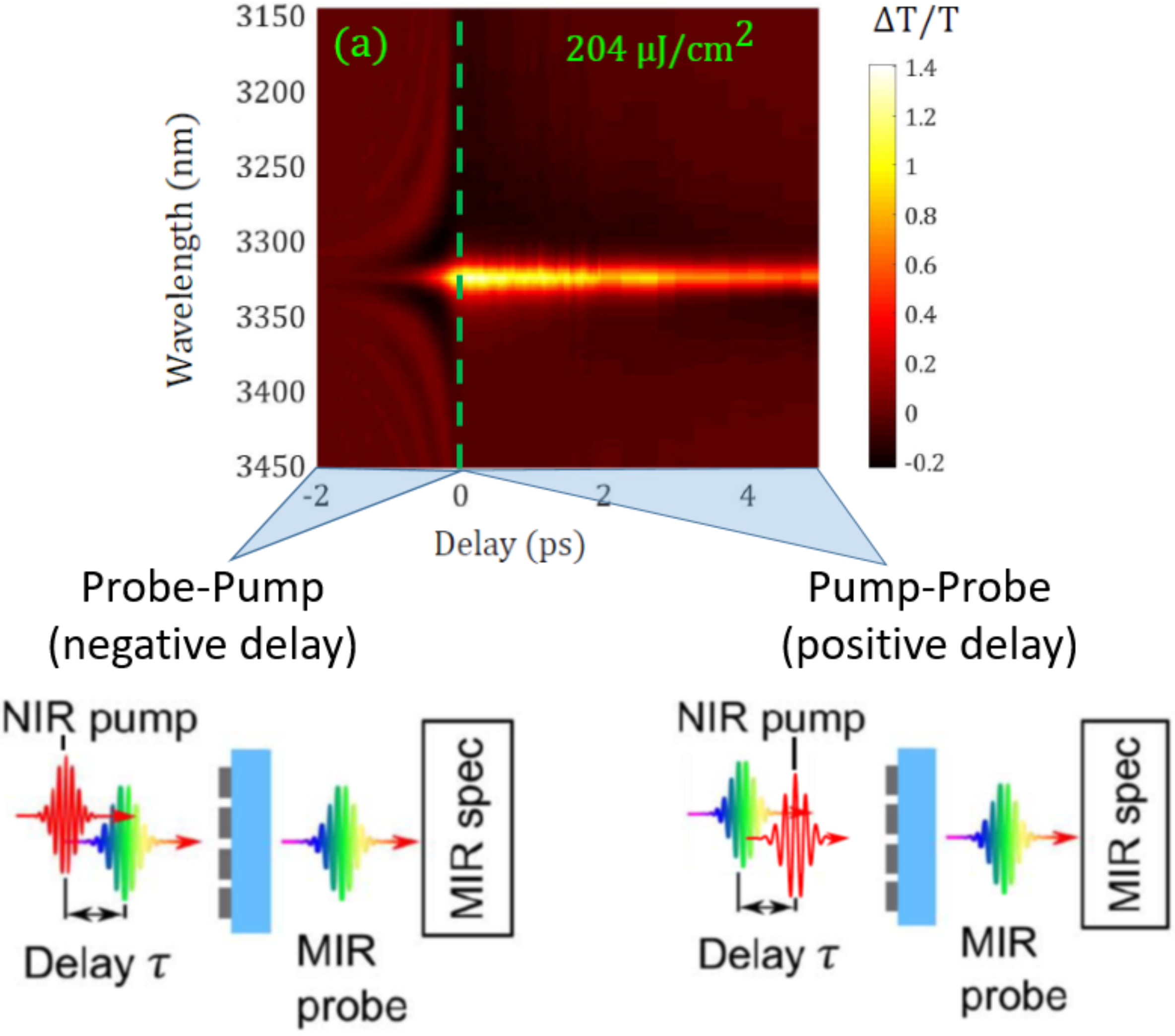

Figure 4.11: Pump-probe (positive delay) and probe-pump (negative delay) regimes studied in this system. The dotted green line shows the crossover at $t = \tau = 0$.

4.4.3 Negative Delay Times

For negative probe delay times, the differential transmission exhibits a characteristic spectral undulations resulting in bands of negative extinction (NE). The extinction coefficient of light passing through any photonic structure is defined as the deficit of optical power in transmission. Because optical extinction is caused by absorption, reflectance, and scattering, it must be positive as long as the structure is composed of gain-free time-invariant material. Moreover, for dispersive materials and photonic structures, the frequency-dependent extinction coefficient $E(\lambda) \equiv 1 - T(\lambda) > 0$ must be positive for every wavelength λ of the incident light, where $T(\lambda)$ is the transmission coefficient. Time cuts of this behavior is shown in Fig. 4.12.

This behavior can be understood in the framework of coupled mode theory (CMT) where the NIR pump pulse introduces time-dependent losses in SAMs leading to an abrupt deterioration of the MIR mode's Q factor [100]. In other words, the MIR pulse excites the photonic mode of the system and within its radiative lifetime the refractive index of the a-Ge metasurface is changed by the NIR pulse resulting in rapid damping of the mode. Thus, the transient lineshape of the MIR resonance exhibits spectral modulations characteristic for a Fourier transform of an abrupt change in field amplitude as a function of time.

To illustrate this effect, the extinction of an incident optical pulse with complex-valued amplitude $s^{+}(t)$ by a single-mode time-varying metasurface (TVM) characterized by its amplitude $a(t)$, natural frequency ω_0, time-dependent damping rate $\gamma(t)$, and radiative coupling rate γ_r are calculated. Within the framework

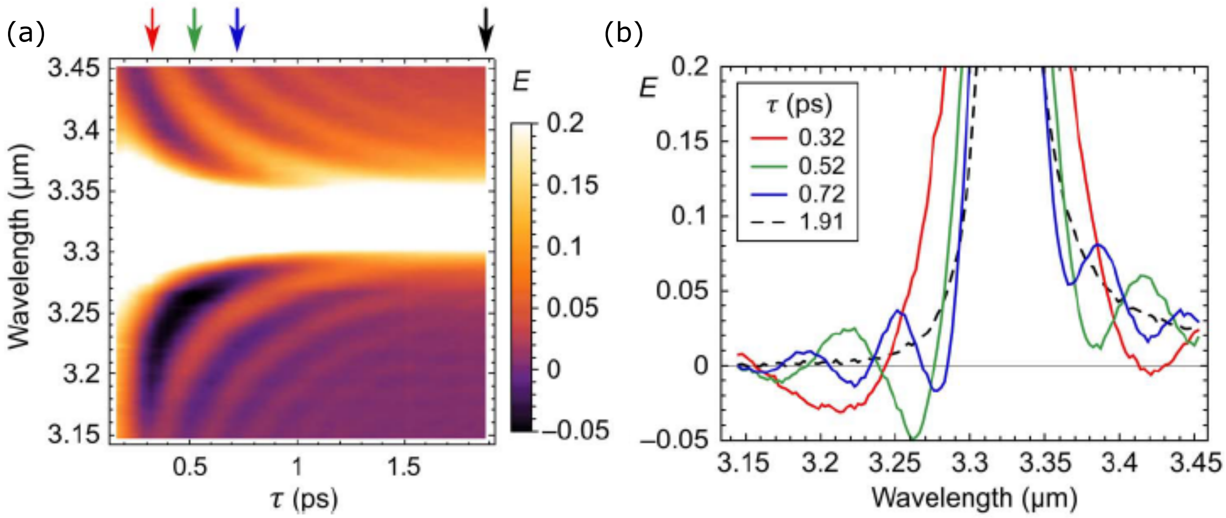

Figure 4.12: Time cuts of the transmittance at 0.25, 1, 2 ps along with the steady state value.

of CMT, the transmitted wave $s_-(t)$ is calculated according to the equations below:

$$\frac{\mathrm{d}}{\mathrm{d}t}a(t) - i\omega_0 a(t) + \left[\gamma_r + \gamma_{nr}(t)\right] a(t) = \sqrt{\gamma_r} s^+(t) \tag{4.8}$$

$$s^-(t) = s^+(t) - \sqrt{\gamma_r} a(t) \tag{4.9}$$

where $\gamma_{nr}(t) = \gamma(t) - \gamma_r(t) > 0$ is a non-radiative damping rate of the mode. When the quality factor defined as

$$Q(t) \equiv \frac{\omega_0}{2\left[\gamma_r + \gamma_{nr}(t)\right]}, \tag{4.10}$$

rapidly decreases from its high initial value of $Q_i \ll 1$ to its final value of $Q_f < Q_i$ due to rapid increase of non-radiative losses, the TVM is assumed to be Q-switched.

For a Gaussian input signal

$$s^+(t) = s_0 \exp\left(-i\omega_0 t - \frac{t^2}{\tau_{\text{probe}}^2}\right), \tag{4.11}$$

incident on an instantaneously Q-switched TVM (from $Q_i = 100$ to $Q_f = 5$ at $t = \tau$), the mode evolution $a(t)$ is plotted in Fig. 4.13a. It is assumed that the following pulse and TVM parameters: $\omega_0 = 2\pi c/\lambda_0$ (where $\lambda_0 = 3.3$ μm and $c = 3 \times 10^9$ m/s is the speed of light.) and $\tau = 200$ fs. The transmission spectrum

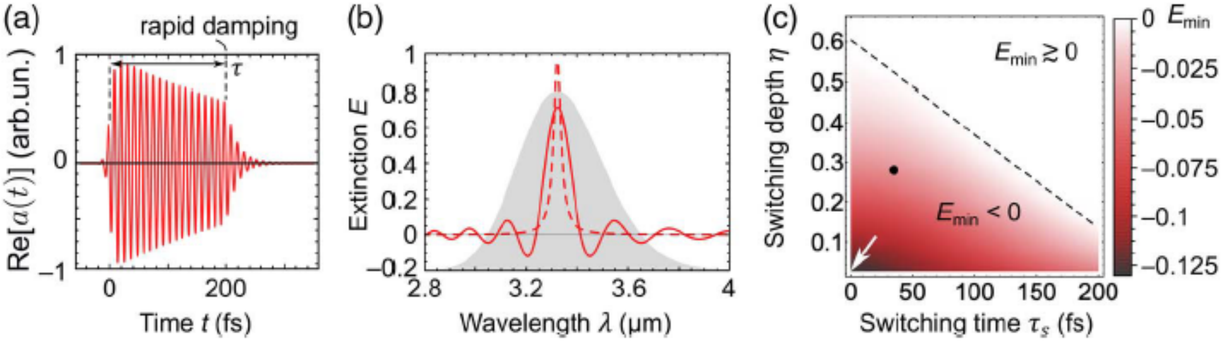

Figure 4.13: Theory of negative light extinction by a TVM. (a) Evolution of the mode before and after the abrupt Q-switching at $t = \tau$ from $Q_i = 100$ to $Q_f = 5$ ($\eta = 0.05$). (b) Extinction spectra for $\tau = 200$ fs (solid line) and ∞ (dashed line). Redistribution of spectral components manifests in several regions of $E < 0$. Shaded area: spectrum of the incident pulse $s^+(\lambda)$. (c) Conditions for negative extinction: Q-switching must be fast (horizontal axis) and deep (vertical axis); τ has been optimized to minimize E. The arrow indicates the parameters from panels (a, b), and the dot shows the experimental parameters.

is given as

$$T(\lambda,\tau) \equiv \frac{|s^-(\lambda,\tau)|^2}{|s^+(\lambda)|^2}, \tag{4.12}$$

which depends on the Q-switching time τ and extinction $E(\lambda,\tau) \equiv 1 - T(\lambda,\tau)$, are calculated. The latter is plotted in Fig. 4.13b. While $E > 0$ for a metasurface that does not vary during the trapping time of the pulse (dashed line), NE spectral regions corresponding to $E < 0$ emerge for a TVM with $\tau < Q_0/\omega_0$. Intuitively, NE originates from (i) spectral broadening of the captured (resonant) photons caused by the dynamic Q-switching and (ii) their subsequent constructive interference with the non-resonant photons present in the broadband incident pulse. The spectral spacing $\Delta\lambda \approx \lambda)^2/2\pi c\tau$ between the NE regions is determined by the delay τ between TVM excitation at $t = 0$ and switching at $t = \tau$.

In a more realistic CMT calculation, finite switching times $\tau_s < \tau$ were used to establish the conditions for the emergence of the NE spectral region. According to Fig. 4.13c, $E(\lambda,\tau) < 0$ is achieved for at least bone value of τ, as long as the switching is fast ($\tau \ll \gamma_r^{-1}$) and deep (small $\eta \equiv Q_f/Q_i$).

4.4.4 Positive Delay Times

For positive delay times, i.e. when MIR pulse arrives after the NIR pulse, ultrafast FC excited state dynamics are observed. In particular, a strong shift of the center energy and the full width-half maximum (FWHM) of the resonance occur. These effects are due to the changes of the refractive index from induced FC density excited by the NIR pump excitation. Thus, they do not exhibit the characteristic power scaling of a Kerr-type

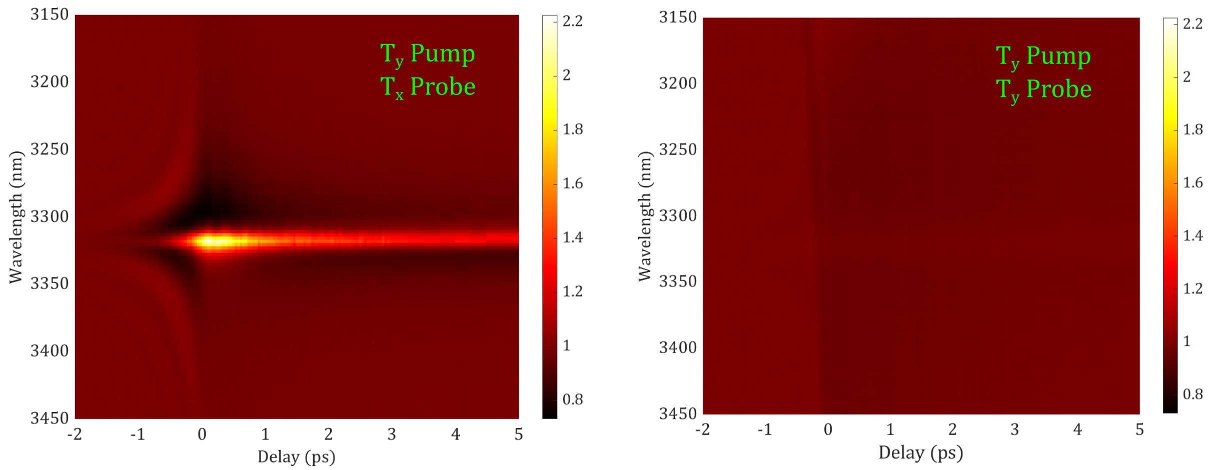

Figure 4.14: Dynamics for T$_y$ pump at 15.3 μW/cm^2 and T$_x$ probe configuration. Dynamics for T$_y$ pump at 204 μW/cm^2 and T$_y$ probe configuration.

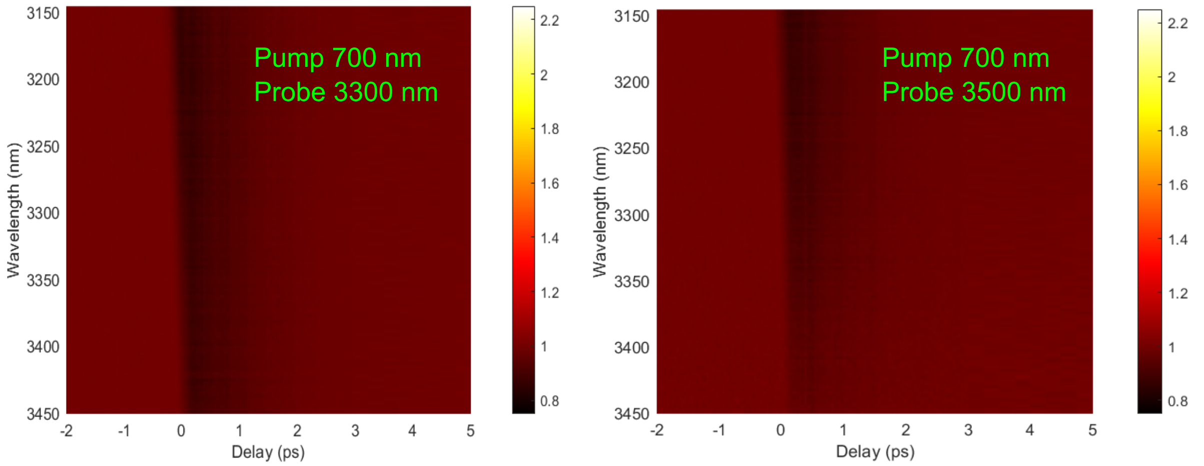

Figure 4.15: Transient spectral response of the Ge film for fluences of 204 μJ/cm^2. The pump wavelength and power is the same for both spectra while the probe center wavelength is changed.

nonlinearity or TPA [12]. As FC concentration increases in the system, the imaginary part of the complex permittivity is modified, changing the FWHM of the resonance dip. Furthermore, due to the the Kramers-Kronig relations in section 1.2.4, changes to the imaginary part of the permittivity will be accompanied by an induced change in its real part, leading to a shift of the resonant energy of the mode [2].

Polarization dependence measurements in the pump probe configuration were performed on the SAM's and are shown in Fig. 4.14. The ultrafast response when the pump beam is polarized perpendicular ($\mathrm{T_y}$) to the photonic mode with a fluence of 15.3 μW/cm^2 while the probe is polarized parallel ($\mathrm{T_x}$) to the resonance. A strong response is seen for this configuration. This is expected as only the probe beam should have polarization dependence since only it is directly coupling to the photonic mode. Additionally, the ultrafast response is seen to vanish when the probe beam is rotated 90 degrees, even for fluences up to 204 μW/cm^2.

The ultrafast response of an a-Ge film void of microstructures gives negligible response. The transient spectral response of the Ge film for fluences of 204 μJ/cm^2 is shown in Fig. 4.15. The pump wavelength and power is the same for both spectra while the probe center wavelength is changed from 3300 to 3500 nm. In both cases, an ultrafast transient response with a negligibly small amplitude is observed. This is comparable to the weak response observed in Fig. 4.14 when the system is probed perpendicular to the photonic resonance. This clearly demonstrates the observed strong amplitude modulation in this work is due to the presence of the aGe micro-resonators.

Typically, the magnitude of the ultrafast optical response is evaluated solely using the $\Delta T/T$ ratio. One main reason for this is because $\Delta T/T$ is the experimental value usually being measured rather than

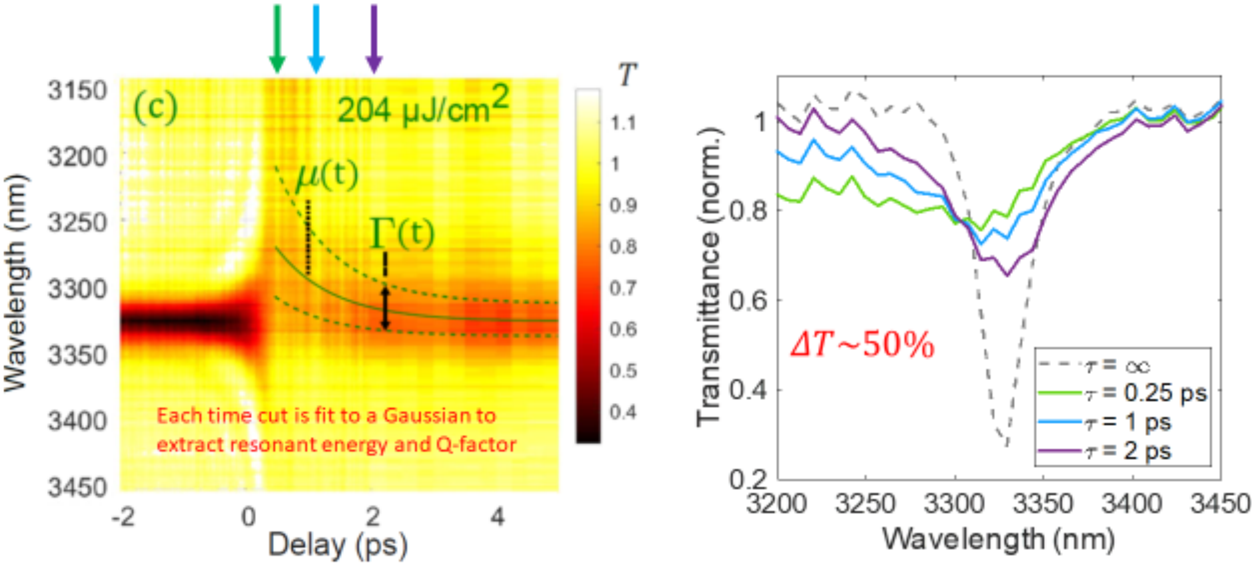

Figure 4.16: Time cuts of the transmittance at 0.25, 1, 2 ps along with the steady state value.

T. This modulation depth is typically small for most of the samples and materials often reaching values of $\Delta T \lesssim 10^{-2}$. One drawback of this approach is that $\Delta T/T$ does not capture the absolute changes of transmittance magnitude. For example, a material which exhibits a change of transmittance of 100% to 90% at a certain wavelength will have the same $\Delta T/T$ value as one which changes from 10% to 9%. In this work, we consider the absolute transmittance as a function of probe delay time to (i) simplify the analysis of the temporal dynamics, and (ii) to highlight the large absolute magnitude of ~50% for transmittance change achieved for a-Ge MRMs. Time cuts of the transient signal and the corresponding amplitude change in transmittance is shown in Fig. 4.16.

The absolute transmittance for excitation powers $P = 204\ \mu\text{J/cm}^2$ and $P = 7.6\ \mu\text{J/cm}^2$ are shown in Figs. 4.10c and 4.10d. As the induced FC distribution begins to thermalize in the material the index of refraction returns to its initial pre-pumped values and the resonances begin to trend back towards their equilibrium values. Time cuts of T can be seen in Fig. 4.16 showing the dispacement of μ and Γ along with the strong modulation depth. The FC populations are assumed to decay exponentially considering only thermalization as the main contributor of the FC relaxation process. To extract the values of the resonance energy and linewidth as function of time delay we fit the transmittance data using a Gaussian function. The mean energy, $\mu(t)$, and FWHM, $\Gamma(t)$, of the resonance are then extracted from the fits and plotted as functions of delay time in Figs. 4.17a and 4.17b for the two fluence values. The extracted values $\mu(t)$ and $\Gamma(t)$ for various fluence values are shown with a mono-exponential decay fits in Figs. 4.17a and 4.17b. The

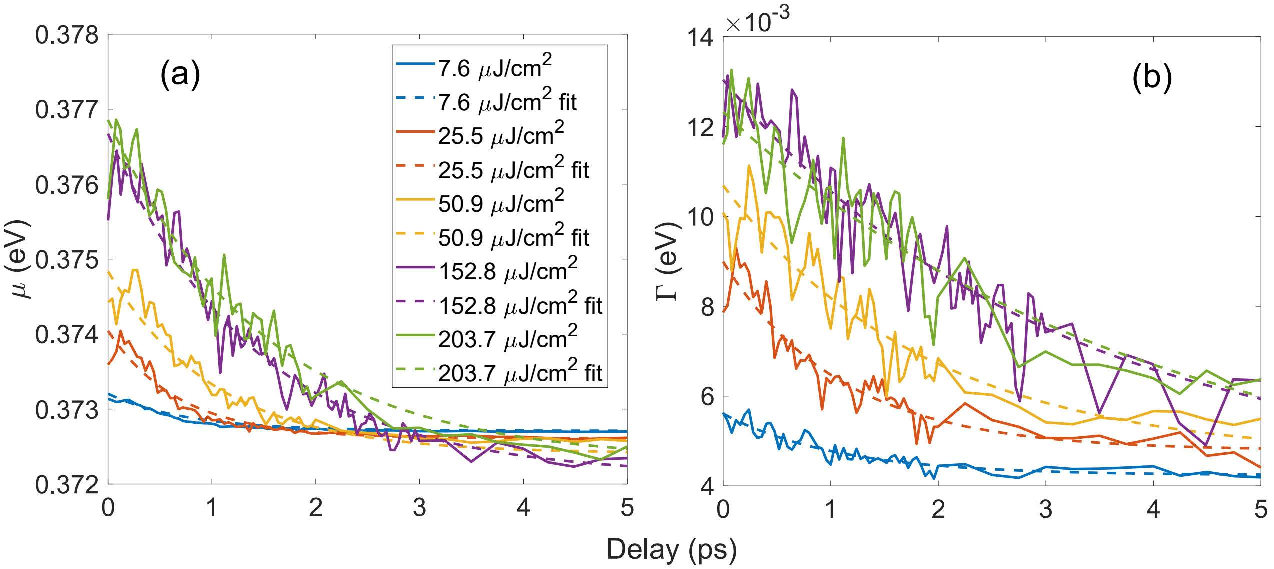

Figure 4.17: Resonance relaxation in a-Ge metasurfaces. (a) Mean resonance energy $\mu(t)$ (solid lines) with corresponding exponential fits (dashed lines) for pump fluences within the range 7.6–204 $\mu\mathrm{J/cm}^2$. (b) Same for the resonance width $\Gamma(t)$.

same dynamics is found by fitting a Fano lineshape in Figs. 4.10a and 4.10b. Note that we do not observe a continuous rate change as function of delay time, as our data can be fit with a good accuracy using only one exponent; hence, the Auger recombination contributions can be neglected in our system. From simple visual inspection of this data, two main trends can be noticed. First, the amplitude of both signals grows with increasing excitation power due to the larger number of FCs being produced in the conduction band. Second, the decay times associated with both central energy and the FWHM of the resonance tend to get longer with increased excitation powers.

The large spectral shifts and broadening observed in the ultrafast response of the SAMs results in high values of $\Delta T/T$, as seen in Fig. 4.18a. Thus, at moderate excitation fluences of $P \approx 50$ $\mu\mathrm{J/cm}^2$ values of $\Delta T/T \approx 1$ can be observed near the resonance wavelengths. These large modulation amplitudes are unprecedented for metal and semiconductor nanostructures and can be very attractive for all optical switching applications. The maximum resonance shifts and spectral broadening show similar power dependence (Fig. 4.18b), starting to saturate for fluences above $P \approx 50$ $\mu\mathrm{J/cm}^2$.

The characteristic time scales $\tau_\mu(P)$ & $\tau_\Gamma(P)$ are extracted by a single exponent best fit for each power are shown in Figs. 4.18c and 4.18d. The transient decays and mono-exponential fits of the FWHM and mean energy are shown plotted semi-logarithmically in Fig. 4.19. These plots are normalized to their fitted constant factor (c in $a\exp(-bt)+c$) such that they go to zero at large times. In this way, when plotted semi-logarithmically, the signal and fits should be linear. Indeed they are and the slopes are seen to flatten

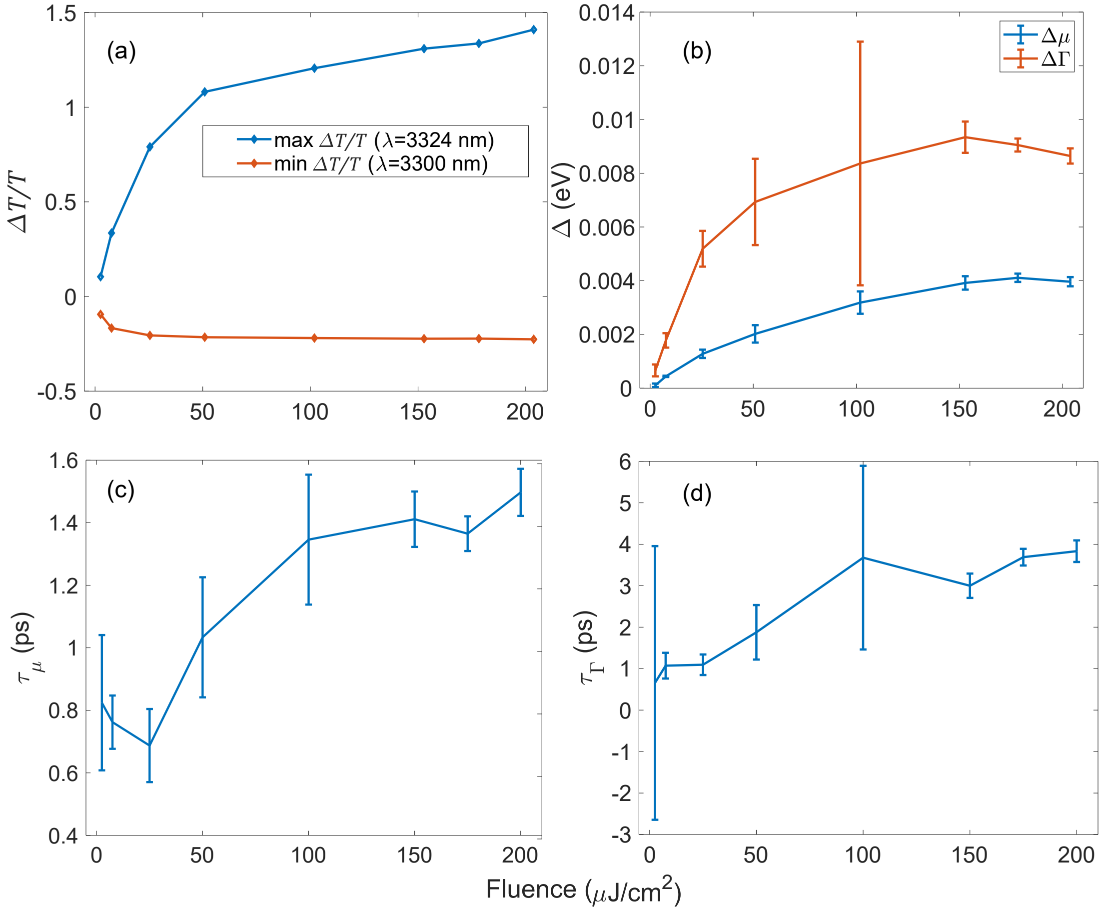

Figure 4.18: (a) The maximum and minimum values of $\Delta T/T$ for each pump fluence, occurring at close to zero pump–probe delay. The maximum $\Delta T/T$ is observed at a probe wavelength of $\lambda_{\text{probe}} = 3.324\ \mu$m (close to the resonance dip), whereas the minimum $\Delta T/T$ is observed at a probe wavelength of $\lambda_{\text{probe}} = 3.3\ \mu$m, on the blue side of the resonance. (b) The maximum initial displacement for $\mu(t=0)$ and $\Gamma(t=0)$ for each pump fluence. (c), (d) The extracted decay times of τ_μ and τ_Γ, respectively, extracted from the exponential fits as functions of the pump fluence.

with increasing power indicating increasing decay lifetimes.

For lower fluences ($2.5-50\ \mu$J/cm^2), the extracted timescales from the decays exhibit picosecond dynamics. For higher powers ($100-200\ \mu$J/cm^2) the characteristic timescales of the decay to equilibrium are seen to increase monotonically. Importantly, the timescales extracted from both μ and Γ for a given power are in a good agreement with one another, differing only by a factor of ~ 2. The discrepancy between τ_μ and τ_Γ the relaxation times at high fluences can be attributed to the asymmetric contributions of the phonon density to these quantities, as seen in Fig. 4.17. Even though these quantities appear to have different relaxation times, microscopically, they are governed by the same quantity, the hot free carrier density, which is used in the theoretical model below. The longer relaxation times at increased excitation power densities can be attributed to the electronic plasma heat capacity, which is a temperature-dependent quantity, resulting in

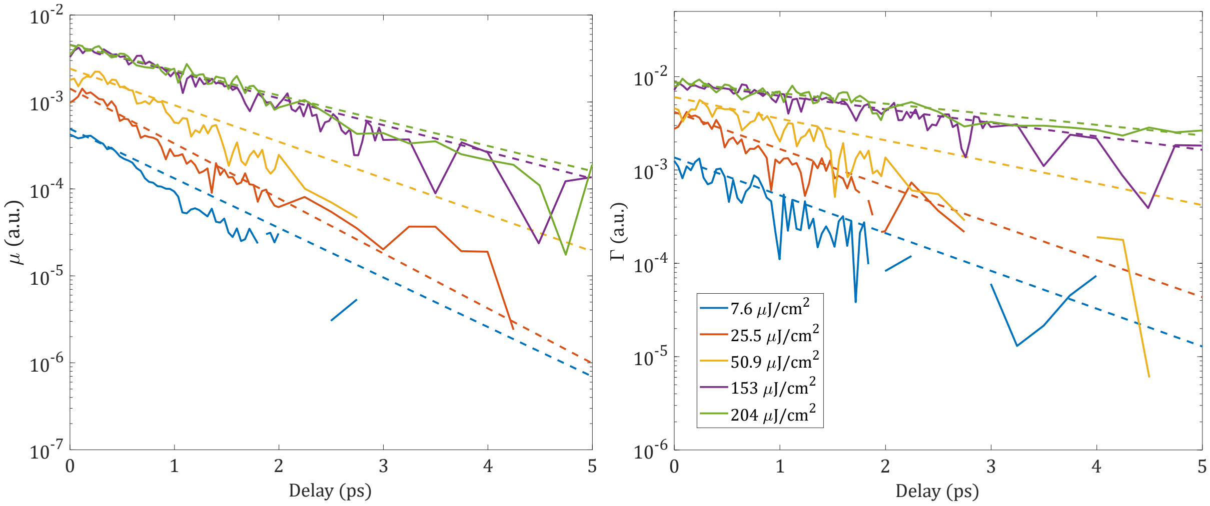

Figure 4.19: Mean energy and FWHM plotted semi-logarithmically.

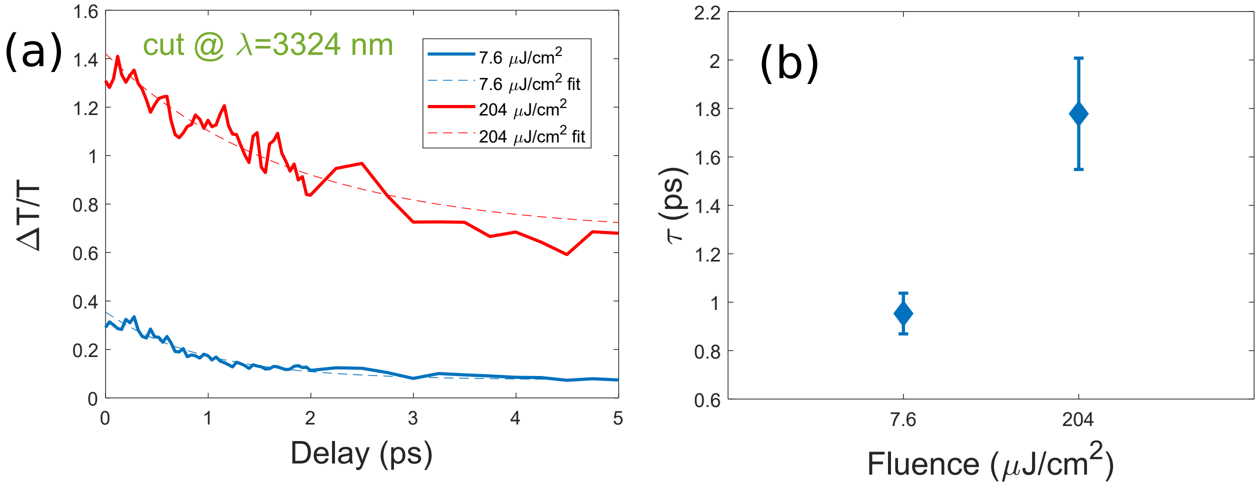

Figure 4.20: (a) $\Delta T/T$ trace cut at $\lambda = 3324$ nm for 7.6 & 204 μJ/cm^2. Dotted lines show the mono-exponential fits. (b) Decay times extracted from fit parameters.

longer electron-phonon coupling times at elevated electron temperatures [12, 109].

The decay dynamics of the $\Delta T/T$ traces for fluences of 7.6 & 204 μJ/cm^2 shown in Figs. 4.10a and 4.10b are shown in Fig. 4.20a. A mono-exponential fit was used at the resonant wavelength, cut at $\lambda = 3324$ nm of the $\Delta T/T$ traces. The mono-exponential fits are of the form $ae^{-bt} + c$ where c is obtained from experimental data. The fits are in good agreement with the transient signals. The decay parameters are extracted and shown in Fig 4.20b. For 7.6 μJ/cm^2 the decay time was found to be 0.95 ps within a 95% confidence interval of 0.88 and 1.04 ps. For 204 μJ/cm^2 the decay time was found to be 1.78 ps within a 95% confidence interval of 1.58 and 2.04 ps. These are in excellent agreement with the decay parameters shown in Fig. 4.18c extracted from Gaussian fitting to T traces shown in Figs. 4.10c and 4.10d.

4.5 Theoretical Model

An optical pulse with a photon energy above the band gap of an intrinsic semiconductor such as Ge gets absorbed and generates carriers, electrons and holes, in the conduction and valence bands, respectively. The increased electron and hole concentration results in the modification of semiconductor permittivity [134] via the Drude model as discussed in section 1.5.4 as

$$\epsilon = \epsilon_{\mathrm{bg}} - \frac{\omega_{\mathrm{p,e}}^2}{\omega^2 + i\omega\gamma_{\mathrm{e}}} - \frac{\omega_{\mathrm{p,h}}^2}{\omega^2 + i\omega\gamma_{\mathrm{h}}}, \tag{4.13}$$

where ϵ_{bg} is the permittivity of Ge structure without the optical pump, $\omega_{\mathrm{p,e}}$ is the plasma frequency contributed by electrons and equal to $\sqrt{N_{\mathrm{e}}e^2/\epsilon_0 m_{\mathrm{e}}}$, N_{e} is the concentration of electrons, m_{e} is the conductivity effective mass of electrons occupying the conduction band (equal to $0.12m_0$, where m_0 is the mass of a free electron), $\omega_{\mathrm{p,h}}$ is the plasma frequency contributed by holes and is equal to $\sqrt{N_{\mathrm{h}}e^2/\epsilon_0 m_{\mathrm{h}}}$, N_h is the concentration of holes, m_h is the effective mass of holes generated in the valence band (equal to $0.3m_0$), γ_{e} and γ_{h} are the damping rates of electrons and holes, respectively.

An estimate for the given experimental parameters used show that the single-band effective mass approximation is reasonable to assume. Nonparabolic bands can be described by

$$\frac{\hbar^2 k^2}{2m^*} = E + CE^2, \tag{4.14}$$

were C is a constant characterizing the nonparabolicity of bands [135]. This will cause the effective mass of free carriers (FCs) at high energy states to be smaller than the effective masses at the conduction band minimum and the valence band maximum. This reduced effective mass of FCs attributed to nonparabolicity of bands leads to the red-shift of plasma frequency in crystalline and amorphous ENZ materials, such as ITO [119] and doped CdO [136]. However, the effective mass only increases 15% when pumped with a fluence of 339 μJ/cm^2, which is higher than what is used here. The plasma frequency only has a slight change when the FC temperature is below 2000 K. Compared with the main contribution of increased order of magnitude of FC concentration, the small influence on the plasma frequency from the reduced effective mass due to nonparabolic bands can be neglected. The increased FC concentrations make plasma frequency significantly blue shift while the effect of nonparabolicity results in slight red shifts. Hence, the overall effect is dominated by variations of the FC concentrations instead of effective masses, especially when the electron temperature is only 1000-2000 K, as used in this work. The blue shift was also identified by the resonance shift of our metasurface in experiments. There are still some small discrepancies of spectral resonance between simulations and experiments. Simulations predict larger blue shifts than what the measured spectrum showed in the case of 204 μJ/cm^2. Finally, it is important to note that kT is only 0.17 eV at 2000 K. Assuming that the excited carriers are predominately generated at the gamma point, the band nonparabolicity becomes significant at energies that are at least factor of two higher than kT. Therefore, it is reasonable to believe that the effective mass approach is justified, and both the non-parabolicity of bands and higher-order transitions may be neglected.

The number of generated electrons and holes is assumed to be the same in intrinsic semiconductors without any doping. Here, $N_{\mathrm{e}} \approx N_{\mathrm{h}}$, namely the carrier concentration denoted by $N = N_{\mathrm{e}} = N_{\mathrm{h}}$ as is shown in Fig. 1.9 (a). Here it is assumed that the intrinsic carrier concentration in the steady state can be neglected compared with the FCs generated by optical pumping.

The carrier concentration, N, is related to the carrier temperature, T, via

$$N = 2\left(\frac{2\pi kT}{h^2}\right)^{3/2} \left(m_{\mathrm{e,d}} m_{\mathrm{h}}\right)^{3/4} M_{\mathrm{e}}^{1/2} \exp\left(\frac{-E_{\mathrm{g}}}{2kT}\right) \tag{4.15}$$

where k is Boltzmann's constant, h is Planck's constant, $m_{\mathrm{e,d}}$ is the density-of-state effective mass of electrons in conduction band (equal to $0.22m_0$), M_{e} is the number of equivalent minima in the conduction band (equal to 4) and E_{g} is the band gap energy (here equal to 0.66 eV). The ellipsoidal equal-energy surface for Ge makes different transverse mass and longitudinal mass so there are slight differences between the conductivity effective mass and the density-of-state effective mass. The density-of-state effective mass is defined by the geometric mean rather than the harmonic mean such as what is used for the conductivity effective mass in the Drude model [137]. It should be noted that amorphous materials do not have a well-defined bandstructure as with crystalline materials. So it is feasible the real effective mass in the material could be slightly different from the value in this model. The relation of eq. 4.15 means that the more FCs are injected by optical pumping, the higher temperature they are thermalized to.

The initial injected carrier concentration is proportional to the pump fluence, P, as

$$N = \frac{P A p_x p_y}{E_{\mathrm{photon}} V} \tag{4.16}$$

where A is the absorption of the metasurface at the pump wavelength equivalent to the photon energy of E_{photon}, p_x and p_y are the periods along x and y, respectively, and $V = h w_x w_y$ is the volume of a single Ge cuboid. The above equation is based on the assumption that each absorbed photon will generate an electron in the conduction band and a hole in the valence band and that carriers are uniformly distributed in Ge structures. Hence, carrier concentrations and associated carrier temperatures at zero time delay for different pump fluences in experiments are calculated and shown in Table 4.1 along with the calculated

Table 4.1: Calculated carrier concentration, carrier temperature, electron (hole) plasma frequency and damping rate for a given pump fluence.

Pump fluence (μJ/cm^2)	Carrier concentration (cm^{-3})	Carrier temperature (K)	Electrons		Holes	
			Plasma frequency $\times10^{13}$ rad/s	Damping rate $\times10^{14}$ rad/s	Plasma frequency $\times10^{13}$ rad/s	Damping rate $\times10^{14}$ rad/s
2.55	2.65×10^{17}	810	8.4	8.0	5.3	5.1
7.6	7.9×10^{17}	980	14.5	8.8	9.2	5.6
25.5	2.65×10^{18}	1250	26.5	9.9	16.7	6.3
50.9	5.3×10^{18}	1470	37.4	10.8	23.7	6.8
102	1.06×10^{19}	1760	53	11.8	33.5	7.4
153	1.59×10^{19}	1970	65	12.5	41	7.9
178	1.85×10^{19}	2070	70	12.7	44	8.1
204	2.13×10^{19}	2150	75	13.0	48	8.2

plasma frequency and decay rate for both electrons and holes for reference.

The damping rates of electrons and holes in the Drude model are also temperature-dependent. The damping rate is equal to $1/\tau$, where τ is the average collision time of carriers. The collision time τ is estimated as $\ell_{\text{free}}/v_{\text{th}}$, where v_{th} is the thermal velocity of carriers equal to $\sqrt{3kT/m_{\text{e/h}}}$ for electrons and holes, and ℓ_{free} is the mean free path of carriers [138]. The mean free path in a-Ge is significantly shorter than that in crystalline Ge due to the dominant disorder-mediated scattering mechanism and depends on the degree of disorder characterized by a small number ξ. An approximate estimation of the mean free path is given by

$$\ell_{\text{free}} = \frac{a}{\xi^2} \tag{4.17}$$

where a is the crystalline spacing equal to 2.5 Å [139, 140]. Hence, the FC temperature-dependent damping rate can be calculated by the following

$$\gamma_{\text{e/h}} = \sqrt{\frac{3kT}{m_{\text{e/h}}}}\frac{\xi^2}{a}. \tag{4.18}$$

The time dependence of the normalized carrier concentration can be seen in Fig. 4.21a for two fluences. For higher fluence, the decay time can be seen to be much larger than for the lower value, corresponding to the different pump-induced temperatures. The calculated carrier concentration is also plotted semi-logarithmically in Fig. 4.22. Again, a linear slope is observed showing the goodness of the mono-exponential fit.

Based on the above analysis, the pump fluence affects the carrier concentration and the latter affects the plasma frequency and the carrier temperature. The carrier temperature further influences the damping rate of carriers. Therefore, the pump fluence finally determines the permittivity of a-Ge according to the Drude model. The real and imaginary parts of the permittivity of a-Ge structure with different pump fluences used in the experiments can be calculated and are shown in Fig. 4.21b.

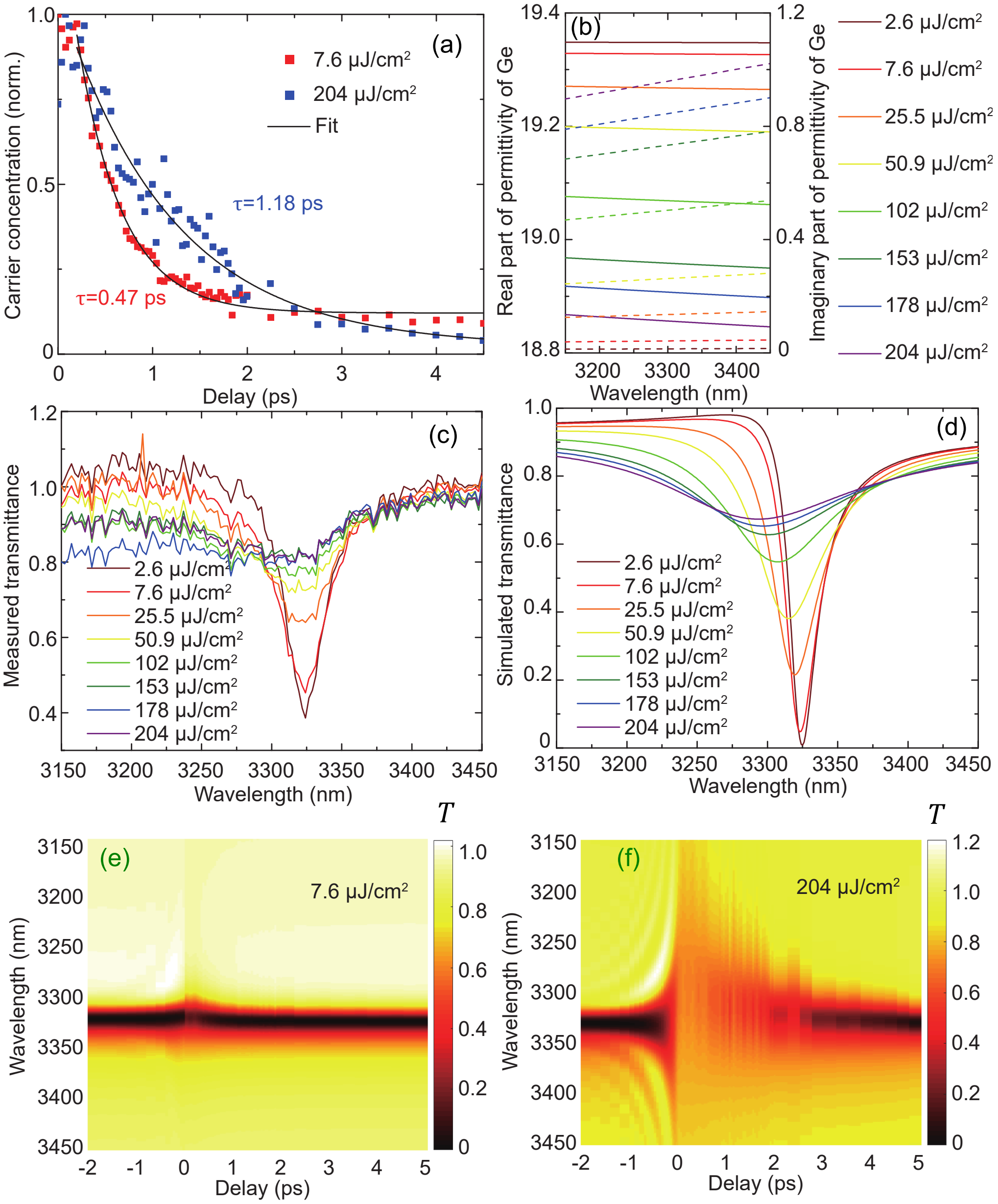

Figure 4.21: (a) Calculated carrier concentration as a function of time for the highest and lowest fluences. (b) Calculated real and imaginary parts of a-Ge permittivity. (c) Experimental transmittance at $\tau = 0$ ps for various fluences. (d) Simulated data at $\tau = 0$ ps for the same fluence values as in (c). (e) Simulated transmittance for 7.6 μJ/cm^2 and (f) 204 μJ/cm^2

Experimental transmissions at zero time delay are shown in Fig. 4.21c. Comparison shows that ξ should be set at 0.6 for best agreement between the simulated results (Fig. 4.21d) and experimental data. Given the modified permittivity by the pump pulse, the transmissions of the metasurface with different pump fluences can be calculated and are shown in Figs. 4.21e and 4.21f.

4.6 Simulations

Transmittance spectra of the metasurface for the positive time delay were simulated by the open sourced Matlab code [141] based on rigorous coupled wave analysis (RCWA). The geometric parameters were the same as those shown in the SEM image and the refractive index of Ge and CaF_2 were set as 4.4 and 1.42, respectively. With optical pumping, the permittivity of Ge was modeled by the Drude model using eq. 4.13, where plasma frequencies and damping rates at different fluence were obtained from the aforementioned theoretical model.

Transmission spectra for the negative time delay were simulated by the time-dependent solver in COMSOL Multiphysics. In the time domain, the constitutive relation in Ge described by the Drude model between the electric displacement $\vec{D}$ and the electric field $\vec{E}$ should be written by

$$\vec{D}(\vec{r},t) = \epsilon_0\epsilon_{\mathrm{bg}}\vec{E}(\vec{r},t) + \vec{P}_{\mathrm{e}}(\vec{r},t) + \vec{P}_{\mathrm{h}}(\vec{r},t) \tag{4.19}$$

where ϵ_0 is the vacuum permittivity constant, ϵ_{bg} is relative permittivity of the background, $\vec{P}_{\mathrm{e}}$ and $\vec{P}_{\mathrm{h}}$ are the polarization fields contributed by free electrons and holes, respectively. The dynamics of $\vec{P}_{\mathrm{e}}$ and $\vec{P}_{\mathrm{h}}$ in

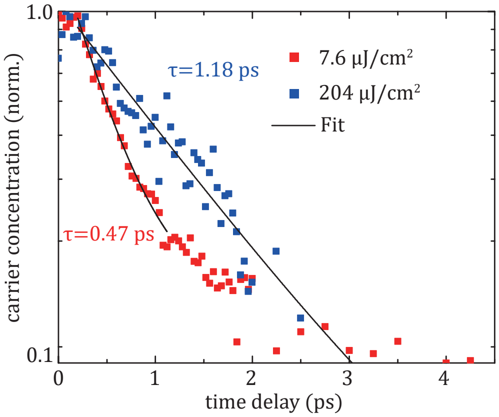

Figure 4.22: Calculated carrier concentration plotted semi-logarithmically.

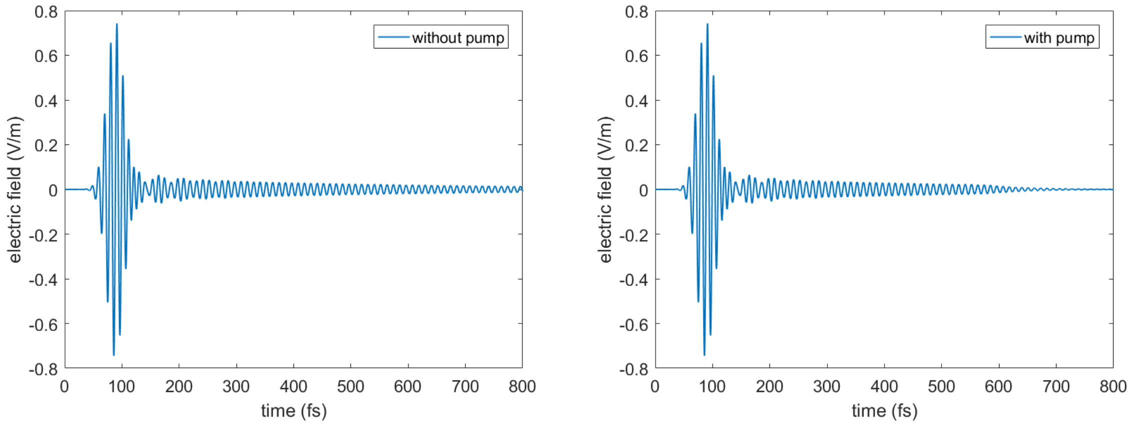

Figure 4.23: Time domain for pump fluence of 204 μJ/cm^2 at delay time of -0.5 ps.

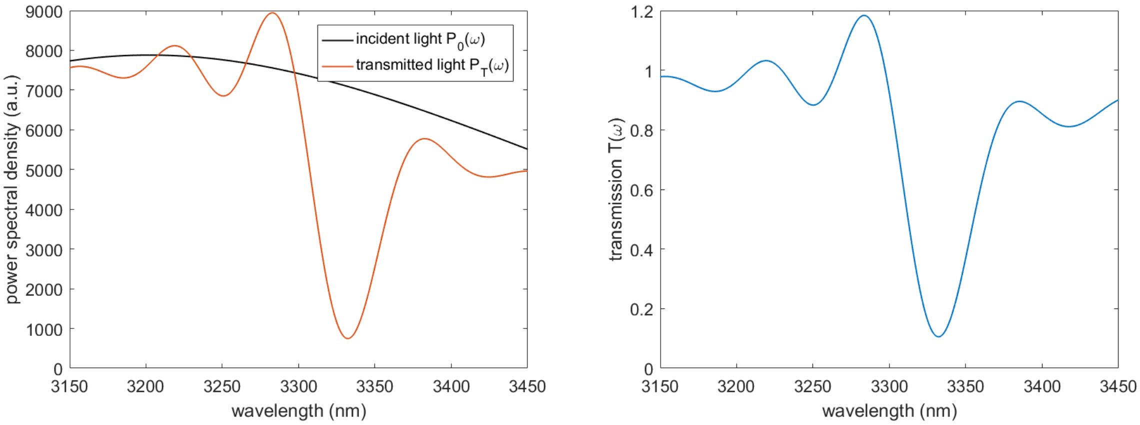

Figure 4.24: Frequency domain for pump fluence of 204 μJ/cm^2 at delay time of -0.5 ps.

time domain driven by the electric field $\vec{E}$ follow the equations

$$\frac{\partial^2}{\partial t^2}\vec{P}_{\mathrm{e}}(\vec{r},t)+\gamma_{\mathrm{e}}\frac{\partial}{\partial t}\vec{P}_{\mathrm{e}}(\vec{r},t)=\epsilon_0 f(t)\omega_{\mathrm{p,e}}^2\vec{E}(\vec{r},t) \tag{4.20}$$

$$\frac{\partial^2}{\partial t^2}\vec{P}_{\mathrm{h}}(\vec{r},t)+\gamma_{\mathrm{h}}\frac{\partial}{\partial t}\vec{P}_{\mathrm{h}}(\vec{r},t)=\epsilon_0 f(t)\omega_{\mathrm{p,h}}^2\vec{E}(\vec{r},t) \tag{4.21}$$

where $f(t)$ is a unit step function equal to 1 after the time of the pump pulse arrival and equal to 0 before that.

A Gaussian enveloped pulse polarized along the short axis of aGe structures was used as the light source, with an electric field expressed as

$$E_0(t)=\cos(\omega_0 t)\exp\left[-(t-t_0)^2/\Delta t^2\right] \tag{4.22}$$

where ω_0 is the central frequency corresponding to the wavelength of 3.3 μm, Δt is the pulse length of 20 fs and t_0 is the time shift set as 60 fs. Such a source covers the wavelength from 3000 nm to 3500 nm. The transmitted electric field, which has the same polarization with the incident field, at 3.5 μm below the Ge structures was retrieved as $E_{\mathrm{T}}(t)$ when simulations were finished. The resulted transmission $T(\omega)$ in frequency domain was calculated via Fourier transform as below

$$T(\omega) = P_{\mathrm{T}}(\omega)/P_0(\omega) = \epsilon_{\mathrm{sub}} \left| FT\left\{E_{\mathrm{T}}(t)\right\}\right|^2 / \left|FT\left\{E_0(t)\right\}\right|^2 \tag{4.23}$$

where $P_{\mathrm{T}}(\omega)$ is the transmitted power spectral density, $P_0(\omega)$ is the incident power spectral density, $FT\{.\}$ denotes the Fourier transform and ϵ_{sub} is the relative permittivity of the $\mathrm{CaF_2}$ substrate equal to 1.42. An example for pump fluence of 204 μJ/cm^2 at delay time of -0.5 ps for the time and frequency domains is given in Figs. 4.23 & 4.24.

The Drude-Lorentz polarization model was used to describe the FC dynamics in the Ge antenna, where oscillator strengths were set as a time-dependent step function starting from zero to describe FC injections due to the arrival of the pump pulse. Resonance frequencies were zero due to the ignored Lorentz parts. Damping rates and plasma frequencies were also calculated following the procedure outlined in the Theoretical Model section. The electric field distributions on resonance were simulated by frequency-domain solver in COMSOL Multiphysics.

4.7 Discussion

Typically, metallic FC-based optical switching offers faster dynamics than dielectric counterparts [104, 113]. However, the dependence of the system on the effective temperature, T_{eff}, is a large draw back as the modulation speed of the optically switched system will need longer than picosecond dynamics to return to equilibrium, which is undesirable. This is originated by the fact that the electron-phonon coupling rate, $\Gamma_{\mathrm{e-ph}}$, is inversely proportional to the induced temperature [109]. Therefore, the higher effective temperature, the lower the ability to dissipate this thermal energy into lattice, and the longer it takes to return to equilibrium. The main contributor of subpicosecond dynamics are electron-electron scattering processes, $\Gamma_{\mathrm{e-e}}$. However, these dynamics are typically very fast, on the order of 1–10 fs, much shorter than the resolution of the pump-probe technique used in this work, and so cannot be considered as a viable mechanism of the observed phenomena [109, 142]. It is proposed that because of the amorphous structure of the a-Ge material, there is substantially more scattering of FCs in this SAM. This results in more efficient coupling of thermal energy transfer back into the lattice, resulting in faster dynamics. However, this does not affect the efficiency of initial FC production, as this occurs afterwards. Therefore, the strong signal switching strength and also low power consumption associated with FCs are maintained, but with additional fast picosecond dynamics due to increased electron-phonon scattering.

These results presented here show great merit for all-optical switching when weighing the three main considerations of power consumption, switching speed and signal modulation. A comparison with the results in this work to state-of-the-art all-optical switching platforms [110, 113, 115, 119, 143] is given in Table 4.2. Both the reported differential and absolute modulation values (if readily available) are given from the referenced works to highlight their overall modulation responses and better illustrate the comparison to and significance of this presented work. These findings surpass previous works in all the mentioned categories as compared to other metamaterial platforms which operate in the MIR spectral range. Additionally, these results are comparable or greater in one or more categories when compared to NIR and visible wavelength ranges. Although some of the devices listed in this table have provided better figures for one of the characteristics, the device utilized in this study served as a platform where all three parameters are optimized.

In conclusion, experimentally observed efficient and ultrafast all-optical switching in semiconductor active metasurfaces based on a-Ge is reported. Transmittance modulations at $\Delta T/T \approx 1$, with pump fluences at $P \approx 50$ μJ/cm^2 and FC relaxation at $\tau \sim 0.5$ ps (Fig. 4.25) are attributed to increased electron-phonon scattering of FCs due to the amorphous structure of a-Ge lattice, as well as to the presence of an engineered high Q-factor resonance determined by the shape of the metasurface's constituent elements. Designer a-Ge metasurfaces offer a novel and robust platform for optical switching, to find applications in

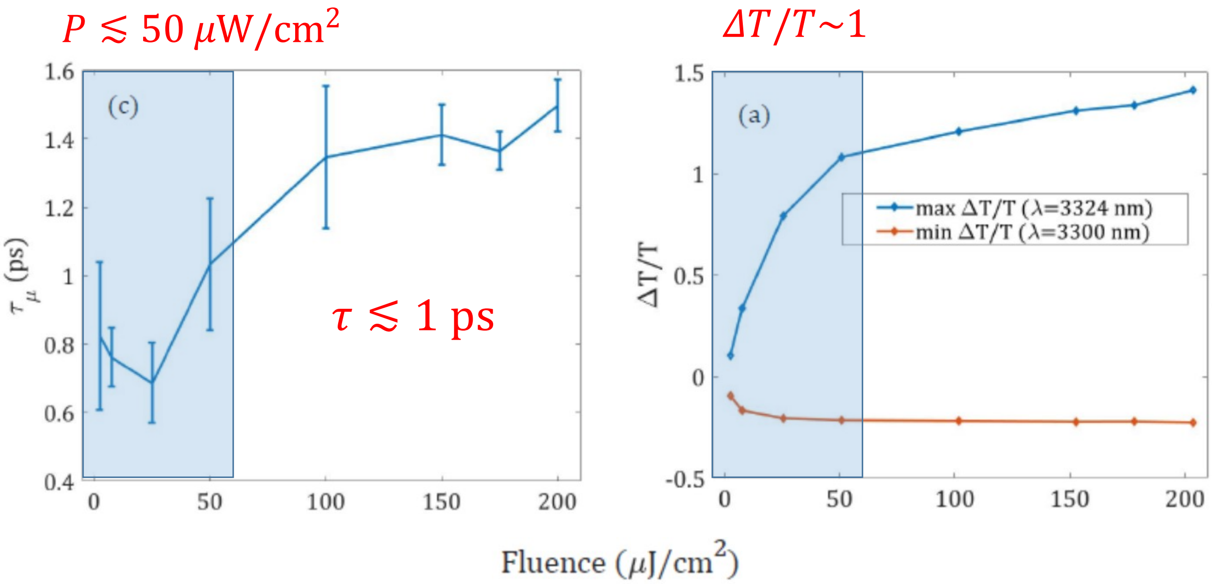

Figure 4.25: Graphic highlighting the conclusions and attributes of the aGe SAM.

Table 4.2: Comparison of platform, operating fluence, switching speed, signal modulation, spectral width and spectral range to other works.

Reference	Metamaterial Platform	Operating Fluence (μJ/cm^2)	Switching Speed (fs)	Signal Modulation (%)	Spectral Width (nm)*	Spectral Range
this work	a-Ge cuboid micro-arrays	50	1000	36(ΔT) 100 ($\Delta T/T$)	~3250-3350 (11 meV)	MIR
this work	a-Ge cuboid micro-arrays	7.6	470	13 (ΔT) 33 ($\Delta T/T$)	~3290-3350 (7 meV)	MIR
[113]	a-Si nanodisks	1000	65	50 (ΔT)	~760-785 (52 meV)	NIR
[115]	GaAs nanopillars	150	2500	31 (ΔR)	~960-975 (20 meV)	NIR
[119]	ITO nanoresonator array	7000	600	20 (ΔT)	~1400-1900 (233 meV)	NIR, MIR
[143]	a-Si negative-index metamaterial	1200	600	20 (ΔT)	~1500-1800 (138 meV)	NIR
[110]	plasmonic nanorod metamaterial	7000	760	80 ($\Delta T/T$)	~450-600 (689 meV)	Visible
[123]	GaP film	22000	30	70 ($\Delta T/T$)	~600-1000 (827 meV)	Visible
[124]	GaP nanodisks	1000	100	40 ($\Delta R/R$)	~790-830 (76 meV)	Visible
[125]	a-GaP film	500	20	5 ($\Delta R/R$)	~670-710 (104 meV)	Visible/NIR

* The spectral width in units of meV is calculated by $(hc/e)(1/\lambda_{\text{short}} - 1/\lambda_{\text{long}})$ where h is Planck's constant, c is the speed of light, e is the elementary charge and λ_{short} & λ_{long} are the shortest and longest wavelengths for a given spectral range.

active spatiotemporal beam shaping and all-optical data processing.

Concluding Remarks

The systems studied in this dissertation exhibit novel and exciting optical and electronic behavior. What's quite remarkable is that most of the observations shown here can be explained with relatively simple models which only need to consider the dynamics of hot-carriers (HCs) in the system. We summarize the main results of the presented three studies and their contribution to the understanding of the physics in each respective system in this final section.

Chapter 2 demonstrates spatially confined nanostructure geometries which exhibit very efficient HC generation. Photoluminescence (PL) from rough metallic films has been previously observed and seen to have a characteristic nonlinear behavior which is a function of the HC distribution temperature. This behavior was attributed to intraband transitions within the conduction band, made possible via momentum scattering from strongly localized plasmon modes. However, the exact mechanism of PL from metal nanostructures is still somewhat contentious, and other works featuring different geometries and methods have suggested that mechanisms such as Raman scattering or multiphoton processes are the dominate effects. Most studies have only explored this effect in a binary way in the form of rough versus smooth film PL or single particle versus aggregate particles. By restricting to merely the limiting cases of surface features via these binary methods, discrepancies between studies is perhaps unsurprisingly a common occurrence. Although the role of surface features supporting plasmon modes is generally agreed to facilitate PL, the onset of this momentum scattering process due to spatial symmetry breaking and its influence on intraband transitions has not been systematically investigated.

Fundamental to understanding plasmon-mediated transitions of this sort is the role of Landau damping of the associated plasmonic modes which is wavevector dependent. In this mechanism, larger wavevectors are damped exponentially more than smaller ones. It is by this physical process that the plasmon energy and momentum are actually dissipated into the material and excitation of HCs is possible. We show the onset and enhancement of Landau damping by correlating the efficiency of PL emission with progressively larger imposed wavevectors associated with increasingly spatially confined geometries of the plasmon modes. We support this conclusion by simultaneously eliminating potential contributions to the PL signal from other effects known to have influence on emission. This is done by systematically probing emission contributors such as field enhancement, plasmonic polarization dependence, surface roughness and laser fluence. We find these geometries result in very efficient HC promotion for very low fluences. Additionally, and perhaps most exciting, is the observation of signatures of non-Fermi athermal electron distributions in the nonlinear power dependence of the PL for higher fluences. Such “population inversion” like distributions have been inferred from ultrafast pump-probe experiments, but not observed directly via some radiative process such as PL. We find that the characteristic lineshape for non-Fermi distributions shows strikingly similar qualitative behavior to the observed power law lineshapes for increasingly confined spatial geometries, including the appearance of two linear regimes and tapering of the power exponent in the high and low emitted photon energy regimes. Our findings show that HC promotion is dramatically enhanced via Landau damping in these nanoscopic plasmonic geometries, potentially to the point of facilitating the formation of non-Fermi HC distributions which are long lived enough to be involved with the PL emission process. The characteristic power law lineshape for this non-Fermi distribution has not been reported to the best of the authors knowledge. However, the clear reproducibilty of the many qualitative features of NPL suggests that this mechanism should be considered along with previously mentioned emission processes for analysis of light emission from plasmonic nanostructures.

Chapter 3 outlines fabrication procedures for producing ultrathin (< 5 nm) fully percolated ultrasmooth gold films on oxide substrates. It is well known that coinage metals such as gold do not adhere well with oxides. A result of this is poor quality films at the interface between these materials. This is unfortunate as many favorable optical and electronic properties are expected from structures of this type. However, because of poor film quality, these properties are not readily realizable. We show that fully percolated plasmonic gold films on oxide substrates down to record thin 3 nm thicknesses can be achieved via cryogenic cooling of substrate temperatures prior to gold film deposition. Additionally, we show preliminary data which demonstrates some of the novel optical effects which are possible via films of this type such as dramatically enhanced NPL emission.

Chapter 4 illustrates several novel and ultrafast optical properties of a semiconductor based active metasurface comprised of amorphous Germanium microstructure arrays supporting high Q-factor photonic resonances in the MIR spectral region. We find two regimes of particular interest via ultrafast pump-probe measurements. In the traditional pump-probe configuration, the results presented here show great merit for efficient all-optical switching when weighing the three main considerations of power consumption, switching speed and signal modulation. In other state of the art all-optical switching platforms it is typical to have one or two of these attributes optimized at the sacrifice of the others. We report transmittance modulations of $\Delta T/T \approx 1$, with pump fluences at $P \approx 50\ \mu\text{J/cm}^2$ and FC relaxation at $\tau \sim 0.5$ ps. These properties are attributed to increased electron-phonon scattering of FCs due to the amorphous structure of a-Ge lattice, as well as to the presence of an engineered high Q-factor resonance determined by the shape of the metasurface's constituent elements. We also report observations of femtosecond frequency conversion due to dynamic Q-factor switching. This results in novel spectral undulations in the transient optical response in probe-pump configuration, a phenomenon which was unreported to the best of the authors knowledge at the time of our original publication. We find that both of these spectral responses, i.e. in the pump-probe and probe-pump regimes can be completely modeled and reproduced with a simple model based on a dynamic FC density and increased damping due to amorphous structure considerations.

Published Work at Emory

1. R. Lemasters, M. R. Shcherbakov, G. Yang, Z. Fan, J. Song, T. Lian, H. Harutyunyan and G. Shvets, "Deep Optical Switching on Subpicosecond Timescales in an Amorphous Ge Metasurface." *Advanced Optical Materials* **9**(10), 2100240, (2021)

2. A. V. Agrawal, R. Lemasters, C. Li, A. Mojibpour, P. Bharadwaj, H. Harutyunyan and M. Kumar, "Comparison of Enhanced Second Harmonic Generation in Pyramid-like In-Plane MoS$_2$ Flakes to Vertical Aligned MoS$_2$ Flakes Due to Defect Engineering." *Journal of Applied Physics* **129**(6), 063106, (2021)

3. R. Freeman, R. Lemasters, T. Kalejaiye, F. Wang, G. Chen, M. Wu, V. Demidov, S. Demokritov, H. Harutnyunyan and S. Urazhdin, "Brillouin Light Scattering of Spin Waves Inaccessible with Free-Space Light." *Physical Review Research* **2**(3), 033427, (2020)

4. H. Harutyunyan, F. Suchanek, R. Lemasters and J. J. Foley IV, "Hot-Carrier Dynamics in Catalysis." *MRS Bulletin* **45**(1), 32-36, (2020)

5. R. Lemasters, C. Zhang, M. Manjare, W. Zhu, J. Song, S. Urazhdin, H. Lezec, A. Agrawal and H. Harutyunyan, "Ultrathin Wetting Layer-Free Plasmonic Gold Films." *ACS Photonics* **6**(11), 2600-2606, (2019)

6. M. R. Shcherbakov, R. Lemasters, Z. Fan, J. Song, T. Lian, H. Harutyunyan and G. Shvets, "Femtosecond Frequency Conversion by Dynamic Losses in a Time-Variant Metasurface." *Optica* **6**(11), 1441-1442, (2019)

7. F. Wang, M. Manjare, R. Lemasters, C. Li and H. Harutyunyan, "Enhancing Second Harmonic Generation Using Dipolar-Parity Modes in Non-Planar Plasmonic Nanocavities." *Optics Letters* **44**(11), 2787-2790, (2019)

8. S. H. Shams Mousavi, R. Lemasters, F. Wang, A. Eshaghian Dorche, H. Taheri, A. A. Eftekhar, H. Harutyunyan and A. Adibi, "Phase-Matched Nonlinear Second-Harmonic Generation in Plasmonic Metasurfaces." *Nanophotonics* **8**(4), 607-612, (2019)

9. [Manuscript in Preparation] R. Lemasters, M. Manjare, R. Freeman, L. Pierce, F. Weng, G. Yang, C. Li, S. Urazhdin and H. Harutyunyan, "Effects of Spatial Confinement on Nonlinear Light Emission from Plasmonic Nanostructures." (Expected 2021)

Bibliography

[1] L. Novotny and B. Hecht, *Principles of nano-optics.* Cambridge, UK: Cambridge University Press, 2012.

[2] L. Landau, E. M. Lifshitz, J. B. Sykes, J. S. Bell, M. J. Kearsley, and L. P. Pitaevskii, *Electrodynamics of continuous media. Volume 8 of Course of Theoretical Physics.* Oxford, United Kingdom.: Pergamon Press., 1 ed., 1960.

[3] R. W. Boyd, *Nonlinear Optics.* Elsevier, AP Academic Press, 2020.

[4] B. E. A. Saleh and M. C. Teich, *Fundamentals of Photonics.* Wiley, 2nd ed., 2011.

[5] U. Kreibig and M. Vollmer, *Optical properties of metal clusters.* Berlin: Springer., 1995.

[6] C. F. Bohren and D. R. Huffman, *Absorption and scattering of light by small particles.* New York: Wiley, 1983.

[7] R. Trebino, "Rick trebino complete course lectures." https://frog.gatech.edu/talks.html, Access date: June 15th 2021.

[8] L. Novotny and N. van Hulst, "Antennas for light," *Nat. Phot*, vol. 5, pp. 83–90, 2011.

[9] S. H. Shams Mousavi, R. Lemasters, F. Wang, A. E. Dorche, H. Taheri, A. A. Eftekhar, H. Harutyunyan, and A. Adibi, "Phase-matched nonlinear second-harmonic generation in plasmonic metasurfaces," *Nanophotonics*, vol. 8, no. 4, p. 607–612, 2019.

[10] F. Wang, M. Manjare, R. Lemasters, C. Li, and H. Harutyunyan, "Enhancing second-harmonic generation using dipolar-parity modes in non-planar plasmonic nanocavities.," *Opt. Lett.*, vol. 44, no. 11, pp. 2787–2790, 2019.

[11] A. V. Agrawal, R. Lemasters, C. Li, A. Mojibpour, P. Bharadwaj, H. Harutyunyan, and M. Kumar, "Comparison of enhanced second harmonic generation in pyramid-like in-plane mos_2 flakes to vertically aligned mos_2 flakes," *Journal of Applied Physics*, vol. 129, no. 6, p. 063106, 2021.

[12] M. Taghinejad and W. Cai, “All-optical control of light in micro- and nanophotonics.,” *ACS Photonics.*, vol. 6, no. 5, pp. 1082–1093, 2019.

[13] V. Myroshnychenko, J. Rodríguez-Fernández, I. Pastoriza-Santos, A. M. Funston, C. Novo, P. Mulvaney, and F. J. Liz-Marzán, L. M.and García de Abajo, “Modelling the optical response of gold nanoparticles,” *Chem. Soc. Rev.*, vol. 37, no. 9, p. 1792, 2008.

[14] H. Kuwata, H. Tamaru, K. Esumi, and K. Miyano, “Resonant light scattering from metal nanoparticles: Practical analysis beyond rayleigh approximation,” *App. Phys. Lett.*, vol. 83, no. 22, pp. 4625–4627, 2003.

[15] W. Rechberger, A. Hohenau, A. Leitner, J. R. Krenn, B. Lamprecht, and F. R. Aussenegg, “Optical properties of two interacting gold nanoproperties,” *Opt. Comm*, vol. 220, pp. 137–141, 2003.

[16] H. Hu, H. Duan, J. K. W. Yang, and Z. X. Shen, “Plasmon-modulated photoluminescence of individual gold nanostructures,” *Am. Chem. Soc. Nano*, vol. 6, pp. 10147–10155, 2012.

[17] H. Harutyunyan, A. B. F. Martinson, D. Rosenmann, L. K. Khorashad, L. V. Besteiro, A. O. Govorov, and G. P. Wiederrecht, “Anomalous ultrafast dynamics of hot plasmonic electrons in nanostructures with hot spots,” *Nat. Nano.*, vol. 10, pp. 770–775, 2015.

[18] F. Benz, B. de Nijs, C. Tserkezis, R. Chikkaraddy, D. O. Sigle, L. Pukenas, S. D. Evans, J. Aizpurua, and J. J. Baumberg, “Generalized circuit model for coupled plasmonic systems,” *Optics Express*, vol. 23, no. 26, p. 33255, 2015.

[19] C. Sonnichsen, T. Franzl, T. Wilk, G. von Plessen, and J. Feldmann, “Drastic reduction of plasmon dephasing in gold nanorods,” *Phys. Rev. Lett*, vol. 88, p. 077402, 2002.

[20] T. Frölich, C. Schönenberger, and M. Calame, “Additional peak appearing in the one-photon luminescence of single gold nanorods,” *Opt. Soc. Am*, vol. 41, pp. 1325–1328, 2016.

[21] A. Hoggard, L. Wang, L. Ma, Y. Fang, G. You, J. Olson, Z. Liu, W. Chang, P. M. Ajayan, and S. Link, “Using the plasmon linewidth to calculate the time and efficiency of electron transfer between gold nanorods and graphene,” *Am. Chem. Soc. Nano*, vol. 7, pp. 11209–11217, 2013.

[22] L. Landau, “On the vibrations of the electronic plasma,” *Collected Papers of L.D. Landau*, pp. 445–460, 1945.

[23] W. Herr, “Introduction to Landau Damping,” p. 27 p, 2014. Comments: 27 pages, contribution to the CAS - CERN Accelerator School: Advanced Accelerator Physics Course, Trondheim, Norway, 18-29 Aug 2013.

[24] E. H. Kennard, “Zur quantenmechanik einfacher bewegungstypen,” *Zeitschrift Fur Physik*, vol. 44, no. 4-5, p. 326–352, 1927.

[25] R. Loudon, *The quantum theory of light.* Oxford: Oxford University Press, 2010.

[26] N. W. Ashcroft and N. D. Mermin, *Solid State Physics.* New Delhi, India.: Cengage Learning., 1 ed., 1976.

[27] A. O. Govorov, H. Zhang, and Y. K. Gun’ko, “Theory of photoinjection of hot plasmonic carriers from metal nanostructures into semiconductors and surface molecules,” *J. Phys. Chem*, vol. 117, pp. 16616–16631, 2013.

[28] M. L. Brongersma, H. J. Naomi, and P. Norlander, “Plasmon-induced hot carrier science and technology,” *Nat. Nano.*, vol. 10, pp. 25–34, 2015.

[29] G. V. Hartland, “Optical studies of dynamics in noble metal nanostructures,” *Am. Chem. Soc*, vol. 111, pp. 3858–3887, 2011.

[30] C. Sun, F. Vallée, L. H. Acioli, E. P. Ippen, and J. G. Fujimoto, “Femtosecond-tunable measurement of electron thermalization in gold,” *Phys. Rev. B*, vol. 50, no. 20, pp. 15337–15348, 1994.

[31] J. J. Quinn, “Range of excited electrons in metals,” *Phys. Rev*, vol. 126, no. 4, pp. 1453–1457, 1962.

[32] A. Manjavacus, J. G. Liu, V. Kulkarni, and P. Nordlander, “Plasmon-induced hot carriers in metallic nanoparticles,” *Am. Chem. Soc. Nano*, vol. 8, pp. 7630–7638, 2014.

[33] A. O. Govorov, H. Zhang, H. V. Demir, and Y. K. Gun’ko, “Photogeneration of hot plasmonic electrons with metal nanocrystals: Quantum description and potential applications,” *Nano. Today*, vol. 9, pp. 85–101, 2014.

[34] H. Zhang and A. O. Govorov, “Optical generation of hot plasmonic carriers in metal nanocrystals: The effects of shape and field enhancement,” *J. Phys. Chem*, vol. 118, pp. 7606–7614, 2014.

[35] L. Roloff, P. Klemm, I. Gronwald, R. Huber, J. M. Lupton, and S. Bange, “Light emission from gold nanoparticles under ultrafast near-infrared excitation: Thermal radiation, inelastic light scattering, or multiphoton luminescence?,” *Nano Letters*, vol. 17, no. 12, p. 7914–7919, 2017.

[36] T. Haug, P. Klemm, S. Bange, and J. M. Lupton, "Hot-electron intraband luminescence from single hot spots in noble-metal nanoparticle films," *Phys. Rev. Lett*, vol. 115, p. 067403, 2015.

[37] G. T. Boyd, Z. H. Yu, and Y. R. Shen, "Photoinduced luminescence from the noble metals and its enhancement on roughened surfaces," *Physical Review B*, vol. 33, no. 12, pp. 7923–7936, 1986.

[38] P. Muhlschlegel, H. J. Eisler, O. J. F. Martin, B. Hecht, and D. W. Pohl, "Resonant optical antennas," *Science*, vol. 308, no. 5728, pp. 1607–1609, 2005.

[39] Y. Cai, E. Sung, R. Zhang, L. J. Tauzin, J. G. Liu, B. Ostovar, Y. Zhang, W. Chang, P. Norlander, and S. Link, "Anti-stokes emission from hot carriers in gold nanorods," *Nano Lett.*, vol. 19, no. 2, pp. 1067–1073, 2019.

[40] A. Mooradian, "Photoluminescence of metals," *Phys. Rev. Lett*, vol. 22, pp. 185–187, 1968.

[41] J. P. Heritage, J. G. Bergman, Pinczuk, and J. M. Worlock, "Surface picosecond raman gain spectroscopy of a cyanide monolayer on silver," *Chemical Physics Letters*, vol. 67, no. 2-3, pp. 229–232, 1978.

[42] A. Otto, "Surface enhanced raman scattering (sers), what do we know?," *Applications of Surface Science*, vol. 6, no. 3-4, pp. 309–355, 1980.

[43] J. C. Tsang, J. R. Kirtley, and T. N. Theis, "Surface plasmon polariton contributions to strokes emission from molecular monolayers on periodic ag surfaces," *Solid State Communications*, vol. 35, no. 9, pp. 667–670, 1980.

[44] T. Heilpern, M. M., A. O. Govorov, G. P. Wiederrecht, S. K. Gray, and H. Harutyunyan, "Determination of hot carrier energy distributions from inversion of ultrafast pump-probe reflectivity measurements," *Nature Communications*, vol. 9, no. 1, 2018.

[45] Nanopartz INC., "Gold nanoparticles for nanotechnology." https://www.nanopartz.com/, Access date: June 24th 2021.

[46] M. Manjare, F. Wang, S. G. Rodrigo, and H. Harutyunyan, "Exposing optical near fields of plasmonic patch nanoantennas," *Applied Physics Letters*, vol. 111, no. 22, p. 221106, 2017.

[47] P. O. Oviroh, R. Akbarzadeh, D. Pan, and R. A. M. Coetzee, "New development of atomic layer deposition: processes, methods and applications," *Science and Technology of Advanced Materials*, vol. 20, no. 1, pp. 465–496, 2019.

[48] R. Lemasters, C. Zhang, M. Manjare, W. Zhu, J. Song, S. Urazhdin, H. J. Lezec, A. Agrawal, and H. Harutyunyan, "Ultrathin wetting layer-free plasmonic gold films," *ACS Photonics*, vol. 6, no. 11, p. 2600–2606, 2019.

[49] N. Meinzer, W. L. Barnes, and I. R. Hooper, "Plasmonic meta-atoms and metasurfaces," *Nat. Photonics*, vol. 8, p. 889, 2014.

[50] A. Poddubny, I. Iorsh, P. Belov, and Y. Kivshar, "Hyperbolic metamaterials," *Nat. Photonics*, vol. 7, p. 948, 2013.

[51] P. Genevet, F. Capasso, F. Aieta, M. Khorasaninejad, and R. Devlin, "Recent advances in planar optics: from plasmonic to dielectric metasurfaces," *Optica*, vol. 4, pp. 139–152, 2017.

[52] K. M. McPeak, S. V. Jayanti, S. J. P. Kress, S. Meyer, S. Iotti, A. Rossinelli, and D. J. Norris, "Plasmonic films can easily be better: Rules and recipes," *ACS Photonics*, vol. 2, pp. 326–333, 2015.

[53] P. Nagpal, N. C. Lindquist, S.-H. Oh, and D. J. Norris, "Ultrasmooth patterned metals for plasmonics and metamaterials," *Science*, vol. 325, pp. 594–597, 2009.

[54] C. Zhang, D. Zhao, D. Gu, H. Kim, T. Ling, Y.-K. R. Wu, and L. J. Guo, "An ultrathin smooth, and low-loss al-doped ag film and its application as a transparent electrode in organic photovoltaics," *Adv. Mater*, vol. 26, pp. 5696–5701, 2014.

[55] S. A. Maier, *Plasmonics: Fundamentals and Applications.* 2007.

[56] P. Berini, "Long-range surface plasmon polaritons," *Adv. Opt*, vol. 1, pp. 484–588, 2009.

[57] C. Haffner, D. Chelladurai, Y. Fedoryshyn, A. Josten, B. Baeuerle, W. Heni, T. Watanabe, T. Cui, B. Cheng, S. Saha, D. L. Elder, L. R. Dalton, A. Boltasseva, V. M. Shalaev, N. Kinsey, and J. Leuthold, "Low-loss plasmon-assisted electro-optic modulator," *Nature*, vol. 556, pp. 483–486, 2018.

[58] W. Zhu, T. Xu, H. Wang, C. Zhang, P. B. Deotare, A. Agrawal, and H. J. Lezec, "Surface plasmon polariton laser based on a metallic trench fabry-perot resonator," *Sci. Adv*, vol. 3, p. e1700909, 2017.

[59] M. I. Stockman, "Nanoplasmonic sensing and detection," *Science*, vol. 348, pp. 287–288, 2015.

[60] K. M. Mayer and J. H. Hafner, "Localized surface plasmon resonance sensors," *Chem. Rev*, vol. 111, pp. 3828–3857, 2011.

[61] N. Yu, P. Genevet, M. A. Kats, F. Aieta, J.-P. Tetienne, F. Capasso, and Z. Gaburro, "Light propagation with phase discontinuities: Generalized laws of reflection and refraction," *Science*, vol. 334, pp. 333–337, 2011.

[62] C. Zhang, C. Pfeiffer, T. Jang, V. Ray, M. Junda, P. Uprety, N. Podraza, A. Grbic, and L. J. Guo, "Breaking malus' law: Highly efficient, broadband, and angular robust asymmetric light transmitting metasurface," *Laser Photonics Rev*, vol. 10, pp. 791–798, 2016.

[63] R. A. Maniyara, D. Rodrigo, R. Yu, J. Canet-Ferrer, D. S. Ghosh, R. Yongsunthon, D. E. Baker, A. Rezikyan, G. de Abajo, F. J., and V. Pruneri, "Tunable plasmons in ultrathin metal films," *Nat. Photonics*, vol. 13, pp. 328–333, 2019.

[64] B. O'Connor, C. Haughn, K.-H. An, K. P. Pipe, and M. Shtein, "Transparent and conductive electrodes based on unpatterned, thin metal films," *Appl. Phys. Lett. 4*, vol. 93, p. 22330, 2008.

[65] J. Yun, "Ultrathin metal films for transparent electrodes of flexible optoelectronic devices," *Adv. Funct. Mater*, vol. 27, no. 16066, p. 41, 2017.

[66] R. B. Pode, C. J. Lee, D. G. Moon, and J. I. Han, "Transparent conducting metal electrode for top emission organic light-emitting devices: Ca–ag double layer," *Appl. Phys. Lett*, vol. 84, pp. 4614–4616, 2004.

[67] D. S. Hecht, L. Hu, and G. Irvin, "Emerging transparent electrodes based on thin films of carbon nanotubes, graphene, and metallic nanostructures," *Adv. Mater*, vol. 23, pp. 1482–1513, 2011.

[68] C. Zhang, Q. Huang, Q. Cui, C. Ji, Z. Zhang, X. Chen, T. George, S. Zhao, and L. J. Guo, "High-performance large-scale flexible optoelectronics using ultrathin silver films with tunable properties. acs appl," *Mater. Interfaces*, vol. 11, pp. 27216–27225, 2019.

[69] I. I. Smolyaninov, *Hyperbolic Metamaterials.* Morgan & Claypool Publishers, 2018.

[70] G. Subramania, A. J. Fischer, and T. S. Luk, "Optical properties of metal-dielectric based epsilon near zero metamaterials," *Appl. Phys Lett. 7*, vol. 101, p. 24110, 2012.

[71] G. Vidal, J. I. Latorre, E. Rico, and A. Kitaev, "Entanglement in quantum critical phenomena," *Phys. Rev Lett. 2*, vol. 90, p. 22790, 2003.

[72] H. Qian, Y. Xiao, and Z. Liu, "Giant kerr response of ultrathin gold films from quantum size effect," *Nat. Commun*, vol. 7, p. 13153, 2016.

[73] R. S. Sennett and G. D. Scott, "The structure of evaporated metal films and their optical properties," *JOSA*, vol. 40, pp. 203–211, 1950.

[74] I. Doron-Mor, Z. Barkay, N. Filip-Granit, A. Vaskevich, and I. Rubinstein, "Ultrathin gold island films on silanized glass: Morphology and optical properties," *Chem. Mater*, vol. 16, pp. 3476–3483, 2004.

[75] A. B. Tesler, L. Chuntonov, T. Karakouz, T. A. Bendikov, G. Haran, A. Vaskevich, and I. Rubinstein, "Tunable localized plasmon transducers prepared by thermal dewetting of percolated evaporated gold films," *J. Phys. Chem. C*, vol. 115, pp. 24642–24652, 2011.

[76] A. Todeschini, M. ane Bastos da Silva Fanta, F. Jensen, J. B. Wagner, and A. Han, "Influence of ti and cr adhesion layers on ultrathin au films," *ACS Appl. Mater. Interfaces*, vol. 9, pp. 37374–37385, 2017.

[77] J. Xie, Y. Bi, M. Ye, Z. Rao, L. Shu, P. Lin, X. Zeng, and S. Ke, "Epitaxial ultrathin au films on transparent mica with oxide wetting layer applied to organic light-emitting devices," *Appl. Phys. Lett*, vol. 114, p. 081902, 2019.

[78] A. Kossoy, V. Merk, D. Simakov, K. Leosson, S. Kéna-Cohen, and S. A. Maier, "Optical and structural properties of ultra-thin gold films," *Adv. Opt. Mater*, vol. 3, pp. 71–77, 2015.

[79] D. I. Yakubovsky, Y. V. Stebunov, R. V. Kirtaev, G. A. Ermolaev, M. S. Mironov, S. M. Novikov, A. V. Arsenin, and V. S. Volkov, "Ultrathin and ultrasmooth gold films on monolayer mos2," *Adv. Mater. Interf*, vol. 0, p. 1900196, 2019.

[80] K. Leosson, S. Ingason Arni, A. B., K. A., O. S., and G. M. C., "Ultra-thin gold films on transparent polymers," *Nanophotonics*, vol. 2, p. 3, 2013.

[81] Z. M. Abd El-Fattah, V. Mkhitaryan, J. Brede, L. Fernández, C. Li, Q. Guo, A. Ghosh, A. R. Echarri, D. Naveh, F. Xia, J. E. Ortega, and F. J. García de Abajo, "Plasmonics in atomically thin crystalline silver films," *ACS Nano*, vol. 13, pp. 7771–7779, 2019.

[82] C. T. Campbell, "Ultrathin metal films and particles on oxide surfaces: structural, electronic and chemisorptive properties," *Surf. Sci. Rep*, vol. 27, pp. 1–111, 1997.

[83] N. Kaiser, "Review of the fundamentals of thin-film growth," *Appl. Opt*, vol. 41, pp. 3053–3060, 2002.

[84] U. Diebold, J. M. Pan, and T. E. Madey, "Growth mode of ultrathin copper overlayers on $\mathrm{tio}_2(110)$," *Phys. Rev. B*, vol. 47, pp. 3868–3876, 1993.

[85] T. C. Zhang, Z. X. Mei, Y. Guo, Q. K. Xue, and X. L. Du, "Influence of growth temperature on formation of continuous ag thin film on zno surface by ultra-high vacuum deposition," *J. Phys. D: Appl. Phys*, vol. 42, p. 065303, 2009.

[86] W. F. Egelhoff and I. Jacob, "Reflection high-energy electron diffraction (rheed) oscillations at 77 k," *Phys. Rev. Lett*, vol. 62, pp. 921–924, 1989.

[87] N. P. Sergeant, A. Hadipour, B. Niesen, D. Cheyns, P. Heremans, P. Peumans, and B. P. Rand, "Design of transparent anodes for resonant cavity enhanced light harvesting in organic solar cells," *Adv. Mater*, vol. 24, pp. 728–732, 2012.

[88] T. Stefaniuk, P. Wróbel, E. Górecka, and T. Szoplik, "Optimum deposition conditions of ultrasmooth silver nanolayers," *Nanoscale Res. Lett*, vol. 9, p. 153, 2014.

[89] H. A. van der Vegt, H. M. van Pinxteren, M. Lohmeier, E. Vlieg, and J. M. C. Thornton, "Surfactant-induced layer-by-layer growth of ag on ag(111)," *Phys. Rev. Lett*, vol. 68, pp. 3335–3338, 1992.

[90] D. Jing, B. Ünal, F. Qin, C. Yuen, J. W. Evans, C. J. Jenks, D. J. Sordelet, and P. A. Thiel, "Stranski–krastanov-like growth of an ag film on a metallic glass," *Thin Solid Films*, vol. 517, pp. 6486–6492, 2009.

[91] H. R. Pruppacher and J. D. Klett, *Microphysics of Clouds and Precipitation.* Springer, 2nd ed., 2011.

[92] S. C. Parker and C. T. Campbell, "Kinetic model for sintering of supported metal particles with improved size-dependent energetics and applications to au on $\text{tio}_2(110)$," *Phys. Rev. B*, vol. 75, p. 035430, 2007.

[93] D. W. Lynch and W. R. Hunter, "Comments on the optical constants of metals and an introduction to the data for several metals," in *Handbook of Optical Constants of Solids* (E. D. Palik, ed.), pp. 275–367, Academic Press: Burlington, 1997.

[94] C. Zhang, N. Hong, C. Ji, W. Zhu, X. Chen, A. Agrawal, Z. Zhang, T. E. Tiwald, S. Schoeche, J. N. Hilfiker, L. J. Guo, and H. J. Lezec, "Robust extraction of hyperbolic metamaterial permittivity using total internal reflection ellipsometry," *ACS Photonics*, vol. 5, pp. 2234–2242, 2018.

[95] R. Secondo, D. Fomra, N. Izyumskaya, V. Avrutin, J. N. Hilfiker, A. Martin, Ü. Özgür, and N. Kinsey, "Reliable modeling of ultrathin alternative plasmonic materials using spectroscopic ellipsometry," *Opt. Mater. Express*, vol. 9, pp. 760–770, 2019.

[96] N. Kinsey, M. Ferrera, G. V. Naik, V. E. Babicheva, V. M. Shalaev, and A. Boltasseva, "Experimental demonstration of titanium nitride plasmonic interconnects," *Opt. Express*, vol. 22, pp. 12238–12247, 2014.

[97] M. José-Yacamán, C. Gutierrez-Wing, M. Miki, D. Q. Yang, K. N. Piyakis, and E. Sacher, "Surface diffusion and coalescence of mobile metal nanoparticles," *J. Phys. Chem. B*, vol. 109, pp. 9703–9711, 2005.

[98] S. Groβmann, D. Friedrich, M. Karolak, R. Kullock, E. Krauss, M. Emmerling, G. Sangiovanni, and B. Hecht, “Nonclassical optical properties of mesoscopic gold,” *Physical Review Letters*, vol. 122, no. 24, 2019.

[99] R. Lemasters, M. R. Shcherbakov, G. Yang, J. Song, T. Lian, H. Harutyunyan, and G. Shvets, “Deep optical switching on subpicosecond timescales in an amorphous ge metamaterial,” *Advanced Optical Materials*, p. 2100240, 2021.

[100] M. R. Shcherbakov, R. Lemasters, Z. Fan, J. Song, T. Lian, H. Harutyunyan, and G. Shvets, “Time-variant metasurfaces enable tunable spectral bands of negative extinction.,” *Optica.*, vol. 6, no. 11, p. 1441, 2019.

[101] H. Chen, A. Taylor, and N. Yu, “A review of metasurfaces: physics and applications.,” *Reports on progress in physics.*, vol. 79, no. 7, p. 076401, 2016.

[102] N. Rivera, I. Kaminer, B. Zhen, J. Joannopoulos, and M. Soljačić, “Shrinking light to allow forbidden transitions on the atomic scale.,” *Science.*, vol. 353, no. 6296, pp. 263–269, 2016.

[103] C. Ciracì, R. Hill, J. Mock, Y. Urzhumov, A. Fernández-Domínguez, S. Maier, J. Pendry, A. Chilkoti, and D. Smith, “Probing the ultimate limits of plasmonic enhancement.,” *Science.*, vol. 337, no. 6098, pp. 1072–1074, 2016.

[104] H. Harutyunyan, A. Martinson, D. Rosenmann, L. Khorashad, L. Besteiro, A. Govorov, and G. Wiederrecht, “Anomalous ultrafast dynamics of hot plasmonic electrons in nanostructures with hot spots.,” *Nature Nano.*, vol. 10, pp. 770–775, 2015.

[105] A. Shaltout, V. Shalaev, and M. Brongersma, “Spatiotemporal light control with active metasurfaces.,” *Science.*, vol. 364, no. 6441, p. eaat3100, 2019.

[106] N. Yu and F. Capasso, “Flat optics with designer metasurfaces.,” *Nat. Mat.*, vol. 13, no. 2, pp. 139–150, 2014.

[107] X. Fang, M. Lun Tseng, J. Ou, K. MacDonald, D. Ping Tsai, and N. Zheludev, “Ultrafast all-optical switching via coherent modulation of metamaterial absorption.,” *Appl. Phys. Lett.*, vol. 104, no. 114, p. 141102, 2014.

[108] A. Arbabi, Y. Horie, M. Bagheri, and A. Faraon, “Dielectric metasurfaces for complete control of phase and polarization with subwavelength spatial resolution and high transmission.,” *Nat. Nano.*, vol. 10, no. 11, p. 937, 2015.

[109] C. Voisin, N. Del Fatti, D. Christofilos, and F. Vallée, “Ultrafast electron dynamics and optical nonlinearities in metal nanoparticles.,” *J. Phys. Chem.*, vol. 105, pp. 2264–2280, 2001.

[110] G. A. Wurtz, R. Pollard, W. Hendren, G. P. Wiederrecht, D. J. Gosztola, V. A. Podolskiy, and A. V. Zayats, “Designed ultrafast optical nonlinearity in a plasmonic nanorod metamaterial enhanced by nonlocality.,” *Nat. Nano.*, vol. 6, pp. 107–111, 2011.

[111] F. Wang, A. Martinson, and H. Harutyunyan, “Efficient nonlinear metasurface based on nonplanar plasmonic nanocavities.,” *ACS Photonics*, vol. 4, no. 5, pp. 1188–1194, 2017.

[112] F. Wang and H. Harutyunyan, “Tailoring the quality factors and nonlinear response in hybrid plasmonic-dielectric metasurfaces.,” *Opt. Express*, vol. 26, no. 1, pp. 120–129, 2018.

[113] M. R. Shcherbakov, P. P. Vabishchevich, A. S. Shorokhov, K. E. Chong, D. Y. Choi, I. Staude, A. E. Miroshnichenko, D. N. Neshev, A. A. Fedyanin, and Y. S. Kivshar, “Ultrafast all-optical switching with magnetic resonances in nonlinear dielectric nanostructures.,” *Nano. Lett.*, vol. 15, no. 10, pp. 6985–6990, 2015.

[114] M. R. Shcherbakov, S. Liu, V. V. Zubyuk, A. Vaskin, P. P. Vabishchevich, G. Keeler, T. Pertsch, T. V. Dolgova, I. Staude, I. Brener, and A. A. Fedyanin, “Ultrafast all-optical tuning of direct-gap semiconductor metasurfaces.,” *Nature Communications.*, vol. 8, no. 1, 2017.

[115] N. Karl, P. P. Vabishchevich, S. Liu, M. B. Sinclair, G. A. Keeler, G. M. Peake, and I. Brener, “All-optical tuning of symmetry protected quasi bound states in the continuum.,” *Appl. Phys. Lett.*, vol. 115, p. 141103, 2019.

[116] T. Tanabe, M. Notomi, S. Mitsugi, A. Shinya, and E. Kuramochi, “All-optical switches on a silicon chip realized using photonic crystal nanocavities.,” *Appl. Phys. Lett.*, vol. 87, no. 8, p. 151112, 2007.

[117] T. Tanabe, K. Nishiguchi, A. Shinya, E. Kuramochi, H. Inokawa, M. Notomi, K. Yamada, T. Tsuchizawa, T. Watanabe, H. Fukuda, H. Shinojima, and S. Itabashi, “Fast all-optical switching using ionimplanted silicon photonic crystal nanocavities.,” *Appl. Phys. Lett.*, vol. 2, no. 8, p. 465, 2007.

[118] M. Ren, B. Jia, J. Ou, E. Plum, J. Zhang, K. MacDonald, A. Nikolaenko, J. Xu, M. Gu, and N. Zheludev, “Nanostructured plasmonic medium for terahertz bandwidth all-optical switching.,” *Adv. Mat.*, vol. 23, no. 46, pp. 5540–5544, 2011.

[119] P. Guo, R. Schaller, J. Ketterson, and R. Chang, "Ultrafast switching of tunable infrared plasmons in indium tin oxide nanorod arrays with large absolute amplitude.," *Nat. Photonics.*, vol. 10, no. 4, p. 267, 2016.

[120] M. C. Nuss, D. H. Auston, and F. Capasso, "Direct subpicosecond measurement of carrier mobility of photoexcited electrons in gallium arsenide.," *Phys. Rev. Lett.*, vol. 58, no. 22, p. 2355, 1987.

[121] C. Husko, A. D. Rossi, S. Combrié, Q. V. Tran, F. Raineri, and C. W. Wong, "Ultrafast all-optical modulation in gaas photonic crystal cavities.," *Appl. Phys. Lett.*, vol. 94, no. 2, p. 021111, 2009.

[122] W. Z. Lin, L. G. Fujimoto, and E. P. Ippen, "Femtosecond carrier dynamics in GaAs.," *Appl. Phys. Lett.*, vol. 50, no. 3, p. 124, 1987.

[123] G. Grinblat, M. P. Nielsen, P. Dichtl, Y. Li, R. F. Oulton, and S. A. Maier, "Ultrafast sub-30-fs all-optical switching based on gallium phosphide.," *Science Advances*, vol. 5, no. 6, 2019.

[124] G. Grinblat, H. Zhang, M. P. Nielsen, L. Krivitsky, R. Berté, Y. Li, B. Tilmann, E. Cortés, R. F. Oulton, A. I. Kuznetsov, and S. A. Maier, "Efficient ultrafast all-optical modulation in a nonlinear crystalline gallium phosphide nanodisk at the anapole excitation.," *Science Advances*, vol. 6, no. 34, 2020.

[125] B. Tilmann, G. Grinblat, R. Berté, M. Özcan, V. F. Kunzelmann, B. Nickel, I. D. Sharp, E. Cortés, S. E. Maier, and Y. Li, "Nanostructured amorphous gallium phosphide on silica for nonlinear and ultrafast nanophotonics.," *Nanoscale Horizons*, vol. 5, no. 11, pp. 1500–1508, 2020.

[126] A. Rudenko, K. Ladutenko, S. Makarov, and T. E. Itina, "Symmetry breaking in nanoparticles: Photo-generated free carrier-induced symmetry breaking in spherical silicon nanoparticle.," *Advanced Optical Materials*, vol. 6, no. 7, p. 1870023, 2018.

[127] A. Esser, K. Seibert, H. Kurz, G. N. Parsons, C. Wang, B. N. Davidson, G. Lucovsky, and R. J. Nemanich, "Ultrafast recombination and trapping in amorphous silicon.," *Physical Review B.*, vol. 41, no. 5, pp. 2879–2884, 1990.

[128] R. Soref, "Mid-infrared photonics in silicon and germanium.," *Nature Photonics*, vol. 4, no. 8, pp. 495–497, 2010.

[129] F. T. A. Pilon, A. Lyasota, Y. M. Niquet, V. Reboud, V. Calvo, N. Pauc, J. Widiez, C. Bonzon, J. M. Hartmann, A. Chelnokov, J. Faist, and H. Sigg, "Lasing in strained germanium microbridges.," *Nature Communications*, vol. 10, no. 1, 2019.

[130] A. Osman, M. Nedeljkovic, J. S. Penades, Y. Wu, Z. Qu, A. Z. Khokhar, K. Debnath, and G. Z. Mashanovich, "Suspended low-loss germanium waveguides for the longwave infrared.," *Optics Letters*, vol. 43, no. 24, p. 5997, 2018.

[131] Q. Liu, J. M. Ramirez, V. Vakarin, X. L. Roux, A. Ballabio, J. Frigerio, D. Chrastina, G. Isella, D. Bouville, L. Vivien, C. A. Ramos, and D. Marris-Morini, "Mid-infrared sensing between 52 and 66 μm wavelengths using ge-rich sige waveguides.," *Optical Materials Express*, vol. 8, no. 5, p. 1305, 2018.

[132] K. Nozaki, T. Tanabe, A. Shinya, S. Matsuo, T. Sato, H. Taniyama, and M. Notomi, "Sub-femtojoule all-optical switching using a photonic-crystal nanocavity.," *Nat. Photonics.*, vol. 4, no. 7, pp. 477–483, 2010.

[133] M. Bosch, M. R. Shcherbakov, and G. Fan, Z. Shvets, "Polarization states synthesizer based on a thermo-optic dielectric metasurface.," *Journal of Applied Physics.*, vol. 126, no. 7, p. 073102, 2019.

[134] S. Makarov, S. Kudryashov, I. Mukhin, A. Mozharov, V. Milichko, A. Krasnok, and P. Belov, "Tuning of magnetic optical response in a dielectric nanoparticle by ultrafast photoexcitation of dense electron-hole plasma.," *Nano Letters*, vol. 15, no. 9, pp. 6187–6192, 2015.

[135] T. Pisarkiewicz and A. Kolodziej, "Nonparabolicity of the conduction band structure in degenerate tin dioxide.," *Physica Status Solidi (b)*, vol. 158, no. 1, 1990.

[136] Y. Yang, K. Kelley, E. Sachet, S. Campione, T. Luk, J. Maria, M. B. Sinclair, and I. Brener, "Femtosecond optical polarization switching using a cadmium oxide-based perfect absorber.," *Nature Photonics.*, vol. 11, no. 6, pp. 390–395, 2017.

[137] S. M. Sze, *Physics of Semiconductor Devices.* New York, USA.: John Wiley & Sons, 2 ed., 1981.

[138] D. A. Neamen, *Semiconductor physics and devices: Basic principles.* New York, USA.: McGraw-Hill, 4 ed., 2012.

[139] A. H. Clark, "Electrical and optical properties of amorphous germanium.," *Phys. Rev. Lett.*, vol. 154, no. 3, p. 750, 1967.

[140] J. Tauc, R. Grigorovici, and A. Vancu, "Optical properties and electronic structure of amorphous germanium.," *Physica Status Solidi.*, vol. 15, no. 22, pp. 627–637, 1966.

[141] J. Hugonin and P. Lalanne, *Reticolo Software for Grating Analysis.* Plaiseau, France.: Institut d'Optique, 2005.

[142] C. Sun, F. Vallée, L. H. Acioli, E. P. Ippen, , and J. G. Fujimoto, “Femtosecond-tunable measurement of electron thermalization in gold.,” *Phys. Rev. B*, vol. 50, no. 20, pp. 15337–15348, 1994.

[143] K. Dani, Z. Ku, P. Upadhya, R. Prasankumar, S. Brueck, and A. Taylor, “Subpicosecond optical switching with a negative index metamaterial,” *Nano. Lett.*, vol. 9, no. 10, pp. 3565–3569, 2009.